Silesian University of Technology

Faculty of Automatic Control, Electronics and Computer Science

Doctoral Thesis

Measurements, modelling and control of flow in grinding installation with electromagnetic mill

Author:
Oliwia Krauze

Supervisor:
prof. dr hab. inż. Marek Pawełczyk

Gliwice, 2023

Declaration of Authorship

I, the undersigned, declare that:

a) this thesis, titled "Measurements, modelling and control of flow in grinding installation with electromagnetic mill", is the outcome of my own research activity and was created without the unauthorized participation of third parties,

b) I have attributed all source materials and reviews that I had used, and the resultant thesis does not infringe third party copyrights,

c) the attached electronic version of the thesis is identical to the printout of the dissertation.

Date: _____

Signed: _____

Abstract

Measurements, modelling and control of flow in grinding installation with electromagnetic mill

Doctoral dissertation by Oliwia Krauze
Silesian University of Technology

Comminution of raw materials is a massive and large-scale process present in numerous branches of industry. New equipment and technologies are constantly being developed to improve product quality and throughput, and to decrease costs and environmental impact. One of new solutions to ultrafine grinding of hard materials is an electromagnetic mill with its dedicated grinding installation with pneumatic material transport. Being still a new invention, the system requires extensive studies (including experimental research), e.g., on dedicated measurement methods, mathematical modelling of system components, automatic control algorithms.

This thesis proposes some indirect methods for measurement of raw material features, such as flow rate, particle size and moisture content. These experimental methods are fast and contactless, though approximate, and they are based on vibration, acoustic or vision signals.

Secondly, this dissertation presents several steady-state and dynamic models (mainly of black box type), based on experiments carried out on the grinding installation with electromagnetic mill. Some models assess the mutual effects between material moisture and particle classification subsystem. Others describe steady-state and dynamic relationships between positions of air dampers (actuators) and air flows or pressures in key parts of the pneumatic transport system.

Lastly, this work introduces the hierarchical layout of control loops in the grinding installation and focuses on control of transport air flow in the lowest (direct) control layer. The flow of air is a crucial factor as it determines the flow of the processed material, thus affecting particle size distribution of the product, efficiency of the grinding process, and even its stable operation. A simulation framework is prepared to easily test air flow control schemes. Then, several types of control algorithms are tuned, assessed and compared.

The above-mentioned findings help to monitor or control some key parts of the grinding installation with electromagnetic mill, and to do it efficiently. Moreover, some research outcomes — mainly, the methods of indirect measurements — may be utilized also in other plants and processes.

Acknowledgements

I would like to thank my supervisor, prof. dr hab. inż. Marek Pawełczyk, who gave me the opportunity to work in the grinding system project (SYSMEL), suggested promising areas of investigation and kept an eye on me while still giving me a free hand in my research. Very many thanks go to all my co-researchers and co-authors — you helped me greatly during the experiments, data processing and paper preparation. Especially, dr inż. Dariusz Buchczik deserves my deep gratitude as he willingly spent hours on academic discussions with me, or in our laboratory. Also, other members of the SYSMEL project, particularly dr hab. inż. Szymon Ogonowski and mgr inż. Jan Wegehaupt, are gratefully acknowledged for their support in technical issues of the research. I express my true appreciation to my friends and colleagues from the Department of Measurements and Control Systems at the Silesian University of Technology. Along my way, you provided numerous valuable remarks, ideas for development and suggestions for problem solutions, at the same time showing general support and kindness.

All of the works presented in this thesis are linked to the grinding installation with electromagnetic mill. Thus, I hereby express my gratitude to the National Centre for Research and Development in Poland, who co-financed the installation and a substantial part of related research works under their Applied Research Programme, project number PBS3/B3/28/2015 (SYSMEL).

This endeavour would not have been possible without my family providing me enough time to work — my most sincere thanks. Special appreciation goes here to my husband Piotr, also an automatic control researcher. Apart from "standard family help", he supported me with discussions and feedback directly in my field of research. Many thanks to my fellow doctoral students, especially Karol Jabłoński and Jarosław Rzepecki — you helped to keep my motivation and spirits on a proper level. Lastly, I would like to recognize all the friends whose faith in me was sometimes bigger than my own.

I hope that we will all be satisfied with the outcome of our joint efforts.

Contents

List of Figures

List of Tables

Abbreviations

AIC	**A**kaike **I**nformation **C**riterion
EM	**E**lectro**M**agnetic
FFT	**F**ast **F**ourier **T**ransform
HSL	**H**ue, **S**aturation, **L**ightness (color space)
IAE	**I**ntegral of **A**bsolute **E**rror
MAD	**M**edian **A**bsolute **D**eviation
MAE	**M**ean **A**bsolute **E**rror
MIMO	**M**ultiple-**I**nput **M**ultiple-**O**utput (system)
MISO	**M**ultiple-**I**nput **S**ingle-**O**utput (system)
PID	**P**roportional-**I**ntegral-**D**erivative (control)
PLC	**P**rogrammable **L**ogic **C**ontroller
PSD	**P**ower **S**pectral **D**ensity
RGB	**R**ed, **G**reen, **B**lue (color space)
RMSE	**R**oot **M**ean **S**quared **E**rror
SAD	**S**um of **A**bsolute **D**ifferences
SCADA	**S**upervisory **C**ontrol **A**nd **D**ata **A**cquisition
SISO	**S**ingle-**I**nput **S**ingle-**O**utput (system)
SP	**S**et**P**oint
WMSE	**W**eighted **M**ean **S**quared **E**rror
ZOH	**Z**ero-**O**rder **H**old

Symbols

Latin symbols

AIC	Akaike Information Criterion	[–]
$\mathrm{AIC_c}$	Akaike Information Criterion corrected for small sample size	[–]
c	proportionality factor between mean and maximum air speed in pipe cross-section	[–]
D	pipe's inner diameter	[m]
D_{inch}	pipe's inner diameter	[inch]
e	pipe wall roughness	[m]
f_{EM}	frequency of electromagnetic field rotation	[Hz]
g	gravitational acceleration constant	9.80665 $\mathrm{m/s^2}$
J_P	power index for vibration/acoustic signals	$[\mathrm{m^2/s^4}]$
K	pressure loss coefficient for a pipe fitting	[–]
$\mathbf{K}$	vector of all loss coefficients calculated by optimization procedure	[–]
K_1	one of pressure loss coefficients in 2-K method	[–]
K_∞	the other pressure loss coefficient in 2-K method	[–]
k	DC gain of a transfer function	(units vary)
L	pipe length	[m]
MC	relative moisture content in the material (gravimetric wet-based moisture content)	[%]
m	mass	[kg]
m_{grind}	mass of grinding media	[kg]
N	number of observations in a dataset	[–]
n	number of parameters in a model	[–]
OS	overshoot of a dynamic response	[–]

PC	(point on the) partition curve of a particle classifier	[–]
p	relative pressure	[Pa]
p_{abs}	absolute pressure	[Pa]
p_{atm}	atmospheric pressure (absolute)	[Pa]
Q	volumetric flow rate of air	[m^3/s]
q	mass flow rate of air	[kg/s]
R^2	coefficient of determination	[–]
$\mathrm{R}^2_{\mathrm{adj}}$	adjusted coefficient of determination	[–]
Re	Reynolds number	[–]
r_{P}	Pearson's correlation coefficient	[–]
r_{S}	Spearman's rank correlation coefficient	[–]
s	Laplace variable	[1/s]
T	air temperature	[K]
T_0	time delay in a transfer function	[s]
T_1	time constant in a transfer function	[s]
T_2	second time constant in a transfer function	[s]
T_s	sampling period of a signal	[s]
t	time	[s]
$t_{n\%}$	time between the occurrence of a step change on input and the first time instant when step response reaches $n\%$ of its final steady state	[s]
u	input to a system	(units vary)
v	maximum (centerline) air speed in pipe cross-section	[m/s]
w	mean air speed in pipe cross-section	[m/s]
x	[0; 100], actual position (opening) of air damper	[%]
x_{req}	[0; 100], requested position (opening) of air damper	[%]
y	output of a system	(units vary)

Greek symbols

α	[0; 1], level of significance (in statistics)	[–]
β	[0; 1], factor describing how much the flow is laminar	[–]
$\Delta\bullet$	difference or deviation from steady-state value of signal $\bullet$	[unit of $\bullet$]
ζ	damping ratio in a transfer function	[–]

Θ	vector of all model parameters	(units vary)
λ	Darcy friction factor	[–]
μ	dynamic viscosity of air	[Pa·s]
ρ	air density	[kg/m^3]
σ	standard deviation	(units vary)
ϕ	diameter	[m] or [mm]
ω	natural (undamped) pulsation in a transfer function	[rad/s]

Non-letter symbols

$\overline{\bullet}$	average value of signal $\bullet$	[unit of $\bullet$]
$\widehat{\bullet}$	modelled value of signal $\bullet$	[unit of $\bullet$]

Frequently used subscripts

a	**a**dditional air stream
c	precise **c**lassifier
in	**in**put
m	**m**ain air stream
r	**r**ecycle air stream
SP	**s**et**p**oint
w	**w**orking chamber of the mill

To all of You who gave me all kinds of support along the way.
With gratitude.

Chapter 1

Introduction

Comminution (crushing and grinding) of raw materials is an essential stage of a wide range of industrial processes worldwide. Some examples are: coal pulverization for fossil-fuel power plants; metal ores enrichment; production of mortars and cements, paints, and paper; manufacturing of cosmetics, pharmaceuticals and food; waste recycling.

The comminution processes usually involve massive amounts of raw material and high energy consumption. For example, at mine sites the comminution stage is the most energy-consuming process, accounting typically for about 30–50% of total energy usage at the plant [4; 100] and about 35–55% of its total operating costs [24]. In total, comminution processes consume nearly 2% of all electric power generated worldwide [72]. Moreover, specific energy grows with decreasing particle size. This means more energy per unit weight of material is required to reduce average particle size N times for smaller input particles than for larger ones [59; 109]. Also, the smaller the particles, the harder it is to grind them further, and conventional technologies — such as tumbling (ball, rod, etc.) mills — are even not capable of very fine grinding [109]. Hence, considerable research and development effort is constantly devoted to improve the existing comminution technologies and to invent new ones — especially in fine and ultrafine grinding, that is, in production of particles sized tens of micrometers and less. The goal of these works is to achieve higher product quality (in terms of desired particle size, shape, surface area etc.), throughput and energetic efficiency. These improvements would be impossible without the use of dedicated measurement and control systems in the grinding installations, which creates many research opportunities in the automatic control field.

One of novel approaches to fine and ultrafine grinding involves an electromagnetic mill, which is believed to address all of the above demands. However, the device is a relatively new invention; and the innovative complete grinding system built around it, which is considered in this dissertation, is an even younger design (from year 2015 [82]). Thus,

the topic needs substantial research work, part of which was conducted by the author of this thesis and is described hereby.

It is necessary to acknowledge here the project "SYSMEL: System for grinding mineral materials in electromagnetic mill, including control system, providing high technological efficiency and low energy consumption in micro- and macroindustrial applications" (project no. PBS3/B3/28/2015). It was financed by the National Centre for Research and Development, Poland, under Applied Research Programme. A substantial amount of the work presented in this thesis, and also much of other scientists' research, was done within or in relation to this project. Also, a major part of the considered grinding installation was financed from the project.

1.1 Electromagnetic mill

Electromagnetic (EM) mill [58; 90; 95] is a powerful and versatile device used, e.g., for grinding, mixing and activation of hard substances. The mill consists mainly of an inductor of strong rotary electromagnetic field. The research included in this dissertation used an EM mill designed and manufactured by ELTRAF company [58]; it has a salient-poles inductor with a hexagonal yoke surrounding six radially arranged electromagnets (Fig. 1.1).

In the middle of the inductor, perpendicularly to it, a cylindrical working chamber is located. It is made of non-magnetic material, such as ceramics, titanium or austenitic stainless steel [34; 90]. The working chamber may be shaped as a capsule with a lid (for batch processing) or as a pipe fragment (for continuous, flow-through processing of materials). The treated substances (feed material) are supplied into the working chamber together with small ferromagnetic elements (grinding media), which are usually rod-shaped. They are shown in Fig. 1.2. The rotating electromagnetic field moves the grinding media inside the working chamber. There, they collide with the particles of the feed material. The process occurs in the whole volume of the working chamber [95]; it is turbulent and rapid. This creates a unique combination of phenomena simultaneously affecting the treated material [34; 35; 90]:

- alternating electric field of high intensity,
- alternating magnetic field of high intensity,
- high temperature,
- high local pressures,
- friction,
- acoustic phenomena (including ultrasounds).

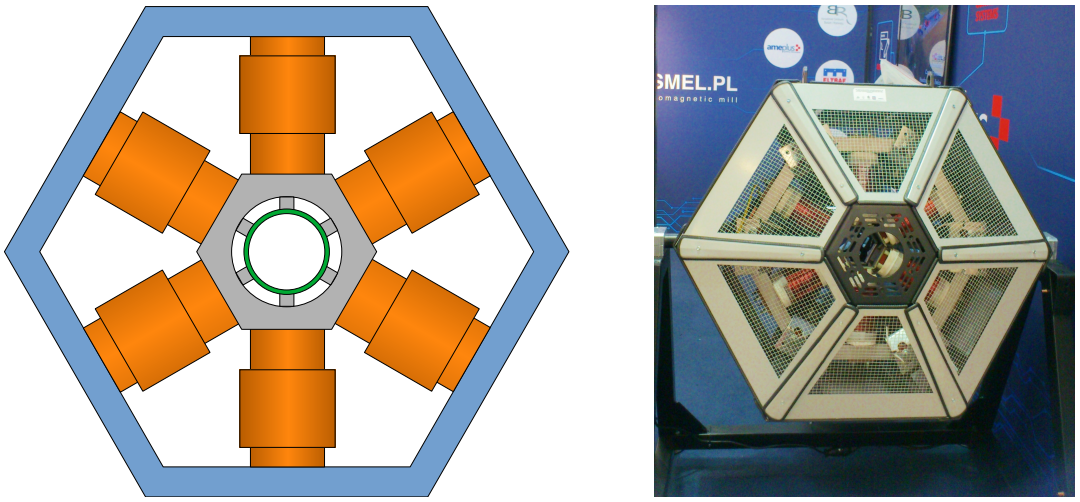

(A) (B)

FIGURE 1.1: Electromagnetic mill designed and manufactured by ELTRAF company. (A) Diagram of EM inductor: blue — yoke, orange — coils, gray — ring stabilizing the coils, green — tube serving as the working chamber (strictly, not a part of the inductor, but part of the mill). (B) Inductor in casing.

FIGURE 1.2: Standard grinding media for the EM mill: ferromagnetic rods of 10 mm length and about 1 mm diameter

Such principle of operation makes the electromagnetic mill a multifunctional device which may be used in multiple branches of industry for [34; 35; 58; 90]:

- fast fine or ultra-fine grinding of solids (in dry or wet environment),
- mixing of hard granular materials,
- mixing of liquids and gases,
- production of permanent emulsions,

– surface activation of hard materials,
– catalysing chemical reactions,
– producing active powders and compositions thereof (including mechanical alloying),
– mechanochemical synthesis of new materials,
– fluid catalytic cracking,
– modifying physical and chemical properties of substances,
– grinding and activation of fly ash, and more.

The characteristic features of the electromagnetic mill are the following:

- The intensity of the processes occurring inside the working chamber is so high that the necessary residence time of the treated materials is in the order of several to several tens of seconds. This is dozens to thousands of times faster than in conventional devices [90]. Such great speed of processing provides good throughput despite the small capacity of the working chamber (one or several litres [34; 35]).

- The mill is capable of batch or continuous processing because the working chamber may be a closed capsule or a pipe. In the case of continuous flow of material, the magnetic field itself keeps most of the grinding media inside the working area and prevents them from flowing outside, together with the processed material. The grinding elements (or their fragments) that manage to escape the working chamber may be easily isolated from the material by means of magnetic separation [34].

  What is worth noticing, many conventional devices, e.g. many mills, operate only in batch manner, which might be a drawback for some industrial processes.

- Feed material for the EM mill might be dry granular material, moistened granular material, slurry (mixture of powders and liquids), or liquid. Of course, each of them may require specific supply and transport devices, but the mill itself may operate with each of them without modifications.

- Feed material should be non-magnetic.

- When used for grinding of solids, the EM mill produces fine or ultrafine particles (i.e., sized about hundreds or tens of microns). The size of feed material's particles must also be small — up to ca. 1 mm for working chamber of diameter 100 mm, up to ca. 1.5–2 mm for chamber diameter 200 mm.

- By default, the grinding media are small steel rods of length about 10–15 mm and diameter about 1–2 mm [94; 110]. Different sizes or shapes of grinding media may be used to match the input or target particle size, or other particle parameters. For example, bigger grinding media or mixes of different sized elements seem to be more suitable for coarser feed [94; 110].

- By changing the conditions of the grinding process (such as amount of material in the working chamber; particle residence time in the working chamber; grinding media amount, size and shape; frequency of EM field rotation; moisture content in feed material; etc.), the operator may influence some physico-mechanical parameters of the output particles: their size, shape, specific surface area, surface properties, etc.

- The processed material is warmed and dried during grinding or mixing because of the heat produced inside the working chamber. This phenomenon may be especially useful if the produced material needs to have low moisture content (no or less additional drying is necessary). Moreover, high temperature helps to break up the ground particles.

- By introduction of various gases into the working chamber, the grinding or mixing processes may be conducted in specific atmosphere — reducing, oxidizing or protective — if necessary [90].

- The electromagnetic mill is relatively small, compared to conventional solutions. Its small footprint may be a big advantage for many industrial plants. For example, a ϕ100 mill (with 100 mm diameter working chamber) manufactured by ELTRAF company — inductor together with metal casing and cooling fans — is sized 113.5×70×115 cm (width×depth×height) and weighs 520 kg [35]. Their ϕ200 mill (with 200 mm diameter working chamber) has dimensions about 1.5 times bigger than ϕ100 mill and weighs 950 kg [34].

- Contrary to conventional mills, the electromagnetic mill does not include any large-size moving parts. This provides less mechanical wear of the device and less faults, which also means lower operating costs.

The research presented here regards a ϕ100 version of the EM mill [35], that is, one with working chamber of 100 mm diameter. However, the company has also designed and manufactured ϕ200 and ϕ320 mills. They are larger, have bigger capacity, induce stronger magnetic field, and also consume more power [34]. They are suitable for processing slightly coarser granular material than ϕ100 mills, and for higher-throughput applications.

1.2 Grinding systems with electromagnetic mill

1.2.1 Existing setups with EM mill

The simplest setup with EM mill involves a standalone mill operating in batch mode, with the working chamber being a cylinder with a tight lid. This capsule is not hermetic, but it is equipped with a pressure release valve for safety reasons [80; 114].

For continuous operation with continued material flow through the mill, the literature reports several setups for laboratory or industrial uses. A simple solution is a tilted EM mill, in which the feed material is sliding down the wall of the working chamber. However, this means uncontrolled sliding speed — and in effect, no or little control over grinding time. The fixed position also limits the available range of material throughput [79].

Patent application [91] proposes a tilted EM mill with adjustable tilt degree. It provides some control over the material's residence time in the working chamber. For example, grinding of coal [87], copper compounds [97] or fly-ash [25] was performed in this manner. However, this way it is still difficult to precisely control the speed of sliding particles.

In patent [88], the material is falling down a vertically positioned mill chamber, which gives even less control over grinding process. This device is mainly targeted at material drying, and grinding plays only a secondary role there. Thus, the parameters of the latter process are not much adjustable in this design.

The setups described above usually lack particle classification and recycle systems — they mainly operate with open-loop flow of the material, with no re-grinding of oversized particles. Only the solution in patent application [91] uses a sieve at mill output to classify the desired and oversized particles; but sieves are easily clogged with material.

To overcome these limitations on grinding process control and to leverage the capabilities of electromagnetic mill, an entirely new solution was proposed and patented [82]. It is used to fine-grind dry or moist materials (but still powders) and it includes a vertically positioned mill chamber, particle classifiers, recycle of coarse particles (to be re-ground), underpressure material transport and a hierarchical automatic control system to ensure best process control and optimization. This system was used for most of the research presented in this dissertation. Its details are described in the next section.

To complement the above list of setups with EM mill, it is worth noting that the mill may also perform wet grinding, that is, grinding of slurries — mixtures of solid and liquid

materials, supplied with pumps. Examples of open- and closed-loop circuits (i.e., without and with recycle of coarse material) are shown e.g. in [80, Figure 5].

1.2.2 Dry grinding circuit with electromagnetic mill

Within the mentioned SYSMEL project, a grinding system was designed, patented [82] and built that incorporated the electromagnetic mill, a dedicated underpressure system for material transport and classification, and a measurement and control system. The setup is shown in Fig. 1.3–1.4 and was described in detail e.g. in [77; 111]. The system was created to leverage the EM mill potential by providing continuous flow of material and automatic recycle of oversize particles, for the case of dry grinding, i.e. in air or other gaseous medium (not in liquids).

The working chamber of the EM mill is oriented vertically, with fresh feed material and grinding media supplied from the top by means of a controllable screw feeder. The grinding media are sustained in the mill chamber simply by magnetic force; and material particles are suspended in the air stream supplied from the bottom. Controlling this air stream provides regulation of residence time of the particles inside the mill. Small enough particles are carried from the working chamber upwards, to the preliminary classifier integrated with the mill. This element forms an internal recycle stream and prevents the particles from exiting the mill chamber prematurely. Next, a precise particle classifier is located; inertial-impingement classifier was employed [112], but other designs are also possible to use. This classifier selects the particles of the desired fineness and directs them to the cyclone, where they are separated from the transport air and collected as final product; coarser particles are recycled (to be re-ground) and transported back to the mill chamber in a stream of air. This recycle material is supplied to the working chamber from the bottom, making sure that the particles come in contact with the grinding media before they are blown upwards again. Contrary, the fresh feed is deliberately delivered from the top. This allows the feed particles which are already small enough to immediately leave the mill chamber, increasing mill throughput and reducing the amount of overground (too small) particles in the final product. Additionally, water moist may be supplied to increase moisture content in the material. This helps to create optimal conditions in the mill chamber (e.g., size and shape of product particles, and energetic efficiency of grinding change with moisture level). Also, safe handling of possibly explosive dust is ensured this way.

The air flow in the system is forced by a blower mounted at the end of the installation (near air exhaust). This makes the material be transported in underpressure, rather than overpressure, which prevents dust escape through inevitable leaks in the piping. The air

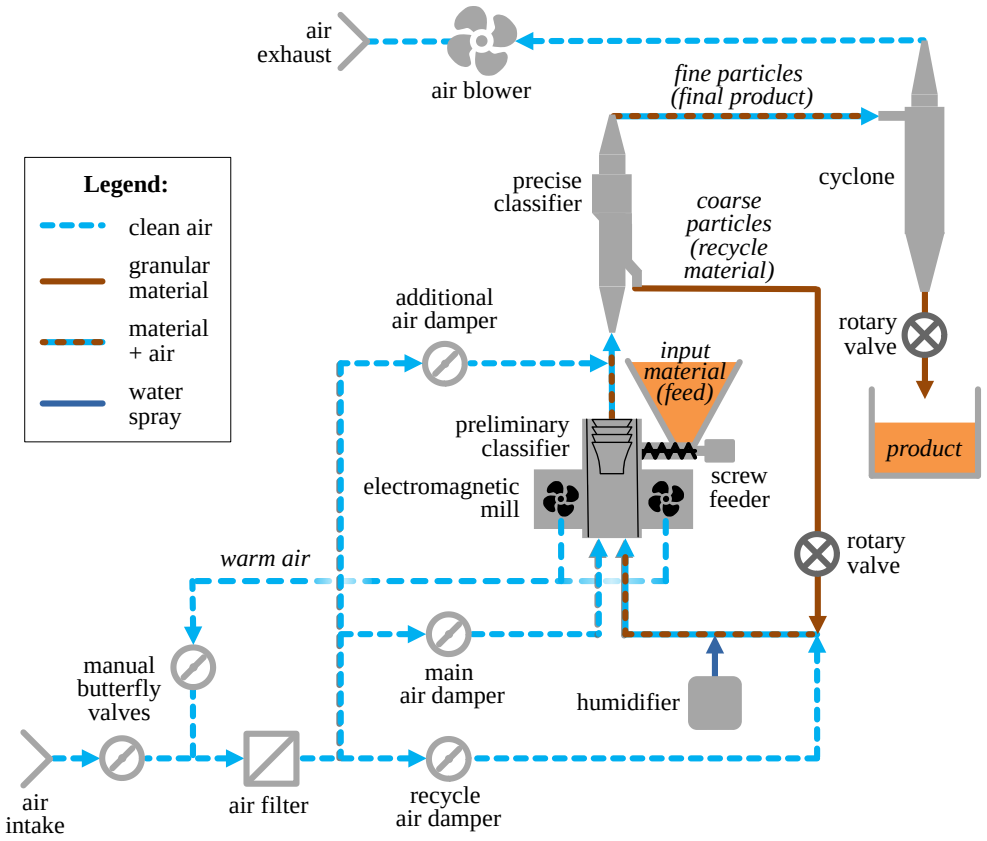

FIGURE 1.3: Diagram of dry grinding system with electromagnetic mill

FIGURE 1.4: Dry grinding system with electromagnetic mill built at the Silesian University of Technology. Rear right — EM mill and precise classifier, front right — cyclone and transport air pipes, rear left — control cabinet for automatic control systems, front left — power supply and control cabinet for EM mill's inductor.

is supplied from a single filtered intake through three streams with controllable butterfly dampers. The main air stream keeps the material in the mill chamber. The recycle air stream also contributes to it, and carries the coarse product of classification back to the mill. The additional air stream allows to achieve the required air flow through the precise classifier without having excessive flow through the mill chamber.

The electromagnetic field inductor creates significant amounts of heat during operation and needs cooling. So, several fans are installed in the mill casing. The warm air at their output is collected at another pipe and may be directed to the input of pneumatic transport system. (Another controllable butterfly valve allows for mixing the warm "recycle" air from the cooling fans with fresh air from the intake.) This heat recovery system improves energetic efficiency of the process: it allows for even more intensive drying of (possibly damp) input material, if necessary, and aids particle breakage in the working chamber of the mill, as the heat accelerates this process.

The measurement system of the grinding circuit is quite extensive and covers many quantities throughout the whole installation. Some examples include measurements of [77; 111]:

- air speed, temperature, humidity, and pressure in several points of the pneumatic system;
- temperature of various sections of the installation;
- electric power consumed by mill inductor;
- mass of product material in the collection tank.

Moreover, some indirect measurement methods have been developed specially for this installation, such as:

- vibration (or acoustic) method for approximation of particle size and flow rate in the pipeline — see Section 2.1;
- vibroacoustic assessment of the amount of material in the mill chamber [79; 81];
- evaluation of grinding media amount in the mill chamber, based on measurements of active power generated by frequency inverter supplying the mill inductor [79];
- measurement of moisture content in feed and product material based on impedance (surface resistance) measurement and near infrared absorption [11; 101; 102];
- computer vision analysis of material moisture (Section 2.2.1), or particle size and other parameters of the final product [12–15].

On the other hand, there are numerous signals that act as manipulated variables in the control system of the grinding process. These control signals are, for example:

- base and output frequencies of the inverter supplying mill inductor;
- flow rate of fresh feed (controlled with the frequency setting of the inverter supplying the screw feeder);
- supply of grinding media;
- openings of butterfly air dampers;
- flow of water mist moisturizing the processed material.

The long list of input signals (controlled variables as well as disturbances) and output variables shows that the grinding system is a complicated plant. It appears even more complex when taking into account very different time horizons on which the many disturbances and setpoint changes occur. Moreover, there are other challenges, such as nonlinear characteristics of many elements, couplings between signals and subsystems, and the instability of material flow through the mill chamber in open-loop operation. This instability means that without proper control of the air flow, the processed material may easily fall onto mill bottom and clog the air inlet; or the opposite — the particles may be immediately blown upwards, to the classifier. This complexity makes control of the whole system a challenging task, and requires a hierarchical control system. More details on it are given in Chapter 5.

1.3 Objective and thesis of this dissertation

The objective of the dissertation is to enhance or even enable the operation of dry grinding circuit with electromagnetic mill, by: providing indirect measurement methods of material flow rate and quality, modelling of selected system components, and developing algorithms for control of transport air flow.

The thesis of the dissertation is formulated as follows:

Data processing algorithms, in particular indirect measurements and experiment-based modelling, allow to monitor and control the operation of dry grinding installation with electromagnetic mill.

1.4 Scope of the dissertation

The content of this dissertation is organized as follows:

- Chapter 2 focuses on the raw material processed in the grinding installation. Methods of measuring material flow rate, particle size and moisture content are developed and discussed. Mutual relations between material moisture and particle classification process are also investigated.

– Chapter 3 describes static and dynamic modelling of the inlet air flow in the grinding installation. Identification experiment and the hardware used in it are also detailed there.

– Chapter 4 presents inlet air flow simulator based on the above models, with its design and validation procedures.

– Chapter 5 introduces the layered control system of the grinding installation and then focuses on control of air flow. Many control schemes are designed, parametrized and then tested using extended version of the air flow simulator.

– Chapter 6 summarizes the dissertation.

– Original contributions of the author of this thesis are listed in "Author Contributions".

Chapter 2

Indirect Measurements of Raw Material Features

Modern grinding systems aim at delivering high quality end product while providing energetic efficiency. These goals require advanced automatic control systems. In turn, they need appropriate input: measurements of various quantities. Preferably, these are automatic online measurements, without taking samples for a laboratory analysis. The quantities that are essential for efficient operation of grinding plants are, among others, the ones describing the processed material — such as flow rate, but also particle size or moisture content.

Firstly, flow rate of raw material should be known in various parts of the grinding system. It is easy to estimate it for the fresh feed, which is usually supplied in a controlled way (in the discussed grinding circuit, this happens through a screw feeder with controlled rotational frequency). However, determination of material flow rate is more complicated in other points of the installation (e.g., in recycle stream), whereas these measurements are often essential. For example, material flow rate may affect the necessary flow rates of transport media, moist, heat, or amount of grinding media [55]. Moreover, excessive amounts of recycled material indicate too short grinding time and consequently, a loss in efficiency.

Secondly, particle size of the grinding product is usually the most important factor determining product quality, as too coarse or too small particles are of no use in the target processes or in the following technological stages. Thus, particle size distribution or mean size, or maximum size, etc. of the final product are valuable feedback signals for the grinding process. On the other hand, particle size of the input material (fresh feed or recycle stream) may be used in feed-forward manner. This allows for a priori parametrization of the grinding process, providing further improvement in efficiency.

Material moisture is another important parameter, in many ways [53]. Water content in the ground material affects, e.g., the necessary grinding time and shape of produced particles. Appropriate moisture level is also necessary for material transport within the grinding installation: too damp powders tend to stick to the inner walls of pipes and other elements, and too dry — pose a risk of explosion. Moreover, there might exist some requirements on the moisture content in the final product. These demands may arise from technological usability of the product, methods of its transport and storage, shelf life (durability), and so on.

Some indirect methods of measuring these quantities were developed and described in this chapter. In the case of flow rate and particle size estimation, the presented experiments and all stages of data processing were performed solely by the author of this dissertation. In the research on moisture measurements, the author was a member of a bigger team. She did not develop the measurement methods themselves, but she took part in the experiments and then in the high-level data processing. The contribution was significant enough to include also this research topic in this dissertation.

2.1 Material flow rate and particle size

2.1.1 Existing methods of solids flow measurement

In industry, volumetric or mass flow rate of solid materials in pneumatic or free-fall pipelines is measured in quite many ways. Some examples are shortly described below [38; 54; 71].

Impact flowmeter, the oldest and most common solution [71], operates on gravity-fed material. The particles flow is guided to hit a slanted sensing plate. Then, load cells or linear variable differential transformers (LVDT) measure the horizontal component of the impact force; this way, the meter determines the instantaneous mass flow rate. Taking into account only the horizontal component makes the measurement result insensitive to potential material build-up on the plate. Additional advantages of the device are easy calibration and wide measurement range. However, the contact with the material gradually damages the sensing plate, and some periodic cleaning of the plate is also needed [39].

Coriolis mass flow meter [36; 71] directs the material particles to a vaned wheel (measuring wheel) which is constantly rotated by a motor. As a result, the particles are accelerated to the wheel's speed. This generates Coriolis force (proportional to material

mass flow rate), observed on the motor as reaction torque. There are numerous advantages of such a design: the measurements are of high accuracy, not disturbed by material density, moisture content or inter-particle friction. The device is also rather small. The motor part of the meter is dust-tight, unaffected by the flowing particles. However, it is not so with the measuring wheel, so it wears from attrition. Moreover, the meter is relatively expensive and power consuming (due to the motor operation).

Another method is to generate microwave radiation inside a pipe. Thanks to Doppler effect, frequency and amplitude of microwaves reflected by flowing particles carry information about material mass flow rate [69; 71; 96]. No moving parts and practically no contact with the measured material make the sensor wear resistant. It is also relatively small. It may be used in both free-fall and pneumatic transport systems, but some limitation is that it requires metallic pipes. The mounting method is a borehole in the pipe wall plus a welded mounting bracket; so, it is only a bit intrusive, much less than in the case of the previous meters. It is also less expensive than them, but less accurate, too (compared, e.g. to Coriolis flowmeters).

It is also possible to measure pipe capacitance, proportional to material concentration inside. In combination with particle speed this produces flow rate readings [71]. To get the speed of material flowing, two sensors are mounted within a specified distance along the pipe, and the phase shift (so, time difference) between their readings is analysed. These readings may show, for instance, electrical charge, generated naturally by friction between the material and pipe walls [33; 38]. Such solution is contactless, relatively low-cost and suited to both gravity-fed and pneumatic transport systems. On the other hand, it is not very accurate and it involves three sensors for one flow rate measurement.

A similar method uses gamma or X-ray radiation in place of capacitive measurement [5]. A radiation source is placed on the pipe and the beam is attenuated mainly by the mass of material flowing across beam trajectory. So, the attenuation, measured by a radiation detector mounted opposite the source, reflects particle concentration. The method is highly accurate, contactless and non-invasive to the piping (source and detector are mounted outside the pipe, so it is not cut). However, the equipment is costly, and ionising radiation poses a risk to the plant staff. As a result, this method is often used only to calibrate other sensors. Furthermore, the radiation source needs a housing (usually made of lead and steel), which is thick and heavy, and so — requires proper support [38].

2.1.2 Existing methods of particle size measurement

A common and accurate method of assessing particle size, that gives the whole size distribution curve, is sieving on a set of laboratory sieves of decreasing aperture size (sieve hole size). However, this is an offline method — it requires material sampling, trained personnel and significant amount of time. As a result, it is rather unacceptable for continuous monitoring of long-term grinding processes. Thus, online methods were also developed (or semi-online, that is, ones that reguire taking material samples). Some of them are explained below [54].

The classical laboratory setup was adopted to continuous operation by introducing material outlet at each of the vibrating sieves in the stack [3; 44; 46]. Measuring flow rate or, simply, the increase in weight of each fraction produces current particle size distribution curves. Apart from the measurement, the material is separated into the selected size fractions, which may be an advantage for some applications. The solution is suitable for free falling material, and sieve apertures must be selected a priori. Unfortunately, sieve screens require regular cleaning because they easily get clogged with the processed material. Usually this is done automatically, by applying additional periodic excitation –e.g. with electromagnetic vibrators or unbalanced motors [108]. However, the initial sieve throughput remains impaired. Also, attrition causes gradual screen wearing.

A different approach involves machine vision systems, in several configurations. In contrast to sieving, these methods are contactless and provide size distribution curves with nearly arbitrary detail level — introducing more analysed size fractions does not involve extra equipment. Additionally, particle shapes may be investigated, not only sizes. However, processing of vision information requires strong computing capabilities.

One of such vision methods uses a light source and a line scan camera to observe the shadows of individual falling particles [107]. Such measured diameters are totalized into size distribution curves. Some difficulty is that the stream of material must be shaped into a single layer to observe single particle shadows. This is achieved with a small vibrating hopper. It also means that a representative sample from the whole stream must be provided, or the flow needs to be much limited. One more drawback is the 2D only analysis, which may give false results depending on particle orientation in space while falling (but this is the case with sieving as well). A natural extension of this setup is a 3D system containing two pairs of light source and detector, mounted at 90 degrees to each other [48].

Another group of vision methods use a camera with top view on static (not moving) material sample [12–14]. A macro lens may be necessary. A light source (or, possibly, two sources at different angles [15]) and dedicated image processing algorithms produce

particle size distributions or other statistic measures of particle size. Particle shapes, liberated metal content or more descriptors may also be provided. The mechanical setup of the material sampler might be simpler here, but it is still necessary. Also, the equipment is rather costly.

A very different principle is used in measurements of acoustic emissions caused by particles' impact on a metallic obstacle in the pipeline [41]. Particle size estimations come from peak voltages measured by the acoustic emission sensor, combined with particle speed assessed by cross-correlating three electrostatic measurements. The method may be used with pneumatic material transport. The advantages are low sensor cost, relatively little invasiveness, and less computational requirements than in vision systems. However, the accuracy is much affected by signal-to-noise ratio, so it is better for bigger particles and higher speeds. Also, some calibration is needed to match the particular type of material.

2.1.3 Proposed vibration method

The wide range of existing methods, and the list of their advantages and limitations, indicate that no solution is universally good. In particular, it is not that easy to find a method which is simultaneously online, contactless (or wear resistant), inexpensive, and uses equipment simple to install and use. There is still room for innovation, so an indirect method was proposed based on vibration sensing [51; 54; 55]. It satisfies all the above industrial requirements; however, as such, it gives only approximate results, but sufficient for providing feedback to control loops. Additional benefit of the developed method is simultaneous estimation of particle size and flow rate, from the same measurement data and using many common processing stages. Besides, vibration-based measurements are already widely used in industry (e.g. in fault detection, condition monitoring). Thus, it should be easy to introduce one more method of this type to the, rather conservative, industrial community.

When particle stream is transported in a pipeline, it causes vibrations dependent on particle size, mass and speed. They are most pronounced when the material impacts an obstacle. It may be specially introduced into some pipe cross-section, or a natural shape of the installation may be leveraged, e.g. a place where the loose material is fed, or falls, on top of some element or into a pipe. In general, the material, dimensions and other properties of the element/pipe might be optimised to accordingly shape the vibration modes. The vibrations induced by impacting particles may then be measured and processed using the numerous and well-established digital signal processing techniques.

Many approaches were examined [51], and the most effective one is presented below; but firstly, the test rig and experiment scenario are explained.

2.1.3.1 Experiment

A dedicated laboratory rig was assembled for this research (Fig. 2.1). It was built of two slanted metal channels to ensure gravitational movement of loose solids. The material

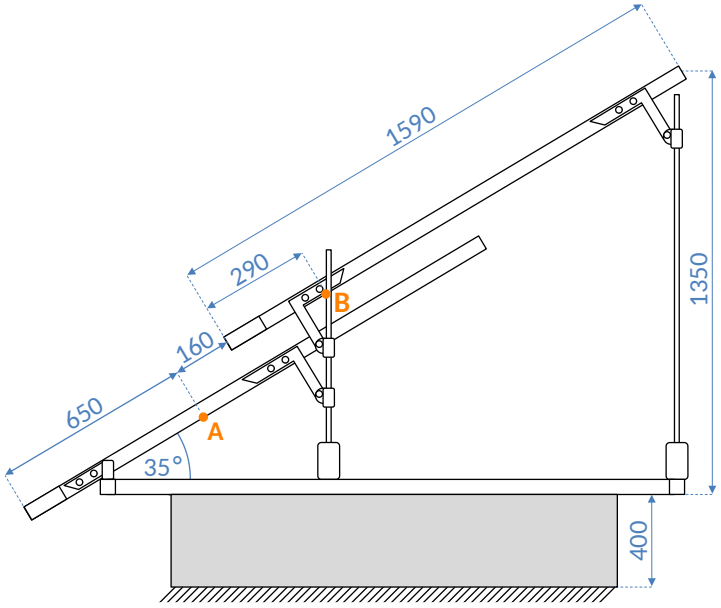

(A) Geometric dimensions. Notation: A — accelerometer location, B — material supply location.

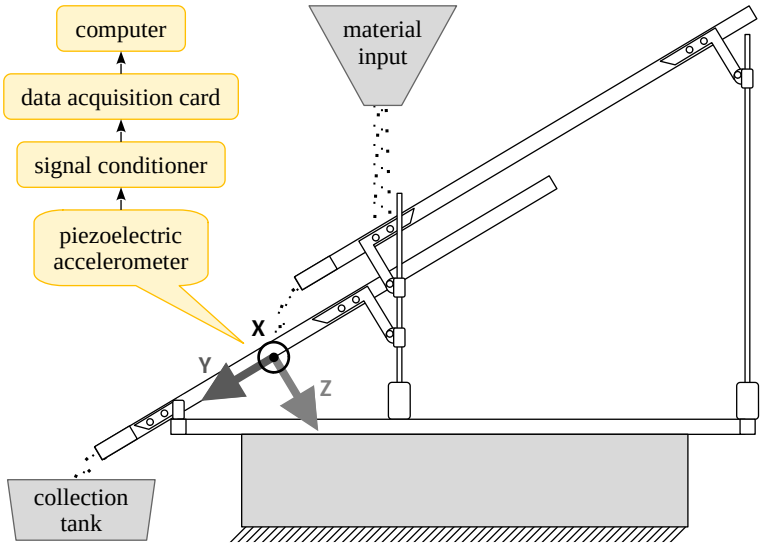

(B) Full experiment setup. "XYZ" denote accelerometer axes.

FIGURE 2.1: Test rig used for experiments with vibrational measurements of particle size and material flow rate

was supplied to the upper channel. Then the particles were sliding down and falling onto the lower channel. At its bottom surface, close to the point of impact, an accelerometer was mounted. Vibration was measured along Y and Z axes of the sensor (see Fig. 2.1b), so along the channel and along the normal to its surface. Data were recorded during material flow, and also before and after each test run, to gather noise background. The measurements were stored on computer disk for offline processing, to enable testing various methods. However, the same setup is also capable of online operation during a technological process (such as grinding), if needed. Similarly, the finally developed signal processing algorithms need very little adjustment to operate in real time.

2.1.3.2 Raw material

Loose material used in the experiment was fine-ground carbonate copper ore. The material was sieved into four size fractions ranging from 71 µm to 1 mm (see Table 2.1). Such choice represents a material actually used in industrial applications (e.g. grinding systems) that are the aim of the developed measurement method. However, this involves some difficulty: copper ore minerals are rather soft (about 2–4 in Mohs scale [92]), so their particles may get fragmented during handling. This disturbs the initially prepared particle size ranges.

A sample of each size fraction was supplied to the test rig in a continuous stream. This resembled the real operating conditions in technological processes. The material was supplied using three sizes of feeding devices, so three flow rates A, B, C were examined for each fraction. However, the flow rates were not identical among different fractions, due to the type of the supply method. In future research, a different device may be used for this — e.g., a screw feeder powered through a frequency inverter — thus allowing to achieve comparable mass flow rates for all tested material types.

Each size fraction was supplied to the test rig through each feeding device several times to achieve reasonable duration of the recorded signals. Measured data from all these runs, having the same particle size and flow rate settings, will be called a dataset from now on.

Furthermore, for each material fraction and feeder type, the material was supplied to the test rig several times (6–10) to record the total mass of the sample and its feeding time. These were transformed into mass flow rate estimates. The average estimates for each dataset (± sample standard deviation) are listed in Table 2.1.

TABLE 2.1: Particle sizes and approximate flow rates (± sample standard deviation) used in the experiment

Size fraction	Particle size [µm]		Mass flow rate [kg/h]		
	from	to	A	B	C
fraction 1	71	100	20.5±0.3	22.6±1.0	20.6±0.1
fraction 2	100	200	34.1±0.1	41.6±0.2	43.5±0.2
fraction 3	200	500	35.4±0.1	44.4±0.2	52.2±0.2
fraction 4	500	1000	34.0±0.2	34.4±1.9	46.2±0.3

2.1.3.3 Measurement equipment

The accelerometer was a triaxial piezoelectric sensor, model M356A17 by PCB Piezotronics [83]. Only two measurement axes were used: Y and Z. The sensor had measurement range ±10 g (±98 m/s^2) at peaks, more than enough for the purpose of these tests. What is important, it provided high sensitivity, over 500 mV/g (51 mV/(m/s^2)) for each measurement axis. Also, noise floor was quite low, so the signal-to-noise ratio was very good. Accelerometer's frequency range was 0.4–4000 Hz and so, this range was analysed during vibration data processing.

Apart from the sensor, the measurement system included a signal conditioning device, necessary for the accelerometer. It was also manufactured by PCB, model 482A16. Two of its four channels were used, with gains set to ×1 or ×10, depending on the vibration signal amplitudes. (Gains ×1, ×10 and ×100 were available.)

The analog signals provided by the signal conditioner were digitalized using data acquisition card NI-USB 6251 BNC, manufactured by National Instruments [73]. It offered 16-bit resolution and analog input ranges of ±{0.1, 0.2, 0.5, 1, 2, 5, 10} [V]; ranges ±{2, 5, 10} [V] were used. For simultaneous sampling of multiple channels, the maximum rate was 1 MS/s (aggregate sampling rate for all channels currently in operation). Thus, in the case of two active channels, the resultant maximum rate was 500 kS/s per channel. This was enough to set sampling rate beyond twice the highest-frequency components in the acquired signals, taking into account both the nature of the impact-induced vibrations and the resonant frequency of the accelerometer [83].

2.1.3.4 Signal processing methods

Computer programs for data acquisition and signal processing were written in LabVIEW graphical environment. The code was kept modular, allowing for re-use of the same blocks in different parts of the algorithm.

Processing of vibration data was performed mainly in frequency domain — namely, using power spectral density (PSD). This allows to efficiently remove the noise, especially wideband, as was in this case. Also, it is convenient to devise signal processing schemes in frequency domain.

The proposed algorithm included many stages responsible for noise removal from the recorded vibration data. Firstly, in frequency-domain characteristics of noise there were peaks that indicated single-frequency or very narrow-band components. They came e.g. from other devices plugged to the same power grid. This kind of disturbances could be effectively avoided if a separate power source (e.g. a battery) was used solely for the measurement equipment. However, this solution is not always feasible, due to extra expenses or necessary installation and maintenance works. Thus, a signal-processing method of removing these spectral artifacts is also desired. The mentioned peaks in the PSD estimates were removed first, not to disturb the averaged noise characteristics calculated further. The latter one was necessary to perform spectral subtraction — the second part of the de-noising procedure. This stage, in turn, diminished the influence of wideband noise on the useful signal.

After de-noising, a simple outlier detection mechanism was employed to improve reliability of the data analysed further. Analogous procedure was applied also to noise data, when calculating the representative noise characteristics for spectral subtraction.

After removing the detected noise and outliers, the PSD characteristics of useful signals were subjected to feature extraction in various ways [51]. The results were examined for correlation with particle size or mass flow rate of the material sample. The most promising methods are detailed in the next sections; they involve the shape of the processed PSD curve in a specific frequency band, and a numerical index related to signal power, that is, to the integrated PSD characteristics of the signal.

Note 1: In real conditions, with continuous size and flow rate measurements, it is recommended to add one more stage at the end. It is some kind of averaging (lowpass-filtering) the estimates produced from the features extracted from the characteristics. This should improve the accuracy of flow rate and particle size estimation, as outlying values will be removed — and the true values of the measured quantities should not change abruptly, especially the mean particle sizes. If overlapping time segments of the measured vibrations are used in the beginning stages, then the less probable it is that the true values undergo sudden changes, so such final filtering is the more justified. Time constants of these filters (or, more generally, structure and parameters of the filters) should be adjusted to the expected dynamics of flow rate and particle size changes, so that the outlying estimates are indeed neglected, but actual increases or decreases in the measured quantities are captured with no excessive delay.

Note 2: Some high-level parts of the algorithm could be modified with no harm to the others, if needed. For example, outlier detection mechanism could be based on different statistical measures, or the whole de-noising algorithm could be changed to better suit particular disturbances present at the given measurement stand. In the end, what matters the most is the cleaned and smoothened characteristics of useful signal, that undergoes feature extraction. Nevertheless, the particular methods proposed here were designed to be quite versatile.

All processing stages are summarized in the block diagram in Fig. 2.2. Their details are described below.

Cropping (of raw measurements) Noise and useful signal fragments were extracted from the raw data files. As indicated in Fig. 2.3, only the periods of stabilised flow rate were concerned. These time intervals were omitted that correspond to starting and finishing of supplying the material onto the test rig.

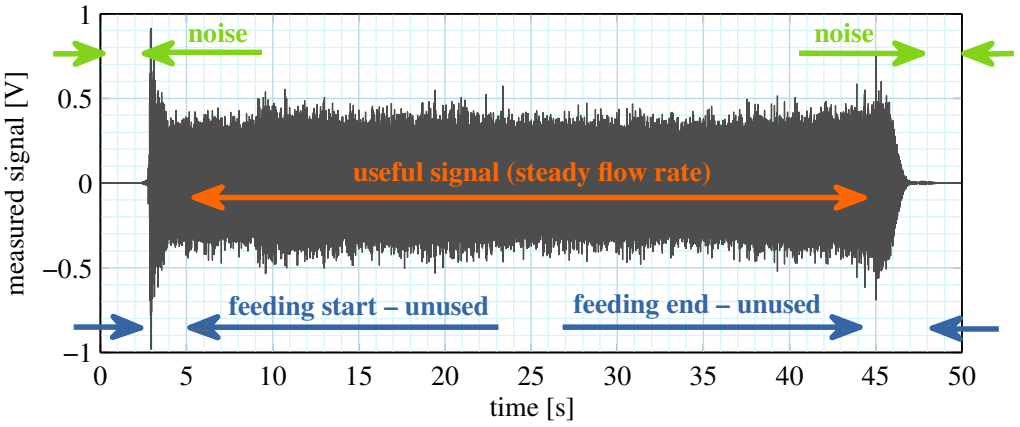

FIGURE 2.3: Exemplary raw vibration signal collected in the experiments. Accelerometer Z axis, material fraction 3 (200–500 µm), flow rate C.

Splitting into segments Both noise and useful vibration waveforms were split into segments of constant length. This created handy data chunks for further processing, and more importantly, this made the algorithm suitable for handling continuous measurements, such as in the real-world applications.

The segments were 2 seconds long. This resulted in number of samples high enough to produce good frequency resolution in further stages. Simultaneously, this was short enough not to introduce excessive averaging of collected signal features (power spectral density was calculated later from the whole segment). Moreover, signals of such number of samples could be handled quickly by the processor in all subsequent calculations.

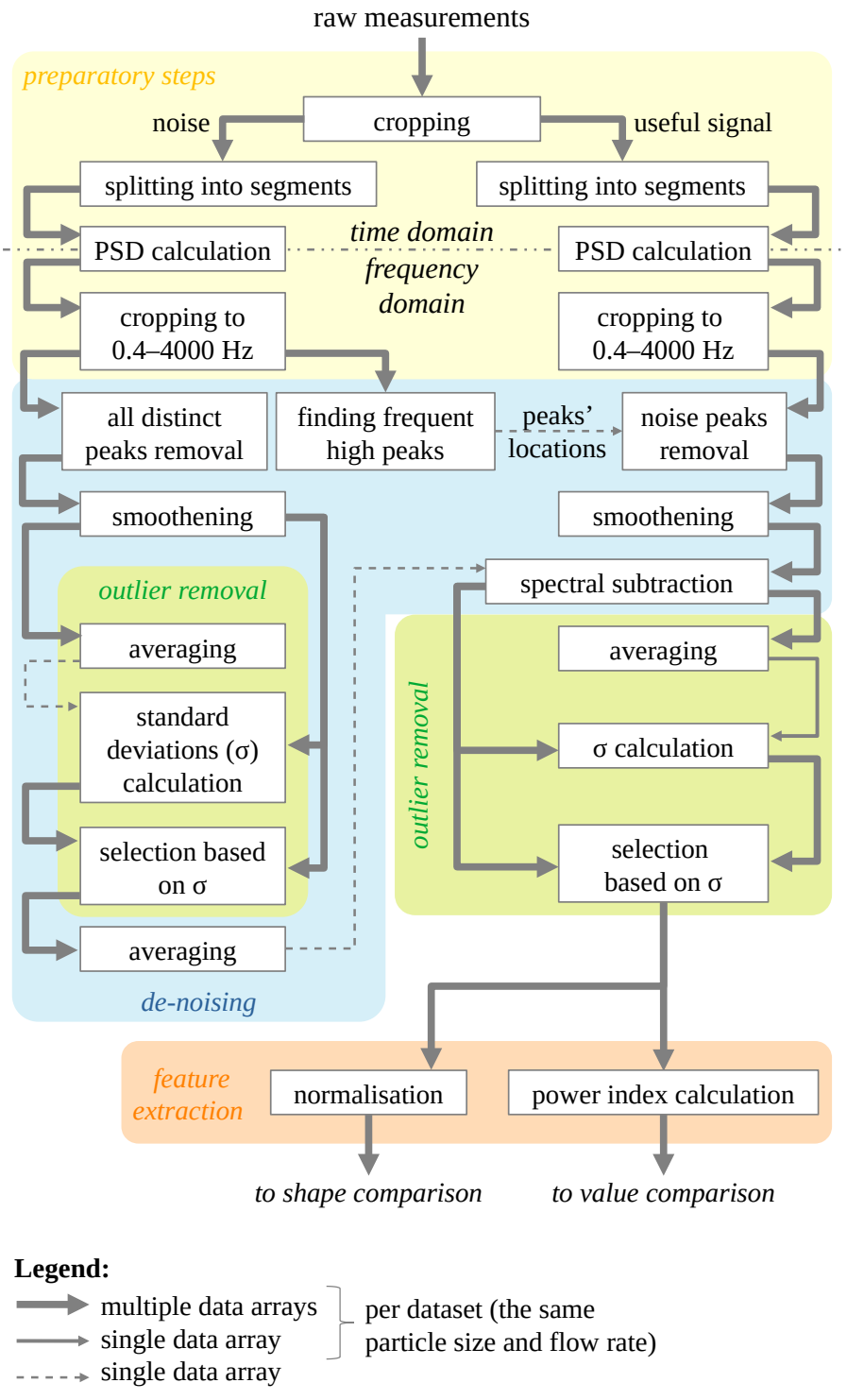

FIGURE 2.2: The proposed algorithm for vibration data processing. Abbreviations: PSD — power spectral density.

Additionally, these 2-second windows were overlapped by 66.67%. In online measurements, this would produce more frequent output of estimation result — so, faster reaction to changes in the observed material stream — without shortening the window length, which would decrease frequency resolution.

In general, segment length and amount of overlap may be selected to match the dynamics of changes in the monitored material stream. It is also recommended to set the window length (in samples) as a power of 2, to make use of the efficient Fast Fourier Transform in the next stage.

For data from the considered experiment, this stage of the algorithm produced about 500–1100 segments of useful signal per dataset, and more than 200 noise segments. These numbers of items were reasonably high for averaging and other statistical treatment, which was performed in further stages.

PSD calculation One-sided power spectral density of each segment was calculated with Fast Fourier Transform (FFT) algorithm. Hann (Hanning) window was applied to the signal before taking the FFT. Windowing was necessary to prevent the artifacts otherwise introduced by discrete finite Fourier transform. Particularly, Hann window was used because it performs well with many signal types, has quite small side lobes and, most importantly, is zero-valued at the edges [51]. Afterwards, the window's influence on PSD values was removed with division by a factor: $w^2(i)/L_\mathrm{w}$, where $w(i)$ is the i-th sample of the window and L_w is the window length (here, the length of the whole analysed signal fragment).

Cropping to 0.4–4000 Hz Only the PSD fragments corresponding to frequencies 0.4–4000 Hz were analysed further. As already mentioned in Section 2.1.3.3, this was the accelerometer's frequency range, so bins outside this interval carried no reliable information.

All distinct peaks removal Each noise PSD vector was cleared of all distinct peaks. Namely, these unwanted peaks were defined as values higher than 5 times (chosen experimentally) the median value in a sliding window. The window length was experimentally selected as 10% of the whole PSD vector's length. The removed values were replaced with linear interpolation of values at the nearest neighbouring bins.

Finding frequent high peaks High peaks in noise PSD characteristics were identified. Namely, they were defined as values exceeding 10 times (chosen experimentally)

the median value computed in a sliding window. Again, the window length was 10% of the whole PSD vector's length. These peak locations (frequency bins) were remembered that repeated often among all noise segments, that is, in at least 20% of segments.

Noise peaks removal In useful signal characteristics, PSD values at bins identified in the previous stage were removed as potential noise peaks. The removed PSD values were replaced with linear interpolation of the nearest remaining ones.

Smoothening Each characteristics was smoothened to focus on the general shape instead of particular fluctuations. The smoothening filter was weighted moving average of length equal to 10% of the whole characteristics' length (chosen experimentally). The weights used were Hann window values, and the window was centered at the currently processed bin.

Averaging Average PSD value was calculated at each frequency bin (so, it was a kind of ensemble average). In the case of noise, all available data vectors were averaged, as the noise was apparently stationary. (During long-term online operation of the algorithm, rather some lowpass filtering should be used for each frequency bin — to forget the old values and adapt to the possibly changing noise characteristics.) In the case of useful signal, averaging was performed separately for each dataset.

Standard deviations (σ) calculation For each PSD characteristics, standard deviation was calculated relative to the average defined in the previous stage. This could be called an ensemble standard deviation, as opposed to the classical sample standard deviation. Again, noise data were treated collectively, and useful signal data were treated dataset-wise.

Selection based on σ PSD characteristics much different than the appropriate average were assumed as outlying and excluded from futher analysis. Namely, these were the characteristics with standard deviation higher than 1.5 times the median σ in the dataset, for any of the accelerometer axes. After such selection there remained about 68% of noise vectors and 72–93% of useful signal vectors, depending on the dataset.

The outlying data fragments might have been caused e.g. by accidental extra vibrations introduced by objects or people in the neighbourhood of the test rig. In the case of useful signal, outliers could also be due to, e.g. momentary fluctuations in flow rate of the material.

Spectral subtraction The prepared representative characteristics of noise was subtracted bin-wise from each characteristics of useful signal. Thus, noise suppression procedure was finished.

Normalisation Each characteristics of useful signal was normalised to zero mean value and unit standard deviation. Of course, this involved the usual averages and standard deviations from a sample, not their ensemble versions. Note: transforming the original characteristics to a zero-mean curve was not required by further processing steps, it only helped to visually compare (in the plots) the curves for different signals. On the other hand, normalisation to unit standard deviation was necessary to produce unambiguous results later.

This stage allowed to compare the shapes rather than the values of the characteristics. So, distribution of power into subsequent frequency bands (proportions between power contained in them) could be analysed instead of specific power in each band. The resultant curve will be called a PSD variability curve from now on.

Power index calculation Apart from the shapes, also the values of the processed characteristics were of interest. For easy comparison of different cases, a numerical index was derived. It was simply based on integration of the processed PSD characteristics, so it was related to the power of the vibration signal:

$$J_P = \frac{1}{T_s} \cdot \sum_{i=0}^{N-1} PSD(i)\,, \tag{2.1}$$

where: T_s — sampling period of the time-domain signal, i — frequency bin number, N — length of PSD characteristics (total number of bins), PSD — the finally processed version of PSD characteristics, i.e., after removing outliers, but without normalisation (which was done in a parallel path of the whole algorithm).

What is important, previous research [51] showed that it is necessary to smoothen the PSD estimate before calculating the power index. Power estimates calculated directly from the unsmoothened frequency-domain characteristics did not form any apparent relationship to particle size or flow rate of raw material.

2.1.4 Vibration method results

2.1.4.1 Comparison of shapes of the processed PSD characteristics

When analysing the shapes of the processed characteristics, firstly, a bin-wise average of the variability curves was examined for each dataset. These averages are plotted in Fig. 2.4.

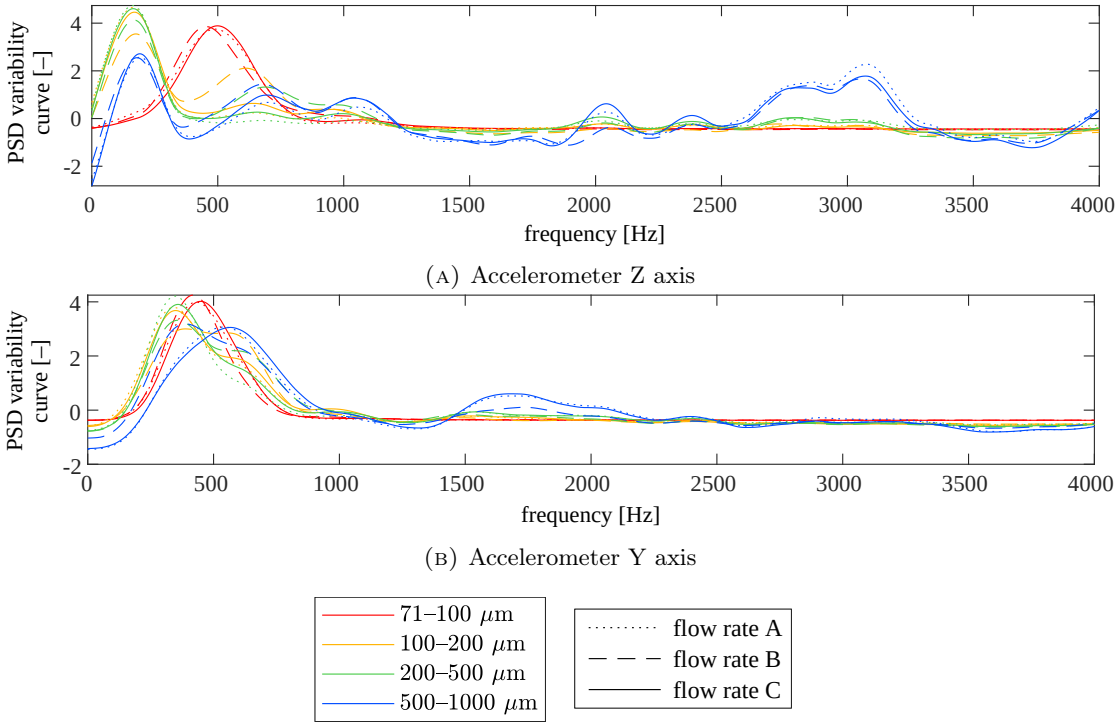

(A) Accelerometer Z axis

(B) Accelerometer Y axis

FIGURE 2.4: PSD variability curves for vibration signals — ensemble average for each dataset

In Z axis data for the finest material fraction, the main peak of the curve is sigificantly shifted to higher frequencies, compared to the coarses particles' data. This may reflect the specific way in which such small particles were sliding down the test rig — they tended to accumulate on the surface of the transport channel, instead of sliding freely. Probably they were small and lightweight enough to bring into focus the adhesive forces between the particles and the metal channel; perhaps, these were the electrostatic phenomena.

Some irregularity also occurs in the Y axis data for the most coarse material, flow rate B. The main peak there behaves more like the peaks for finer fractions, instead of being similar to peaks for other flow rates for the same fraction. This is the more interesting because A and B flow rate values were very similar for this material, and quite distinct from flow rate C (see Table 2.1). Probably the feeding device B behaved slightly differently for this type of material and hence the modified PSD characteristics.

These two observations are only some singularities in the locations or shapes of the most prominent peaks in the characteristics. They do not show any universal dependencies between the analysed quantities. Apart from these single features, the low frequency range (up to about 1000 Hz) does not seem to carry much valuable information regarding particle sizes or material flow rates. However, the higher frequency range (approximately 1200 Hz and above) could be more effective in this matter. The values at successive bins in this range vary much, but only for coarse particles. The finer the material, the more flat the curve. Thus, sample standard deviation was calculated from the variability curve's values only in the 1200–4000 Hz range, to quantify variability of the observed PSD estimates. The results are shown in Fig. 2.5.

The mentioned sample standard deviation strongly depends on particle size, and this relation is nearly linear (Fig. 2.5a, 2.5b). For Z axis data and significantly different particle sizes (fractions 3 and 4), the value ranges of the standard deviations do not overlap, so these two fractions are fully distinguishable. Also, the finest fraction can be clearly differentiated from the next one, especially using Y axis data.

The examined standard deviations exhibit only little dependence on flow rates (Fig. 2.5c, 2.5d). This means that material flow rate is not a significant disturbance to particle size assessment with this method, at least for the tested range of flow rate values. The mass flow rate itself apparently does not correlate with sample standard deviation.

The measures of variability of the processed PSD estimates might be fine-tuned to achieve best distinguishability between size fractions (least overlap of value ranges between different fractions). For example, sample standard deviation could be changed to a different function. However, so far median absolute deviation (MAD) and sum of absolute differences between consecutive samples (SAD) were tested with no effect. Namely, SAD performed very similar to sample standard deviation, and MAD was slightly worse than them, i.e. the range overlap between different material fractions was a bit bigger when using MAD. Nevertheless, the option to change the function should be kept in mind when analysing data associated with other installations or other types of raw material. It is also possible to modify the frequency range used for statistical analysis (currently 1200–4000 Hz) — perhaps a slightly different one would give more clearly separated material fractions. Moreover, the optimal (and even: meaningful) frequency range probably varies with the chemical composition of the raw material; shape, size and material of the transport installation; and maybe even with the method of raw material supply.

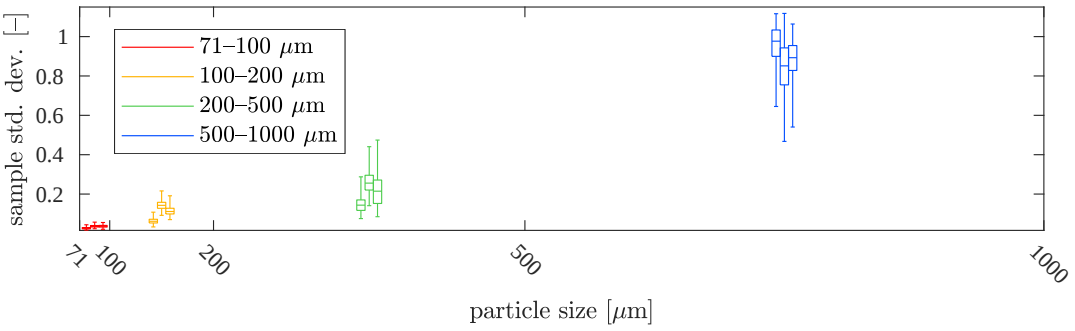

(A) Standard deviation vs particle size, accelerometer Z axis

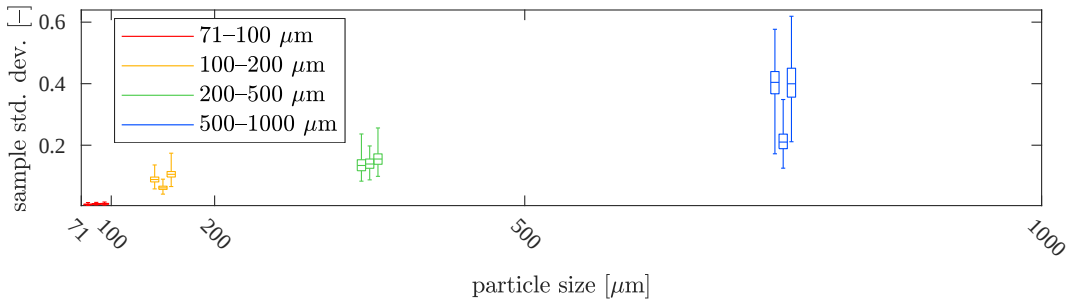

(B) Standard deviation vs particle size, accelerometer Y axis

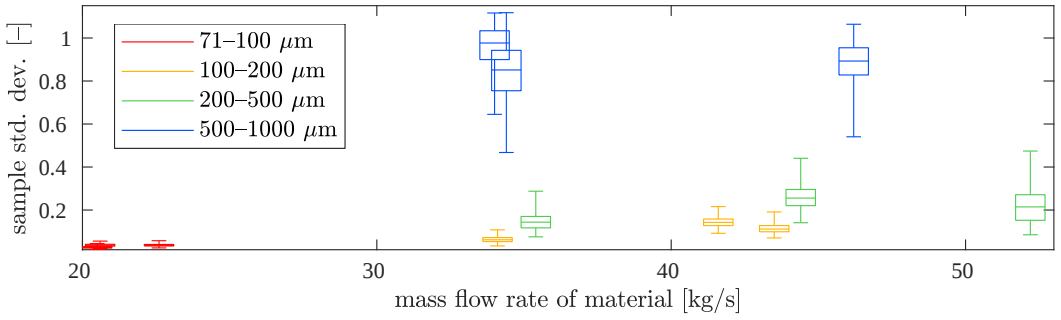

(C) Standard deviation vs flow rate, accelerometer Z axis

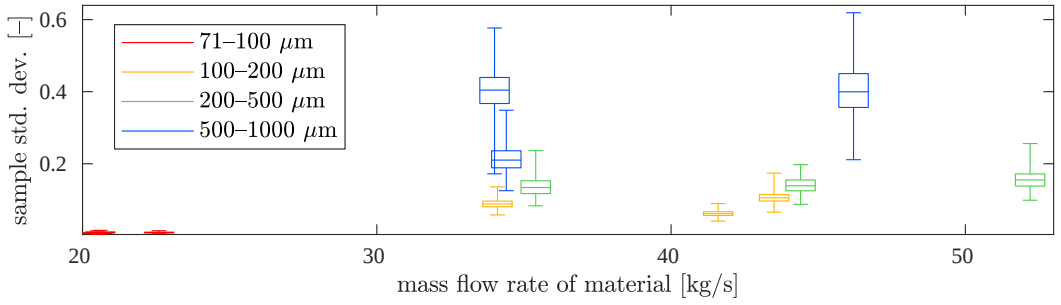

(D) Standard deviation vs flow rate, accelerometer Y axis

FIGURE 2.5: Sample standard deviation calculated in 1200–4000 Hz range from PSD variability curves of vibration signals.
Bottom, middle and top horizontal lines in the boxes indicate 1st, 2nd and 3rd quartiles, respectively. Whiskers extend to the minimum and maximum values in each dataset. In panels (A) and (B), the three boxes for each fraction are data associated with flow rates A, B, C (from left to right), and they are horizontally centered within their associated particle size range.

2.1.4.2 Comparison of values of the processed PSD characteristics (power index values)

The values of power index (2.1) compared among all datasets, plotted against particle size, are shown in Fig. 2.6. Please note the logarithmic vertical scale of the plots, due to widely spread index values.

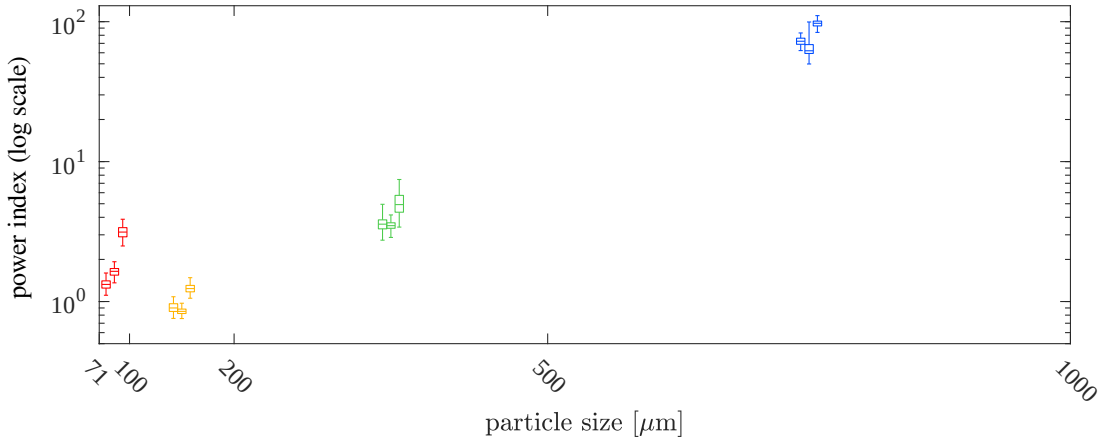

(A) Accelerometer Z axis

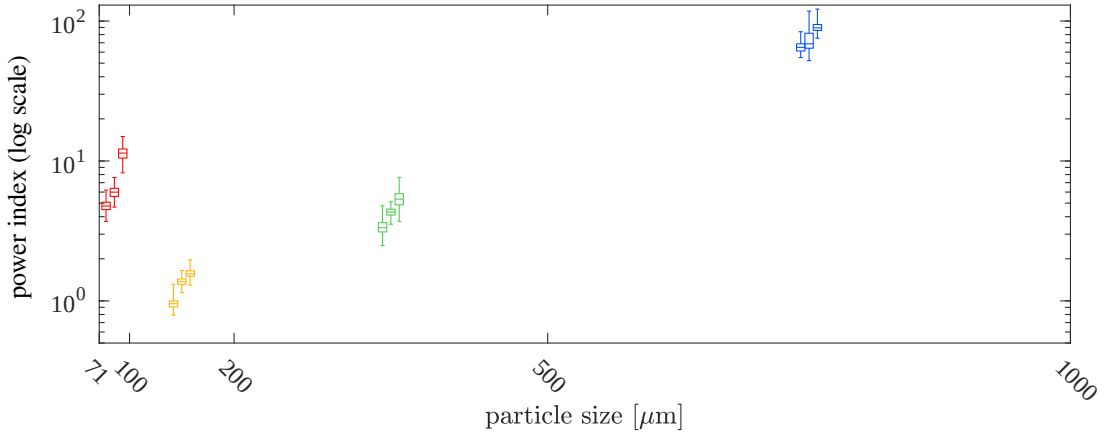

(B) Accelerometer Y axis

FIGURE 2.6: Power index (2.1) of the vibrations, in relation to particle size. Bottom, middle and top horizontal lines in the boxes indicate 1st, 2nd and 3rd quartiles, respectively. Whiskers extend to the minimum and maximum values in each dataset. The three boxes for each fraction are data associated with flow rates A, B, C (from left to right), and they are horizontally centered within their associated particle size range.

The influence of particle size on the index values is much stronger than the influence of flow rate, at least for their value ranges tested in this experiment. Nevertheless, the effect of flow rate is still noticeable and it will be examined in the following plots.

The finest fraction stands out from the log-linear trend observed in data for the other size fractions. Except for these finest particles, the fractions may be clearly distinguished from each other, as the value ranges occupied by subsequent fractions do not overlap. The wide spread between these ranges suggests that far narrower fractions could still be correctly distinguished with this method. Alternatively, the sizes used in the experiment could be discriminated even if wider range of flow rates was in use. Summarizing, if particle sizes in the examined material range from about 100 µm up (at least to 1 mm), the power index method alone is capable of estimating the size with good accuracy and good resolution.

The smallest particles need to be treated with a different method. It may be, e.g. the one just decribed (Section 2.1.4.1) that uses variability of the processed PSD in 1200–4000 Hz range. In such a case of potentially very fine particles, a fusion of the mentioned two methods is recommended. Firstly, the PSD variability method should be used to get a rough estimate of particle size. If size smaller than 0.1 mm is indicated, the algorithm should finish. Actually, for such small particles the estimation result would be of quite good quality (unambiguous), especially when using Y axis data — see Fig. 2.5b. If coarser particles are detected, then the estimation result should be refined with power index method.

The plots that examine the relation between power index and material flow rate are shown in Fig. 2.7–2.8. Figure 2.7 compares all size fractions together to give an overall view. Again, here the vertical scale in the plots is logarithmic, due to its wide value range. Figure 2.8 presents all size fractions individually to show more details, and the vertical scale there is linear.

The graphs confirm the general positive correlation between mass flow rate and power index. However, to use this index in mass flow rate estimation, particle size needs to be known first (e.g., estimated as just explained), because it has a dominant impact on J_P values. Moreover, such flow rate estimation may only be approximate, as value ranges of power index significantly overlap between the tested flow rates. Perhaps some of this uncertainty would be reduced if material flow rates in the experiment were more constant (with even smaller fluctuations than estimated in Table 2.1). This hypothesis needs to be verified in another experiment, with more accurate feeding equipment. Also, maybe the accuracy of flow rate estimation could be improved with continuous operation of the algorithm and averaging (lowpass filtering) many estimates on a longer time interval. It is suggested by the inter-quartile ranges (boxes in the plots) being much narrower than the min-max ranges (whiskers in the plots).

Some data do not follow the positive correlation of flow rate and power index — these are all data for the smallest particles (Fig. 2.8a–2.8b) and Z axis data for the most

coarse particles (Fig. 2.8g). Probably this was caused by some specific type of vibrations introduced by one (or more) particular feeding devices to these particular materials. The data could be more predictable with a different type of feeder (e.g. having more rigid construction), but this needs to be verified.

Data for Y axis of the accelerometer (along the axis of the metal channel) have nearly linear dependence on flow rate, and data for Z axis do not. This indicates Y axis might be more convenient to use in flow rate estimation. That needs to be tested experimentally on flow rate values which are more numerous and distributed in a broader range.

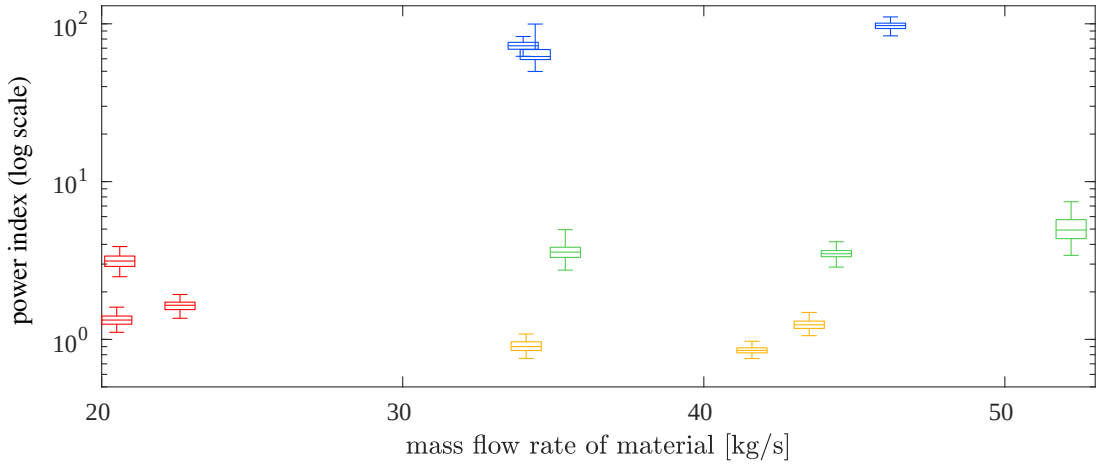

(A) Accelerometer Z axis

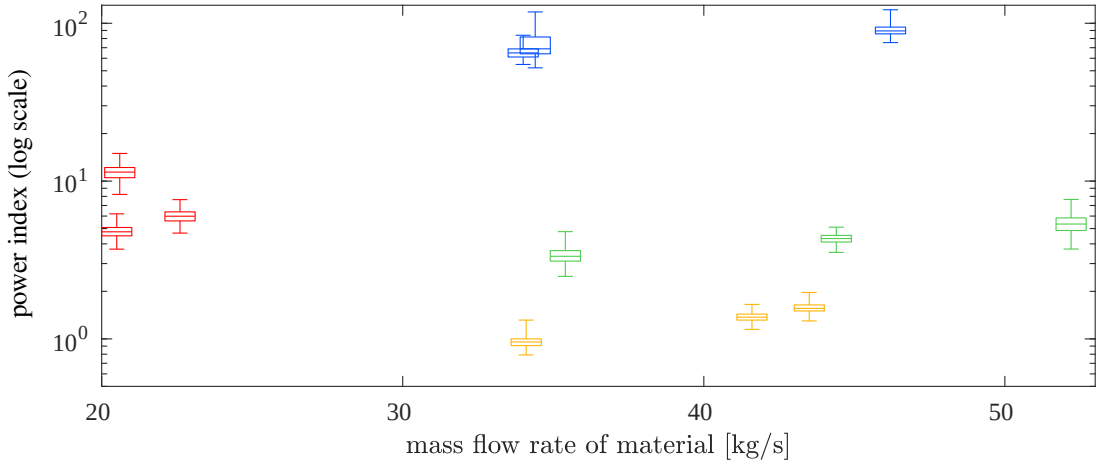

(B) Accelerometer Y axis

FIGURE 2.7: Power index (2.1) of the vibrations, in relation to mass flow rate of the material — all size fractions compared.
Bottom, middle and top horizontal lines in the boxes indicate 1st, 2nd and 3rd quartiles, respectively. Whiskers extend to the minimum and maximum values in each dataset.

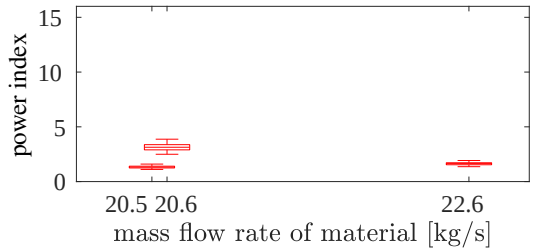

(A) Fraction 1 (71–100 µm), accelerometer Z axis

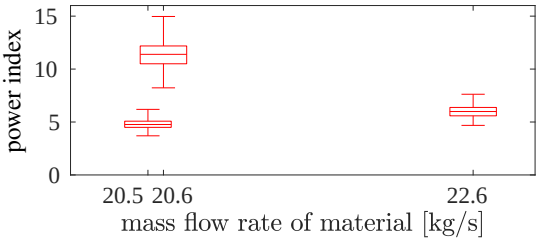

(B) Fraction 1 (71–100 µm), accelerometer Y axis

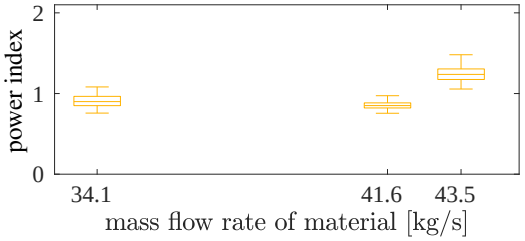

(C) Fraction 2 (100–200 µm), accelerometer Z axis

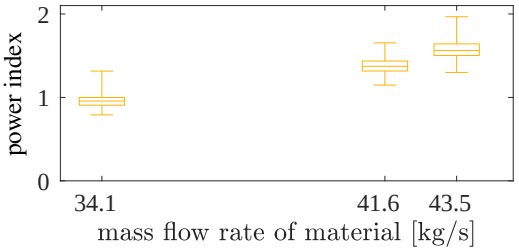

(D) Fraction 2 (100–200 µm), accelerometer Y axis

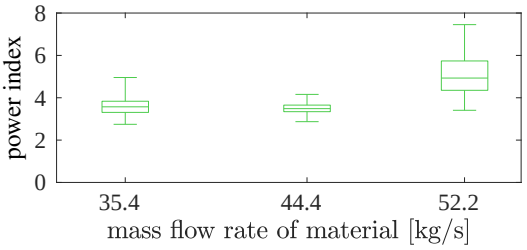

(E) Fraction 3 (200–500 µm), accelerometer Z axis

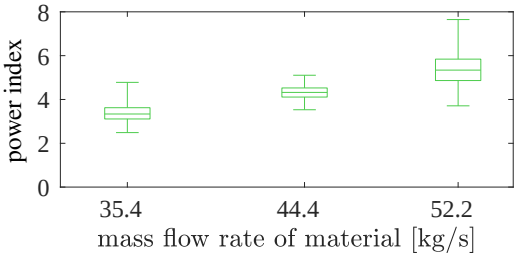

(F) Fraction 3 (200–500 µm), accelerometer Y axis

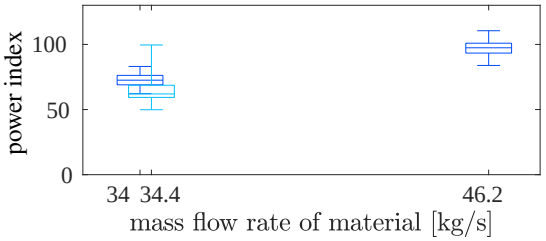

(G) Fraction 4 (500–1000 µm), accelerometer Z axis

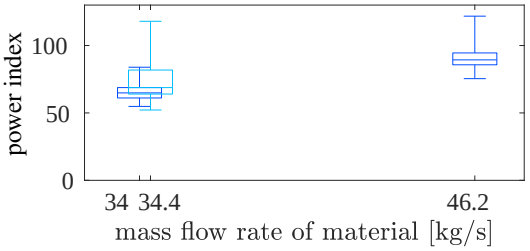

(H) Fraction 4 (500–1000 µm), accelerometer Y axis

FIGURE 2.8: Power index (2.1) of the vibrations, in relation to mass flow rate of the material — individually for each size fraction.
Bottom, middle and top horizontal lines in the boxes indicate 1st, 2nd and 3rd quartiles, respectively. Whiskers extend to the minimum and maximum values in each dataset.

2.1.5 Modification: acoustic method

An approach was also examined that used sound recordings instead of vibration measurements. Experiment scenario and raw material were the same as in the experiment with vibration method (see Section 2.1.3.2). Also, the test rig was nearly identical (see Section 2.1.3.1), but instead of the accelerometer mounted on the bottom surface of the transport channel, a microphone was placed nearby. It was an omnidirectional condenser

microphone, model MM 1 by beyerdynamic, operating within 20–20,000 Hz frequency range [7]. (A properly oriented unidirectional microphone could also be used to minimize the impact of other sound sources. However, such equipment was not available at the time of conducting this experiment. So, quiet ambient conditions were provided for the duration of the measurements.) Sound recordings were made with a handheld audio recorder, model H4n Pro Black by Zoom. It operated at 44,100 S/s sampling rate, and analog-to-digital conversion used 24 bits (16 bits physically with oversampling ×128) [118].

Sound processing followed the same stages as with the vibration data (Section 2.1.3.4). The only modification was that PSD characteristics were cropped to 20–20,000 Hz interval instead of 0.4–4000 Hz interval, to match the frequency range of the new sensor.

At the beginning of data processing, there were 50 fragments of background noise, and 90–326 fragments of useful signal per dataset. After removing outliers, there remained 36 noise characteristics (72% of the original number), and 74–219 characteristics of useful signal, corresponding to 65–92% of all fragments, depending on the dataset. This was enough to perform reliable statistic calculations.

Note: Industrial operating conditions are far from the quietness of the laboratory, and the acoustic disturbances often are non-stationary. To effectively suppress them, it is advisable to use two microphones (or even more, if needed). The primary one should be placed possibly close to the material transport installation, and the other(s) within some distance, so that they collect practically only the background noise. Then, an adaptive filter could be used, parametrized e.g. with least mean squares algorithm, to model the dynamic dependence between the primary and secondary microphones' signals. (The geometrical arrangement of the microphones relative to the unwanted sound sources would introduce some differences in times at which the disturbances reach the primary and secondary microphones, and also in recorded sound intensities.) The filtered background noise — so, the estimate of the disturbance at the primary microphone — should be subtracted from the measured signal to yield an estimate of clean useful signal, further subjected to feature extraction stage of the algorithm. Such de-noising method was not necessary in the case of the presented laboratory measurements, so it was not used, but it would be beneficial in real-life applications, where sound sources are multiple and changing.

Actually, such approach could also be used with vibration data. A secondary accelerometer could be mounted close to devices that generate significant vibrations and disturb the measurements used for flow rate and particle size estimation. In the case of the considered grinding installation, such secondary vibration sensor could be located e.g. near the outlet pipe from the electromagnetic mill. However, this noise filtering

method seems more easily applicable to acoustic measurements, as the secondary microphones may be placed anywhere in space, also relatively close to the primary microphone (which gives good estimates of noise components in the primary signal). In contrast, vibration sensors need to stay in contact with vibrating parts of the installation, so they cannot be placed arbitrarily.

2.1.6 Acoustic method results

Processing results will be presented in the same way as for the vibration method. Firstly, the shape (the variability) of the PSD characteristics will be analysed, and then the PSD values transformed into a single-number power index (2.1).

2.1.6.1 Shapes of the processed PSD characteristics

The bin-wise averages of PSD variability curves in each dataset are shown in Fig. 2.9. Again, variation of the curve increases with growing particle size — the same as it was for the vibration data (see Fig. 2.4). The plot with acoustic data suggests that a suitable frequency range for calculating statistical measures is approximately 3–20 kHz.

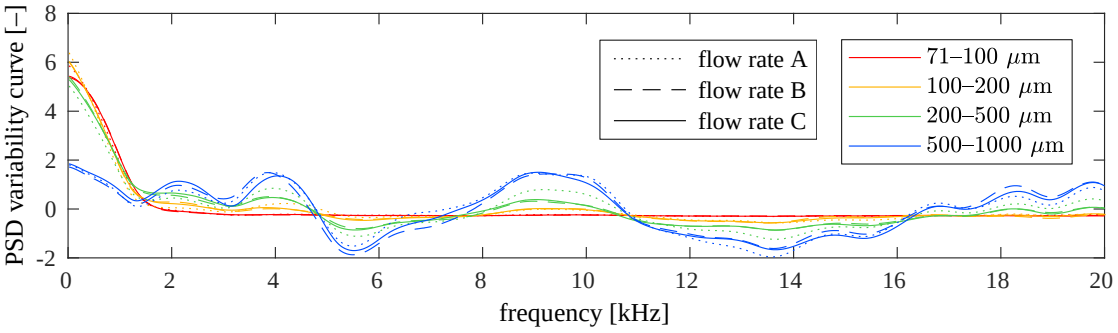

FIGURE 2.9: PSD variability curves for acoustic signals — ensemble average for each dataset

Sample standard deviation, sum of absolute differences and median absolute deviation were calculated in 3–20 kHz range from each PSD variability curve of useful signal. All these measures of variation performed very similarly, but the first two had a single outlying result in the dataset for fraction 1, flow rate A. In contrary, MAD was able to suppress the outlying values in this particular curve, so this time, MAD was plotted instead of standard deviation (Fig. 2.10).

The results are very similar to the ones for vibration data (see Fig. 2.5). Firstly, the coarser the particles, the higher the statistic measure, and the trend is close to linear. Secondly, flow rate has little effect on the calculated statistics and there is no clear trend

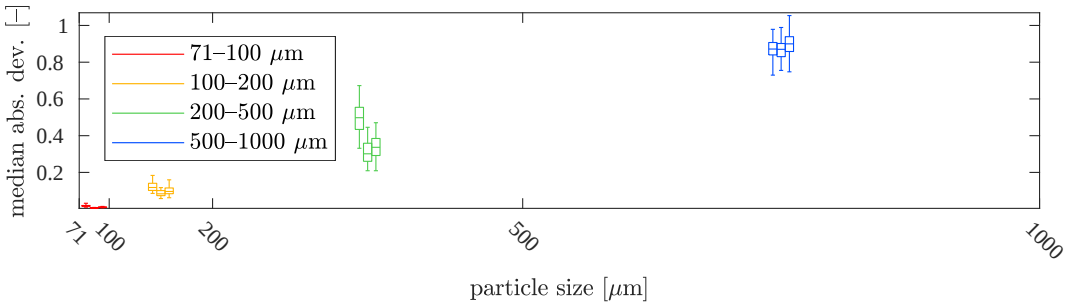

(A) Median absolute deviation vs particle size

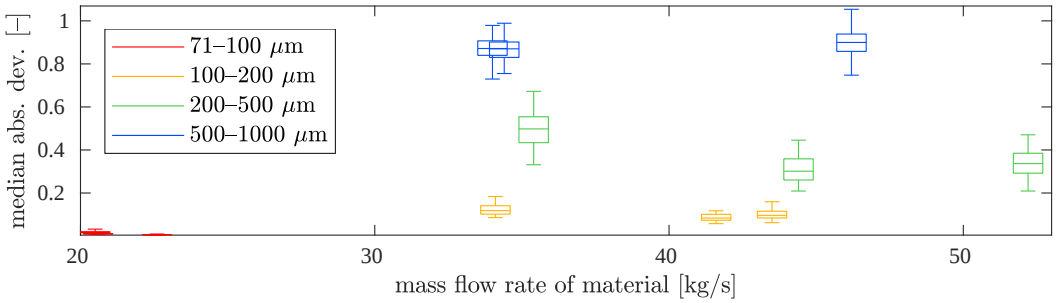

(B) Median absolute deviation vs flow rate

FIGURE 2.10: Median absolute deviation calculated in 3–20 kHz range from PSD variability curves of acoustic signals.
Bottom, middle and top horizontal lines in the boxes indicate 1st, 2nd and 3rd quartiles, respectively. Whiskers extend to the minimum and maximum values in each dataset. In panel (A), the three boxes for each fraction are data associated with flow rates A, B, C (from left to right), and they are horizontally centered within their associated particle size range.

between them, at least for the tested range of mass flow rates. An improvement compared to vibration method is that MAD value ranges do not overlap between different size fractions, at least for these particular experimental results (Fig. 2.10a). However, exact comparison of performance of these two methods is not possible, as the measurement data presented here come from two distinct experiments (the sound and vibrations were not measured simultaneously during the same tests, but on different days — during similar, but not the same, test runs).

2.1.6.2 Power index values of the processed PSD characteristics

Figures 2.11 and 2.12 show power index (2.1) calculated from the acoustic data, compared among all tested size fractions and all tested flow rates, respectively. The vertical scale of the plots is logarithmic. Then, the relation between power index and flow rate for individual size fractions is presented in more detail in Fig. 2.13, using linear vertical scale.

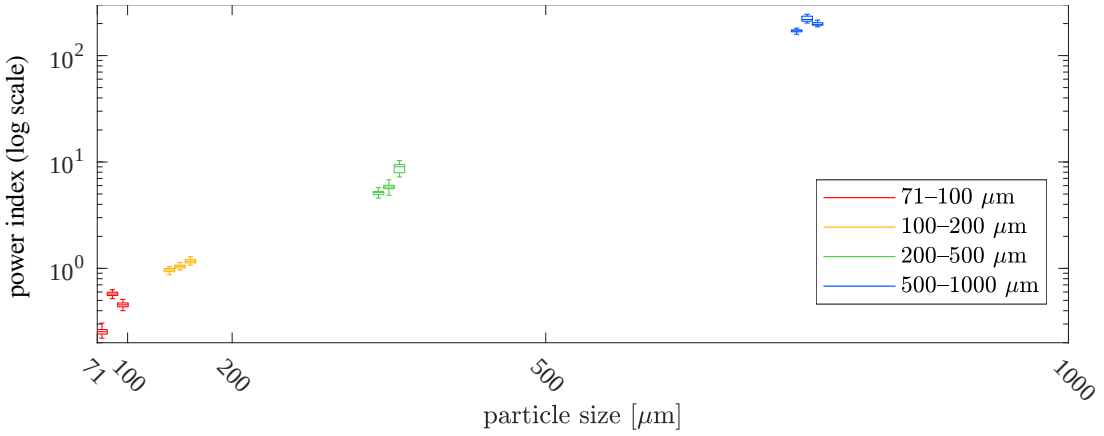

FIGURE 2.11: Power index (2.1) of the acoustic signal, in relation to particle size. Bottom, middle and top horizontal lines in the boxes indicate 1st, 2nd and 3rd quartiles, respectively. Whiskers extend to the minimum and maximum values in each dataset. The three boxes for each fraction are data associated with flow rates A, B, C (from left to right), and they are horizontally centered within their associated particle size range.

Once more, the observations are similar as in the case of vibrations (see Fig. 2.6–2.8). A log-linear trend is again observed in the first plot, and particle sizes may be clearly distinguished, as value ranges of power index are far from overlapping (Fig. 2.11). There is one remarkable improvement in comparison to vibration data — this time, results for the finest particles agree well with the overall trend. So, when using sound recordings, particle size could be determined solely with the power index method, without using the shape (variability) of processed PSD characteristics.

For flow rates (Fig. 2.12 and 2.13), the value ranges associated with different datasets are not that distinct and in many cases they have significant amount of overlap — at least for the tested range of flow rates, which was not very wide. Nevertheless, the positive correlation between power index and flow rate is apparent for most size fractions. On the other hand, the shape of this relation differs — it is concave for fraction 1 and convex for fractions 2 and 3 (Fig. 2.13). The data for the coarsest particles do not follow any monotonic relationship. However, this may be due to some specific operation of one of the feeding devices, as similar behaviour (though, not that strong) was already observed for the vibration signal. In general, conclusions regarding flow rate estimation need to be verified in another experiment, with more flow rates in a broader range.

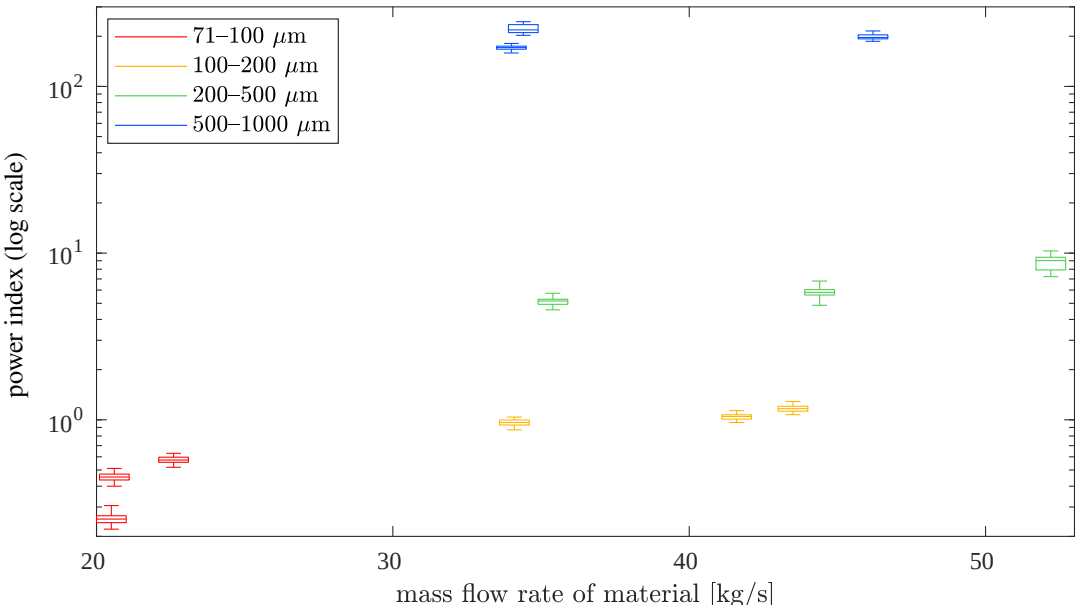

FIGURE 2.12: Power index (2.1) of the acoustic signal, in relation to mass flow rate of the material — all size fractions compared.
Bottom, middle and top horizontal lines in the boxes indicate 1st, 2nd and 3rd quartiles, respectively. Whiskers extend to the minimum and maximum values in each dataset.

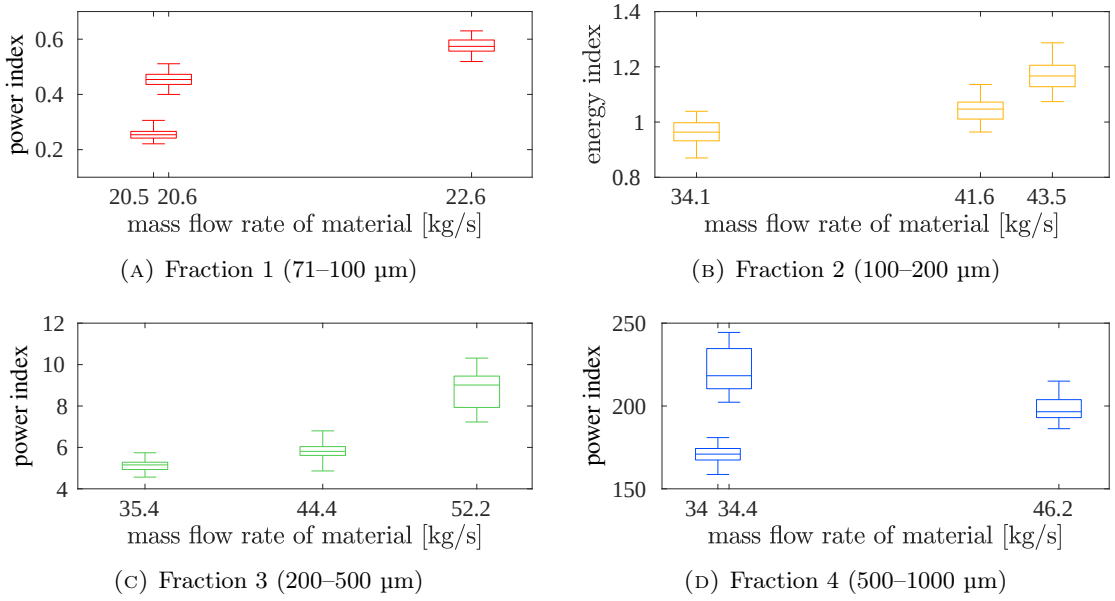

(A) Fraction 1 (71–100 µm)

(B) Fraction 2 (100–200 µm)

(C) Fraction 3 (200–500 µm)

(D) Fraction 4 (500–1000 µm)

FIGURE 2.13: Power index (2.1) of the acoustic signal, in relation to mass flow rate of the material — individually for each size fraction.
Bottom, middle and top horizontal lines in the boxes indicate 1st, 2nd and 3rd quartiles, respectively. Whiskers extend to the minimum and maximum values in each dataset.

2.1.7 Comments and conclusions

A hypothesis was formed that particle size and flow rate of bulk material may be estimated by processing of vibrations or acoustic signals generated by the moving particles. The above findings confirmed this suggestion. Especially, results of particle size assessment were much promising: they came from a fusion of two approaches, using shapes and values of the processed PSD characteristics. This fusion improved estimation accuracy. Flow rate approximations were also possible, though probably more coarse (the exact results need to be verified in a new experiment).

Processing of acoustic data produced slightly better results than processing of vibrations. Also, suppressing non-stationary disturbances may be easier with sound measurements. However, type of measured signal needs to be selected individually for the particular measurement case, so that the disturbances are minimized. Also, fusion of results from these two indirect measurements is possible, and may further improve the accuracy.

The advantage of the proposed method is simultaneous estimation of both particle size and flow rate of bulk material, using a single sensor and even using much similar processing algorithms (many stages at the beginning are common to both algorithms and so, need to be performed only once). More sensors may be used to improve the de-noising procedure or to perform fusion of vibration and acoustic data; but essentially, measuring of the two quantities is possible using only one accelerometer or one microphone. Other benefits of the method are: online operation (no need to take material samples), contactless working (no excessive sensor wear), inexpensive equipment, easy and non-intrusive mounting. The drawbacks are limited accuracy, and the need to calibrate the method to the particular type of raw material and to the specific measurement point (material transport installation).

This research, though fruitful, appeared to be somehow preliminary. There are some tentative conclusions to be verified on more datasets. Also, the results might be extended in many ways. Future experiments could provide, for example:

- narrower size fractions, to verify size estimation methods proposed here;
- more ultrafine fractions (<100 µm) — especially if the method is to be used in fine and ultrafine grinding installations — and more coarse fractions, to find the particle size range to which the method is applicable;
- test runs using a mix of several size fractions previously examined individually, to check if estimation results rather show the mean particle size, or maximum size, or other quantity — this is important in many real-life measurements;

- more flow rate values (especially higher than in this experiment, as these were quite small), to verify the proposed methods of flow rate estimation;
- more stable (constant) flow rates, to get more reliable value ranges of the extracted PSD features;
- other types (chemical compositions) of the raw material[1] and other types (geometries, compound materials) of the transport installation[2], to verify if the method is applicable universally, or only to some particular cases.

However, so far these ideas were not much explored. The topic is broad and may provide many findings, but also it requires quite extensive experiments. Thus, advances in this research path were postponed for the future, and the results gathered thus far were assumed sufficient for now. The scientific effort of the author was directed to other areas, also important to the research on EM mill installation, and equally — or even more — developing to the author.

2.2 Moisture content

2.2.1 Indirect moisture measurements

In the grinding installation with electromagnetic mill, water content should be measured in fresh feed and recycle material streams to then estimate the (physically unmeasurable) total water content in the material inside the working chamber of the mill. Also, moisture in the final product is of interest, as it may be subject to limitations imposed by the recipient or by demands of the following technological processes. To measure water content in these material streams, some innovative methods were proposed by the team working in SYSMEL project. These were based on impedance measurements and near infrared absorption [11; 101; 102] or computer vision and thermovision analysis [10]. The author of this dissertation took part in the experiments and results analysis for the last method mentioned, so it is shortly described below; more details may be found in the published paper [10].

[1] Some work in this area, using construction sand instead of copper ore, was published by the author of this dissertation in [54]. However, this was the first study in this topic; material supply methods were quite simple, and the accelerometer used there operated in a much narrower frequency range. Thus, the results should be considered preliminary.

[2] Some experiments with copper ore were performed on recycle and product pipes in the grinding installation with electromagnetic mill [11]. However, the pipe walls (stainless steel, 2 mm thick) appeared to suppress the vibrations too strongly to perform any analyses of useful signal. In such a case, a small obstacle should be introduced into the pipe cross-section just next to the sensor placement — to amplify the vibrations caused by particle impact — and then the experiment should be repeated.

This research developed a contactless method for approximate measurement of moisture content in granular material, for use in industrial plants, especially. The experiments incorporated fine-ground carbonate copper ore, but most probably the same methodology could be used also with other materials. However, calibration would be needed, that is, acquisition and processing of a series of images showing the new material at several different moisture levels.

2.2.1.1 Experiments

In the experiments, ground copper ore was sieved into five size fractions: 0–0.1 mm, 0.1–0.2 mm, 0.2–0.5 mm, 0.5–1 mm and 1–2 mm. A mixture of these was also tested, with composition detailed in Fig. 2.14. Such particle size distribution of the mixture emulated a possible feed to the electromagnetic mill, as the developed measurement methods could also be applied in the grinding installation.

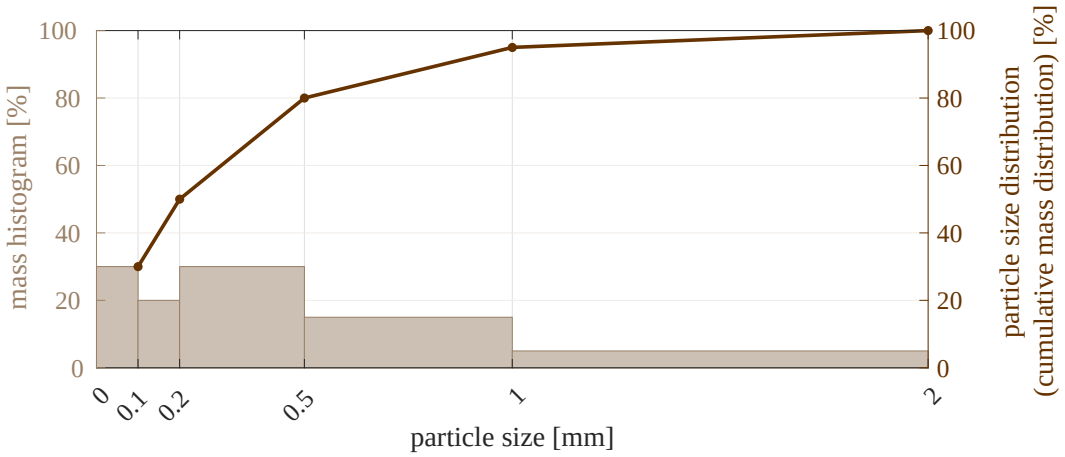

FIGURE 2.14: Composition of the mixed-size material: mass histogram (bar graph) and particle size distribution (curve).
Source [10]: Buchczik D.; Budzan S.; Krauze O.; Wyzgolik R. Moisture determination for fine-sized copper ore by computer vision and thermovision methods. *Sensors* **2023**, 23, 1220. https://doi.org/10.3390/s23031220, Fig. 3.
Re-used under Creative Commons Attribution (CC BY) license (https://creativecommons.org/licenses/by/4.0/).

All material fractions were moistened with demineralised water, to have relative moisture content around 0.5, 1, 3, 5, 7, 9 and 11%. The accurate values were determined with Radwag MA 110.R moisture analyzer [85]. This was the broadest range of moistures possible to be tested in such conditions. At 11% relative moisture content, especially with the coarser particle fractions, the water started to accumulate at the bottom of the container — i.e., free (not adsorbed) moisture appeared [74] — and the sample needed nearly continuous mixing to remain homogeneous. The moisture values used here were

wet-based mass percentages [10, eq. (1)]:

$$\mathrm{MC} = \frac{m_{\mathrm{water}}}{m_{\mathrm{wet}}} \cdot 100\% = \frac{m_{\mathrm{wet}} - m_{\mathrm{dry}}}{m_{\mathrm{wet}}} \cdot 100\% \ , \tag{2.2}$$

where m is mass and the subscripts "water", "wet" and "dry" denote, respectively, the contained water, wet (moisturized) material and completely dried material.

After moisturizing the ore, thermovision images (in long-wavelength infrared) and vision (color) images of all samples were taken using standard and macro lenses. Details of the hardware setup may be found in [10], if needed — here they will be skipped for brevity.

2.2.1.2 Image processing methods and their results

The thermograms were assessed for their mean surface temperature, under the assumption of ore's emissivity equal to 0.9. It was expected that presence of water — which itself has high emissivity (0.95–0.98) — combined with the assumed fixed emissivity of the sample (0.9) would modify the temperature readings even though the actual sample temperature remained constant. However, this effect was not visible in the acquired data [10, Sec. 4.1]. On the other hand, the thermograms showed different sample textures with increasing moisture, which was attributed to particles agglomerating more and more [10, Fig. 12]. This could probably be leveraged by using image processing approach on the thermal images. This is planned for the future, as well as changing the infrared range to near, short or medium wavelength, but the latter requires preparation of new imaging equipment.

For vision images, the processing was as follows [10, Sec. 3.4]. The images had the white balance corrected to normalize colors in all of them. Also, a border of 150 pixels was cropped from each side of an image in case it showed some particles which already started to dry out (this sometimes happened near sample edges). Then, each image was sectioned into quarters to produce more data points for analysis from each sample. Later, two processing paths were applied. Firstly, the color images were transformed to grayscale; i.e., pixel intensity was calculated from the R, G, B (red, green, blue) channels. Secondly, the color images were converted from RGB to HSL (hue, saturation, lightness) color space, and pixel saturation was extracted as a representation of color purity. Then, median value of pixel intensity or saturation was determined for each image. For easier analysis, the median values acquired for all the collected images were normalized (by the maximum of them) to have the new maximum value equal to 1. The most interesting results are compiled in Fig. 2.15–2.16; more graphs may be found in [10, Sec. 4.2]).

The error bars in the plots represent expanded measurement uncertainties, calculated according to [10, Appendix A].

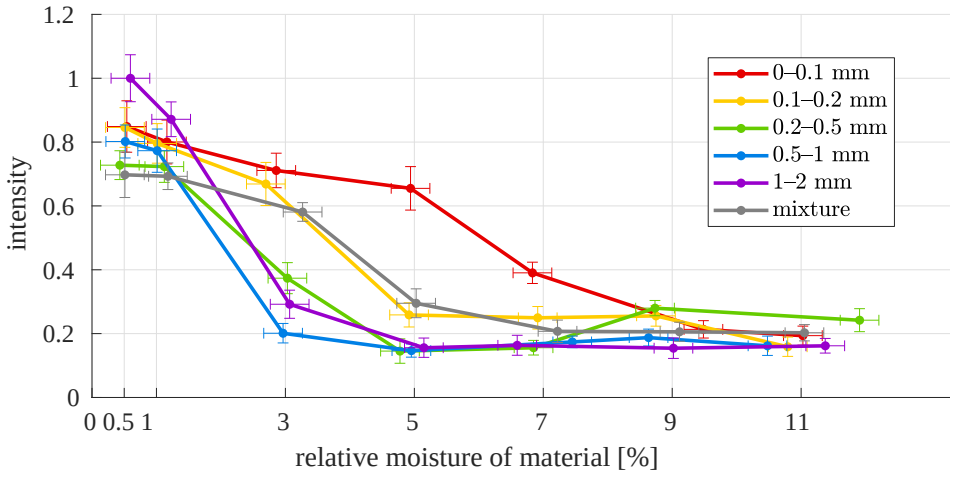

FIGURE 2.15: Median intensity of an image related to sample moisture, for different size fractions of the ore.
Source [10]: Buchczik D.; Budzan S.; Krauze O.; Wyzgolik R. Moisture determination for fine-sized copper ore by computer vision and thermovision methods. *Sensors* **2023**, 23, 1220. https://doi.org/10.3390/s23031220, Fig. 17.
Re-used under Creative Commons Attribution (CC BY) license (https://creativecommons.org/licenses/by/4.0/).

In general, median intensity of the image decreases with the increase in sample moisture (Fig. 2.15). However, the exact values, and even the shape of the curve, vary between material fractions, so a separate intensity-moisture model is needed for each curve (for each size fraction). In the same time, the observed curves overlap, which means particle size needs to be known first (to select the appropriate model) and then the moisture content may be assessed. Fortunately, if information on the particle sizes is not known from other sources, it may be obtained from the same image as is used for moisture estimation, using algorithms such as [12–15].

For a single analysed fraction (apart from the finest one), intensity values are quite similar for all moistures higher than 5%. This means that the presented method of analysing median image intensity may be used for moisture assessment only in the range up to about 5% (gravimetric) relative moisture. This is some limitation of the method but still, it may be useful in practice — such moistened material resembles damp sand used for building castles, so it is alredy a noticeable amount of moisture.

Median saturation of the image usually increases with growing moisture, but not in the whole moisture range (Fig. 2.16). Also, measurement uncertainty is much higher here than for the intensity. This makes median image saturation not much useful as an indicator of copper ore moisture. Only image intensity will be used further, i.e., for modelling intensity-vs.-moisture relationships.

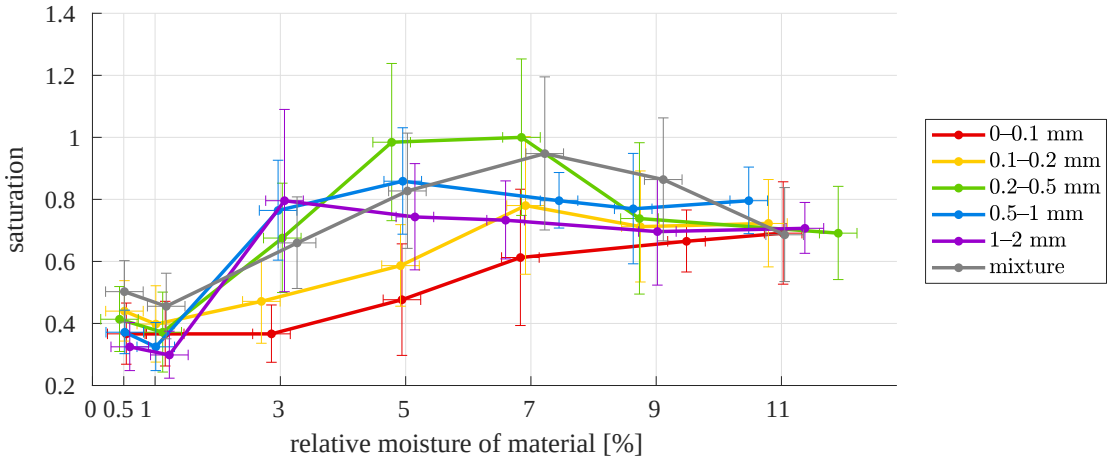

FIGURE 2.16: Median saturation of an image related to sample moisture, for different size fractions of the ore.
Source [10]: Buchczik D.; Budzan S.; Krauze O.; Wyzgolik R. Moisture determination for fine-sized copper ore by computer vision and thermovision methods. *Sensors* **2023**, 23, 1220. https://doi.org/10.3390/s23031220, Fig. 22.
Re-used under Creative Commons Attribution (CC BY) license (https://creativecommons.org/licenses/by/4.0/).

2.2.1.3 Models and their validation

To describe the relation between median image intensity and sample moisture, several model structures were tested:

- linear function,
- quadratic function,
- cubic smoothing spline.

Predictor variable was the accurate value of moisture content (measured with moisture analyzer) and response variable was the median intensity of an image. One dataset was associated with one size fraction, so there were six datasets. Each contained four data points per each of four moistures (around 0.5, 1, 3, 5%), in total 16 points per dataset.

The coefficients of the first two models were estimated using ordinary least squares method. Using weighted least squares method was assumed as not feasible in this case, as uncertainties in predictor variable were the same for all data points, and uncertainties in response variable were all similar and also small compared to the whole signal range (see Fig. 2.15). Higher order polynomials were also tested, but they produced excessive ripples in-between data points and so, were not included in the following analysis. Spline models were identified with the built-in MATLAB function `fit` [62]. The output of created models is shown in Fig. 2.17, and some measures of goodness of fit are listed in Table 2.2. These quality indices are:

- root mean squared error:

$$\mathrm{RMSE} = \sqrt{\frac{1}{N}\sum_{i=1}^{N}(y_i - \widehat{y}_i)^2}\,; \tag{2.3}$$

- coefficient of determination [106]:

$$\mathrm{R}^2 = 1 - \frac{\sum_{i=1}^{N}(y_i - \widehat{y}_i)^2}{\sum_{i=1}^{N}(y_i - \overline{y})^2}\,; \tag{2.4}$$

- adjusted coefficient of determination [99; 116]:

$$\mathrm{R}^2_{\mathrm{adj}} = 1 - \left(1 - \mathrm{R}^2\right) \cdot \frac{N-1}{N-1-n}\,, \tag{2.5}$$

where: $N = 16$ is the number of data points in the dataset, y_i — measured value of response variable (here: median intensity of an image), $\widehat{y}_i$ — sample of model output, $\overline{y}$ — mean value of response variable, n — number of model coefficients (not counting the free coefficient, if present).

TABLE 2.2: Goodness-of-fit indices for "direct" models from Fig. 2.17, that is, similarity between measured and modelled intensities of an image. 'quad.' means quadratic function.
Source [10]: Buchczik D.; Budzan S.; Krauze O.; Wyzgolik R. Moisture determination for fine-sized copper ore by computer vision and thermovision methods. *Sensors* **2023**, 23, 1220. https://doi.org/10.3390/s23031220, Table 1.

Measure	Model type	Size fraction [mm]					
		0–0.1	**0.1–0.2**	**0.2–0.5**	**0.5–1**	**1–2**	**mix**
number of coefficients[1]	linear	1	1	1	1	1	1
	quad.	2	2	2	2	2	2
	spline	2.11	2.13	2.09	2.13	2.11	2.09
RMSE (2.3)	linear	0.032	0.053	0.040	0.11	0.11	0.056
	quad.	0.028	0.026	0.039	0.057	0.047	0.020
	spline	0.032	0.028	0.035	0.046	0.041	0.025
R^2 (2.4)	linear	0.842	0.948	0.974	0.874	0.912	0.883
	quad.	0.877	0.987	0.975	0.965	0.983	0.985
	spline	0.876	0.988	0.984	0.982	0.990	0.982
$\mathrm{R}^2_{\mathrm{adj}}$ (2.5)	linear	0.831	0.944	0.972	0.865	0.906	0.875
	quad.	0.858	0.985	0.971	0.960	0.980	0.983
	spline	0.856	0.986	0.982	0.979	0.988	0.979

[1] Excluding free coefficient. This is variable n in Equation (2.5).

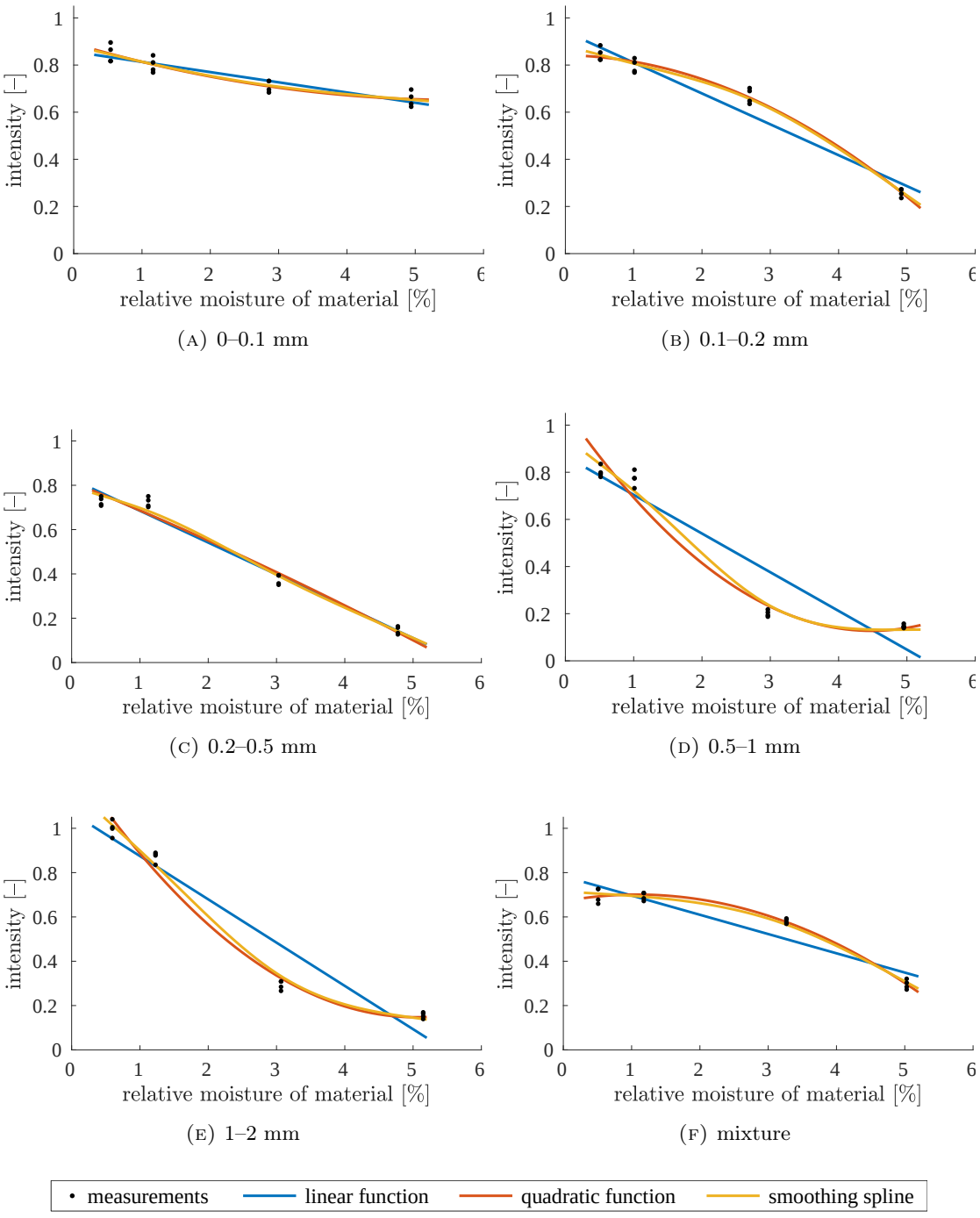

FIGURE 2.17: Median image intensity modelled with respect to material moisture, for different size fractions of ore (A–F), using linear function, quadratic function and smoothing spline models.
Source [10]: Buchczik D.; Budzan S.; Krauze O.; Wyzgolik R. Moisture determination for fine-sized copper ore by computer vision and thermovision methods. *Sensors* **2023**, 23, 1220. https://doi.org/10.3390/s23031220, Fig. 23.

Figure 2.17 and Table 2.2 show that linear fitting is usually very rough and it performs reasonably well only for a few size fractions. Quadratic and spline models provide definitely better fit quality, as confirmed by usually much lower RMSE and much higher coefficients of determination. Those two higher order models perform similarly good, or the spline model is slightly better than the quadratic model, in terms of the calculated quality indices. Of course, of these two models, spline model has more parameters and is more computationally complicated, but still this is not a very complex model. High values of R^2 and R^2_{adj} (all above 0.8, and most of them even above 0.9) confirm strong statistical correlation between median image intensity and moisture content in the sample, and justify such moisture estimation method as presented here.

The models from Fig. 2.17 may be inverted to provide moisture estimates based on median intensity of input image. Namely, for models identified as described above, an intensity value was supplied as a query point and the corresponding moisture content was returned as the queried value. The returned moisture values were limited to 0–5.5% moisture range (assumed as the operating range of this measurement method) to possibly prevent duplicated results from quadratic or spline functions. This means that when some results were returned from the inverse model, the ones outside the mentioned range were discarded. If afterwards only one value was left, it was — with good probability — reasonably close to the true moisture value of the sample. If all results got discarded, then the one closest to the 0–5.5% range was coerced to 0% or 5.5% value (which was closer) and returned as the final result. Some warnings on possibly out-of-range measurements could be issued then in the measurement system. Moreover, quadratic and spline models could also produce no results. In such a case, the measurement system should also raise some out-of-range warning, and no moisture estimate could be specified. In real-world applications with continuous flow of measured material — at which the presented measurement method is especially targeted — the zero-result case could be handled by re-using the last valid moisture estimate. This should give acceptable results provided that the measurements are taken frequently enough for the real material moisture not to change rapidly. Similarly, if quadratic function or smoothing spline models would return two results in range, the one closer to the last valid estimate could be picked as more probable.

To assess the quality of such inverse models, leave-one-out validation was performed [86]. This way, data points used for model validation were not used in model training (i.e., in model identification), which produced possibly reliable estimates of model performance on new images. The results of this cross-validation are presented in Fig. 2.18 and Tables 2.3–2.4. Goodness-of-fit indices in Table 2.3 were calculated with the same formulas as for the "direct" models in Table 2.2, but then, the compared signals were the measured and modelled image intensities, and now they were the measured and modelled moisture

values. While evaluating goodness of fit, in the cases when the model returned two results, the worse of the two errors was used in calculations. In turn, in the cases when the model returned zero results, the value was just omitted in calculation of quality indices; so actually, for some datasets, the models which returned zero results (see Table 2.4) performed worse than indicated by corresponding index values in Table 2.3.

TABLE 2.3: Goodness-of-fit indices for inverse models from Fig. 2.18 tested in leave-one-out manner, that is, similarity between measured and modelled moisture content in the material. 'quad.' means quadratic function.
Source [10]: Buchczik D.; Budzan S.; Krauze O.; Wyzgolik R. Moisture determination for fine-sized copper ore by computer vision and thermovision methods. *Sensors* **2023**, 23, 1220. https://doi.org/10.3390/s23031220, Table 3.

Measure	Model type	Size fraction [mm]					
		0–0.1	**0.1–0.2**	**0.2–0.5**	**0.5–1**	**1–2**	**mix**
RMSE (2.3)	linear	0.72	0.45	0.31	0.74	0.61	0.65
	quad.	0.72	0.35	0.33	0.62	0.38	0.80
	spline	0.70	0.32	0.32	0.60	0.33	0.66
R^2 (2.4)	linear	0.823	0.932	0.966	0.820	0.880	0.866
	quad.	0.773	0.957	0.962	0.875	0.951	0.785
	spline	0.833	0.964	0.964	0.882	0.966	0.864
R^2_{adj} (2.5)	linear	0.810	0.928	0.964	0.808	0.871	0.856
	quad.	0.732	0.949	0.956	0.856	0.942	0.738
	spline	0.805	0.959	0.958	0.862	0.961	0.842

TABLE 2.4: Number of cases (out of total 16 images per size fraction) when the inverse model tested in leave-one-out manner returned: no outputs at all (*0*); only some out-of-range outputs which were then coerced to a single value (*coer.*); single output (*1*); two outputs (*2*).
Source [10]: Buchczik D.; Budzan S.; Krauze O.; Wyzgolik R. Moisture determination for fine-sized copper ore by computer vision and thermovision methods. *Sensors* **2023**, 23, 1220. https://doi.org/10.3390/s23031220, Table 2.

Size fraction	Linear function				Quadratic function				Smoothing spline			
	0	***coer.***	***1***	***2***	***0***	***coer.***	***1***	***2***	***0***	***coer.***	***1***	***2***
0–0.1 mm	0	3	13	0	2	1	13	0	0	3	13	0
0.1–0.2 mm	0	1	15	0	2	0	14	0	0	1	15	0
0.2–0.5 mm	0	0	16	0	0	0	16	0	0	0	16	0
0.5–1 mm	0	0	16	0	0	0	12	4	0	0	16	0
1–2 mm	0	0	16	0	1	0	14	1	0	0	16	0
mixture	0	3	13	0	4	0	10	2	0	2	14	0

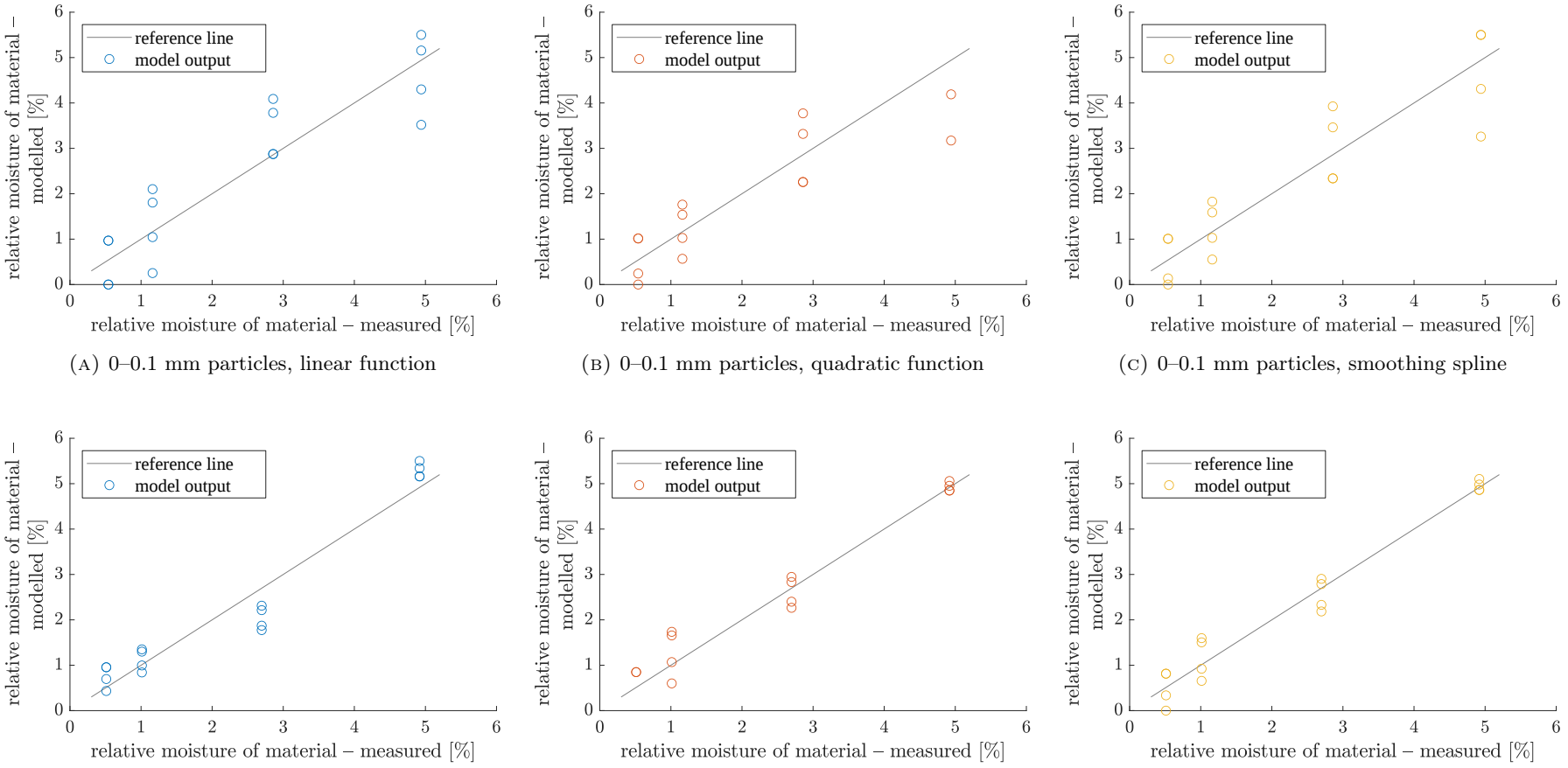

(A) 0–0.1 mm particles, linear function

(B) 0–0.1 mm particles, quadratic function

(C) 0–0.1 mm particles, smoothing spline

(D) 0.1–0.2 mm particles, linear function

(E) 0.1–0.2 mm particles, quadratic function

(F) 0.1–0.2 mm particles, smoothing spline

FIGURE 2.18: Outputs of inverse models (material moisture vs image median intensity) as obtained in leave-one-out cross-validation. Source [10]: Buchczik D.; Budzan S.; Krauze O.; Wyzgolik R. Moisture determination for fine-sized copper ore by computer vision and thermovision methods. *Sensors* **2023**, 23, 1220. https://doi.org/10.3390/s23031220, Fig. A1.

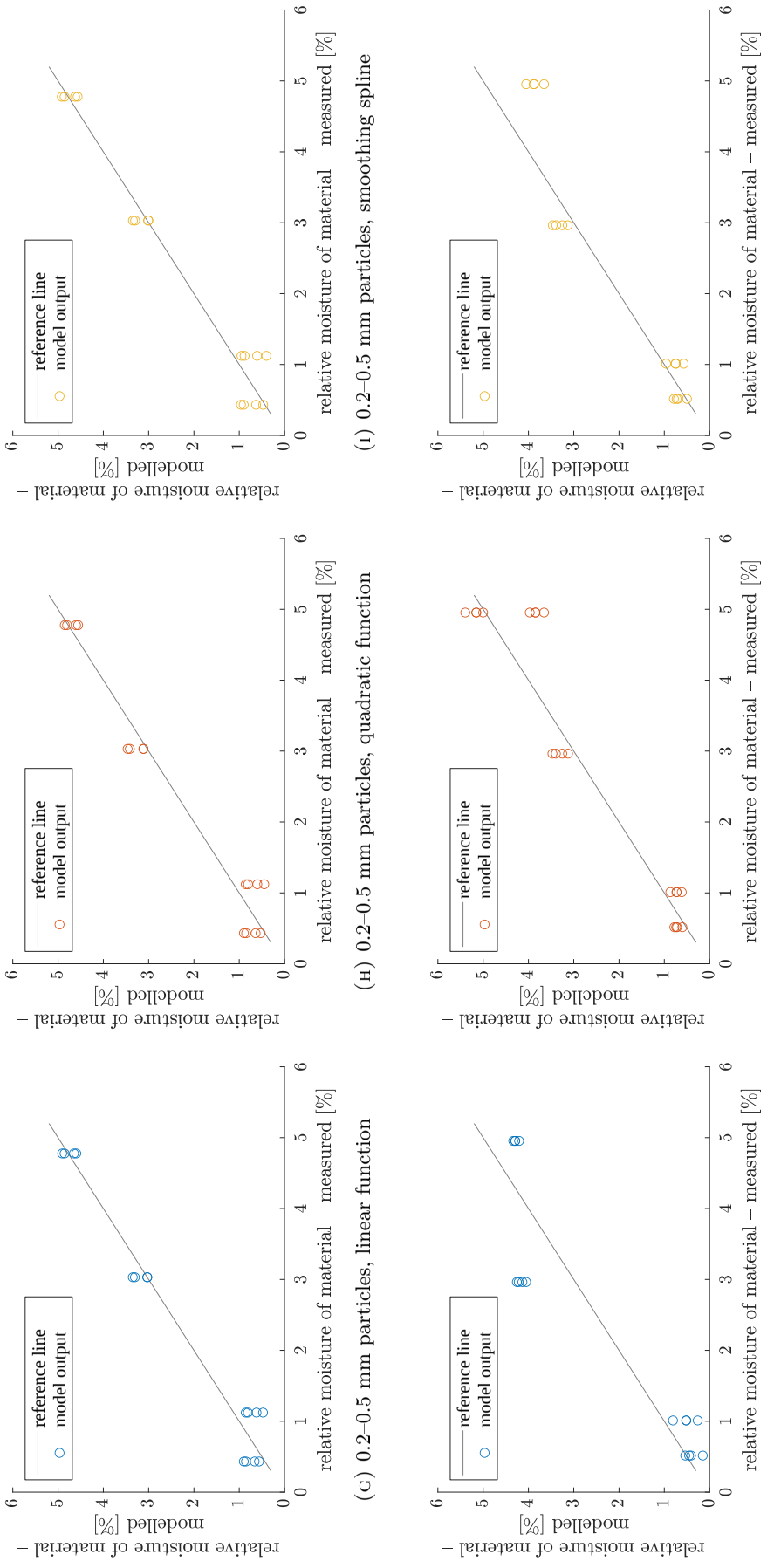

(g) 0.2–0.5 mm particles, linear function (h) 0.2–0.5 mm particles, quadratic function (i) 0.2–0.5 mm particles, smoothing spline

(j) 0.5–1 mm particles, linear function (k) 0.5–1 mm particles, quadratic function (l) 0.5–1 mm particles, smoothing spline

FIGURE 2.18: Outputs of inverse models (material moisture vs image median intensity) as obtained in leave-one-out cross-validation. (Cont.)

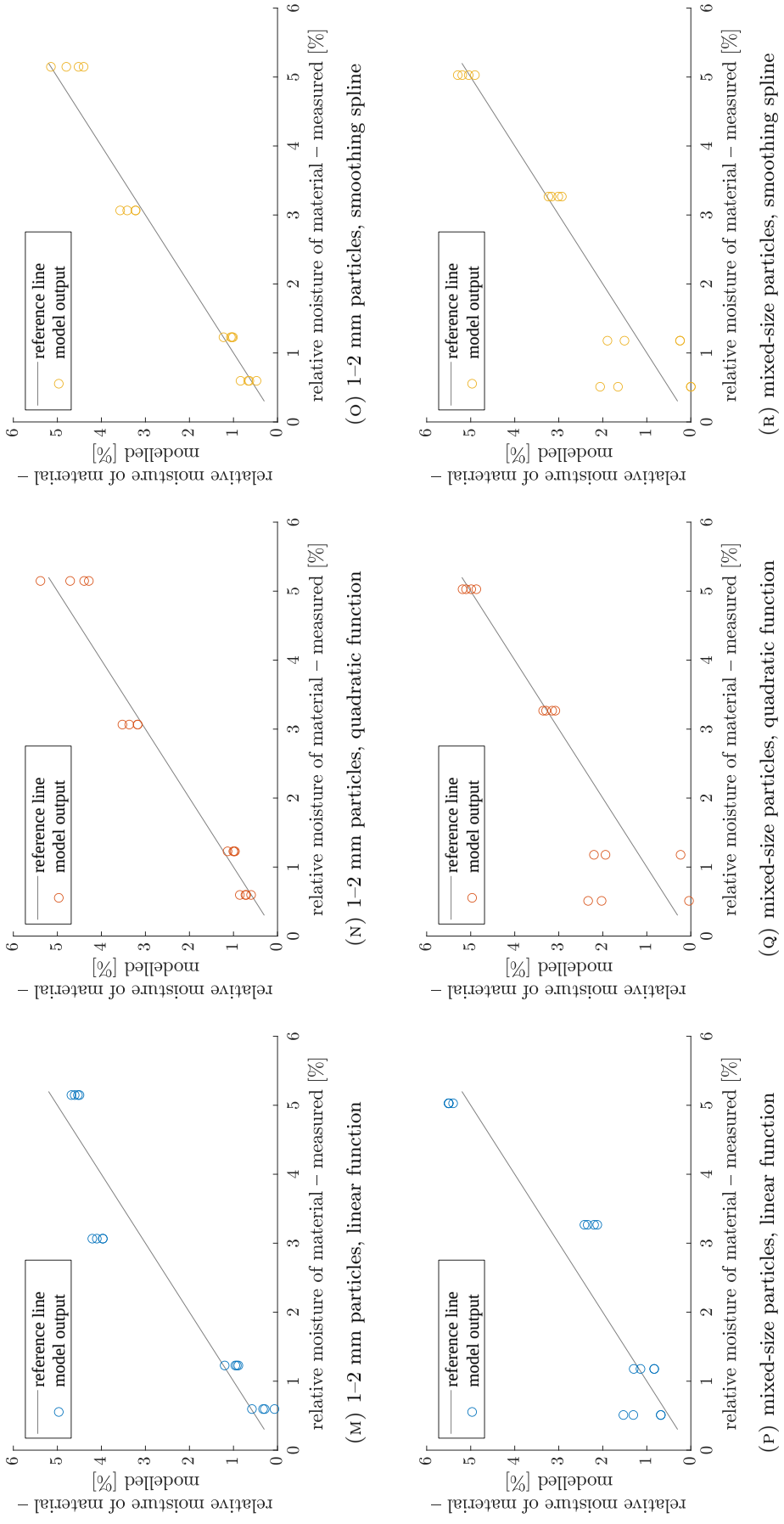

(M) 1–2 mm particles, linear function

(N) 1–2 mm particles, quadratic function

(O) 1–2 mm particles, smoothing spline

(P) mixed-size particles, linear function

(Q) mixed-size particles, quadratic function

(R) mixed-size particles, smoothing spline

FIGURE 2.18: Outputs of inverse models (material moisture vs image median intensity) as obtained in leave-one-out cross-validation. (Cont.)

Figure 2.18 and Table 2.3 suggest that fit quality depends more on the dataset than on the model type. However, there were some datasets (e.g., for fractions 0.5–1 mm, 1–2 mm and mixture) where higher order models performed significantly better than linear function models.

RMSE values (Table 2.3) were usually less than 0.8% moisture, which constitutes less than 15% of the assumed measurement range of the method (i.e., 0–5.5% moisture). This indicates the method is suitable for approximate measurement of moisture content in carbonate copper ore (in this value range). Coefficients R^2 and R^2_{adj} were high (mostly above 0.8, often well above 0.9), which also justifies the use of the proposed method.

Linear function is inherently not capable of returning no results or duplicate ones, which is some advantage. However, spline models appeared equally good from this point of view (Table 2.4), and also they sometimes had better goodness of fit, as already mentioned. Quadratic function models performed quite poorly in this regard (Table 2.4), producing a total of 9 "no results" cases and 7 two-value results, out of 96 images tested. This is a serious argument for not using quadratic models in the presented moisture estimation method, unless some new tests with more data points suggest otherwise. All in all, smoothing spline models are recommended thus far for use in this moisture measurement method.

2.2.1.4 Comments and conclusions

This research proposed a novel contactless method for approximate measurement of moisture content in fine-ground carbonate copper ore, for moistures in range from about 0% to about 5–5.5% of wet-based moisture (gravimetric). Higher moisture values cannot be differentiated with this method, unless the ore particles are very fine (below 0.1 mm). Probably the method may be adapted to other material types, but this requires taking additional test images of the given material at several moisture levels. The achievable moisture measurement range may then appear different.

The method is based on simple analysis of vision images. In essence, median intensity of the image is used, so probably even grayscale images would suffice. Some tests were also carried out with color image saturation and with thermal images, but the former did not produce much useful results and the latter require further research, as was detailed above.

The proposed method has several advantages. It may be used on site, especially with processes using continuous flow of material. The measurement is contactless. Image proccessing algorithm is uncomplicated, so it may be carried out fast and on simple processing units. The equipment is not very costly, and may even come without any additinal

costs — if vision images are already used in the technological installation for estimating other material features, such as particle size or shape, material composition, etc. Then, moisture could be approximated very easily even from the same images.

A drawback of this measurement method is that it is sensitive to particle size (different calibration curve needs to be used for different particle sizes). Fortunately, this may be assessed from the same image, using vision processing algorithms like [12–15]. Also, the method gives only approximate results, but this is because it was intended for fast, uncomplicated estimation, even as an extra side-effect of taking other vision-based measurements.

The image intensity–material moisture models developed here should be treated as preliminary and approximate. To make them more accurate and more reliable, similar experiments could be repeated several times, to obtain images of many independent samples for each size fraction and moisture level. Also, once the optimal moisture range for the method is known, more moisture values could be tested in this range to verify the shapes of model curves.

2.2.2 Modelling of moisture content throughout the grinding installation

Apart from measuring water content in specific places, such as feed material inlet, product outlet or recycle pipe, moisture content should be known — at least approximately — throughout the whole transport system in the grinding installation. This is necessary to ensure safe and efficient transport of the material, as too damp powders stick to pipe walls, and too dry powders might explode (if transported simply in air, instead of special non-flammable gaseous atmosphere). Thus, some research was conducted on modelling the moisture content of the material in the grinding installation [53; 103]. So far, this included the classification part of the grinding circuit, that is, the part downstream the EM mill and its integrated preliminary classifier, up to the outlet of final product.

2.2.2.1 Test rig

The test rig used for this research is shown in Fig. 2.19. This was a fragment of the grinding installation with EM mill (see Fig. 1.3), but the mill itself and the inlet air pipes were disconnected from the rest of the system. The screw feeder supplying raw material was mounted directly below the inlet to the precise classifier, which divided the particles into two streams. Because of the lack of the mill, the coarse particles (lower classification product) were not recycled to be re-ground, but they were simply collected

in a tank. It was similar to the fine particles (upper classification product), also collected, as usual.

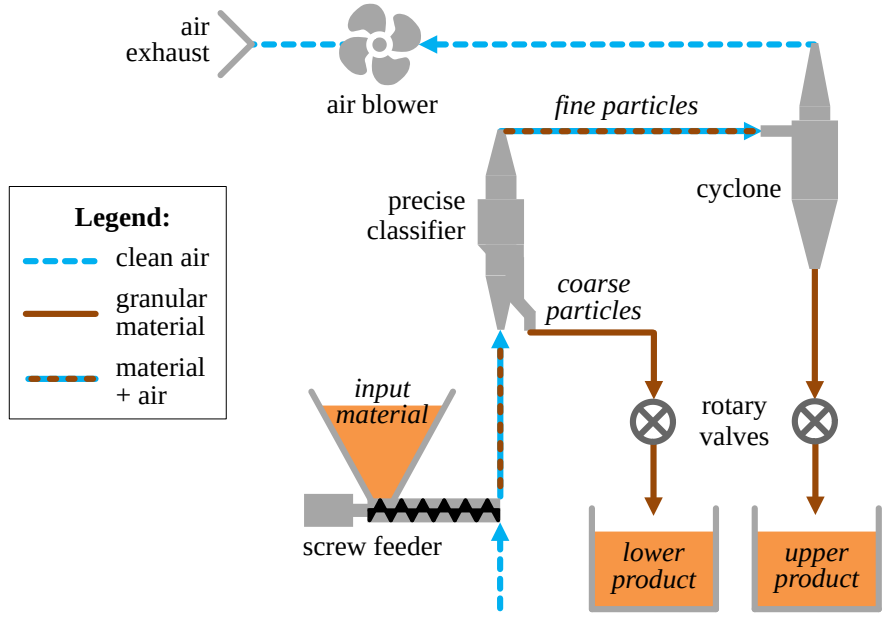

FIGURE 2.19: Diagram of the test rig for research on material moisture in classification system of the grinding installation

A benefit of such setup was the ability to inspect the properties of the coarse material (e.g. moisture content, particle size distribution), which would be impossible in the standard arrangement with material recycle to the mill. On the other hand, the reason for excluding the mill etc. from the experiment was to reduce the complexity of the analysed system [103]. Mill operation produces significant amount of heat, which dries the material in the working chamber. In contrary, extra moist may be supplied to the material in the recycle stream, which then enters the mill. These phenomena should be inspected in a separate study. All the material produced as a result of these enters the precise classifier in a single stream of particles, and this situation was analysed in the presented research. The material normally leaving the mill was emulated with the use of the screw feeder. The feeder itself was controlled through a variable frequency drive, which allowed for testing different feeding rates.

2.2.2.2 Raw material

Granular material in these experiments was again carbonate copper ore, ground to particles sized 0–1.25 mm. Such range definitely would not be exceeded in classifier input during normal operation of the grinding installation. The ore was sieved into several size fractions, using sieves with apertures 0.12 mm, 0.25 mm, 0.49 mm and 0.75 mm. Then, a mixture of these fraction was composed such that fine particles were the most abundant

— as it would be with the product of grinding in EM mill. The exact composition of the feed is presented in Fig. 2.20.

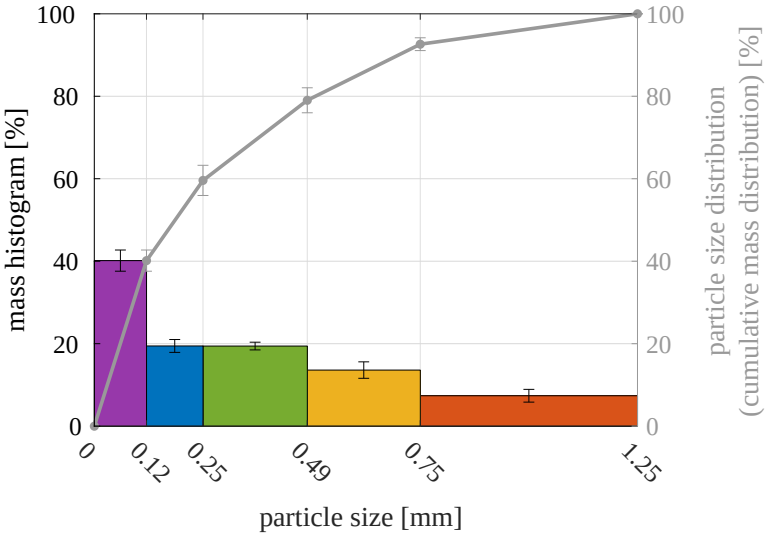

FIGURE 2.20: Particle size distribution of feed material — histogram and cumulative histogram. Average values (color bar heights or points on the curve) and sample standard deviations (error bars) from all test runs are presented.

2.2.2.3 Test scenario

In subsequent test runs, feed material was intensely mixed with demineralised water, in amounts appropriate to achieve approximately 0.5, 1, 1.5, 2, ..., 5% relative moisture. An illustration to give a sense of these values is as follows: relative moisture of 0.5% meant oven-dried material (when drying bulk amounts for about 30 minutes in approximately 130 °C), 5% resulted in consistency appropriate for building sand castles. Higher moisture levels were also tested, but such material was sticking to the inner pipe walls and was not moving freely. Thus, these cases were not included in the analysis as being out of operational range of the installation.

The exact water content was verified with moisture analyzer Radwag MA 110.R [85]. The device uses thermogravimetric method of moisture measurement, i.e., it thoroughly dries a small sample of the measured material and compares its weight before and after drying. The resultant relative mass moisture content in material is defined as:

$$\mathrm{MC} = \frac{m_{water}}{m_{wet}} \cdot 100\% = \frac{m_{wet} - m_{dry}}{m_{wet}} \cdot 100\% \ . \tag{2.6}$$

Symbols m_{water}, m_{wet}, m_{dry} denote masses of: water contained in the sample, wet (damp) sample and completely dried sample. Details of the method and measurement

uncertainties estimated for this particular type of material are described in [11, Section IV.A.3] and [103, Section III.C]. Finally, the above sources estimated the expanded uncertainty of moisture measurement as 0.3%, with 95% confidence level.

In the experiment, before each test run, three samples of about 8 g were taken from different areas of the input material tank. Their moisture content was measured and the average of the three values was used in the following analyses.

The moistened input material was supplied to the test rig using 50% and 100% of the nominal throughput of the screw feeder, that is, using supply current of 25 Hz and 50 Hz frequency. The portions weighed about 1.5 kg or 3 kg (in 25 Hz or 50 Hz experiment runs, respectively). This resulted in around 3–4 minutes of continuous material flow through the installation in each case. Material flow rates were around 15–25 kg/h or 30–45 kg/h, respectively for half- and full-throughput experiments. The exact values differed between test runs due to the changing moisture.

Afterwards, the product material in each collection tank was carefully mixed and then sampled. Three small samples were taken from each tank to measure the moisture content again, using the same procedure as for the feed material. A bigger sample (about 80–100 g) was collected from each container for determining particle size distribution. The sample was oven-dried, then sieved on the mentioned 0.75 mm, 0.49 mm, 0.25 mm and 0.12 mm screens, and each fraction was weighed. Finally, all the material was mixed together and moistened again for use in the next test run. This way, only several kilograms of copper ore were needed to perform all tests, and also, particle size distribution of the feed was constant throughout the experiment. The mixing of the material or supplying it with a screw feeder did not significantly disturb the feed composition (the particles rather were not further fragmented). This was verified with statistical analysis of size distribution curves coming from subsequent tests. Namely, correlations between ordinal number of experiment and masses of specific size fractions were investigated. The resultant Pearson and Spearman correlation coefficients were not statistically significant for most size fractions, with 95% confidence level. (The details of calculation of correlation coefficients are off the topic of this section. Instead, they may be found in Section 2.2.3.)

Other conditions of the process were kept possibly constant. The most important parameters were: air humidity at intake — ca. 20–28%, air temperature — ca. 18–23 °C, and air flow rate — ca. 2600–3000 L/min, which resulted in air speed of about 7.6–8.8 m/s through the most of the pipeline (86 mm diameter). Such values were typical for operation of this grinding installation.

2.2.2.4 Measurement results

The measured moisture content in lower and upper products of classification, related to moisture in input material, is plotted in Fig. 2.21. For each test case, the single measurement values were indicated, as well as their averages and sample standard deviations. Comparison of the four data series in one chart is shown in Fig. 2.22, with only the average moistures plotted for clarity.

The collected data show that the material was dried by the transport air when the particles moved through the installation elements. Upper classification product was drier because it travelled a longer distance — not only through the classifier, but also through the cyclone and some additional piping (see Fig. 2.19). Particle size surely also affected the final moisture level, but the most important was the effect of farther distance and thus, longer contact with transport air.

Coarse particles were dried in a manner close to linear (in terms of relation to input moisture). Fine particles behaved differently, and their moisture level was saturated at about 1.6–1.7% moisture.

A quantitative model of the relationship between these input and output moistures is desirable, as it would enable to monitor or control the water content in material throughout the entire installation. Such model would also reduce the number of measurement points necessary to achieve this. Two approaches were adopted: I) simple models using straight lines, for easy usage in control algorithms [53]; II) more complex, but also more accurate polynomial models [103].

2.2.2.5 Data processing I: straight line models

Straight line only Linear function models were estimated from the measured moistures, taking into account the uncertainties in both predictor and response variables. This was advisable as both of these had measurement errors of similar magnitudes (see Fig. 2.21). Moreover, the uncertainty varied between data points. Thus, an ordinary least squares algorithm was not sufficient; some weighted modification was necessary to find optimal estimates of model coefficients. Many such methods were studied and compared in a review article [17]. From among them, an iterative method [117] was chosen because in the review paper it was assessed as accurate and convenient. It also computes standard errors of model coefficients, not only coefficients themselves.

The iterative weighted least squares algorithm [117] was adopted for this particular case (moisture modelling) and implemented in a MATLAB script. The algorithm had the following features:

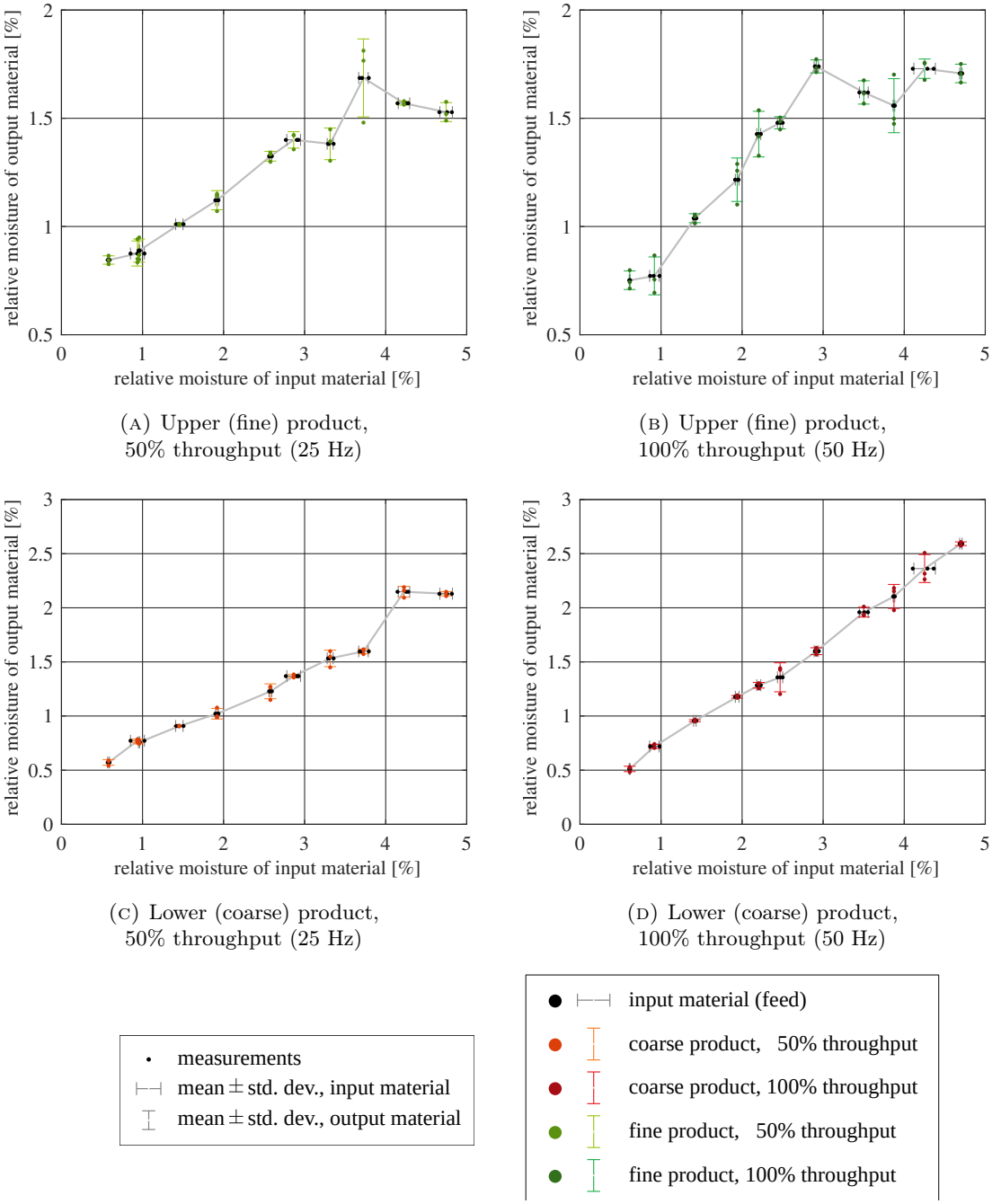

(A) Upper (fine) product, 50% throughput (25 Hz)

(B) Upper (fine) product, 100% throughput (50 Hz)

(C) Lower (coarse) product, 50% throughput (25 Hz)

(D) Lower (coarse) product, 100% throughput (50 Hz)

FIGURE 2.21: Moisture content measured in classification products in relation to moisture content in input material.
Source [53]: Krauze O.; Buchczik D.; Budzan S. Measurement-based modelling of material moisture and particle classification for control of copper ore dry grinding process. *Sensors* **2021**, 21, 667. https://doi.org/10.3390/s21020667, Fig. 7.

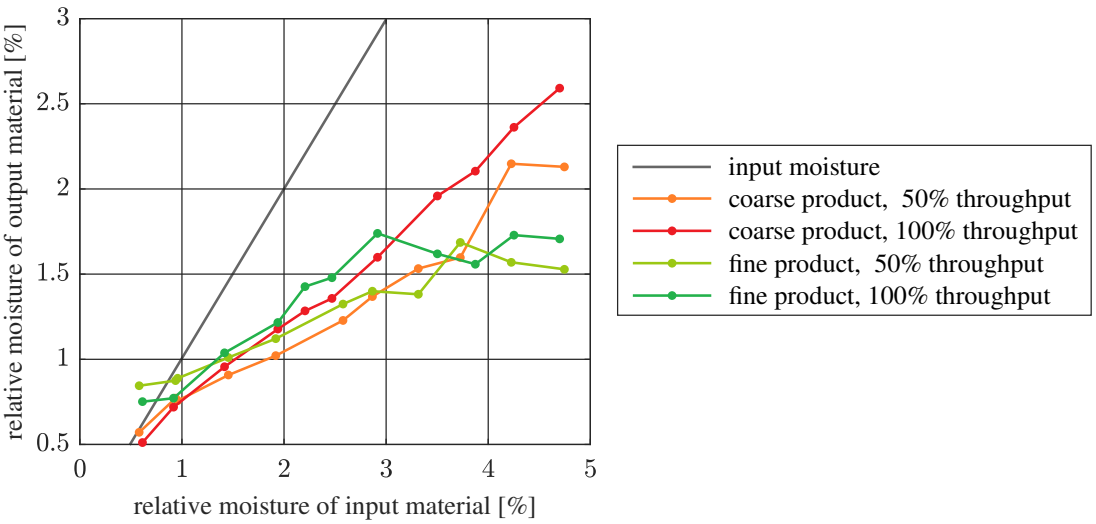

FIGURE 2.22: Average measurements of moisture content compared between classification products and different throughput experiments. Input moisture (gray line) drawn for reference.

- predictor variable was the average of the three input moistures measured for each test run;
- response variable was each single moisture measured for coarse or fine product supplied at half or full throughput (so, there were four datasets and four straight line models);
- the initial weights for predictor and response variables were reciprocals of sample variances calculated from the appropriate three measurements (as suggested in [117]);
- the initial slope of the straight line model was the slope estimated with ordinary least squares method, having predictor and response variables as defined above (as suggested in [117]);
- errors between predictor and response variables were assumed uncorrelated, because the measurements were independent (in the other case, the algorithm may be supplied with a desired correlation function).

The exact method equations are probably too detailed to be cited here; they may be found in the original paper [117]. In general, the operation of the algorithm was as follows. For each i-th data point, the algorithm combined the individual weights for predictor and response variables into a single weight W_i. Then, straight line coefficients were estimated that minimized the sum of squared errors (or, equivalently, mean squared error) weighted with the just mentioned W_i values. (The formula for weighted mean squared error will be given shortly, in (2.7).) In turn, new straight line model produced new values of

weights W_i, and so on. The algorithm stopped when slope estimates from subsequent iterations differed by less than the selected tolerance, set to 10^{-10} in this case. For moisture data from this experiment, this meant convergence after 5–7 iterations. The finally estimated model coefficients are listed in Table 2.5 at the end of this section.

To assess goodness of fit of the model output $\widehat{y}_i$ to measured data y_i, several numeric indices were calculated (they use the final values of weights W_i and number of data points in the dataset N):

- weighted mean squared error:

$$\mathrm{WMSE} = \frac{\sum_{i=1}^{N} W_i \cdot (y_i - \hat{y}_i)^2}{\sum_{i=1}^{N} W_i}\,; \tag{2.7}$$

- coefficient of determination [106]:

$$\mathrm{R}^2 = 1 - \frac{\sum_{i=1}^{N} \left(y_{\mathrm{w},i} - \widehat{y}_{\mathrm{w},i}\right)^2}{\sum_{i=1}^{N} \left(y_{\mathrm{w},i} - \overline{y}_{\mathrm{w}}\right)^2} = 1 - \frac{\sum_{i=1}^{N} W_i \cdot \left(y_i - \widehat{y}_i\right)^2}{\sum_{i=1}^{N} \left(\sqrt{W_i} \cdot y_i - \overline{y}_{\mathrm{w}}\right)^2}\,, \tag{2.8}$$

  with $y_{\mathrm{w},i} = \sqrt{W_i} \cdot y_i$ and $\widehat{y}_{\mathrm{w},i} = \sqrt{W_i} \cdot \widehat{y}_i$ being weighted outputs of the plant and of its model, and $\overline{y}_{\mathrm{w}} = \frac{1}{N} \sum_{i=1}^{N} y_{\mathrm{w},i}$ being the mean value of the weighted measured output[3];

- adjusted coefficient of determination[4] [99; 116]:

$$\mathrm{R}^2_{\mathrm{adj}} = 1 - \left(1 - \mathrm{R}^2\right) \cdot \frac{N - 1}{N - 1 - n}\,, \tag{2.9}$$

  where n denotes number of parameters in the model, excluding the free coefficient (so, for the straight line model, $n = 1$). By accounting for the number of coefficients, $\mathrm{R}^2_{\mathrm{adj}}$ allows comparing different structures of models, which will be used shortly.

The values of these goodness-of-fit measures are collected in Table 2.5 at the end of this section.

Moreover, 95% prediction intervals were computed, according to [28]. Prediction intervals estimate the value range in which a single data point would fall with the probability specified. Small modifications were made to adapt the formulas from [28], which use

[3] In equation (2.8), instead of weighted outputs $y_{\mathrm{w},i}$ and $\widehat{y}_{\mathrm{w},i}$, also the plain unweighted y_i and $\widehat{y}_i$ could be used. According to [106], it is not obvious which of these two formulas is more proper. However, the research presented in this thesis used the formula with weighted output signals, to include the varying quality of the measurements also in the goodness-of-fit indices.

[4] The above remarks apply.

weights in reciprocal form, to the direct-form weights W_i, as used in model estimation algorithm [117]. The final equations were as follows:

- common factor between variances of modelling error at different data points (variance of weighted residuals) [28]:

$$s_e^2 = \frac{\sum_{i=1}^{N} W_i \cdot (y_i - \widehat{y}_i)^2}{N-2} \,; \tag{2.10}$$

- variance of modelling error at specific data point — not present in [28], but added here to get individual variances of unweighted residuals:

$$s_{e_i}^2 = s_e^2 \cdot \frac{1}{W_i} \,; \tag{2.11}$$

- variance of model output at i-th data point [28]:

$$s_{\widehat{y}_i}^2 = \left(1 + \mathbf{X}_i^{\mathrm{T}} \left(\mathbf{X}^{\mathrm{T}} \mathbf{W} \mathbf{X}\right)^{-1} \mathbf{X}_i + s_{x_i}^2 a^2\right) \cdot s_{e_i}^2 \,, \tag{2.12}$$

  where superscript T indicates matrix transpose; matrix $\mathbf{X} = \begin{bmatrix} 1 & x_1 \\ \vdots & \vdots \\ 1 & x_N \end{bmatrix}$ collects values of predictor variable x_i; column vector $\mathbf{X}_i$ is $[1, x_i]^{\mathrm{T}}$; a is the final value of the slope of the straight-line model; $s_{x_i}^2$ is sample variance of the predictor values at i-th data point.

  Note: In general, variance $s_{x_i}^2$ may vary irregularly between the data points. This is also the case with the moisture data analysed here. This produces non-smooth prediction intervals [28].

- prediction interval around model output at i-th data point [28]:

$$\mathrm{PI}_i = \widehat{y}_i \pm t_{\alpha, N-2} \cdot s_{\widehat{y}_i} \,. \tag{2.13}$$

  where coefficient $t_{\alpha,N-2}$ is taken from Student's t-distribution corresponding to $N-2$ degrees of freedom and significance level α (here, probability $1-\alpha = 0.95$ was selected, so $\alpha = 0.05$).

The data points, outputs of straight line models and their 95% prediction intervals are plotted in Fig. 2.23. Moreover, Fig. 2.24 shows the corresponding weighted residuals [106]:

$$e_i = \sqrt{W_i} \cdot (y_i - \widehat{y}_i) \,. \tag{2.14}$$

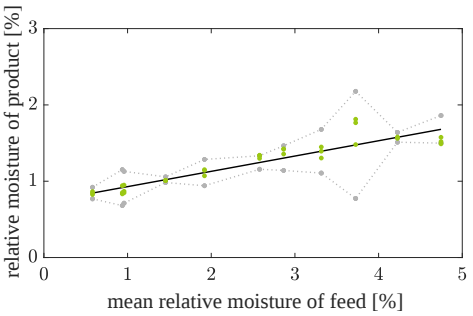

(A) Fine product, 50% throughput

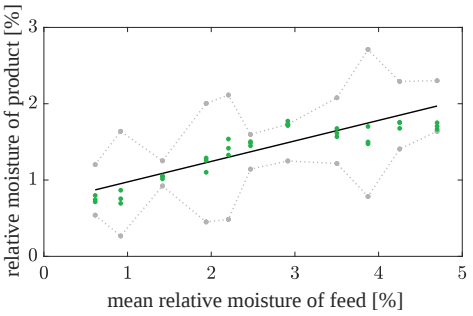

(B) Fine product, 100% throughput

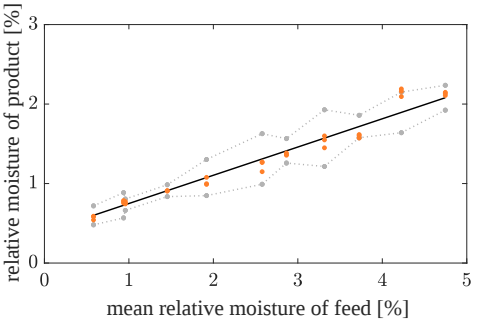

(C) Coarse product, 50% throughput

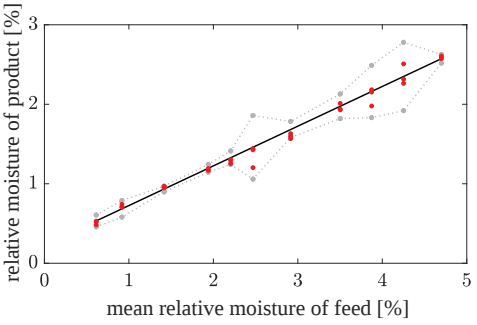

(D) Coarse product, 100% throughput

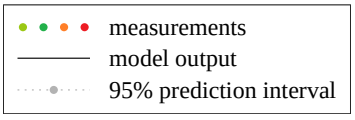

FIGURE 2.23: Straight line models fitted to moisture data

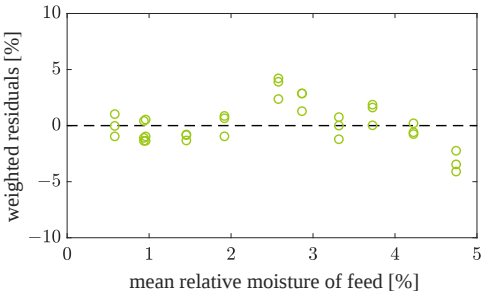

(A) Fine product, 50% throughput

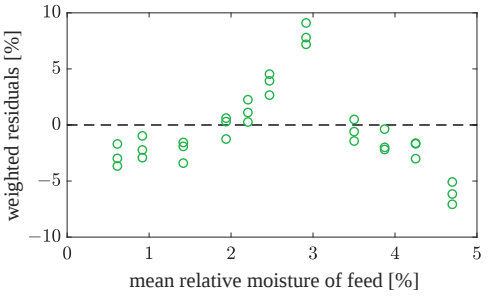

(B) Fine product, 100% throughput

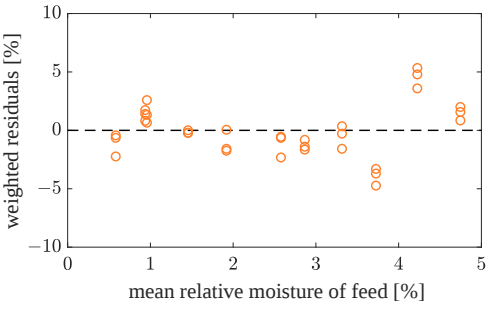

(C) Coarse product, 50% throughput

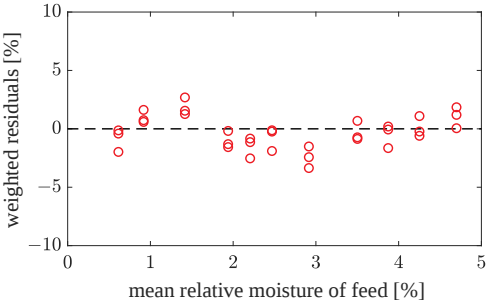

(D) Coarse product, 100% throughput

FIGURE 2.24: Weighted residuals of straight line models from Fig. 2.23

Source [53]: Krauze O.; Buchczik D.; Budzan S. Measurement-based modelling of material moisture and particle classification for control of copper ore dry grinding process. *Sensors* **2021**, 21, 667. https://doi.org/10.3390/s21020667, Fig. 8 (left) and Fig. 9 (right). Re-used under Creative Commons Attribution (CC BY) license (https://creativecommons.org/licenses/by/4.0/).

The figures show that straight lines quite well approximate the moisture of coarse product. Such model is sufficient for simple uses. However, there is some additional nonlinear trend not included in the model, but visible in the residuals. In the case of fine product, the patterns in residuals indicate that the straight line should rather be saturated for high input moistures. Also, prediction interval is very wide for fine product fed at full rate (Fig. 2.23b), and the corresponding residuals are very significant (Fig. 2.24b). The residuals for half-throughput fine product (Fig. 2.24a) have a bit smaller absolute values — similar to these of coarse products — but when related to the whole moisture range achieved in the fine product, these errors become quite big. These observations suggest that a better model structure should be searched for; first, a saturated straight line model was identified.

Straight line saturated for high input moisture This model had three coefficients: slope a and intercept b of the slanted line — fitted to data at lower values of predictor variable — and the "boundary" predictor value x_b above which the model output stayed constant. To estimate these coefficients, the following algorithm was proposed that modified the previous one used for straight line identification:

a) Choose initial value of the predictor variable that indicates the boundary between the slanted and horizontal lines (x_b). In this research, x_b was initially set to 3% moisture, which was a reasonable coarse approximation (see Fig. 2.21a–2.21b).

b) Using the already introduced algorithm [117] (see pages 57–60 in this dissertation), fit a straight line $\widehat{y}_i = ax_i + b$ to the subset of data points at $x_i \leq x_b$.

c) Knowing the slope a and intercept b of this optimal straight line, calculate model output at x_b: $\widehat{y}_b = ax_b + b$. This value is also the model output for inputs $x_i > x_b$, where saturation occurs and the slanted line turns into horizontal one.

d) Compute weights W_i for data points at $x_i > x_b$ in the same manner as in the algorithm [117]. Using them and the weights already calculated for points at $x_i \leq x_b$, determine WMSE (2.7) for the whole dataset.

e) Find optimal x_b value for the given dataset: change x_b and repeat steps b)–d) above until the minimum WMSE is reached. Namely, MATLAB built-in function `fminsearch` [64] was used as optimization procedure.

The final coefficients of saturated straight line models are listed in Table 2.5. They indicate that saturation was used only with fine product datasets, but not with coarse product datasets. Thus, the latter models were actually estimated as identical to the previously identified straight-line models. (This turned out to produce lower WMSE than when applying saturation at any value.)

Goodness-of-fit measures are also specified in Table 2.5. To enable comparison of the two model types, the same quality indices were used as for the models without saturation. Their values confirm that the fit to fine product data was significantly better this time.

TABLE 2.5: Model coefficients and goodness-of-fit measures for straight line models without and with saturation. Notation: *up* — upper (fine) product of classification; *low* — lower (coarse) product of classification; 50% and 100% — fraction of nominal throughput of the screw feeder; SD — standard deviation; WMSE — weighted mean squared error (2.7); R^2 — coefficient of determination, weighted version (2.8); R^2_{adj} — adjusted coefficient of determination, weighted version (2.9); x — predictor variable (relative moisture content in feed material [%]); y — response variable (relative moisture content in product material [%]).
Source [53]: Krauze O.; Buchczik D.; Budzan S. Measurement-based modelling of material moisture and particle classification for control of copper ore dry grinding process. *Sensors* **2021**, 21, 667. https://doi.org/10.3390/s21020667, Tables 2 and 3.

Model type	Quantity	Dataset			
		***up*, 50%**	***up*, 100%**	***low*, 50%**	***low*, 100%**
straight line	slope a	0.2005	0.2689	0.3553	0.4994
	SD of a	0.0032	0.0062	0.0040	0.0034
	intercept b	0.7285	0.706	0.3935	0.2263
	SD of b	0.0076	0.017	0.0086	0.0085
	WMSE	0.0017	0.023	0.0037	0.0012
	R^2	0.9965	0.9512	0.9810	0.9985
	R^2_{adj}	0.9964	0.9496	0.9804	0.9985
saturated straight line	slope a	0.2408	0.437	0.3553	0.4994
	SD of a	0.0072	0.011	0.0040	0.0034
	intercept b	0.675	0.430	0.3935	0.2263
	SD of b	0.012	0.022	0.0086	0.0085
	saturation for $x \geq ...$	3.71	2.91	> 5, so does not occur	> 5, so does not occur
	saturated at $y = ...$	1.57	1.70	not applicable	not applicable
	WMSE	0.00056	0.0025	0.0037	0.0012
	R^2	0.9994	0.9944	0.9810	0.9985
	R^2_{adj}	0.9993 [a]	0.9940 [a]	0.9804 [b]	0.9985 [b]

Number of model parameters used in Equation (2.9):
[a] $n = 2$, as saturation was indeed used;
[b] $n = 1$, as saturation was not actually used.

Outputs of saturated-line models, including 95% prediction intervals (2.13), are plotted in Fig. 2.25. The corresponding weighted residuals (2.14) are shown in Fig. 2.26. For the coarse material datasets — where saturation was not used and the models were actually

plain straight line models — the plots would be identical to the ones in Fig. 2.23–2.24, so these datasets were omitted now. Comparison of figures for plain and saturated straight line models shows that the latter are better fitted to measurement data: prediction intervals are narrower (especially in Fig. 2.25b), residuals have smaller amplitudes (especially in Fig. 2.26b), and error distribution is closer to random.

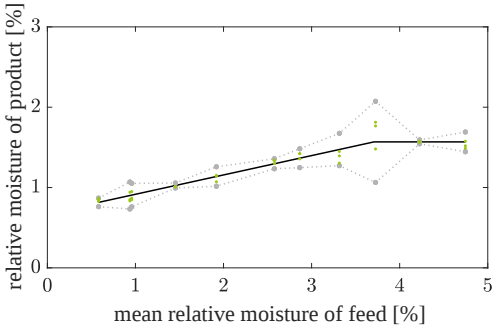

(A) Fine product, 50% throughput

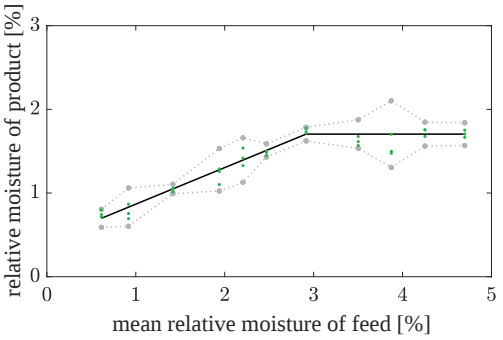

(B) Fine product, 100% throughput

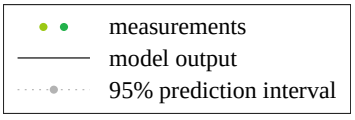

FIGURE 2.25: Saturated straight line models fitted to moisture data. Plots for coarse product were not shown as they are identical to Fig. 2.23c–2.23d.

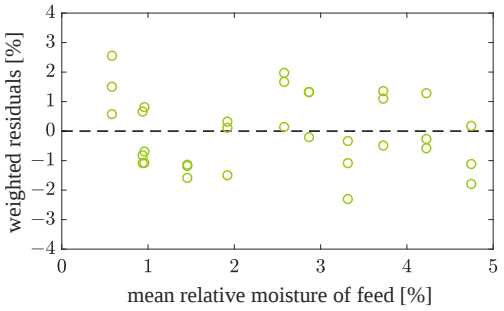

(A) Fine product, 50% throughput

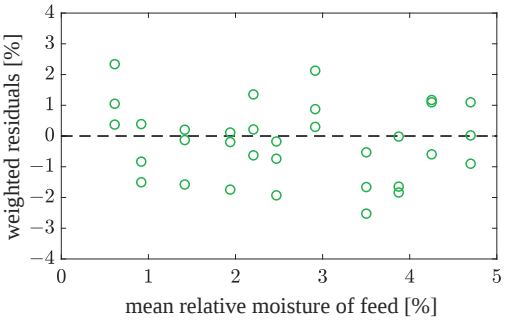

(B) Fine product, 100% throughput

FIGURE 2.26: Weighted residuals of saturated straight line models from Fig. 2.25. Plots for coarse product were not shown as they are identical to Fig. 2.24c–2.24d.

Source [53]: Krauze O.; Buchczik D.; Budzan S. Measurement-based modelling of material moisture and particle classification for control of copper ore dry grinding process. *Sensors* **2021**, 21, 667. https://doi.org/10.3390/s21020667, Fig. 10 (left) and Fig. 11 (right).

2.2.2.6 Data processing II: polynomial models

Polynomial models were identified using the same measurements as for the straight line models (see Fig. 2.21). Predictor variable was the relative moisture of feed material, averaged over the three samples taken from the feed container in each experiment run.

Response variable was relative moisture of given classification product (fine or coarse) under specific screw feeder throughput (half or full nominal throughput). Similar polynomial models were derived in paper [103], co-authored by the author of this dissertation. In the paper, product moisture was used as the average of three samples taken from the material tank in one experiment run; hereby, all three individual values are used. Firstly, this makes the data processing similar to the case with straight line models, and enables better comparison with these models. Secondly, this provides more data points in each set, producing more reliable estimates of model coefficients.

For each dataset, polynomial models of degrees 1–5 were identified with least squares method. To help compare the models' performance, e.g., Akaike Information Criterion (AIC) may be used [2]. For least-squares estimation it may be written in the form [16, p. 63]:

$$\mathrm{AIC} = N \cdot \ln \frac{\mathrm{SSE}}{N} + 2 \cdot n \,, \tag{2.15}$$

with N being the number of observations in the dataset, n — number of model parameters (i.e., degree of polynomial plus one), $\mathrm{SSE} = \sum_{i=1}^{N} (y_i - \widehat{y}_i)^2$ — sum of squared errors, i.e., sum of squared differences between measured moisture y_i and modelled moisture $\widehat{y}_i$. However, especially for higher order polynomials, the ratio N:n (number of data points versus number of parameters estimated from them) is not very high. This suggests using second-order variant of AIC [16, p. 66], that is, AIC corrected for small sample size N [42]:

$$\mathrm{AIC_c} = \mathrm{AIC} + \frac{2 \cdot n \cdot (n+1)}{N - n - 1} \,. \tag{2.16}$$

The lowest criterion value indicates the best model structure amongst the tested ones. All the model structures and their information criteria values will be discussed below.

Fine product, 50% throughput Outputs of models identified for this dataset and their residuals are plotted in Fig. 2.27. The corresponding values of information criteria are shown in Fig. 2.28.

According to AIC and $\mathrm{AIC_c}$ values (Fig. 2.28), the moistures in this dataset should be modelled with a third order polynomial. Looking at the plots in Fig. 2.27, indeed the higher order models produce curve shapes and residual patterns much alike the third order model does, so there is no benefit of raising the model order beyond three. However, the quite sharp drop of the model curve at the end of the examined predictor interval (near 5% feed moisture) looks a bit unnatural in the context of the underlying physical process. At higher input moistures (about 2.5–5%), the second order curve seems more realistic. On the other hand, it is less accurate at lower input moistures (about 0–2.5%), especially near 0%, where product moisture seems underestimated. So, perhaps these

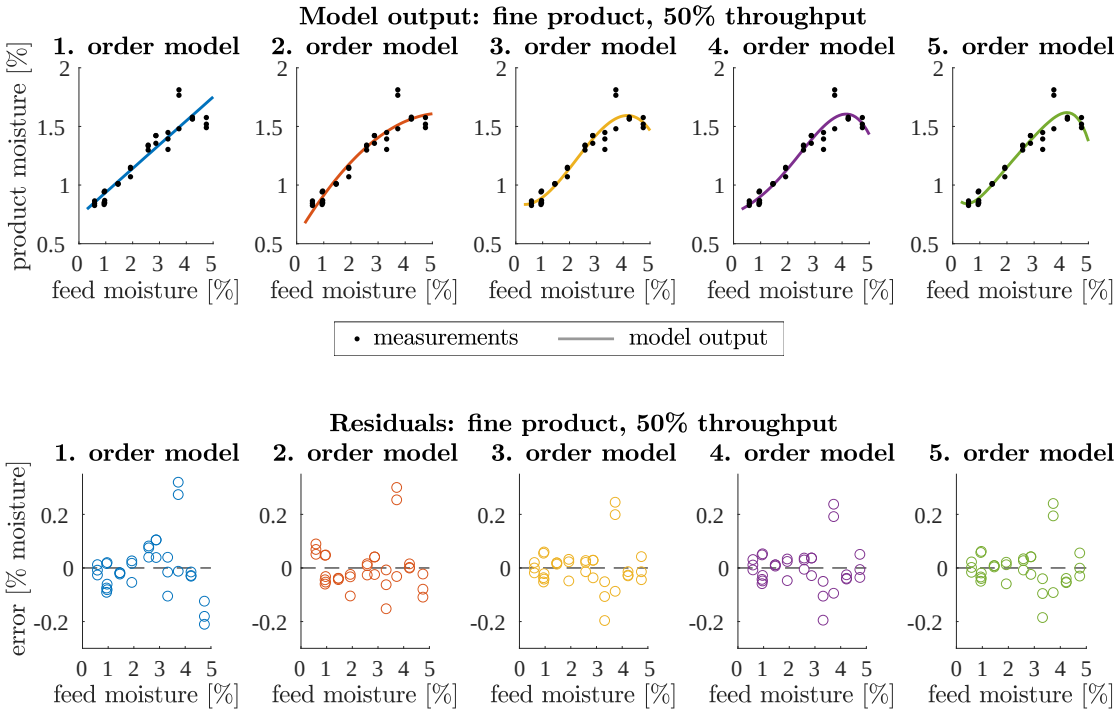

FIGURE 2.27: Polynomial models fitted to moisture data (top row), and their corresponding residuals (bottom row). Dataset: fine classification product, 50% material throughput.

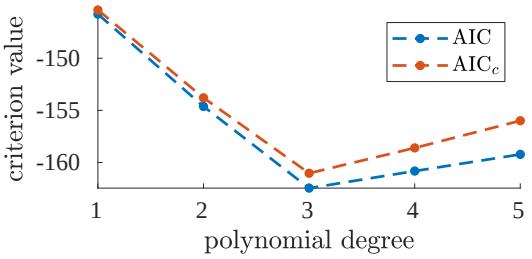

FIGURE 2.28: Information criteria — AIC, eq. (2.15) and AIC$_c$, eq. (2.16) — for the polynomial models. Dataset: fine classification product, 50% material throughput.

two models should be combined:

$$\widehat{\mathrm{MC}}_{\mathrm{fine},50\%} = \\ = \begin{cases} -0.03587 \cdot \mathrm{MC}_{\mathrm{in}}^2 + 0.3888 \cdot \mathrm{MC}_{\mathrm{in}} + 0.5614\,, & \text{if } \mathrm{MC}_{\mathrm{in}} \geqslant 2.7\% \\ -0.02711 \cdot \mathrm{MC}_{\mathrm{in}}^3 + 0.1824 \cdot \mathrm{MC}_{\mathrm{in}}^2 - 0.1114 \cdot \mathrm{MC}_{\mathrm{in}} + 0.8530\,, & \text{if } \mathrm{MC}_{\mathrm{in}} < 2.7\%\,. \end{cases} \tag{2.17}$$

Symbol $\mathrm{MC}_{\mathrm{in}}$ denotes relative moisture of input (feed) material, and $\widehat{\mathrm{MC}}_\bullet$ is the modelled product moisture in the dataset specified by the subscript. Feed moisture of about 2.7% is where the two curves intersect, so it was selected as the boundary value between the two cases. For such combined model, we may assume number of parameters n as the mean between n values for 2nd and 3rd order models ($n_2 = 3$ and $n_3 = 4$) weighted by number

of data points actually covered by these models (N_2 and N_3, where $N_2 + N_3 = N$):

$$n_{2+3} = \frac{n_2 \cdot N_2 + n_3 \cdot N_3}{N_2 + N_3} = \frac{3 \cdot 15 + 4 \cdot 18}{33} \approx 3.545\,. \tag{2.18}$$

Using this n value and the model outputs calculated from (2.17), the information criteria for the combined model are: AIC $= -149.1$ and $\text{AIC}_\text{c} = -148.0$. These are better than for the second order polynomials, but worse than for the third order model. Still, the combined model structure appears the best in terms of curve shape reasonably reflecting the underlying physical processes.

Fine product, 100% throughput Model outputs and residuals for this dataset are shown in Fig. 2.29, and the corresponding information criteria are plotted in Fig. 2.30.

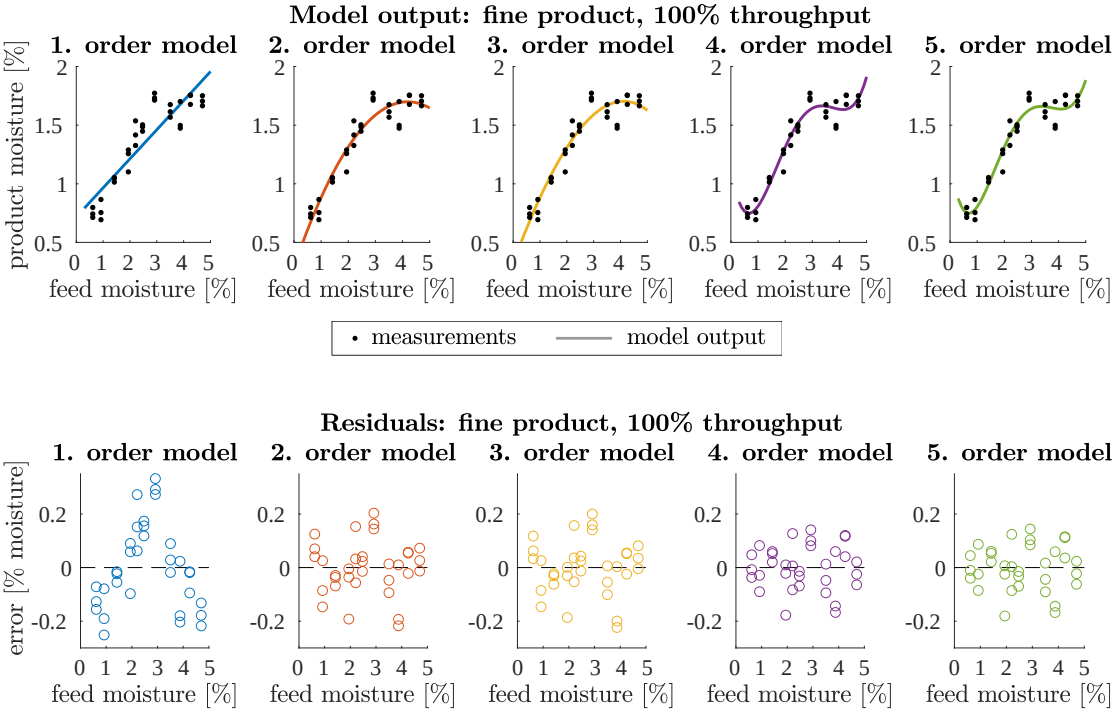

FIGURE 2.29: Polynomial models fitted to moisture data (top row), and their corresponding residuals (bottom row). Dataset: fine classification product, 100% material throughput.

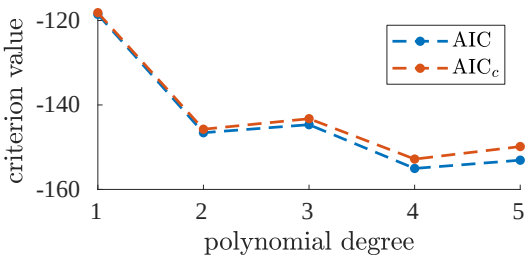

FIGURE 2.30: Information criteria — AIC, eq. (2.15) and AIC_c, eq. (2.16) — for the polynomial models. Dataset: fine classification product, 100% material throughput.

For this dataset, fourth order model was suggested by information criteria, and fifth order model was very similar (Fig. 2.30). Model coefficients were estimated as:

$$\widehat{\mathrm{MC}}_{\mathrm{fine},100\%} = 0.03332 \cdot \mathrm{MC}_{\mathrm{in}}^4 - 0.3621 \cdot \mathrm{MC}_{\mathrm{in}}^3 + 1.255 \cdot \mathrm{MC}_{\mathrm{in}}^2 - 1.229 \cdot \mathrm{MC}_{\mathrm{in}} + 1.111\,. \quad (2.19)$$

However, the plotted model output (Fig. 2.29) is much curved upwards at both ends (near 0 and 5% feed moistures), which does not seem realistic. This is due to a small amount of extrapolated data shown in the graphs; within the strict limits of feed moistures used in the experiment (and these only are included in the information criteria), the model behaves reasonably. In conclusion, it is suggested to be very cautious with the model when feed moisture is close to 0 or 5%.

Models of second and third order were also much alike in curve shape and information criteria values, with quadratic model slightly better of these two (and simpler, of course). These scores were not far from the fourth order model. Near 5% feed moisture, the quadratic function performs reasonably (it shows a small drop in product moisture, which may not be true, but fourth order model first shows a small drop and then a sharp rise, which may be even worse). Near 0% feed moisture, the parabolic curve has low values, which again is more realistic than the upwards "tail" of the fourth order polynomial. So, if important features of the model are its simple structure and sensible behaviour even near the extremes of the operating range of feed moisture, then the small loss in accuracy could be endured and the model should be second order:

$$\widehat{\mathrm{MC}}_{\mathrm{fine},100\%} = -0.08037 \cdot \mathrm{MC}_{\mathrm{in}}^2 + 0.6730 \cdot \mathrm{MC}_{\mathrm{in}} + 0.2908\,. \quad (2.20)$$

Coarse product, 50% throughput The corresponding model outputs and residual plots are shown in Fig. 2.31. Information criteria may be found in Fig. 2.32.

For this dataset, information criteria suggest 5th order polynomial (Fig. 2.32), though its superiority over 4th order model is small. Model outputs in Fig. 2.31 shown an undesired drop near 5% feed moisture for model of order 5, but not for order 4. So, the latter is preferred. It was identified as:

$$\widehat{\mathrm{MC}}_{\mathrm{coarse},50\%} = -0.02296 \cdot \mathrm{MC}_{\mathrm{in}}^4 + 0.2478 \cdot \mathrm{MC}_{\mathrm{in}}^3 - 0.8739 \cdot \mathrm{MC}_{\mathrm{in}}^2 + 1.488 \cdot \mathrm{MC}_{\mathrm{in}} - 0.05063\,. \quad (2.21)$$

If the use of the model favors simpler structures, then actually the parabolic function also performed very well: its curve shape was completely reasonable, whereas AIC and $\mathrm{AIC_c}$ were not much higher than for the 4th order model. So, the following could also be used:

$$\widehat{\mathrm{MC}}_{\mathrm{coarse},50\%} = 0.03006 \cdot \mathrm{MC}_{\mathrm{in}}^2 + 0.2163 \cdot \mathrm{MC}_{\mathrm{in}} + 0.4986\,. \quad (2.22)$$

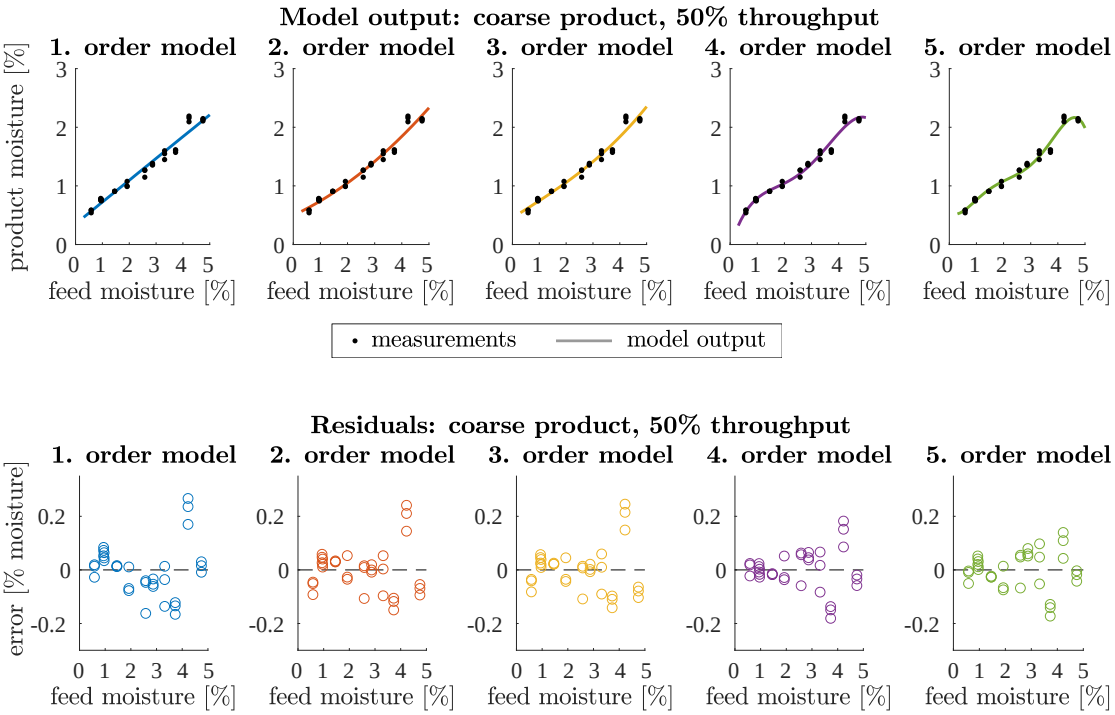

FIGURE 2.31: Polynomial models fitted to moisture data (top row), and their corresponding residuals (bottom row). Dataset: coarse classification product, 50% material throughput.

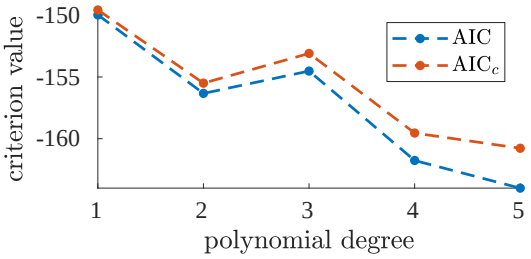

FIGURE 2.32: Information criteria — AIC, eq. (2.15) and AIC_c, eq. (2.16) — for the polynomial models. Dataset: coarse classification product, 50% material throughput.

Coarse product, 100% throughput Model outputs and residuals for this dataset are illustrated in Fig. 2.33. Associated values of information criteria are shown in Fig. 2.34.

In the last dataset, the observations form a pattern even simpler than in the previous case, much close to a straight line (Fig. 2.33). AIC favors the fourth order model, but AIC_c finds it practically equally good as second order one (Fig. 2.34), and the criterion values differ by minimal amounts — in the whole tested range of model orders. Model output curves in Fig. 2.33 do not seem overfitted (there is no excess curvature), and residual patterns (in the same figure) are more random for models of order 4 and 5 than for the other ones. Thus, for best model accuracy, fourth order polynomial should be selected:

$$\widehat{\mathrm{MC}}_{\mathrm{coarse},100\%} = -0.01338 \cdot \mathrm{MC}_{\mathrm{in}}^4 + 0.1522 \cdot \mathrm{MC}_{\mathrm{in}}^3 - 0.5717 \cdot \mathrm{MC}_{\mathrm{in}}^2 + 1.283 \cdot \mathrm{MC}_{\mathrm{in}} - 0.0905\,, \tag{2.23}$$

but usually even the linear function should suffice:

$$\widehat{\mathrm{MC}}_{\mathrm{coarse},100\%} = 0.4968 \cdot \mathrm{MC}_{\mathrm{in}} + 0.2104\,. \tag{2.24}$$

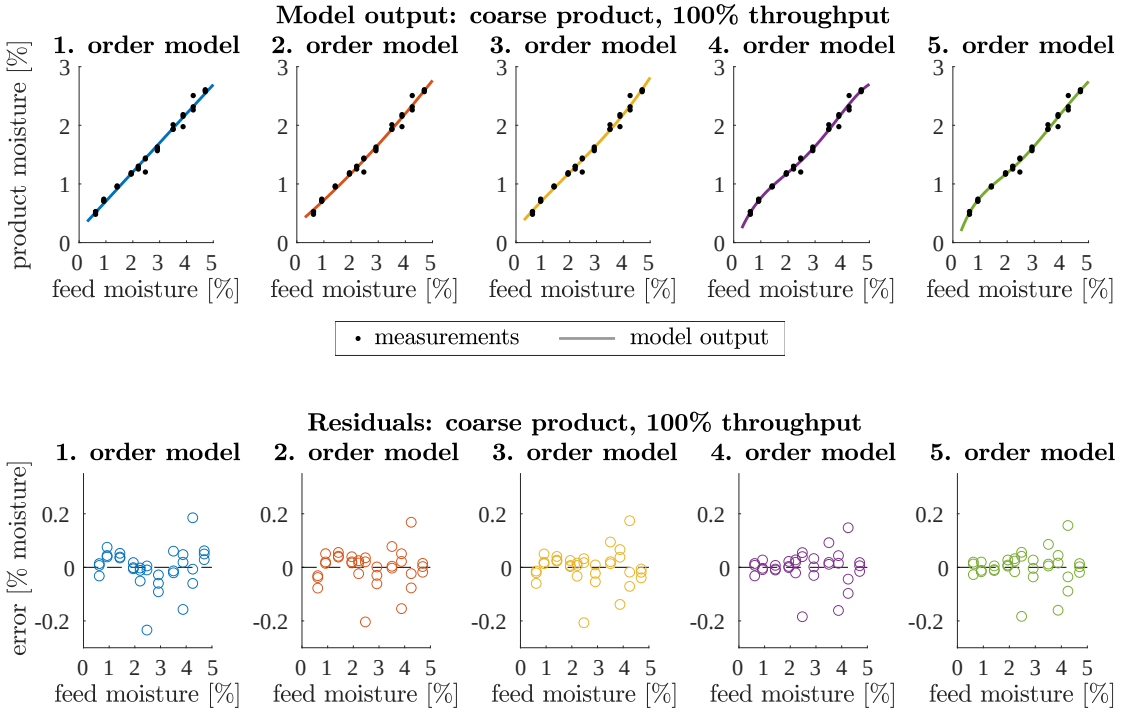

FIGURE 2.33: Polynomial models fitted to moisture data (top row), and their corresponding residuals (bottom row). Dataset: coarse classification product, 100% material throughput.

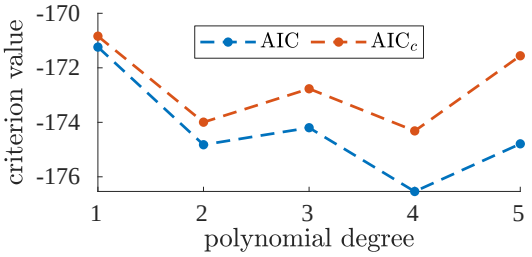

FIGURE 2.34: Information criteria — AIC, eq. (2.15) and AIC$_c$, eq. (2.16) — for the polynomial models. Dataset: coarse classification product, 100% material throughput.

2.2.2.7 Summary

The conducted experiments showed (Fig. 2.22) that both coarse and fine products of classification were significantly dried, compared to the material fed to the precise classifier. (Some exception was the fine product when the feed was extremely dry — near 0.5% relative moisture content — as then the product was slightly moistened by the humid air.) Assuming that classifier feed cannot be more moist than 5% (because otherwise, the particles stick to the inner walls of pipes and fittings), it appeared that recycle material (coarse product of classification) can have up to about 2–2.5% moisture, and final product (fine particles) — up to about 1.7% moisture. If higher water content is needed for some reason, then moisturizers need to be applied.

The product moisture-vs.-feed moisture curves have different shapes for the coarse and fine particle streams, as these two have different capabilities of absorbing water on their surfaces, and also, they travel different paths in the pneumatic transport system. Product moisture is also affected by material flow rate — generally, less material gets dried more effectively by the air, but for small input moistures (less than 1%), the effect of material flow rate is the opposite. Summarizing, each product stream needs its own moisture models to be identified, and they should depend on material flow rate.

Some polynomial and saturated straight line models were proposed for each examined dataset (in Sections 2.2.2.5–2.2.2.6). More tests are required to uncover the exact effect of material amount on product moisture; so far, separate models were identified for each tested throughput. Also, to make the models even more accurate, some further studies are recommended that would examine the influence of transport air parameters, such as temperature, humidity, flow rate.

2.2.3 Investigating impact of moisture on particle classification process

While Section 2.2.2 studied how the classification equipment changed moisture content in the material, the opposite was also true: moisture in the classified material affected the classification process. This was observed in measurements from the same experiment (Sections 2.2.2.1–2.2.2.3), so it was described in the same paper as cited above [53]. These findings are also summarized below.

In each experiment run, classification products were sampled and subjected to sieve analysis (Section 2.2.2.3). This allowed to estimate the partition curves for the classifier, indicating the mass percentage of each size fraction from feed material contained in the lower product of classification (or in the upper product — both definitions are used in literature) [32, p. 89–91]. Partition curve PC_e for e-th experiment run has a point (degree

of separation) $\mathrm{PC}_{e,i}$ for each i-th size fraction of the material. This degree of separation is defined as [113; 115]:

$$\mathrm{PC}_{e,i} = \frac{m_{\mathrm{low},e,i}}{m_{\mathrm{low},e,i} + m_{\mathrm{up},e,i}} \cdot 100\% = \frac{m_{\mathrm{low},e,i}}{m_{\mathrm{in},e,i}} \cdot 100\% \,, \tag{2.25}$$

where $m_{s,e,i}$ is the mass of i-th size fraction (mass of material retained on i-th sieve), during e-th experiment run, in material stream $s = \{\mathrm{low}, \mathrm{up}, \mathrm{in}\} = \{$lower product, upper product, input material$\}$.

Partition curves were ordered by moisture of feed material entering the classifier and plotted in Fig. 2.35. In the graphs, the XZ cross-sections show individual partition curves ($\mathrm{PC}_{e,i}$ for fixed experiment number e); and YZ cross-sections show $\mathrm{PC}_{e,i}$ for fixed i-th size fraction of the material, that is, the YZ cross-sections illustrate the influence of moisture on degree of separation for each size fraction. They are shown in more detail in Fig. 2.36. Degree of separation appears rather constant for coarser fractions, but slightly grows with moisture for finer fractions.

To verify the strength of the observed relationships between feed moisture and separation degree, two correlation coefficients were used:

- Pearson's product–moment correlation coefficient r_{P}, which measures linear correlation between variables x_i and y_i, $i = 1, 2, ..., N$ [84]:

$$r_{\mathrm{P}}(x,y) = \frac{\sum_{i=1}^{N} (x_i - \bar{x})\,(y_i - \bar{y})}{\sqrt{\sum_{i=1}^{N} (x_i - \bar{x})^2 \cdot \sum_{i=1}^{N} (y_i - \bar{y})^2}} = \frac{s_{xy}}{\sqrt{s_{xx} \cdot s_{yy}}} \,. \tag{2.26}$$

  Symbol $\bar{x}$ is the mean of all x_i, s_{xx} is the sample variance of all x_i, the same for $\bar{y}$ and s_{yy}; and s_{xy} denotes the sample covariance of x and y.

- Spearman's rank correlation coefficient r_{S}, which measures any monotonic correlation between variables [93]. Values x_i are sorted in ascenting order and then they are assigned sequential ranks $r_{x,i}$ so that $\min(x_i)$ gets rank 1 and $\max(x_i)$ gets rank N. The same applies to the other variable y. Then, Spearman's correlation coefficient is calculated as Pearson's correlation coefficient between the value ranks r_x, r_y rather than between the x, y values themselves:

$$r_{\mathrm{S}}(x,y) = r_{\mathrm{P}}(r_x, r_y) \,. \tag{2.27}$$

Both these coefficients take values from -1 (perfect negative correlation) to 1 (perfect positive correlation). Value 0 means no linear/monotonic correlation. Fractional values indicate there is some weaker (not perfect) positive or negative correlation, with higher absolute values of r_{P} or r_{S} meaning stronger association between variables.

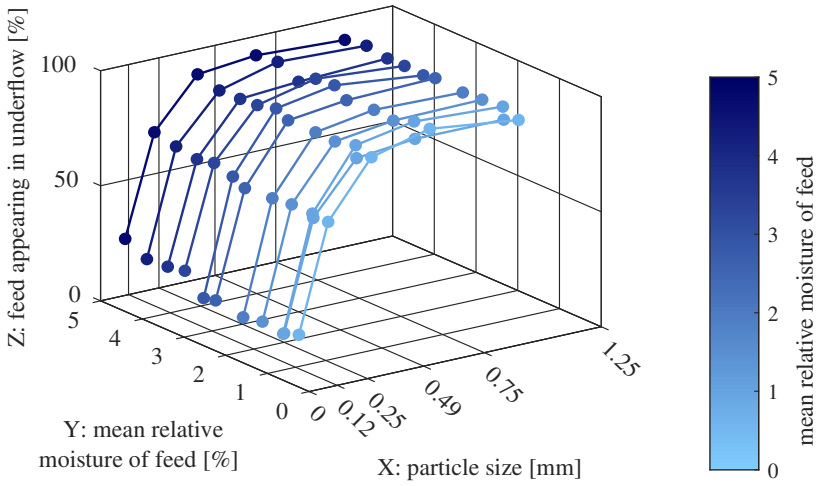

(A) 50% material throughput

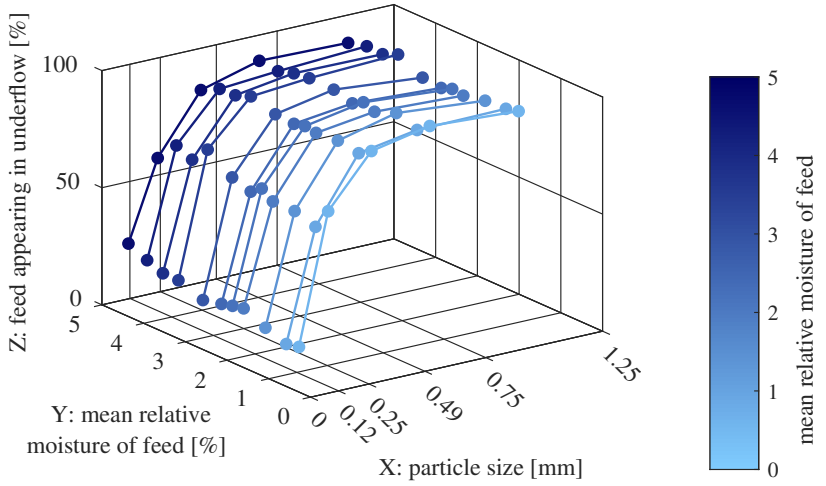

(B) 100% material throughput

FIGURE 2.35: Partition curves for classifier supplied with input material of varying moisture content.
Source [53]: Krauze O.; Buchczik D.; Budzan S. Measurement-based modelling of material moisture and particle classification for control of copper ore dry grinding process. *Sensors* **2021**, 21, 667. https://doi.org/10.3390/s21020667, Fig. 5.
Re-used under Creative Commons Attribution (CC BY) license (https://creativecommons.org/licenses/by/4.0/).

Such obtained correlation coefficients were subjected to Student's t-test to verify their statistical significance [43]. Values of $r = r_P, r_S$ were transformed to:

$$t_r = r\sqrt{\frac{N-2}{1-r^2}}\,. \tag{2.28}$$

The transformed coefficients were then compared with critical value $t_{1-\alpha}$, taken from Student's t-distribution with $N-2$ degrees of freedom and a selected level of significance α. Then if $|t_r| > t_{1-\alpha}$, it means coefficient r is statistically significant at $(1-\alpha)$ confidence level. In this research, there were $N = 11$ observations in each dataset, so

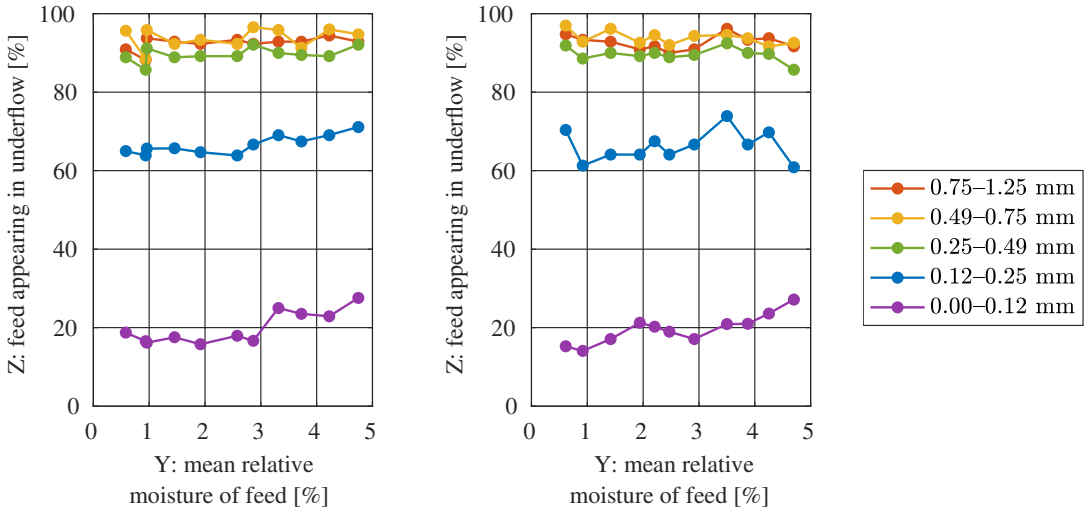

(A) 50% material throughput (B) 100% material throughput

FIGURE 2.36: YZ cross-sections of 3D plots from Fig. 2.35, i.e., degrees of separation in relation to moisture content in input material.
Source [53]: Krauze O.; Buchczik D.; Budzan S. Measurement-based modelling of material moisture and particle classification for control of copper ore dry grinding process. *Sensors* **2021**, 21, 667. https://doi.org/10.3390/s21020667, Fig. 6.
Re-used under Creative Commons Attribution (CC BY) license (https://creativecommons.org/licenses/by/4.0/).

there were $N - 2 = 9$ degrees of freedom; and a commonly used value of $\alpha = 0.05$ was selected. This produced the critical value of $t_{1-\alpha} = t_{95\%} = 2.26$. Calculated values of plain and transformed correlation coefficients, as well as results of their t-tests, are listed in Table 2.6.

Values of correlation coefficients confirm the linear or monotonic relationships between moisture in feed material and degree of separation, but only for finer fractions of the material. In many cases, the identified association was strong: $r_\bullet$ coefficient value was about 0.8 or above, or in other words, transformed coefficient $t_{r_\bullet}$ was well above the critical value. Moreover, cumulative errors were assessed as random (not systematic) [53]. So, there is high probability that the identified correlations are true. It suggests that water makes small particles heavier or even causes agglomeration of particles, so they behave like bigger ones when they undergo classification.

More material fractions were affected when the throughput was smaller. This may be related to fewer collisions between the particles, so, fewer agglomerates broken by impact.

These observations that classifier operation (partition curve) varies with material moisture are important for the whole grinding process. Particle size distribution of the final product is slightly changed (there are more fine particles). Material flow in the recycle stream is increased, which requires many control subsystems to react. It might even

lower the overall throughput of the installation. When the moisture-partition curve dependencies are known, proper adjustments may be made beforehand.

TABLE 2.6: Measures of correlation between material moisture and degree of separation for each particle size fraction. r_P — Pearson's correlation coefficient (2.26), r_S — Spearman's rank correlation coefficient (2.27), t_{r_P} or t_{r_S} — transformed correlation coefficient (2.28), "sig.?" — is the result statistically significant at 95% confidence level?

Source [53]: Krauze O.; Buchczik D.; Budzan S. Measurement-based modelling of material moisture and particle classification for control of copper ore dry grinding process. *Sensors* **2021**, 21, 667. https://doi.org/10.3390/s21020667, Table 1.

50% of nominal throughput						
Particle size	r_P	t_{r_P}	r_P sig.?	r_S	t_{r_S}	r_S sig.?
0.75–1.25 mm	0.527	1.86	no	0.485	1.66	no
0.49–0.75 mm	0.246	0.761	no	0.251	0.778	no
0.25–0.49 mm	0.471	1.60	no	**0.613**	**2.33**	**YES**
0.12–0.25 mm	**0.835**	**4.55**	**YES**	**0.795**	**3.93**	**YES**
0–0.12 mm	**0.812**	**4.18**	**YES**	**0.673**	**2.73**	**YES**
100% of nominal throughput						
Particle size	r_P	t_{r_P}	r_P sig.?	r_S	t_{r_S}	r_S sig.?
0.75–1.25 mm	−0.0170	−0.0510	no	−0.0183	−0.0549	no
0.49–0.75 mm	−0.522	−1.83	no	−0.506	−1.76	no
0.25–0.49 mm	−0.335	−1.07	no	−0.165	−0.502	no
0.12–0.25 mm	0.111	0.335	no	0.0276	0.0828	no
0–0.12 mm	**0.864**	**5.15**	**YES**	**0.802**	**4.03**	**YES**

Chapter 3

Models of Clean Air Flow

Capturing and analysing behaviour of signals in inlet air streams brings many benefits. Static and dynamic models of air pressure and flow rate (or air speed) versus positions of air dampers may be used to:

- design and tune direct-layer algorithms for control of air flow in the three inlet streams (main, recycle and additional);
- design and tune upper-layer algorithms for control of the key air flows in the installation: through the EM mill working chamber, through the precise classifier and in the recycle stream;
- improve performance of air flow controllers thanks to de-coupling of control subsystems using pressure information;
- create a simulator of this part of pneumatic system, which will greatly reduce the time and effort needed to test the control algorithms;

and more. This chapter presents derivation of such models, along with identification experiment performed to collect the necessary input data. Similar research was published firstly (in preliminary version) in [56], then in [52]. Here, the descriptions are more detailed than in the papers.

3.1 Identification experiment

The research in this chapter was based on grinding installation with the flow of clean air only, without raw material or grinding media. Obviously, these substances influence the flow of air as they introduce additional pneumatic resistance to the system; however,

it would be difficult to test everything in a single experiment. The clean air scenario itself requires quite a long-lasting experiment, as will be explained shortly. The addition of other variables would make it overwhelmingly long, as the duration of the experiment grows exponentially then. Thus, this experiment aimed only at providing detailed information on air flow behaviour when the dampers are moved to different positions. Separate tests, probably done only for a limited subset of damper positions, may reveal how these air flows are affected by:

- amount (throughput) of raw material,
- type of raw material (chemical composition, particle size, moisture content, etc.),
- amount of grinding media,
- size and shape of grinding media,
- frequency of EM field rotation.

As this list (probably still not complete) is already quite long, it is resonable to create a "baseline" characteristics using clean air only, and then to adjust it after further measurements are available. (Actually, this thesis' author and her colleagues did a similar thing in [37]. The paper considered how the clean air flows were affected by grinding media mass and rotational frequency. Some details of this research are given in Section 3.3.)

Moreover, a great advantage of clean air tests is that they can be done fully automatically and they do not require excessive masses of raw material (which would need to be prepared, supplied to the system and collected at the output). Thanks to these, damper positions inspected in this experiment were quite numerous, giving a detailed overview of the system's behaviour.

Note: The experiments and data processing techniques described in this chapter led to models that described collectively the behaviour of the process itself, its actuators and sensors. The models were not divided into these three subsystems, but treated as a whole because these sensors and actuators were going to be present also in the control loops, and generally: always during the operation of the grinding installation. However, if any of these elements were replaced, then it would be advisable to check the individual characteristics of the old and new elements, and then to update the "aggregate" plant models accordingly.

3.1.1 Test rig

To create air flow models, an identification experiment was performed on dry grinding installation with electromagnetic mill (see Section 1.2.2, especially Fig. 1.3 there).

Figure 3.1 shows the elements of the grinding circuit that were important for the identification experiment.

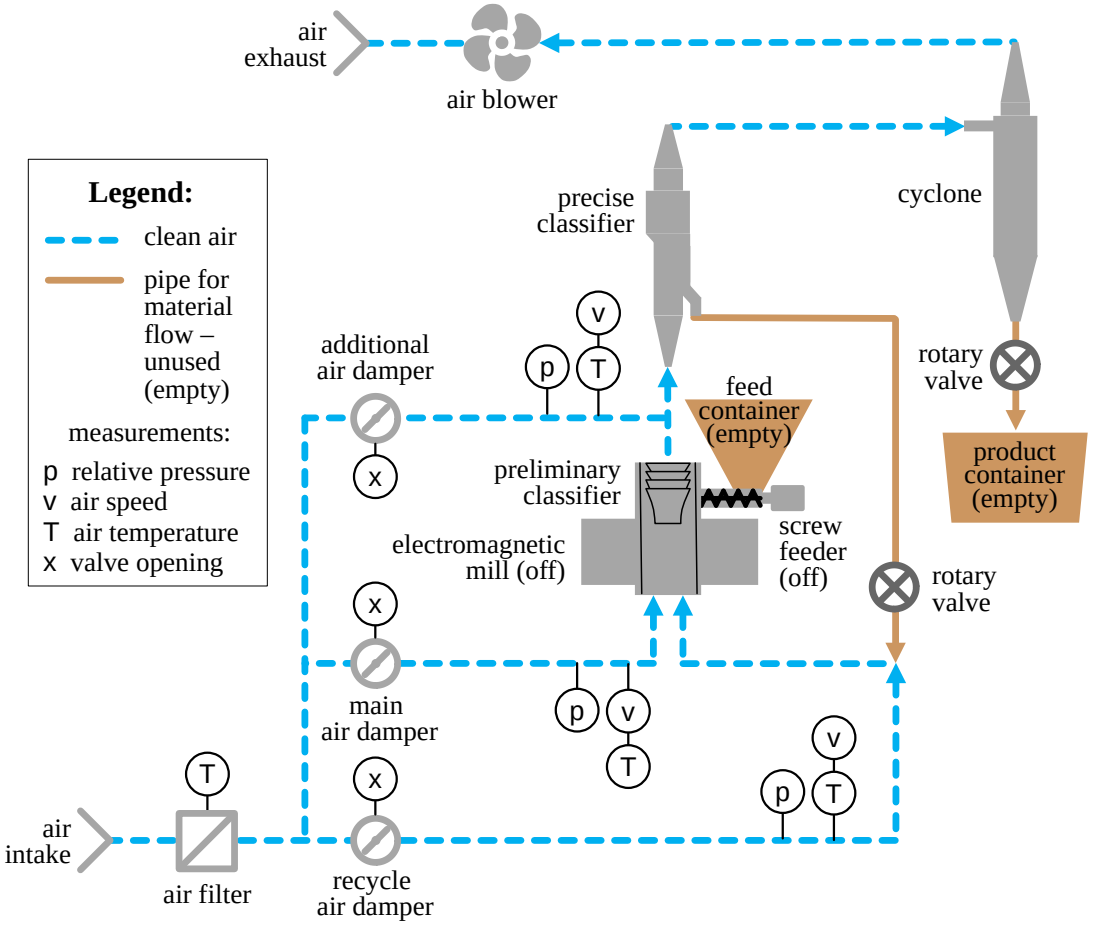

FIGURE 3.1: Diagram of the test rig for identification of air flow models

During the experiment, the SCADA system was automatically switching between the tested operating points, i.e., different positions of air dampers. The blower was turned on to force the flow of air in the installation. Also, rotary valves, which are designed to output the coarse (recycle) material and final product, were turned on to imitate the standard operating conditions of the plant (in terms of air tightness in these places). The EM mill with its cooling fans was switched off, so no heated air was recycled and only fresh air was let in. Thus, the warm air recycling system is not shown in the diagram. Also, the raw material feeder was turned off. The container for input material was sealed with an air-tight lid, which imitated the standard situation when the pile of feed material prevents air inflow through the screw feeder input. This is because the tests were run on clean air only — granular material and grinding media were not present in the installation, as was already explained above.

The input and output signals from the experiment as well as related hardware will be detailed in the next subsections. A brief summary is the following:

- The controlled input signals were the requested positions of the dampers.
- The measured outputs were, in the first place, centerline air velocity and relative pressure in the three inlet air streams, as indicated in Fig. 3.1.
- Air velocity and pressure were also measured near the outlet of the installation, but only for the sake of checking the correctness of plant operation. These values were not used for model development.
- Furthermore, the positions actually achieved by the dampers were recorded.
- Moreover, air temperature was measured in inlet and outlet streams, and near the air intake. Temperature was not an output of the models derived in this research, and the main source of heat — the EM mill — was turned off during this experiment. Thus, air temperature was nearly constant over time and it was very similar in all the measurement points (the differences were usually up to 2 °C). Despite this, temperature was indeed measured, because it was required for calculation of some other physical quantities, as will be explained later (see Section 3.2.1).

3.1.2 Test scenario

The excitation signal in the experiment was defined as a series of step changes of damper position (from closed to open and vice versa), at all possible combinations of the positions of the two remaining dampers. A schematic representation of the design is plotted in Fig. 3.2.

It was necessary to choose specific damper positions in such a way that all the interesting behaviour (such as curvature of the static characteristics) is captured in the experiment. On the other hand, it was reasonable to limit the number of tested damper positions as far as possible, because each extra position could add an hour or more to the total duration of the experiment. Thus, the specific positions for each damper were chosen based on a preliminary experiment, detailed in Section 3.1.6.2. The positions finally examined in the identification experiment were:

- for the main damper: {0, 10, 15, 20, 30, 40, 50, 99} % open;
- for the recycle damper: {0, 10, 15, 20, 30, 50, 99} % open;
- for the additional damper: {10, 20, 30, 40, 50, 70, 99} % open.

After each step change of requested damper position, the SCADA system recorded all the measurements for 40 seconds, which was enough for the signals to settle down. In the cases when step changes had big amplitude (setting a damper from 100% open to

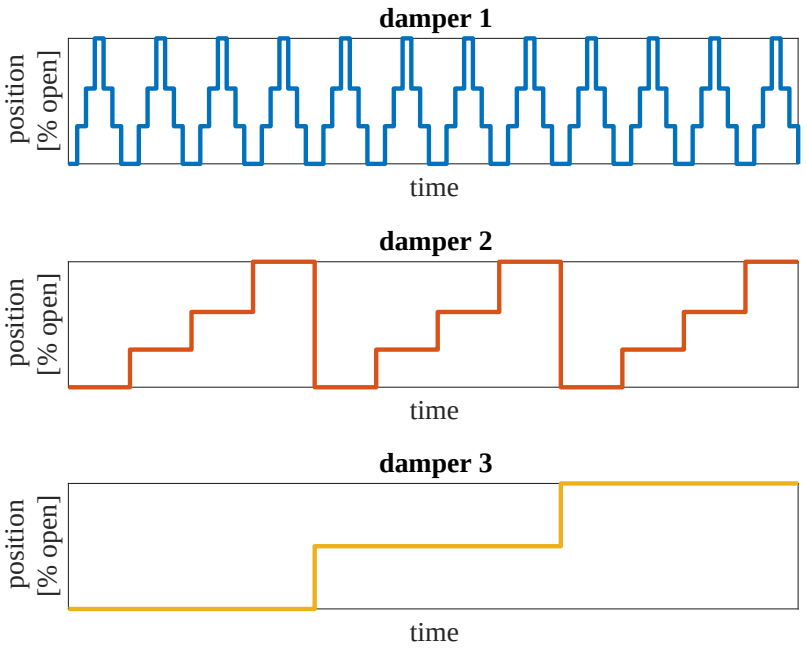

FIGURE 3.2: Schematic graph of the order of changing damper positions during identification experiment. Firstly, the most-often changing damper ("damper 1" in the figure) was the main damper; in the next experimental series, it was the recycle damper; and finally, the additional damper.

some small value), the next step change was issued after 100 seconds instead of the usual 40 seconds.

Sampling period of the signals (both input and output) was 0.5 seconds, which is normally used in the PLCs and SCADA system during the operation of this plant.

3.1.3 Actuators – butterfly air dampers

There are multiple control signals in the whole grinding installation, such as: base and output frequencies of EM mill frequency inverter; frequency of supply current for material feeder; switching on and off the rotary valves or cooling fans, and so on. However, for the sake of the planned identification experiment, only the positions of air dampers were considered as excitation signals.

The dampers are single-plane butterfly valves with double seal around the disc, labeled PJB-U-100T3-SO-UP-C4, manufactured by Smay [89]. Their positions are controlled with electric rotary actuators Belimo LMQ24A-SR (see Fig. 3.3 and datasheet [6]). Each damper may be positioned in the range from 0% (fully closed) to 100% (fully open). A full-range motion takes 2.5 s, according to electric actuator datasheet [6].

The requested position (value sent from the PLC to damper actuator) may be specified in the system with 1% resolution. The actual position of the damper (position feedback)

FIGURE 3.3: Electric actuator placed over a butterfly damper in air inlet pipe of EM mill installation

is returned by damper actuator to the PLC with a greater resolution. This real position is usually a bit smaller than requested, but mostly up to 1% lower (meaning "percent open" as a unit, not as fraction of requested value) — as was observed in the experiment. Such small deviations have little impact on the performance of the pneumatic system. Moreover, these differences vary during damper operation — there is no fixed relationship of actual position versus requested position of a damper. Of course, also the control system has no direct influence on the actual valve opening, only on its requested value. Hence, requested (not actual) damper position will be used as input or output signal in all models and control schemes analysed in this research.

3.1.4 Air velocity and temperature transducers

Air velocity (at pipe centerline, so maximum air velocity) and temperature at the three inlet streams were measured with Delta OHM HD2937T01 transducers (see Fig. 3.4 and datasheet [30]).

Velocity measurement was set to "slow" response time, as is suggested for turbulent flows in sensor documentation. This means each air speed reading was a result of two seconds long integration of values measured in the air stream [30]. Measurement ranges were set to 0.2...10 m/s, resulting in accuracy of ±(0.5 m/s + 3% of measurement) [30]. These were the smallest available ranges that covered all air speeds possibly encountered during the operation of the grinding installation.

These transducers simultaneously measured air temperature in range -10...+60 °C, with accuracy ±0.3 °C [30].

Temperature (and humidity, which was not used here) of air near the intake was measured with Delta OHM HD4917T transducer (see Fig. 3.5 and datasheet [31]). Its operating range is −20...+80 °C, but during the experiments described here, the temperature was between 20 and 30 °C; this meant accuracy of ±0.3 °C [31].

All air speed measurements were taken at the necessary distances downstream the recent obstacles, which allowed for the flows to settle down (see Fig. 3.1). Namely, recycle air velocity was measured about 1.29 m ≈ $12.6D$ (pipe diameters) from the recycle air damper; main and additional air velocity — about 2.21 m ≈ $21.6D$ from their respective air dampers. Recommended run-out distances were also provided, that is, the distances to the nearest following flow obstacles (elbows or reducers): about 0.5 m ≈ $4.9D$ at main and additional pipes, and about 0.4 m ≈ $3.9D$ at recycle pipe. (The latter pipe was shorter than the others, so the run-in and run-out distances were necessarily smaller than at the other pipes.)

FIGURE 3.4: Air speed and temperature transducer mounted in air inlet pipe in EM mill installation

FIGURE 3.5: Air speed and relative humidity transducer mounted in air filter in EM mill installation

3.1.5 Pressure transducers

Underpressure in the three inlet pipes was measured with industrial differential pressure transducers ABB 264DS (see Fig. 3.6 and datasheet [1]). As these are differential sensors, they include two process inputs, labeled "L" and "H". The "L" inputs were connected to the piping with short elastic tubes. The "H" inputs were left without connections, so they were subject to atmospheric pressure. As a result, the sensors were measuring relative pressure in the pipeline.

Sensors' response times were rather fast: 40 ms dead time and about 130 ms time constant [1], with no extra damping (additional damping time constant was set to zero).

Also, physical connections did not introduce much dynamics, as the tubes were of small length — about 20–30 cm.

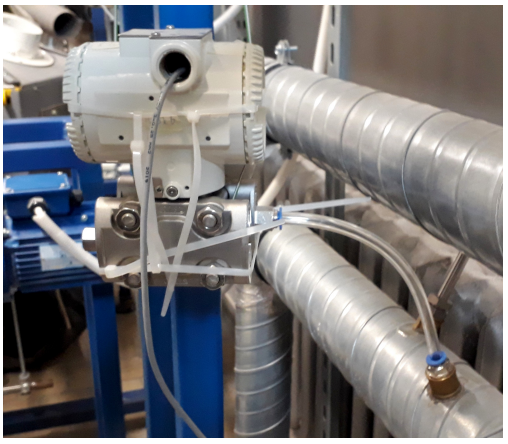

FIGURE 3.6: Pressure transducer connected to air inlet pipe in EM mill installation

3.1.5.1 Verification of pressure readings

According to the datasheet [1], sensor's base accuracy is ±0.075% of calibrated span, which is very good. For the measurement range finally used in the experiment (0...8 kPa), this would give accuracy of 6 Pa. The transducers also allow for calibrating out the zero error in the field, which improves the quality of measurement.

However, factory calibration is valid for 5 years. The devices were manufactured in 2008, and the experiments were conducted in 2021, long after the factory calibration expired. Thus, to verify if good accuracy is still preserved, the sensors were recalibrated before the experiments. The process involved a climatic chamber with temperature setpoint of 25 °C, and Druck DPI 510 precision pressure controller/calibrator. The setup is shown in Figures 3.7 and 3.8.

The transducers were put to the climatic chamber, levelled and let for warming up. Then, they were calibrated one after another, using the following procedure.

Each transducer was connected to the pressure source: "L" input connected to pressure calibrator output, "H" input subject to the atmosphere. It was also plugged to a HART circuit which included a laptop running a dedicated software from the sensor vendor (ABB Field Information Manager). With this program, the transducer was configured to 0 s time constant (no damping) and 0...4 kPa measurement range. (Later, this range appeared to be too small and was modified to 0...8 kPa. Despite this, conclusions from calibration procedure are still valid.) Then, the transducer was zero calibrated at input pressure equal to atmospheric one. Finally, the calibrator issued underpressure of -4 kPa

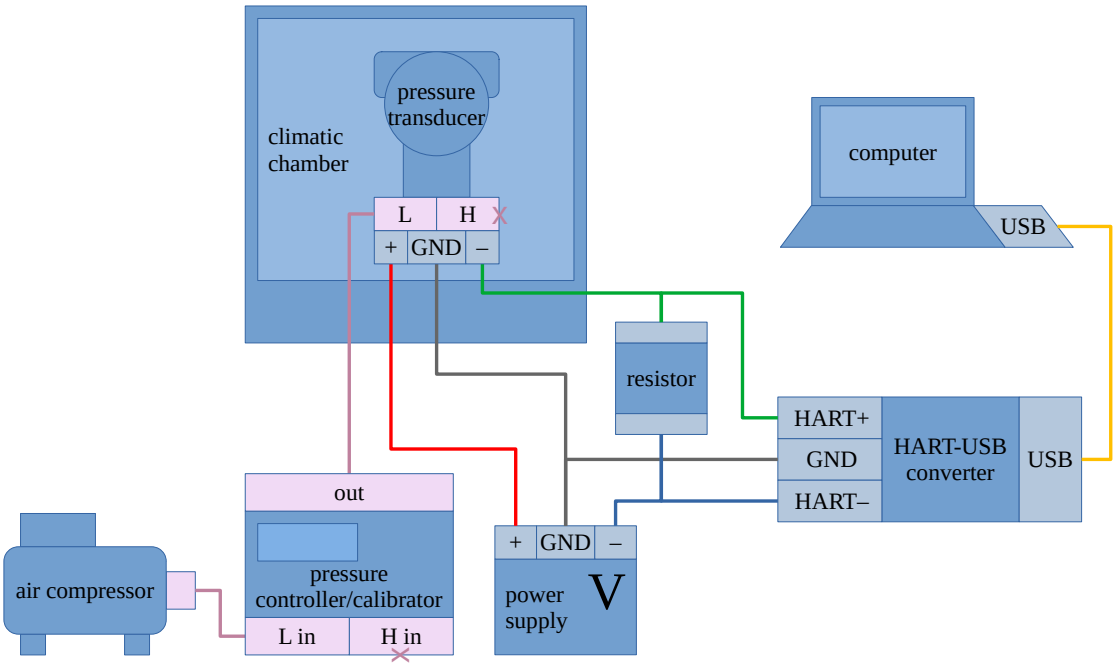

FIGURE 3.7: Diagram of laboratory setup used to verify pressure readings of the used transducers

FIGURE 3.8: Pressure transducers inside climatic chamber

to "L" sensor input and the corresponding measurement result was read from the software (measured values were sent digitally via HART).

The collected pressure measurements are listed in Table 3.1. They indicate that all transducers still have good accuracy and may be used in the experiments.

TABLE 3.1: Pressure calibration of ABB differential pressure transducers

Serial number	6408029152	6408029154	6408030632
Product code	264DS GSSA1BH	264DS GSSA1BH	264DS ESSA2BH
Location in installation	additional stream	recycle stream	main stream
Max range	±65 kPa	±65 kPa	±16 kPa
Calibrated range (CR)	0...4 kPa	0...4 kPa	0...4 kPa
Expected reading (X)	4000 Pa	4000 Pa	4000 Pa
Actual reading (A)	3977 Pa	3970 Pa	3971 Pa
Error ($E = A - X$)	-23 Pa	-30 Pa	-29 Pa
Relative error (E/CR)	-0.58% CR	-0.75% CR	-0.72% CR

3.1.5.2 Verification of output current

With such conclusions from pressure calibration procedure, the transducers were mounted in the grinding installation. They were placed close to the points of measurement, to keep the connecting tubes short and thus, to prevent delays in measurements. The points of measurement themselves were lying 10 cm upstream of air velocity measurement points, so the air streams were settled down in these places. Transducer casings were levelled, and this was also checked directly before each experimental series. The transducers were zero calibrated again in these final positions.

Next, second stage of calibration was carried out, namely: verification of the output current from the transducers, as seen by the PLC–SCADA measurement and data acquisition system. In the first stage of calibration, only digital output values (transmitted via HART) were analysed; now, the physically generated current was examined.

A HART circuit was connected to the existing electrical circuits of the grinding installation. Each pressure transducer was accessed in turn from the vendor software and its output was artificially driven to 4, 12 and 20 mA. These correspond to the lower bound of measurement range, half of the range, and upper bound of the range, respectively. Values of actual output current as seen in the SCADA system were recorded and are listed in Table 3.2. The discrepancies between the theoretical and real values are very small — less than half percent of the range 4–20 mA (usually a lot less). The previous assumption about good measurement accuracy is therefore finally confirmed.

Table 3.2: Verification of output current for ABB differential pressure transducers

Sensor location	**Expected reading** (X)	**Actual reading** (A)	**Error** ($E = A - X$)	**Relative error** ($\frac{E}{20-4} \cdot 100\%$)
additional stream	4 mA	4.023 mA	0.023 mA	0.14%
	12 mA	11.986 mA	-0.014 mA	-0.09%
	20 mA	19.958 mA	-0.042 mA	-0.26%
recycle stream	4 mA	4.014 mA	0.014 mA	0.09%
	12 mA	11.977 mA	-0.023 mA	-0.14%
	20 mA	19.940 mA	-0.060 mA	-0.38%
main stream	4 mA	4.000 mA	0.000 mA	0.00%
	12 mA	12.005 mA	0.005 mA	0.03%
	20 mA	20.000 mA	0.000 mA	0.00%

3.1.6 Preparatory experiments

Some preliminary tests were needed to complete the configuration of measurement devices and to select details of the experiment scenario. They will be explained in this section.

3.1.6.1 Testing signal ranges

The first preparatory experiment aimed at determining the maximum air velocity and underpressure occurring in each point of measurement. To achieve this, appropriate sensors were temporarily set to wide measurement ranges. Then, air dampers were set to all combinations of open and closed positions.

The biggest damper opening in this preliminary experiment was not 100%, but slightly below (98%) — simply because requesting the maximum value puts excessive load on the actuator. This is probably some case of mounting of damper shaft in the actuator. However, the operating characteristics of the valves is very flat at this end of range, so setting the damper to nearly 100% instead of exactly 100% has practically no impact on the measured results.

As for the "closed" state, main and recycle dampers were tested for 0% positions (fully closed), but this value was not used for the additional damper. This is because during normal operation of the plant, the dampers should never be closed all at once. This would cause excessive underpressure and pose a risk of damage to the installation. Moreover, the additional air damper is supposed to never be fully closed because the main classifier

needs substantial air supply — bigger than the devices upstream, such as the working chamber of the mill [76].

The subsequent damper openings and the corresponding measurements in inlet and outlet air streams are listed in Table 3.3. Based on these results, the final measurement ranges of sensors were selected, as specified in the same table. Each chosen measurement range ensured that the whole recorded data interval will be covered with some safety margin.

TABLE 3.3: Air velocity and pressure ranges reached in the pneumatic system of the grinding installation. Maximum values for each signal (each column) are in bold. Abbreviated air stream names: m — main, r — recycle, a — additional.

Requested damper position [% open]			**Measured air velocity [m/s]**			**Measured underpressure [Pa]**		
m	**r**	**a**	**m**	**r**	**a**	**m**	**r**	**a**
0	0	10	0.2	0.6	0.2	**6400**	**6400**	**6900**
98	0	10	**4.1**	0.3	0.3	0	1600	2300
98	98	10	3.2	1.3	0.2	0	90	1700
0	98	10	0.4	**2.4**	0.2	3400	50	3900
0	98	98	0.1	0.6	4.8	100	100	30
98	98	98	1.0	0.4	4.2	0	100	30
98	0	98	1.0	0.1	4.5	0	300	30
0	0	98	0.1	0.1	**5.1**	150	350	40
Selected range			0.2... 10	0.2... 10	0.2... 10	0... 8000	0... 8000	0... 8000
Available ranges			0.05...1, 0.10...2, 0.20...10, 0.20...20			any from -65,000 to +65,000		

3.1.6.2 Selecting damper positions to be examined

Another preliminary test was needed to select damper positions to be used in the main experiment. For identification purposes, the dampers should be positioned to many values in the whole range of 0–100% open. This would allow to properly record the nonlinearities in the dampers' operating characteristics, which had already been noticed during previous experiments. At the same time, the number of tested positions should be strictly limited, because each additional position exponentially increases total duration of the experiment. For example, if about 10 positions per damper are defined, then introducing one more tested position of just one damper prolongs the whole experiment by an hour, approximately.

Previous experiments on the same installation (but with the old dampers) have shown the approximate shapes of dampers' operating characteristics [56]. However, the exact positions for the identification experiment needed to be fine-tuned to match the particular making of the new dampers. Thus, a preliminary test was performed in which the step changes of damper positions were made on a much limited set of values. The exact positions used were as follows:

– for the main and recycle dampers: {0, 15, 30, 50, 70, 98} % open;
– for the additional damper: {15, 30, 50, 70, 98} % open.

During the experiment, all their combinations were applied, but only in the order of increasing damper opening. This yielded $6 \cdot 6 \cdot 5 = 180$ step responses 40 seconds each, so 2 hours of experiments, which is not very long.

As seen above, again, main and recycle dampers were tested for positions starting from 0% (fully closed), and for the additional damper this value was a bit higher. Moreover, the biggest damper opening in this preliminary experiment was not 100%, but slightly below. The reasons for this have already been explained in Section 3.1.6.1.

During this preliminary experiment, steady-state air speed and pressure were measured after each step change of damper positions. The results were coarsely sampled operating characteristics of the dampers. Some examples of these are shown in Fig. 3.9.

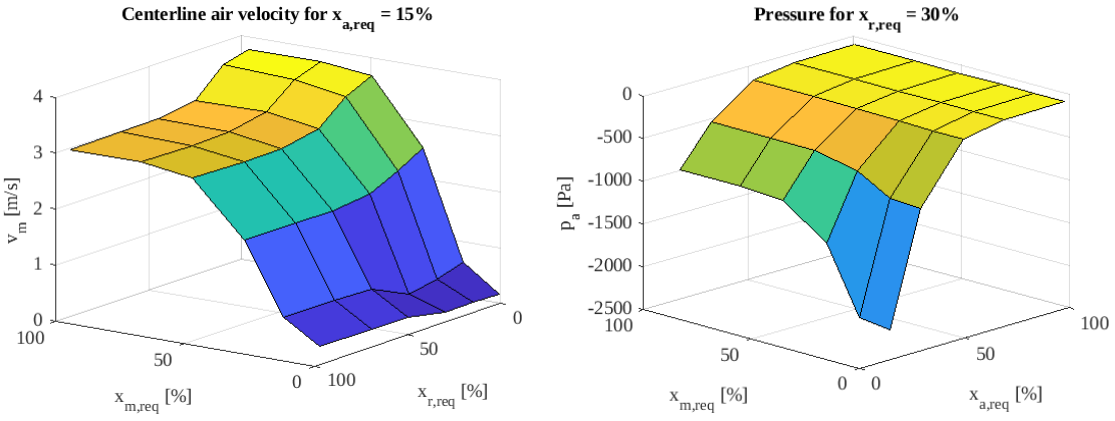

FIGURE 3.9: Examples of coarsely sampled static characteristics gathered in the preliminary experiment

Based on these introductory results, damper positions for the main experiment were selected as:

– for the main damper: {0, 10, 15, 20, 30, 40, 50, 99} % open;
– for the recycle damper: {0, 10, 15, 20, 30, 50, 99} % open;
– for the additional damper: {10, 20, 30, 40, 50, 70, 99} % open.

They follow the rules already specified, ie., they provide good insight into the shape of operating characteristics, but are as sparse as possible to limit time duration of the experiment.

3.1.7 Experiment results

The final identification experiment was prepared and conducted as described above. As a result, about 24 hours 40 minutes of measurements were collected (not at once, but in three runs, about 8 hours each). The following signals were stored:

- requested positions of the main, recycle and additional dampers: $x_{\mathrm{m,req}}$, $x_{\mathrm{r,req}}$, $x_{\mathrm{a,req}}$ [% open];
- actual positions of the main, recycle and additional dampers: x_{m}, x_{r}, x_{a} [% open];
- air velocities at pipe axes in main, recycle and additional streams: v_{m}, v_{r}, v_{a} [m/s];
- relative pressures in main, recycle and additional streams: p_{m}, p_{r}, p_{a} [Pa];
- air temperatures in main, recycle and additional streams: T_{m}, T_{r}, T_{a} [K];
- air temperature near air inlet to the installation: T_{in} [K].

Exemplary fragments of the collected data are shown in Fig. 3.10.

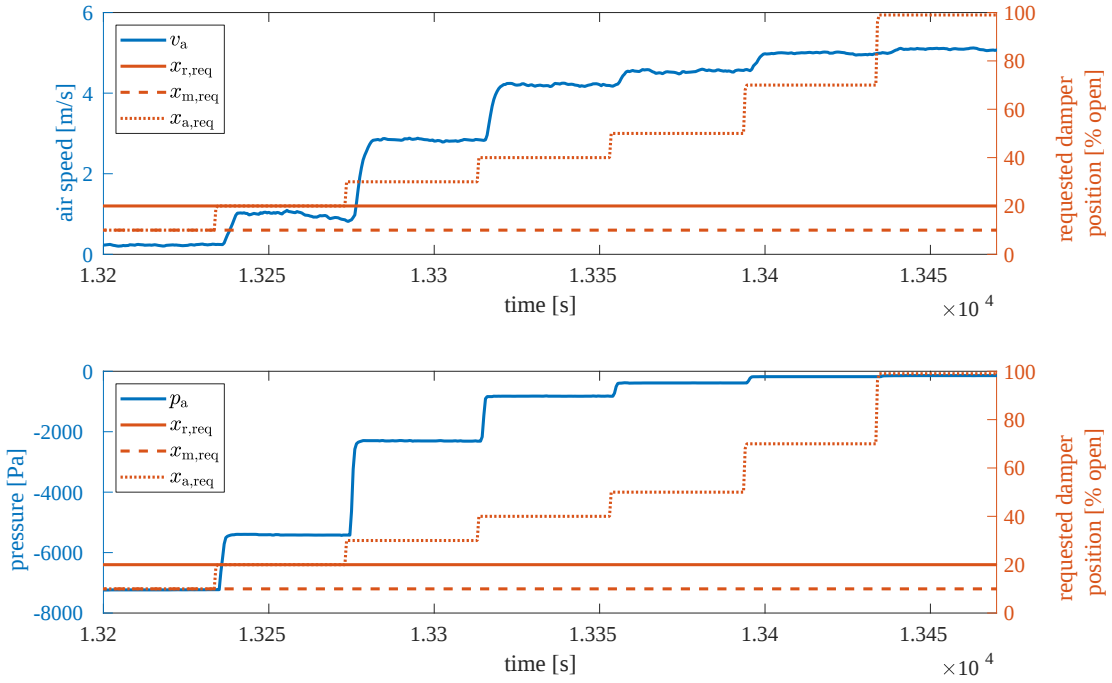

FIGURE 3.10: Exemplary step responses of air speed and relative pressure collected in the experiments

3.2 Measurement data processing

3.2.1 Calculation of derived quantities

The quantities measured in each inlet air stream were:

- air speed at pipe axis v [m/s],
- temperature T [K],
- relative pressure p [Pa].

They were used to derive other physical quantities needed in the modelling process[1]:

- Absolute pressure p_{abs} [Pa]:

$$p_{\text{abs}} = p + p_{\text{atm}}\,; \tag{3.1}$$

  atmospheric pressure p_{atm} was not measured during the experiments, but with reasonable accuracy for the following modelling and estimation procedures, it was assumed as $p_{\text{atm}} = 1013$ hPa.

- Air density ρ [kg/m^3] [45]:

$$\rho = \frac{p_{\text{abs}}}{r \cdot T} = \frac{p_{\text{abs}} \cdot M}{R \cdot T}\,, \tag{3.2}$$

  where specific gas constant $r = R/M$, universal gas constant $R = 8.31446$ J/(mol·K), and molar mass of air was assumed as molar mass of dry air: $M = 28.97$ g/mol, since the discrepancies between dry and humid air are too small here to be of interest.

- Dynamic viscosity of air μ [Pa·s]:

  an approximation valid for temperature range -20...400 °C was used [98]:

$$\mu = 2.791 \cdot 10^{-7} \cdot T^{0.7355}\,. \tag{3.3}$$

- Mean air speed in pipe cross-section w [m/s]:

$$w = c \cdot v\,, \tag{3.4}$$

  where c is a dimensionless proportionality factor explained below.

[1] Derivation of most of the following quantities was covered in [52]. However, here the explanations are more detailed, and extended with friction factor definition.

- Proportionality factor c [–] between mean and maximum air speed in pipe cross-section:

  its value depends on the flow regime (laminar or turbulent), or, more accurately speaking, on Reynolds number Re (defined in the following points).

  – For laminar flow (Re $<$ 2000), axial velocity profile is paraboloid and so, $c = c_{\text{laminar}} = 0.5$ [105, p. 357].

  – For turbulent flow (Re $>$ 4000), axial velocity profile is flatter, so, c is higher. It also changes with growing Reynolds number Re, or, with growing Darcy friction factor λ, which is related to Re (for definition, see the following points). The approximate relationship is [105, eq. (6.43)]:

  $$c = \frac{w}{v} \approx \frac{1}{1 + 1.33\sqrt{\lambda}} \tag{3.5}$$

  but it may be further simplified to a relation to Reynolds number presented in Table 3.4 [105, p. 367].
  Thus, to accurately determine c, firstly λ or Re must be known. However, both the latter depend on w, so both firstly need c value to be specified. In consequence, all of these quantities need to be iteratively approximated until the algorithm converges (the details of such procedure are given in the next point about Reynolds number).
  To simplify this dependency, a constant approximation of $c = c_{\text{turbulent}} = 0.8$ was chosen for turbulent flow. It was based on the fact that Reynolds numbers finally determined from the measured data did not exceed Re $= 28,000$. So, c for turbulent flows encountered in this part of the grinding installation should always lie in the range from about 0.79 to about 0.82, as follows from Table 3.4; and test calculations that used $c = 0.79$ or $c = 0.82$ showed no significant changes in Reynolds numbers, compared to Re calculated with $c = 0.8$. Thus, the selected value of 0.8 appears accurate enough for these particular experimental data.

  – For transitional flow (2000 $<$ Re $<$ 4000), such formula for c was adopted that defined the transition between laminar and turbulent flow in a similar way to Darcy friction factor λ (see the following points). Namely, a weight β,

TABLE 3.4: Approximate relationship between proportionality factor c and Reynolds number Re for turbulent flow. After [105]: White, Frank M. "Fluid Mechanics", 7th edition. New York: McGraw-Hill 2011, p. 367.

Re	4000	10^4	10^5	10^6	10^7	10^8
$\boldsymbol{c = w/v}$	0.794	0.814	0.852	0.877	0.895	0.909

ranging from 0 to 1, is defined that specifies how much the flow is laminar [19, eq. (9)]:

$$\beta = \frac{1}{1 + \left(\frac{\mathrm{Re}}{2720}\right)^9} \,. \tag{3.6}$$

Then, the c values for laminar and turbulent flow are combined, similarly to [19, eq. (1)]:

$$c = (c_{\mathrm{laminar}})^{\beta} \cdot (c_{\mathrm{turbulent}})^{1-\beta} = 0.5^{\beta} \cdot 0.8^{1-\beta} \,. \tag{3.7}$$

This function is plotted in Fig. 3.11.

As seen in the graph, function value is close to 0.5 for Reynolds numbers in the laminar region and close to 0.8 for Reynolds numbers in the turbulent region. This allows to use a single formula (3.7) for calculation of c values in the whole range of Reynolds numbers.

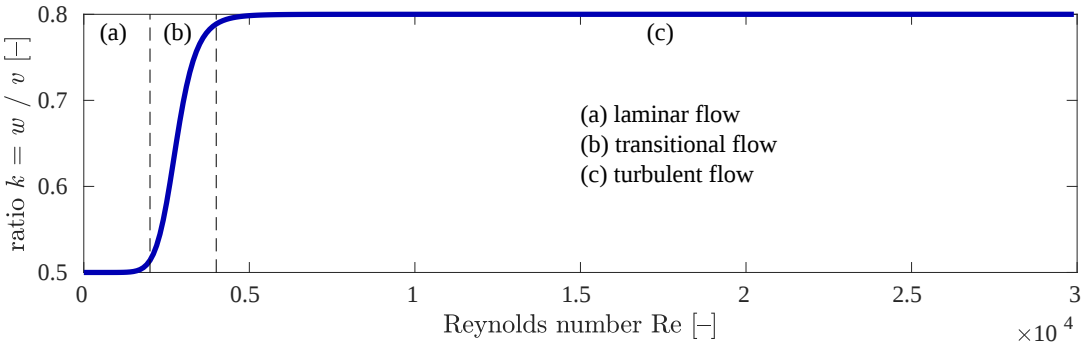

FIGURE 3.11: Ratio c between average and maximum flow velocity, adopted in this research. Calculated from (3.7).

- Reynolds number Re [–] [105, eq. (1.24)]:

$$\mathrm{Re} = \frac{\rho \cdot w \cdot L}{\mu} \,, \tag{3.8}$$

with L being the characteristic length. In the case of flow in circular ducts, L is the pipe's inner diameter D [105, Chap. 5].

Reynolds number depends on average velocity w, which must be computed from the measured maximum velocity using the proportionality factor c, which in turn depends on Reynolds number. So, this loop of dependencies needs to be solved iteratively. The following algorithm was used:

a) Initialization: $c = (c_{\mathrm{laminar}} + c_{\mathrm{turbulent}})/2$, then initial w (3.4) and then Re (3.8) are computed accordingly.

b) Calculate weight β (3.6) from Re.

c) Update proportionality factor c (3.7) from β.

d) Update mean air speed w (3.4) from c.

e) Update Reynolds number Re (3.8) from w.

f) Compare the old and new estimations of Re, denoted here $\mathrm{Re}_{\mathrm{old}}$ and $\mathrm{Re}_{\mathrm{new}}$: if

$$\frac{|\mathrm{Re}_{\mathrm{new}} - \mathrm{Re}_{\mathrm{old}}|}{\mathrm{Re}_{\mathrm{old}}} \leq \mathrm{Re}_{\mathrm{tolerance}}\,, \tag{3.9}$$

then finish the algorithm. Otherwise, repeat points b)–f), starting from $\mathrm{Re}_{\mathrm{new}}$.

Value of $\mathrm{Re}_{\mathrm{tolerance}} = 0.001$ was used. This seems a reasonable accuracy (a promile change in Re) and also, this resulted in stable (converging) algorithm.

- Darcy friction factor λ [–]:

  it describes pressure losses due to friction on pipe walls.

  – For laminar flow [105, eq. (6.13)],

$$\lambda = \lambda_{\mathrm{laminar}} = \frac{64}{\mathrm{Re}}\,. \tag{3.10}$$

  – For turbulent flow, the most accurate representation of friction factor seems to be Colebrook (or Colebrook–White) equation [22]:

$$\frac{1}{\sqrt{\lambda}} = -2\log\left(\frac{e/D}{3.7} + \frac{2.51}{\mathrm{Re}\cdot\sqrt{\lambda}}\right)\,. \tag{3.11}$$

    It incorporates the effect of pipe wall roughness on friction factor: e [m] is roughness height of the pipe's surface, e/D [–] is called relative roughness. The equation is implicit in λ and so, it may be computationally demanding to solve it. This gave rise to numerous explicit approximations discovered and published over the years; however, also some fast and accurate algorithms exist that iteratively solve the exact Colebrook equation (3.11). The latter option was used in the research presented in this thesis — it was a so-called quartic iterations algorithm published together with a ready-made MATLAB function [21].

    Values of $D = 102.3$ mm and $e = 0.05$ mm were used in this dissertation, i.e. the normative inner pipe diameter for the so-called ϕ100 ventilation pipes and recommended wall roughness for steel pipes [105, Tab. 6.1].

  – Transitional flow poses some problem in terms of λ.

    On the one hand, no well-grounded definitions of friction factor exist for the range $2000 \leq \mathrm{Re} \leq 4000$ [105, p. 371], just because of the very nature of such flow [70]. This is even reflected in the famous Moody chart [70] — a graphical representation of both laminar- and turbulent-region friction factors — as no plot lines are drawn in this transitional range.

On the other hand, some practical applications, including modelling and simulation software, require that a value of λ is calculated for each possible set of operating conditions. This also occurs here, in the research just discussed. So, e.g. some interpolation method may be used to define an approximate friction factor in the transitional region.

Such interpolation was found in [19] and was then slightly modified. The cited paper combines several formulas for friction factor. Firstly, it weights formulas for laminar and turbulent regions [19, eq. (1)]:

$$\lambda = (\lambda_{\text{laminar}})^{\beta} \cdot (\lambda_{\text{turbulent}})^{(1-\beta)} \tag{3.12}$$

Weight β was already presented in (3.6). Friction factor for laminar flow λ_{laminar} is the standard equation (3.10); and to get friction factor for turbulent flow $\lambda_{\text{turbulent}}$, the paper [19] suggests a weighting between two formulas for fully smooth and fully rough pipes, analogous to the weighting in (3.12). However, in the research described in this thesis, $\lambda_{\text{turbulent}}$ was substituted directly with the solution of Colebrook equation (3.11). The author of this thesis assumed that such approach would be better suited to industrial ventilation ducts (used in the grinding installation), which have a random distribution of roughness elements, as the author of [19] himself noticed.

Function (3.12) is asymptotic to (3.10) and (3.11) for Reynolds numbers below 2000 or above 4000, respectively (see Fig. 3.12). As such, it may be used as a single formula for calculation of friction factors in the whole range of Reynolds numbers.

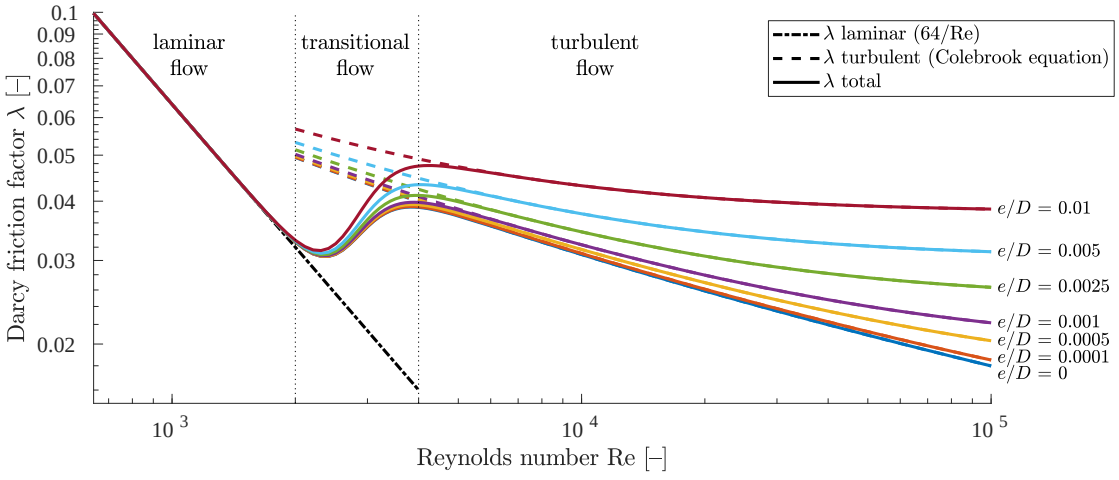

FIGURE 3.12: Friction factor calculated with different formulas: for laminar flow only (3.10), turbulent flow only (3.11) and for all flow regimes (3.12). e/D [–] is relative pipe roughness. Note: Laminar and turbulent friction factors extend into transitional region only for illustrative purposes — they indicate lower and upper limits for transitional friction factor.

- Volumetric flow rate Q [m^3/s]:

$$Q = A \cdot w\,, \tag{3.13}$$

  where A $\left[\mathrm{m}^2\right]$ denotes the area of pipe cross-section, so $A = \frac{\pi D^2}{4}$.

- Mass flow rate q [kg/s]:

$$q = Q \cdot \rho\,. \tag{3.14}$$

Note: the iterative algorithm for calculation of c, w and Re is necessary only when converting the physically measured signals v, p, T to the above derived quantities, so only for the endpoint of each inlet pipe. Calculating the necessary quantities (as model outputs) for other points in the installation is more straightforward, as these calculations are already based on mass flows instead of maximum velocities. So, these mass flows need to be iteratively determined only once (at pipe endpoints) and then, the mass conservation law may be used.

3.2.2 Static characteristics

Several static characteristics of the inlet pipes were estimated from experimental data, namely, steady-state mass flow of air and relative pressure in each of the three air streams, as functions of requested positions of the three air valves: $q_{\mathrm{m/r/a}} = f(x_{\mathrm{m,req}},\ x_{\mathrm{r,req}},\ x_{\mathrm{a,req}})$ and $p_{\mathrm{m/r/a}} = f(x_{\mathrm{m,req}},\ x_{\mathrm{r,req}},\ x_{\mathrm{a,req}})$ [52]. If needed, similar static characteristics for air velocity or volumetric air flow may be calculated — either by using the same methodology on appropriate input data from the experiment, or by arithmetic calculations on the mass flow static characteristics (see Section 3.2.1).

Each static characteristics was calculated in six versions: for each air damper gradually opened or gradually closed. These characteristics differ a bit, showing hysteresis in damper operation. One reason for it is that the actual position of the valve, x, is slightly different when approaching the same requested position x_{req} from lower or higher starting position. Usually, the final x is lower when the valve gets closed from higher x_{req_1} to lower x_{req_2}, than when the valve is opened from some even lower x_{req_3} to the same x_{req_2}. This is visible from the x data returned by damper actuators as damper position feedback. Some contribution to the hysteresis may also be the different positioning of the rubber seals around the valve disc when the damper is opened or closed.

Moreover, mass flow and pressure steady states finally reached after each step change on damper positions sometimes differ between the experiment series even if the direction of particular step changes was the same in all considered series. This may have been caused by slightly different actual positions of the dampers in each series, or slightly varying underpressure generated by the air blower, or similar phenomena.

To mitigate these effects, a seventh version of the static characteristics was also calculated, which is the arithmetic average of all the others. This type of static characteristics is intended for uses that neglect the hysteresis.

Block diagram in Fig. 3.13 summarizes the data processing stages that lead from raw measurement data to the static characteristics. The details of each stage are given in the following subsections.

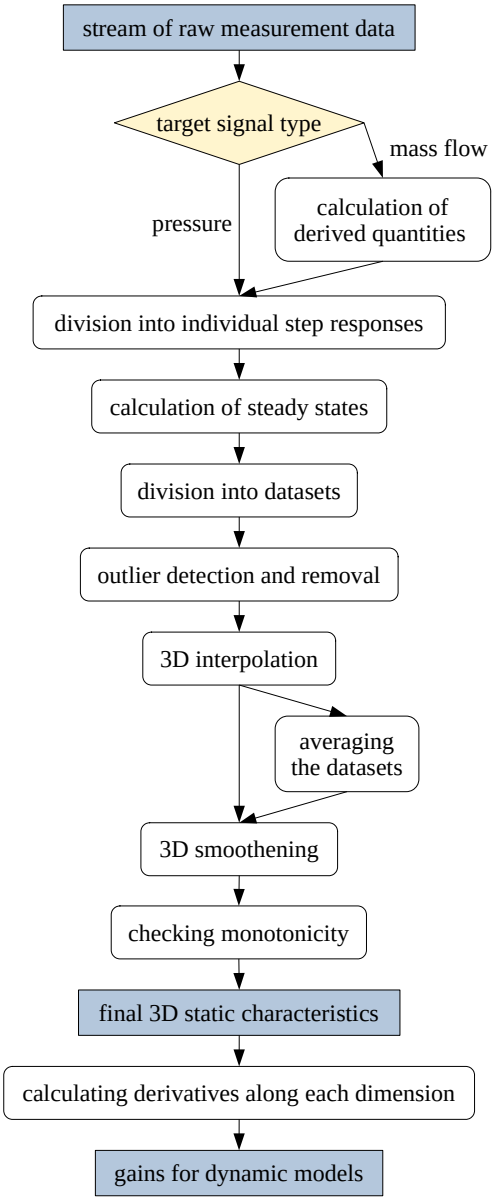

FIGURE 3.13: Data processing stages used to calculate all static characteristics

3.2.2.1 Calculation of derived quantities

In the case of mass flow static characteristics, the mass flow values need to be calculated from the measurement data, as was explained in Section 3.2.1. For pressure static charateristics, this stage is omitted as the pressures are measured directly at the plant.

3.2.2.2 Division of raw measurements into individual step responses

It is easy to differentiate between the signals associated with subsequent step changes — a change in requested position of any damper indicates the beginning of a new step change and step responses. For each step response, the following data were stored for future processing:

- requested positions of the main, recycle and additional dampers: $x_{\mathrm{m,req}},\ x_{\mathrm{r,req}},\ x_{\mathrm{a,req}}$,
- actual positions of the main, recycle and additional dampers: $x_{\mathrm{m}},\ x_{\mathrm{r}},\ x_{\mathrm{a}}$,
- pressure or mass flow of air in the main, recycle and additional streams: $p_{\mathrm{m}},\ p_{\mathrm{r}},\ p_{\mathrm{a}}$ or $q_{\mathrm{m}},\ q_{\mathrm{r}},\ q_{\mathrm{a}}$,
- the damper whose position has just changed (main, recycle or additional),
- direction of this step change (up or down).

3.2.2.3 Calculation of steady states

Steady-state values of air mass flow or pressure were searched from the end of each step response towards the beginning, with some predefined ±margins based on signal values observed in the measured data. If signal fragment contained within such margins lasted for at least 5 seconds, the steady-state value was calculated as the average value in that fragment. If the fragment was too short, the step response was labeled as not reaching its steady state and was discarded from future processing.

3.2.2.4 Division into datasets

All collected step responses of a specific output signal were sorted into six categories, called datasets from now on, which were the basis for the further processing stages. Each dataset contained steady-state data related to one particular damper's position making step changes up or down.

The output signals were mass flow of air or relative pressure in each horizontal inlet pipe of the grinding installation: $q_{\mathrm{r}},\ q_{\mathrm{m}},\ q_{\mathrm{a}},\ p_{\mathrm{r}},\ p_{\mathrm{m}},\ p_{\mathrm{a}}$(six signals). There were three dampers with their requested positions stored: $x_{\mathrm{r,req}},\ x_{\mathrm{m,req}},\ x_{\mathrm{a,req}}$, each differentiated

between two "directions" of step changes. This means 6 groups with $3 \cdot 2 = 6$ datasets in each of them.

3.2.2.5 Outlier detection and removal

A manual review of plotted steady-state data revealed that some values were outlying, being definitely too distant from their neighbours recorded at similar damper positions. So, the following outlier detection mechanism was proposed and run separately on each dataset:

a) Collect all data points from the dataset as an initial population.

b) Calculate the "expected" steady states — for each data point in the original dataset:
   - create a new population by excluding the considered point from the initial population,
   - based on this new population (new set of known datapoints), calculate three-dimensional linear interpolation of the deleted data point.
     Linear interpolation is very simple, but it was chosen on purpose as it creates no excessive ripples in the resultant hypersurface.

c) Define the quality of each data point: calculate the absolute difference between the actual steady state and its "expected", interpolated value.

   As shown by the algorithm results, absolute differences seem to be a reasonable, though simple, quality measure. To be even more effective, in the future this could be substituted with some weighting function that takes into account the reliability of interpolation result, e.g., number of data points used to compute the interpolated value and their distances to the queried point.

d) Calculate a data quality threshold at n-th percentile of the above-mentioned quality values. In this research, $n = 97$ was used.

e) Mark all data points with quality worse than the threshold as possible outliers.

f) Some outliers may have biased the interpolation that calculated the "expected" values for other data points, so:
   - create new initial population that contains all data points that were NOT marked as possible outliers,
   - repeat the actions from b) to e) (note: these actions should be performed on all points from the original dataset, even on those that were already marked as possible outliers),

- compare the indices of possible outliers that were found in this and in previous iteration of the algorithm.

g) Continue the search f) until:

- the indices remain the same (the algorithm converges), or,
- from iteration to iteration, the indices cycle between two sets of values.

In the latter case, the final set of outliers may be defined as intersection or union of the two sets. The author of this thesis decided to use the more cautious option, so to indicate all the suspicious points as outliers.

h) Delete from the original dataset the data points that were finally marked as outliers.

3.2.2.6 3D interpolation

For use in plant simulations or controller design and tuning, it was necessary to interpolate the static characteristics into the range of all damper positions that may be encountered during normal operation of the grinding installation (see Section 3.1.6.1). So, the interpolation target was such a fine grid of damper positions where: $x_{\mathrm{m,req}}$ — from 0 to 100%, $x_{\mathrm{r,req}}$ — from 0 to 100%, $x_{\mathrm{a,req}}$ — from 10 to 100%, all in 1% increments.

To maximally improve the interpolation result, several preprocessing stages were introduced. Firstly, the "coarse grid" of x_{req} (i.e., the positions from the identification experiment) was missing some points. Some step responses did not reach steady states due to excessive disturbances (Section 3.2.2.3). Other data points were removed as probable outliers (Section 3.2.2.5). Moreover, obviously no x_{req} made a step up from the value of 99%, nor a step down from the minimal position. It was advisable to restore these data points to avoid big empty regions in the input data for interpolation. Such missing inputs could strongly deteriorate interpolation results in these regions — especially at x_{req} close to minimum and maximum, because there extrapolation must be used instead of interpolation.

Thus, each missing data point was approximated as average value of corresponding data points in other datasets — preferably, from the datasets associated with the same direction of step changes; if no such data was available, then the average was computed over all other datasets. This made the datasets nearly complete — after this procedure, only a few data points were still missing from each dataset (only the ones that due to excessive disturbances were not defined in any original dataset). Their values were to be interpolated during the main interpolation stage.

The second preprocessing stage was based on the observation that all static characteristics are flat for high x_{req}. This had been observed in preliminary experiments

(Section 3.1.6.2) and was the reason for sparse sampling of x_{req} ranges for wide damper openings: only $x_{\mathrm{m,req}} = \{50,\ 99\}\%$; $x_{\mathrm{r,req}} = \{50,\ 99\}\%$; $x_{\mathrm{a,req}} = \{70,\ 99\}\%$ were used in the experiment. Now, the information about this flatness needed to be contained in the hard data so that the interpolation algorithm would follow this. Otherwise, with some interpolation methods, unnecessary ripples could occur in interpolated data in these regions. So, each dataset was artificially expanded to include intermediate datapoints with 10% increments for these regions. Namely:

- $x_{\mathrm{m,req}} = \{60,\ 70,\ 80,\ 90\}\%$; $\{x_{\mathrm{r,req}},\ x_{\mathrm{a,req}}\}$ = any of the original experimental values;
- $x_{\mathrm{r,req}} = \{60,\ 70,\ 80,\ 90\}\%$; $\{x_{\mathrm{m,req}},\ x_{\mathrm{a,req}}\}$ = any of the original experimental values;
- $x_{\mathrm{a,req}} = \{80,\ 90\}\%$; $\{x_{\mathrm{m,req}},\ x_{\mathrm{r,req}}\}$ = any of the original experimental values.

Data values at these locations were taken from 3D linear interpolation of the existing data points.

Then, the major 3D interpolation stage was performed, calculating the approximate static characteristics over the target fine grid of x_{req}. Several options for multidimensional interpolation were tested:

- MATLAB built-in function `scatteredInterpolant` [67] with interpolation method: linear, nearest neighbour or natural neighbour, combined with extrapolation method: linear or nearest neighbour;
- radial basis functions (RBF) interpolation [20] with methods (selectable jointly for interpolation and extrapolation): Gaussian, thinplate, cubic, multiquadrics, linear. The last one was identical to linear interpolation with `scatteredInterpolant`. Gaussian and multiquadrics methods have an adjustable scalar parameter, whose several values were tested.

Examination of plotted interpolation results showed that for this type of input data, thinplate RBF interpolation yielded the best output, meaning smooth hypersurfaces and very little unnecessary ripples. Unfortunately, this method appeared to introduce many non-monotonic areas to the produced hypersurfaces, which was unacceptable — the real plant's static characteristics are monotonic along each dimension, i.e., each damper position; this means also the gains of incremental dynamic models always have the same sign, and this directly affects the operation of control loops. So, eventually, linear 3D interpolation was used, but is was augmented with 3D smoothening in a later stage to get rid of sharp edges.

3.2.2.7 Averaging the datasets

For each analysed output signal, by taking averages of the corresponding values from all six interpolated static characteristics, a seventh static characteristics was created. It aggregated all measured data into one characteristics per output signal.

3.2.2.8 3D smoothening

Smoothening was performed on interpolated data from each individual dataset and on the average data as well. This provided smooth hypersurfaces which were similar to the real-world behaviour of the plant; also, they were necessary to achieve sensible gains in the next stage.

Smoothening in three dimensions was done with `smooth3` [68], a built-in MATLAB function. It offers a box convolution kernel of selectable size or a Gaussian kernel with selectable standard deviation. After testing several options and examining plotted results, box kernel of size $15 \times 15 \times 15$ was selected as best.

Figure 3.14 shows some examples of smoothened average characteristics. They were used in further research, e.g., for calculation of plant gains (see next section) and in the simulator of inlet air streams (see Chapter 4).

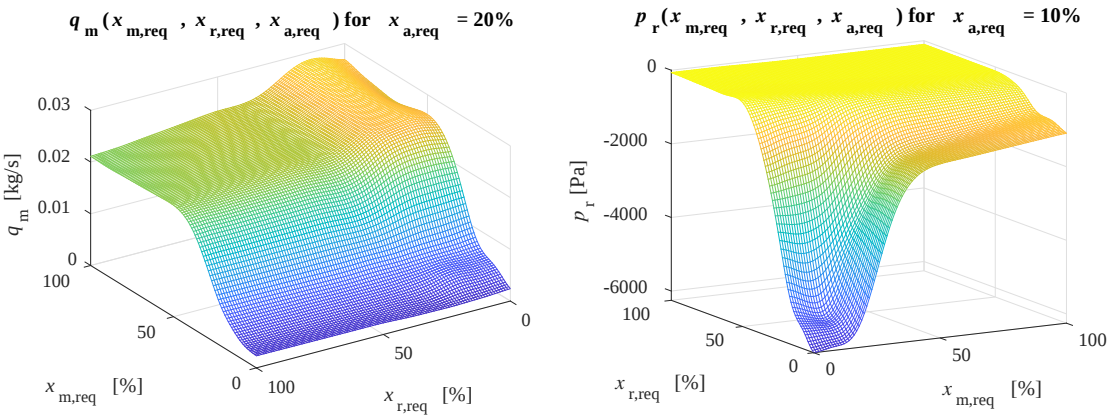

FIGURE 3.14: Examples of averaged static characteristics in their final shape, i.e. after 3D smoothening (2D slices of 3D characteristics are presented)

3.2.2.9 Checking monotonicity

Careful review of measured steady states showed that the static characteristics of the plant are generally* monotonic along each dimension (damper position). Of course, this agrees with the rule of operation of butterfly dampers. Thus, processed (interpolated and smoothened) static characteristics also needed to be monotonic, especially that this

strongly affects the operation of feedback control loops, which will be analysed later (Chapter 5).

The final static characteristics were checked for monotonicity and this showed that thinplate RBF interpolation did not perform well with respect to this criterion. So, the method was changed to 3D linear interpolation with more substantial smoothening, which ensured monotonic hypersurfaces.

* Note: A single but notable exception was at low openings of recycle damper (about 0–15%). In many such regions, the static characteristics were not monotonic, e.g. the recycle air flow had its minimum around 10–15% opening instead of the expected 0%. Repeatability of this phenomenon suggests it really occurred and was not a measurement error. This behaviour could be due to improper (not fully straight at 0% opening) mounting of the recycle damper's disc.

Thus, until this damper is fixed, it is recommended to limit its operating range to 15–100%, as the openings lower than 15% do not provide any new air flow values, but instead they cause problems to the controllers (they introduce non-monotonic behaviour to the plant). These limits will be used in the control part of this research (Chapter 5).

3.2.2.10 Calculating derivatives along each dimension

This stage does not strictly belong to the procedure of calculating static characteristics, but is closely associated with it. For each static characteristics $\overline{y} = f\left(x_{\mathrm{r,req}},\ x_{\mathrm{m,req}},\ x_{\mathrm{a,req}}\right)$, where $\overline{y}$ is the steady state of air mass flow or pressure at the end of a horizontal inlet pipe, the partial derivative of this static characteristics with respect to $x_{\bullet,\mathrm{req}}$ represents the gains of dynamic models of output signal y versus the same input $x_{\bullet,\mathrm{req}}$. (The dynamic models are discussed in more detail in Section 3.2.3.)

In the source code used for static characteristics calculation, the characteristics were 3D matrices of numeric values, with X, Y, Z dimensions corresponding to $x_{\mathrm{r,req}}$, $x_{\mathrm{m,req}}$, $x_{\mathrm{a,req}}$ variables; so, the mentioned partial derivatives were simply directional derivatives of these 3D matrices. They were calculated with MATLAB's built-in function `gradient` [66], which numerically approximates the partial derivatives with central differences for data points in the interior of the input matrix, and with single-sided differences for the points along the edges of the input matrix.

Such approach to gains calculation provided model gains that perfectly matched the static characteristics. This was important to prevent discrepancies in calculations, for instance, during simulation of plant model. This ideal match would not be achieved if

model gains were obtained with the same procedure as was used for determining other model parameters (Section 3.2.3).

Actually, the need to calculate model gains as derivatives of the steady-state characteristics was the very reason for making these static characteristics smooth. Any artificial ripples or edges introduced by the interpolation algorithm would only get amplified during numerical differentiation, producing unnatural, unrealistic variability of gains. Thus, the interpolation method for the static characteristics was carefully chosen (Section 3.2.2.6), and additionally, smoothening was applied (Section 3.2.2.8).

3.2.3 Dynamic models

From the point of view of plant simulation and design of air flow controllers, the dynamic models of interest are flow and pressure responses to changes in requested damper position. Air flow is the quantity that we need to control; pressure may be a helpful extra signal in more advanced control schemes; and requested positions of the dampers are the variables that may be manipulated in the installation. If needed, other models may easily be identified using the same methodology and even the same MATLAB scripts — for example, models with air speed or volumetric flow as outputs, or models with actual damper positions as inputs.

The three analysed air streams are strongly coupled because of the physical pipe interconnections — first at air intake, and then downstream from the dampers: at the mill bottom and just below the main classifier (see Fig. 3.1). Due to these couplings, it was decided to estimate model parameters for each combination of input and output variables. So, for each output variable (mass flow or pressure at each horizontal pipe), three single-input single-output (SISO) models were identified — one for each damper, whose position served as the input. Later, these SISO models were combined to create a three-input single-output model for each output variable; however, this is detailed in Chapter 4 and in paper [52].

From the measured data it follows that each SISO model should have parameters varying with positions of all dampers. So, each step response recorded in the experiment was used to estimate the coefficients of a single "compound model", valid in the vicinity of the operating point defined by all dampers' positions. Moreover, these step responses were treated as deviations from steady state, and the whole multi-input single-output (MISO) model was composed of a static characteristics and three incremental models for three input variables. So, the MISO model resembled a nonlinear dynamic model linearized around specific operating points. Such model structure was convenient to

identify and simulate, and could easily be used to tune some classic controllers or design more advanced, model-based control schemes.

The hysteresis already mentioned in the static characteristics means that also the direction of changes in damper position is important, i.e., dampers opened or closed cause different plant behaviour. So, the measurement data were divided into six datasets that represented each of the three dampers being gradually opened or closed (the same data grouping was performed when calculating static characteristics). Damper position that was changing the most frequently in an experiment series was used as model input; positions of the other two dampers only defined the operating point of the plant. Parameters of dynamic models were identified separately for the input signal increasing or decreasing. Then, also the average of these two variants was calculated for more approximate uses that neglect the small differences between these two situations.

Specific parameters of dynamic models were obtained with a somehow similar methodology as the one used with static characteristics. So, block diagram of the processing stages (Fig. 3.15) contains many operations already explained in Section 3.2.2; the new items are described in the following subsections.

3.2.3.1 Assumed model structure

From the step responses collected in the experiment (see Fig. 3.10 for some examples) it follows that the increments in output variable ΔY versus increments in input variable (damper position) ΔU may be described well enough by first or second order dynamics with delay. So, the following structures of dynamic models were tested:

- 1st order inertia with delay:

$$\frac{\Delta Y(\mathrm{s})}{\Delta U(\mathrm{s})} = \frac{k}{\mathrm{s}T_1 + 1} e^{-\mathrm{s}T_0}\,, \tag{3.15}$$

- 2nd order system with delay:

$$\frac{\Delta Y(\mathrm{s})}{\Delta U(\mathrm{s})} = \frac{k\omega^2}{\mathrm{s}^2 + 2\zeta\omega\mathrm{s} + \omega^2} e^{-\mathrm{s}T_0}\,; \tag{3.16}$$

- 2nd order system (without delay):

$$\frac{\Delta Y(\mathrm{s})}{\Delta U(\mathrm{s})} = \frac{k\omega^2}{\mathrm{s}^2 + 2\zeta\omega\mathrm{s} + \omega^2}\,, \tag{3.17}$$

with: s — Laplace variable, k — DC gain, T_1 — time constant, T_0 — time delay, ω — natural (undamped) pulsation of the system, ζ — damping ratio. General second-order

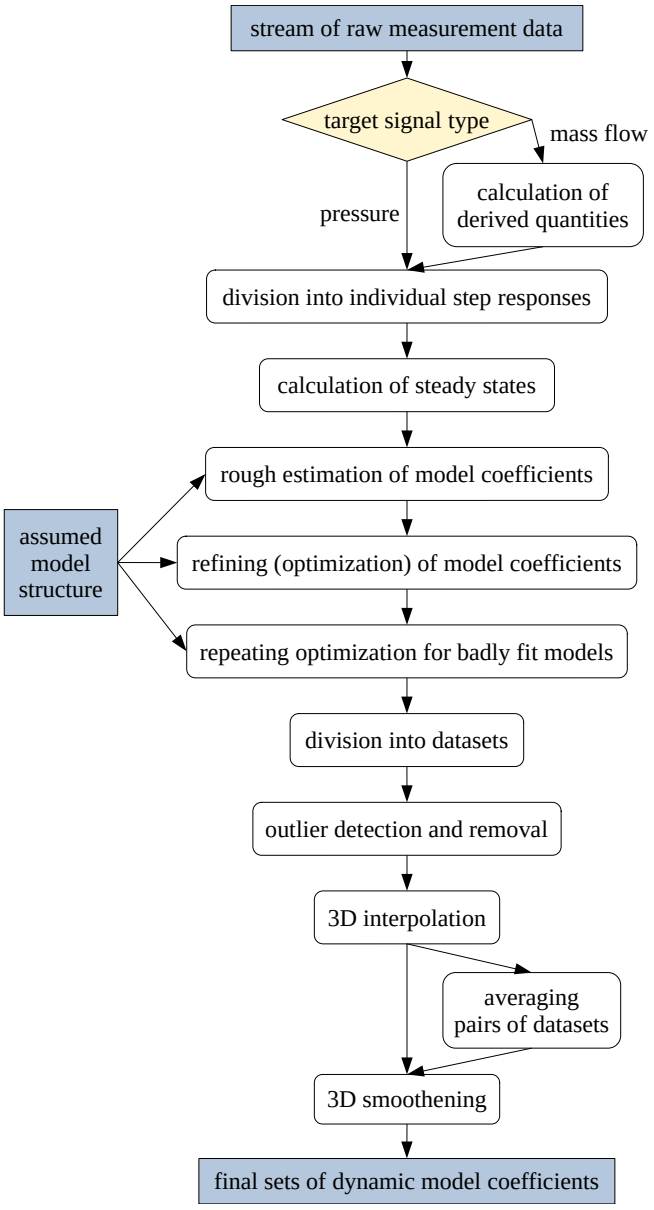

FIGURE 3.15: Data processing stages used to estimate parameters of all dynamic models

dynamics was allowed, not only second-order inertia, because some step responses showed a slight overshoot. Also, second order system without delay was tested in case it was difficult for the identification algorithms to properly differentiate the effects of delay and two time constants.

The transfer functions were defined in Laplace domain, not in discrete domain, because the former form is extremely convenient to use: it may be directly used in continuous-time simulation of the plant; it allows for effortless changes in sampling period of the simulated measurement and control system (if needed); it is used in many tuning rules for classical controllers (e.g., of PID type). If necessary, such continuous models may be

discretized, or (to be even more accurate) discrete-time models may also be estimated directly from the measurements.

Conclusions regarding the optimal model structure are presented in Section 3.2.3.13, after all processing stages are explained.

3.2.3.2 Calculation of derived quantities

Same stage as for static characteristics (Section 3.2.2.1). Mass flow values were calculated from the measurement data, according to the equations in Section 3.2.1. Pressure values were measured directly at the plant and did not require any calculations.

3.2.3.3 Division of raw measurements into individual step responses

Similar stage as for static characteristics (Section 3.2.2.2). For each step response, the following data were stored for future processing:

- requested positions of the main, recycle and additional dampers: $x_{\mathrm{m,req}}$, $x_{\mathrm{r,req}}$, $x_{\mathrm{a,req}}$,
- actual positions of the main, recycle and additional dampers: x_{m}, x_{r}, x_{a},
- pressure or mass flow of air in the main, recycle and additional streams: p_{m}, p_{r}, p_{a} or q_{m}, q_{r}, q_{a},
- steady-state values of all the above signals: just before the step change on input ("old" steady states) and after the step change ("new" steady states),
- the damper whose position has just changed (main, recycle or additional),
- direction of this step change (up or down).

3.2.3.4 Calculation of steady states

Same stage as for static characteristics (Section 3.2.2.3). The steady states were needed for estimation of model gain in the next stage.

3.2.3.5 Rough estimation of model coefficients

Model coefficients may be estimated from characteristic features of the step response, but this method works well only for good quality measurement data. It may return inaccurate or even erroneous values when operating on noisy signals, and this is the case particularly with mass flows, which often showed great turbulences. (Prior to estimation, step response was smoothened using a non-causal filter, but still, improvement provided

by this operation is limited.) So, the results from this estimation method were not used as final model coefficients, but only as some reasonable starting points for the optimization procedure performed in the next stage.

The method operates on deviations Δ of input u and output y from the steady states $\overline{u}_0$, $\overline{y}_0$ which they had right before the step change:

$$\Delta y(t) = y(t) - \overline{y}_0 \,, \tag{3.18}$$

$$\Delta u(t) = u(t) - \overline{u}_0 \,. \tag{3.19}$$

This means that if output signal did not reach steady state after the previous step change on input, then the current step response could not be analysed, due to lack of $\overline{y}_0$ value.

Specific equations used were similar as in [8; 57; 60], but were adapted to include time delay in the model, where necessary.

Gain Gain k is the same for all structures of dynamic models. It is the ratio of magnitude of steady-state change in the output versus magnitude of steady-state change in the input [8; 57; 60]:

$$k = \frac{\overline{y}_{\text{end}} - \overline{y}_0}{\overline{u}_{\text{end}} - \overline{u}_0} = \frac{\overline{\Delta y}_{\text{end}}}{\overline{\Delta u}_{\text{end}}} \,, \tag{3.20}$$

where subscripts "0" and "end" indicate, respectively, the steady states before and after the step change on input. Of course, such defined gain could not be determined if the previous ($\overline{y}_0$) or new ($\overline{y}_{\text{end}}$) steady state was not reached, e.g. due to excessive turbulences in the air stream.

1st order model with delay Assume $t_{n\%}$ as time period between the occurrence of the step change on input and the first time instant at which the output $\Delta y(t)$ reaches or surpasses $n\%$ of its final steady state value. Time constant T_1 and time delay T_0 of 1st order model with delay may then be estimated as:

$$T_1 = 1.25 \cdot (t_{70\%} - t_{33\%}) \,, \tag{3.21}$$

$$T_0 = 0.5 \cdot (3 \cdot t_{33\%} - t_{70\%}) \,. \tag{3.22}$$

2nd order model For computational purposes, 2nd order models need to be differentiated between oscillatory systems (formula (3.17) with damping ratio $0 < \zeta < 1$) and 2nd order inertia systems with two time constants T_1 and T_2:

$$\frac{\Delta Y(\mathrm{s})}{\Delta U(\mathrm{s})} = \frac{k}{(\mathrm{s}T_1 + 1)\,(\mathrm{s}T_2 + 1)} \,. \tag{3.23}$$

Of course, from mathematical point of view, the latter may be transformed to the same general 2nd order formula (3.17), with:

$$\omega = \frac{1}{\sqrt{T_1 T_2}}\,, \tag{3.24}$$

$$\zeta = \frac{1}{2}(T_1 + T_2) \cdot \omega\,, \tag{3.25}$$

which always results in damping ratio $\zeta \geq 1$. However, these two types of models need to follow different numerical procedures to get the estimated model coefficients. This is because using a single estimation method (suited to the more general oscillatory system equation) to both cases results in very inaccurate estimations of natural pulsation and damping ratio for the inertial systems.

→ **2nd order inertia** To recognize from the step response if the system should be oscillatory or not, the ratio $t_{90\%}/t_{50\%}$ was analysed. For a 2nd order inertia, this ratio should lie within range 2.32...3.32 [8]. In such case, time constants T_1 and T_2 were calculated based on the exact $t_{90\%}/t_{50\%}$ ratio and its associated proportions $t_{50\%}/T_1$ and T_2/T_1, as listed in [8, Table 3.1]. Then, time constants were transformed to natural pulsation (3.24) and damping ratio (3.25).

→ **2nd order oscillatory system** A faster step response (with $t_{90\%}/t_{50\%} < 2.32$) indicates a potential 2nd order oscillatory system. In such case, damping ratio was estimated in two ways:

a) Values $t_{100\%}$ and $t_{50\%}$ were determined from the step response. Then, ζ_1 was interpolated from [8, Table 3.2], which lists specific $t_{100\%}/t_{50\%}$ ratios with their corresponding ζ values.

b) Based on suggestions from [8], ζ_2 was calculated using the overshoot of the step response. For positive Δy values, the overshoot OS is defined as:

$$\mathrm{OS} = \frac{\max\left\{\Delta y(t)\right\} - \overline{\Delta y}_{\mathrm{end}}}{\overline{\Delta y}_{\mathrm{end}}}\,, \tag{3.26}$$

and with $\min\left\{\Delta y(t)\right\}$ for negative Δy values. The overshoot is related to damping ratio [9]:

$$\mathrm{OS} = \exp\left(-\frac{\pi\zeta}{\sqrt{1-\zeta^2}}\right)\,. \tag{3.27}$$

From this follows:

$$\zeta_2 = \frac{-\ln(\mathrm{OS})}{\sqrt{\pi^2 + \ln^2(\mathrm{OS})}}\,. \tag{3.28}$$

In case some of these two methods gave invalid numerical results (e.g., "not a number" or infinite), the other result was used. If both methods gave numerically correct values, $\zeta = \frac{1}{2}(\zeta_1 + \zeta_2)$ was used as the final result. Such approach provided some robustness to noisy step responses.

Natural pulsation ω was calculated from the above damping ratio ζ and the period T_{osc} of the actual (damped) oscillations [57]:

$$\omega = \frac{2\pi}{T_{\text{osc}} \cdot \sqrt{1-\zeta^2}} \,. \tag{3.29}$$

Value of T_{osc} was estimated as twice the time t_{extr} from the step change occurrence to the first oscillation's extremum [8].

2nd order model with delay The above methodology for 2nd order models was modified to account for the delay. At first, a very crude (but good enough for this purpose) estimation of time delay was used, verified experimentally:

$$T_0^{\text{approx}} = 0.97 \cdot t_{1\%} \,. \tag{3.30}$$

Then, modified $t_{50\%}$ and $t_{90\%}$ values were calculated with the delay removed:

$$t^*_{n\%} = t_{n\%} - T_0^{\text{approx}} \,, \tag{3.31}$$

and such modified ratio $t^*_{90\%}/t^*_{50\%}$ was used to differentiate between 2nd order inertia and oscillatory systems.

→ **2nd order inertia with delay** For $2.32 \leq t^*_{90\%}/t^*_{50\%} \leq 3.32$, the case of 2nd order inertia with delay was assumed. The delay value estimated so far was adopted as the final delay estimate: $T_0 = T_0^{\text{approx}}$. Also, the delay-stripped $t^*_{50\%}$ and $t^*_{90\%}$ values were used to find the time constants T_1, $T_2$of the model, in the same way as it was with $t_{50\%}$ and $t_{90\%}$ values for the model without delay. Finally, T_1 and T_2 were transformed to natural pulsation and damping ratio, as in (3.24–3.25).

→ **2nd order oscillatory system with delay** In the case of oscillatory system, delay estimate was refined thanks to availability of two methods of ζ calculation. Firstly, damping coefficient was found using the second method just described (method b) above), which is based only on output signal values (on overshoot), not on time measures. Then, the tabularized numeric data from method a) were used "the other way round", that is, to estimate the "true", delay-stripped ratio $t^*_{100\%}/t^*_{50\%} = R_{\text{true}}$ from the known ζ value. At

the same time, the values $t_{50\%}$, $t_{100\%}$ and t_{extr} were determined from the step response. They were biased with the delay, and the "true" ratio R_{true} was not. From these, it follows:

$$t_{100\%} - t_{50\%} = (t^*_{100\%} + T_0) - (t^*_{50\%} + T_0) = t^*_{100\%} - t^*_{50\%} = \\ = R_{\text{true}} \cdot t^*_{50\%} - t^*_{50\%} = (R_{\text{true}} - 1) \cdot t^*_{50\%} \,,$$

so then, sequentially, the following values were calculated:

$$t^*_{50\%} = \frac{t_{100\%} - t_{50\%}}{R_{\text{true}} - 1} \,, \tag{3.32}$$

$$T_0 = t_{50\%} - t^*_{50\%} \,, \tag{3.33}$$

$$t^*_{\text{extr}} = t_{\text{extr}} - T_0 \,, \tag{3.34}$$

$$T_{\text{osc}} = 2 \cdot t^*_{\text{extr}} \,, \tag{3.35}$$

and then natual pulsation ω from (3.29).

3.2.3.6 Refining (optimization) of model coefficients

Model coefficients estimated in the previous stage were good initial values for the optimization procedure, because in most cases they were quite close to the optimal coefficients. However, they still needed to be refined.

The optimization goal was based on mean absolute error (MAE) between Δy coming from the measurements and model output $\widehat{\Delta y}$ for the model excited with the same step change as the real plant:

$$\Theta_{\text{optim}} = \arg\min MAE\left(\widehat{\Delta y}(\Theta), \Delta y\right) = \arg\min \frac{1}{N} \sum_{i=1}^{N} \left| \widehat{\Delta y}_i(\Theta) - \Delta y_i \right| , \tag{3.36}$$

where subscript i means i-th sample of the step response (modelled or measured); Θ_{optim} is the optimal set of parameters; and vector Θ contains all parameters of the currently analysed structure of the model, i.e.: $\Theta = [k,\ T_1,\ T_0]$ or $\Theta = [k,\ \zeta,\ \omega,\ T_0]$, or $\Theta = [k,\ \zeta,\ \omega]$.

Optimization started from initial Θ values as determined in the previous stage (Section 3.2.3.5). Alternatively, if any of these parameters could not be defined (was calculated as "not a number" or infinite), the initial point was assumed as the last optimal parameters found — recently analysed step responses were associated with a rather similar operating point of the plant, so their optimal parameters should also be a bit similar.

Optimization was performed with MATLAB built-in function `fminsearch` [64]. If the minimization ended because of exhausted limit of allowed iterations instead of satisfied tolerance constraints, then the process was repeated from another initial point: from optimal parameters for the previously analysed step response, or from [1, 0, ..., 0]. The best-fit model of all such computed ones was stored.

3.2.3.7 Repeating optimization for badly fit models

As mentioned above, in some cases changing the initial point for the optimization procedure could improve the final fit of the model to the measured data. So, after all step responses were assigned their optimal model parameters (if possible), a ratio of fit function value (MAE) to output signal range was calculated for each step response. The worst-fit models, i.e., the ones for which this ratio was above 95-th percentile, were optimized again. This time the initial parameters for minimization were the optimal parameters for the previous and next step response, and the average of the two (if available). Eventually, the best-fit case of the old and new models was stored.

Note 1: Actually, such re-estimation could be performed for all step responses; however, it was time consuming. Thus, the optimization was repeated only for the worst fitted models, and the others were assumed as good enough and probably not possible to be considerably improved.

Note 2: To determine the badly fit models, the above-mentioned ratio of MAE to output signal range was used, instead of just MAE. This is because the range of output signal in a single step response may vary significantly with the operating point of the installation; and it was undesirable to punish the wide-range step responses with small model inaccuracy more than narrow-range step responses with significant inaccuracies.

3.2.3.8 Division into datasets

Similar stage as for static characteristics (Section 3.2.2.4). In the case of dynamic models, a dataset is defined as collection of all step responses (and their estimated model parameters) that are associated with the same output signal and input signal.

Output signals were mass flow of air or relative pressure in each horizontal inlet pipe of the grinding installation: q_r, q_m, q_a, p_r, p_m, p_a. Input signals were the requested positions of all dampers: $x_\mathrm{r,req}$, $x_\mathrm{m,req}$, $x_\mathrm{a,req}$. This means $6 \cdot 3 = 18$ datasets.

Later in each dataset also two sub-datasets were introduced, that corresponded to increasing and decreasing step changes on input signal.

3.2.3.9 Outlier detection and removal

At this stage, statistic calculations were performed at one dataset at a time (with datasets defined as in the previous paragraph). In the case of dynamic models, outliers may be understood in different ways; several definitions were adopted here. Models indicated as outlying by *any* of these definitions were excluded from further analyses:

- Firstly, all step responses were removed that were marked as outliers in a similar stage of steady-state data processing (see Section 3.2.2.5).
- Secondly, badly fit models were removed, i.e., the ones for which the ratio of fit function value versus output signal range was lying above the 95-th percentile.
- Next, values of individual model parameters were analysed: for each parameter, a histogram was calculated. Then, this portion of the histogram was kept that included at least 95% of data points in the narrowest possible, contiguous interval of histogram bins. (To prevent keeping too many data points due to very wide bins, the number of bins was selectable; it was always set to such value that at least 10 bins were kept.)

  If any parameter for a step response was indicated as outlying, then the whole model (the whole step response) was rejected from further analyses. Estimates of model parameters for a single step response are mutually dependent due to the performed optimization procedure, so even one outlying (that is, probably incorrectly estimated) parameter means that the other parameters are also probably incorrect — even if they happen to lie in a reasonable value range.

After removing outliers, in each dataset there remained 360–538 step responses with their estimated models (479 on average). These represented 54–80% of originally recorded step responses (72% on average).

3.2.3.10 3D interpolation

This stage was similar as for static characteristics (Section 3.2.2.6). This stage operated on sub-datasets instead of whole datasets, as defined in Section 3.2.3.8 — so, separate interpolation was performed for data associated with increasing and decreasing step changes on inputs.

Note: from this point, model gains k were no longer analysed; only the other parameters of the models were interpolated. A more accurate result than a simple interpolation of estimated gains was achieved by numerical differentiation of the static characteristics (Section 3.2.2.10).

Just as it was with steady-state data, the sub-datasets for steps up were obviously lacking data for $x_{\mathrm{req}} = 99\%$, and sub-datasets for steps down contained no data for the minimal x_{req} used in the experiments. Thus, before performing the actual interpolation, the sub-datasets were extended with reasonable approximations of these values. The first version of approximated values were the model parameters at corresponding $\{x_{\mathrm{r,req}}, x_{\mathrm{m,req}}, x_{\mathrm{a,req}}\}$ points for the other direction of step changes (so, from the other sub-dataset). The second version of approximated values were model parameters at the neighbourhood, within the same sub-dataset. The final approximations were assumed as average of these two versions, if both values were available; and if one of them was missing from the data, only the other was used. This operation provided values that were probably more sensible than a pure extrapolation result.

Then, the grid of data points for wide damper openings was expanded with linearly interpolated values at 10% increments of damper positions, identically as it was described for the steady states (Section 3.2.2.6). Static characteristics of the plant were flat in these regions, and the dampers performed similarly within these whole ranges of wide openings, so it was justified to also assume similar dynamic parameters in these regions. These extra datapoints would be useful for more complex interpolation methods to prevent ripples in these areas.

Finally, such prepared sub-datasets were interpolated to fine grids (with 1% increments) of damper positions, the same as for the static characteristics. After some tests, three-dimensional linear interpolation was found sufficient.

3.2.3.11 Averaging pairs of sub-datasets

In each dataset, its two sub-datasets were averaged. This produced a single set of model parameters for each output signal, input signal and operating point $\{x_{\mathrm{r,req}}, x_{\mathrm{m,req}}, x_{\mathrm{a,req}}\}$, regardless of the direction of changes in the input signal. Such model parameters were intended for use in models that neglected the influence of hysteresis in the plant, for simplicity.

3.2.3.12 3D smoothening

This stage was similar as for the static characteristics (Section 3.2.2.8). Smoothening was used to reduce the effect of measurement errors and processing artifacts — in the real plant, dynamic properties would not change abruptly with any damper's position.

3.2.3.13 Analysis of identification results

Best structure of dynamic models The three model structures (Section 3.2.3.1) — 1st order with delay, 2nd order with and without delay — were identified for a few exemplary pairs of input and output signals. The identification algorithm (Fig. 3.15) was performed up to (and including) the stage of outlier removal, and then the resulting final fits were compared — see Fig. 3.16.

These plots reveal that 1st order model with delay, though simple, was completely sufficient to describe the dynamics of the collected plant responses — fit values for this model were no worse (and sometimes better) than for 2nd order model with delay, and often noticeably better than for 2nd order model without delay. Moreover, using 1st order inertia with delay led to more models assumed as correctly estimated than when using 2nd order model with delay (less models and corresponding step responses were rejected in outlier removal stage, as detailed in Section 3.2.3.9). Thus, 1st order inertia with delay was assumed as the best dynamic model type for these measurement data. All models (for all combinations of input and output signals) were estimated based on this structure, this time — using the full processing path from Fig. 3.15, including interpolation and averaging of estimated parameters. These models were used in further research, e.g. in plant simulator (Chapter 4).

Shape of 3D hypersurfaces Time constants and time delays estimated in this procedure did not exhibit any repeatable relationship to damper positions. This suggests that more accurate measurement data should be collected if these model coefficients need to be determined precisely. However, the currently available data are accurate enough to describe the nature of the underlying processes. It is possible to calculate approximations of dynamic model coefficients that are suitable for design and tuning of control algorithms. Besides, the designed controllers need to be robust anyway, because parameter variability is the very nature of the grinding process. Slight hysteresis in operational characteristics of butterfly valves, changes in air temperature and humidity, introduction of different types and amounts of raw material and grinding media, dust build-up on inner surfaces of installation elements, etc. all affect the dynamic parameters of the identified systems, as well as the steady states. Small variations in these constantly happen during the operation of the grinding circuit, so some inaccuracies in estimation of time constants or time delays do not introduce significant errors.

Parameters variability Variability of parameter values was assessed for the finally chosen model type, i.e. 1st order inertia with delay. The models were analysed after the stage of removing outliers, but before parameters interpolation. For each parameter (k,

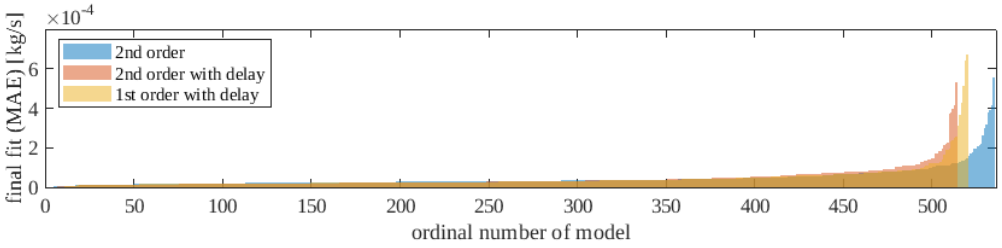

(A) Dynamic models of q_{r} versus $x_{\mathrm{r,req}}$

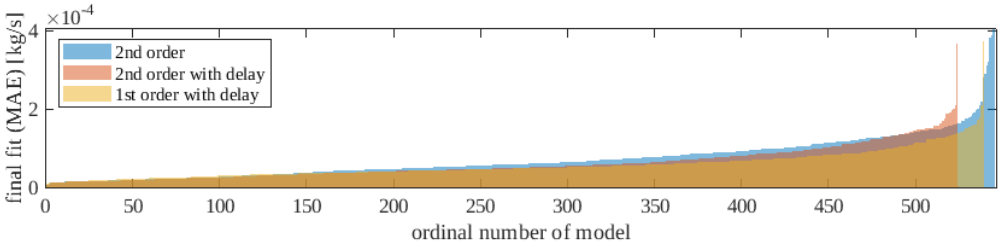

(B) Dynamic models of q_{m} versus $x_{\mathrm{m,req}}$

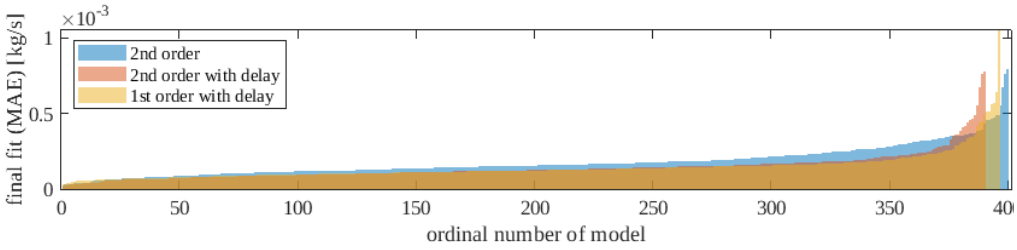

(C) Dynamic models of q_{a} versus $x_{\mathrm{a,req}}$

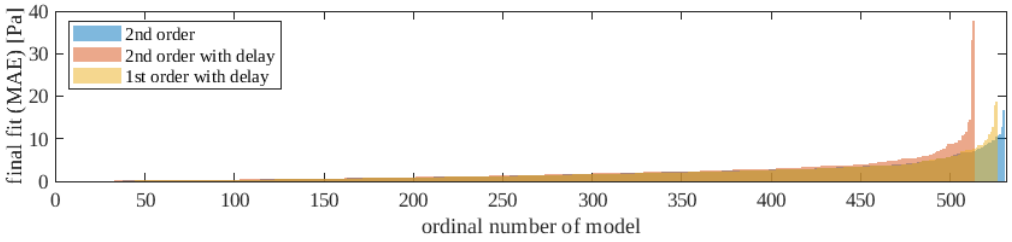

(D) Dynamic models of p_{r} versus $x_{\mathrm{r,req}}$

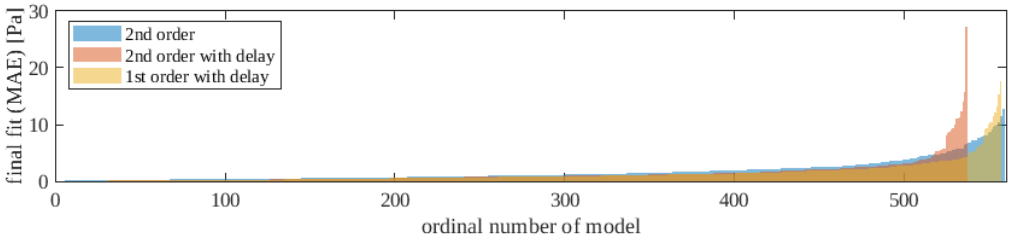

(E) Dynamic models of p_{m} versus $x_{\mathrm{m,req}}$

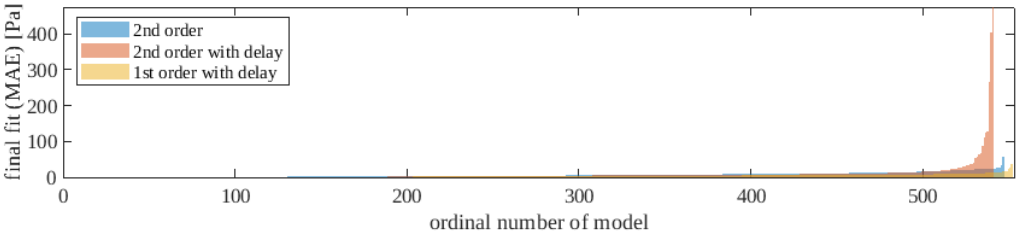

(F) Dynamic models of p_{a} versus $x_{\mathrm{a,req}}$

FIGURE 3.16: Comparison of final values of fit function (mean absolute error, MAE) for different structures of dynamic models. Data for each model type are sorted by ascending MAE (descending goodness of fit).

T_1 and T_0), the following dimensionless measures of variability were calculated over each dataset: quartile coefficient of dispersion:

$$qcd = \frac{Q3 - Q1}{Q3 + Q1}\,, \tag{3.37}$$

where $Q1$ and $Q3$ are 1st and 3rd quartiles of parameter values in one dataset; and similar to it, but based on 5-th and 95-th percentiles $P5$ and $P95$:

$$pcd = \frac{P95 - P5}{P95 + P5}\,. \tag{3.38}$$

The results are listed in Table 3.5. It should be noted that such measures of data dispersion are meaningful only for a positively valued sample. Thus, in the case of model gains, coefficients of dispersion could be calculated only for models of q_s or p_s versus position of the damper in the same pipe s.

TABLE 3.5: Dispersion coefficients for values of dynamic model parameters

Model number	**Model type**	*qcd* **(3.37) for:**			*pcd* **(3.38) for:**		
		k	T_1	T_0	k	T_1	T_0
1.	q_r vs $x_\mathrm{r,req}$	1.07	0.31	0.46	1.89	0.85	0.97
2.	q_m vs $x_\mathrm{m,req}$	0.84	0.22	0.16	0.96	0.72	0.48
3.	q_a vs $x_\mathrm{a,req}$	0.65	0.12	0.13	0.96	0.46	0.32
4.	p_r vs $x_\mathrm{r,req}$	0.98	0.53	0.49	1.15	1.00	1.00
5.	p_m vs $x_\mathrm{m,req}$	0.77	0.16	0.16	0.99	0.42	0.51
6.	p_a vs $x_\mathrm{a,req}$	0.83	0.26	0.11	0.99	0.58	0.48

Variability of model gain k was always bigger than of the other parameters — and quite often, it was even several times bigger. Nevertheless, for some datasets this difference in dispersion was not so pronounced and reached only 15% ($pcd\{k\}$ to $pcd\{T_1\}$ or to $pcd\{T_0\}$ for model 4.), or 33% ($pcd\{k\}$ to $pcd\{T_1\}$ for model 2.).

Consequently, it would be interesting to define a model with varying gains (fitted independently to each operating point of the pneumatic system), but with fixed time constant and time delay (fitted simultaneously to all measurement data, associated with all operating points). Such simplified model could then be used for design and tuning of control algorithms for the pneumatic system. With only the gains changing in the plant model, the structure of a control algorithm could be simpler than in the case when all plant parameters are varying; and simpler algorithms are easier to tune, easier to be implemented in hardware, and also require less hardware resources and less computation time. Thus, possibly there is a lot to gain; but firstly — due to such situations as with the mentioned models 2. and 4. — it needs to be verified if such model simplification

does not exceedingly deteriorate the performance of the control algorithm. This topic is only announced here and will be the subject of future research.

3.2.4 Phenomenological model of pressure losses

For the understanding of the processes going on in the pneumatic system of the grinding installation, it would be beneficial to create a phenomenological model of air flows and pressures in the installation. (The model could also incorporate heat transfer — in the future, when proper experiments and modelling are performed.) However, building a fully phenomenological model requires modelling of the whole installation from air intake to the blower (which has a built-in underpressure indicator), or at least to the point between cyclone and blower where measurements of outlet air are taken. This is a single point where all air streams are joined together and any measurement data on them are available. To accomplish such a model, truly excessive work is needed, and much of it would be of no use for the research considered here, which is focused on inlet air only. Moreover, numerous model parameters would need to be estimated from data originating at very few measurement points. This could lead to problems with parameter optimization procedures, or to low-accuracy estimations. So, this thesis considers only a model of the inlet part of the pneumatic system.

Due to lack of modelling of the joint flows, the mass air flows at the three inlet streams are assumed to come simply from the measurement data (they are given "as is"; only a black box model is created for them, without any physical equations). This is detailed in Section 3.2.2. However, if these mass flows are given, then the pressure losses on subsequent elements of the pipeline may be calculated from theoretical equations. The parameters of such a model are taken from literature where applicable, or fitted to measurement data where necessary. The model is built as follows. Model equations use symbols as defined in Fig. 3.17–3.18.

The model is built using steady-state data with probable outliers detected and removed. The procedure of obtaining such dataset is described in Section 3.2.2 (the part of the algorithm up to "outlier detection and removal" stage, without interpolation and smoothening — see Fig. 3.13). Only these data points are used that have non-outlying both pressure and mass flow values.

3.2.4.1 Mass flow of air

Mass flows of air were determined for all considered points in the installation, using measured data and mass conservation law (so, no air leakage into the pipeline was assumed):

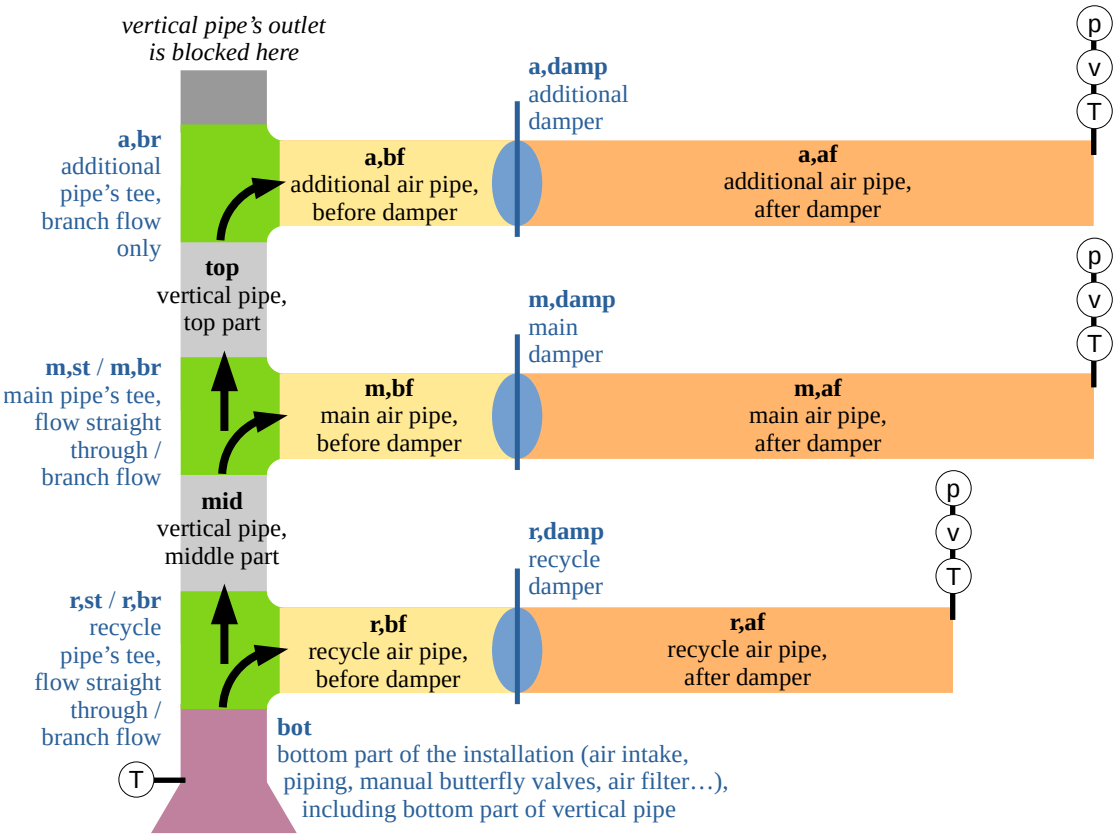

FIGURE 3.17: Inlet part of the pneumatic system with naming conventions used in the phenomenological model. In black: labels associated with straight pipe fragments; in blue: labels associated with pipe fittings and valves. Also, sensor locations are indicated with: p — for relative pressure, v — for air velocity at pipe axis, T — for air temperature measurements.

- Air flows at the ends of the three inlet pipes were calculated from the measurement data as detailed in Section 3.2.1:

$$q_{s\mathrm{D}} = q_s \quad \text{for} \quad s \in \{\mathrm{r}, \mathrm{m}, \mathrm{a}\}\,. \tag{3.39}$$

- Air flow throughout any of the three horizontal pipes is constant:

$$q_{s\mathrm{A}} = q_{s\mathrm{B}} = q_{s\mathrm{C}} = q_{s\mathrm{D}} \quad \text{for} \quad s \in \{\mathrm{r}, \mathrm{m}, \mathrm{a}\}\,. \tag{3.40}$$

- Air flow through the top vertical pipe is the same as through the additional pipe:

$$q_{\mathrm{topA}} = q_{\mathrm{topB}} = q_{\mathrm{a}}\,. \tag{3.41}$$

- Air flow through the middle vertical pipe is the sum of both flows branching from the main pipe's tee, so it is the sum of main and additional pipes' flows:

$$q_{\mathrm{midA}} = q_{\mathrm{midB}} = q_{\mathrm{m}} + q_{\mathrm{a}}\,. \tag{3.42}$$

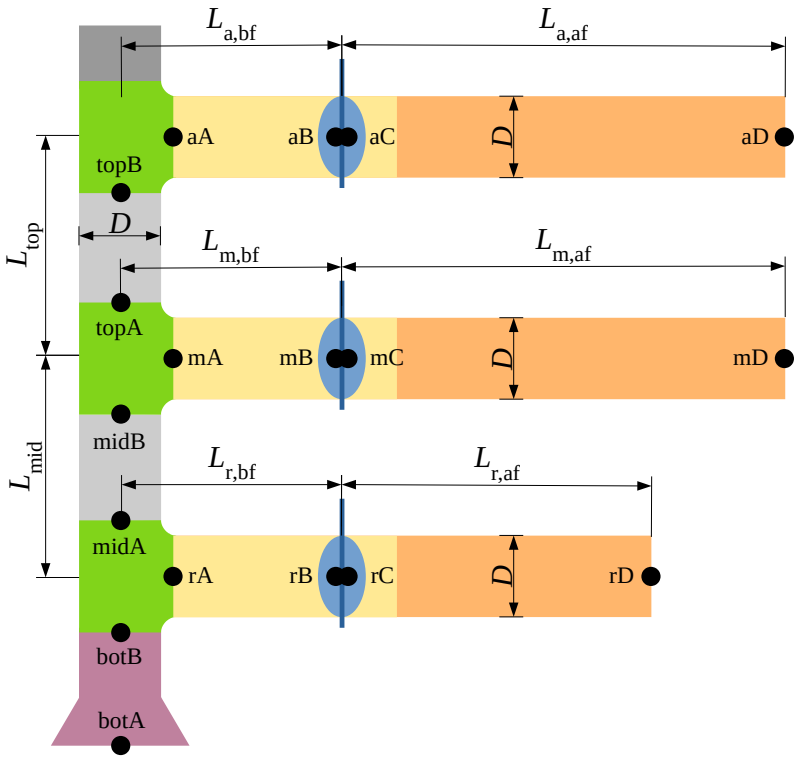

Dimension	Length
D	102.3 mm
L_{top}	0.435 m
L_{mid}	0.235 m
$L_{a,bf}$	0.305 m
$L_{a,af}$	2.02 m
$L_{m,bf}$	0.30 m
$L_{m,af}$	2.075 m
$L_{r,bf}$	0.31 m
$L_{r,af}$	1.09 m

FIGURE 3.18: Inlet part of the pneumatic system with geometrical dimensions indicated. (Scheme not to scale.) Bullets mark the boundaries between piping system elements; at these points, physical quantities were estimated in the phenomenological model.

- Air flow through the bottom part of the installation is the sum of both flows branching from the recycle pipe's tee, so it is the sum of recycle, main and additional pipes' flows:

$$q_{\mathrm{botA}} = q_{\mathrm{botB}} = q_{\mathrm{r}} + q_{\mathrm{m}} + q_{\mathrm{a}}\,. \tag{3.43}$$

3.2.4.2 Air temperature

Temperature values were assumed based on measurements taken near the air filter at the intake (T_{in}) and at the ends of the three horizontal pipes (T_{r}, T_{m}, T_{a}). In the collected data, all these signals have similar values and usually they differ by no more than 2 °C (all these temperatures for any given time instant lie within a range 2 °C wide). So, in the case of modelling that does not include heat transfer phenomena, a single average temperature value could be used in all the locations. However, the actually measured values and some interpolations between them may also be used, just to improve the accuracy of calculating temperature-dependent quantities, such as air density ρ (3.2) or viscosity μ (3.3). The latter approach was adopted, with some very simple approximations of temperature values for intermediate points between sensor locations, as this did not require much effort.

The used temperature values were as follows:

- For the vertical pipe, all temperatures were assumed identical and equal to T_{in} measured at the air filter:

$$T_{\text{botA}} = T_{\text{botB}} = T_{\text{midA}} = T_{\text{midB}} = T_{\text{topA}} = T_{\text{topB}} = T_{\text{in}} \,. \tag{3.44}$$

- At the ends of horizontal pipes, measurements were directly available:

$$T_{s\text{D}} = T_s \quad \text{for} \quad s \in \{\text{r, m, a}\} \,. \tag{3.45}$$

- At A, B, C points along the horizontal pipes, identical temperatures were assumed, as these points lie close to each other in space. The used value was a simple approximation between the temperatures before the appropriate tee and at the end of the pipe. More complicated formulas seem unnecessary as the differences between temperature measurements were quite small in the whole system:

$$T_{\text{rA}} = T_{\text{rB}} = T_{\text{rC}} = \frac{T_{\text{botB}} + T_{\text{rD}}}{2} \,, \tag{3.46}$$

$$T_{\text{mA}} = T_{\text{mB}} = T_{\text{mC}} = \frac{T_{\text{midB}} + T_{\text{mD}}}{2} \,, \tag{3.47}$$

$$T_{\text{aA}} = T_{\text{aB}} = T_{\text{aC}} = \frac{T_{\text{topB}} + T_{\text{aD}}}{2} \,. \tag{3.48}$$

3.2.4.3 Pressure losses

Each straight pipe fragment of length L introduces pressure loss Δp (so-called major loss) in the form [105, Sec. 6.3]:

$$\Delta p = \frac{1}{2} \frac{L}{D} \lambda \rho w^2 \,. \tag{3.49}$$

Also, each pipe fitting, such as elbow, tee or valve, causes pressure loss (called minor or local loss) [105, Sec. 6.9]:

$$\Delta p = \frac{1}{2} K \rho w^2 \,, \tag{3.50}$$

where K denotes dimensionless pressure loss coefficient, dependent e.g. on the shape and size of the fitting.

There are several methods of defining K, e.g., in the order of increasing accuracy: equivalent length method, K (excess head) method [23], Hooper's 2-K method [40], Darby's 3-K method [26; 27]. They also list suggested K values for numerous popular

fittings and valves. In the research presented in this thesis, 2-K method was used [40]:

$$K = \frac{K_1}{\mathrm{Re}} + K_\infty \cdot \left(1 + \frac{1}{D_{\mathrm{inch}}}\right) . \tag{3.51}$$

As the name suggests, the method is based on two parameters: K_1, K_∞. Pipe diameter D_{inch} should be given in inches to use loss coefficients for popular fittings tabularized in the paper. This method accounts for the increase in loss coefficient observed for small Reynolds numbers [40]. This is much desirable in the case of three inlet air streams of the grinding installation, where the flows are often laminar, as shown by Reynolds numbers computed from the experimental data. Loss coefficient's dependence on pipe inner diameter D_{inch} is not that important in this thesis, as all pipes in the considered fragment of the installation have equal diameters, and also all coefficients K_1, K_∞ are estimated from measurement data (not taken from the literature) to be more accurate. For the same reason, in this thesis, 2-K method was favored over 3-K method with three parameters $K_{3K,m}$, $K_{3K,i}$, $K_{3K,d}$ [26; 27]:

$$K = \frac{K_{3K,m}}{\mathrm{Re}} + K_{3K,i} \cdot \left(1 + \frac{K_{3K,d}}{D_{n,\mathrm{inch}}^{0.3}}\right) . \tag{3.52}$$

Symbol $D_{n,\mathrm{inch}}$ is the nominal inner diameter of the pipe in inches. The above formula shows that additional accuracy of 3-K method only comes from better dealing with scaled fitting sizes, which is not applicable to the data analysed in this thesis.

Summarizing: pressure values, due to blower's suction and frictional losses on pipeline elements, were modelled as:

- At air intake (point botA), absolute pressure is equal to atmospheric, so relative pressure is zero:
$$p_{\mathrm{botA}} = 0 . \tag{3.53}$$
- At the end of recycle pipe (point rD), the modelled pressure is:
$$p_{\mathrm{rD}} = p_{\mathrm{botA}} - \Delta p_{\mathrm{bot}} - \Delta p_{\mathrm{r,br}} - \Delta p_{\mathrm{r,bf}} - \Delta p_{\mathrm{r,damp}} - \Delta p_{\mathrm{r,af}} , \tag{3.54}$$
which is to be compared with the actually measured pressure p_{r}.
- At the end of main pipe (point mD), the modelled pressure is:
$$p_{\mathrm{mD}} = p_{\mathrm{botA}} - \Delta p_{\mathrm{bot}} - \Delta p_{\mathrm{r,st}} - \Delta p_{\mathrm{mid}} - \Delta p_{\mathrm{m,br}} - \Delta p_{\mathrm{m,bf}} - \Delta p_{\mathrm{m,damp}} - \Delta p_{\mathrm{m,af}} , \tag{3.55}$$
which is to be compared with the actually measured pressure p_{m}.

- At the end of additional pipe (point aD), the modelled pressure is:

$$p_{\mathrm{aD}} = p_{\mathrm{botA}} - \Delta p_{\mathrm{bot}} - \Delta p_{\mathrm{r,st}} - \Delta p_{\mathrm{mid}} - \Delta p_{\mathrm{m,st}} - \Delta p_{\mathrm{top}} - \Delta p_{\mathrm{a,br}} + \\ - \Delta p_{\mathrm{a,bf}} - \Delta p_{\mathrm{a,damp}} - \Delta p_{\mathrm{a,af}}\,, \quad (3.56)$$

  which is to be compared with the actually measured pressure p_{a}.

Each pressure loss on a straight pipe fragment (3.49) was calculated using geometrical dimensions defined in Fig. 3.18 and other quantities (defined in Section 3.2.1) calculated for the point at the beginning of the pipe fragment. For example, pressure drop over the middle vertical pipe was:

$$\Delta p_{\mathrm{mid}} = \frac{1}{2}\frac{L_{\mathrm{mid}}}{D} \cdot \lambda_{\mathrm{midA}} \cdot \rho_{\mathrm{midA}} \cdot w^2_{\mathrm{midA}}\,, \quad (3.57)$$

and similarly for other straight pipes.

Each pressure loss on a fitting (3.50) was calculated using an individual loss coefficient K (3.51) and other quantities (defined in Section 3.2.1) calculated for the point immediately upstream the fitting. For example, pressure drop over the bottom (inlet) part of the installation was:

$$\Delta p_{\mathrm{bot}} = \frac{1}{2} K_{\mathrm{bot}} \cdot \rho_{\mathrm{botA}} \cdot w^2_{\mathrm{botA}}\,, \quad (3.58)$$

and similarly for tees and butterfly valves.

In the whole model, the following loss coefficients were used:

- for the bottom (inlet) part of the installation: K_{bot},
- for straight-through flows in recycle and main tees: $K_{\mathrm{r,st}}$ and $K_{\mathrm{m,st}}$,
- for branch flows in recycle, main and additional tees: $K_{\mathrm{r,br}}$, $K_{\mathrm{m,br}}$ and $K_{\mathrm{a,br}}$,
- a separate coefficient for each requested position of each butterfly valve: $K_{s,\mathrm{damp},N\%}$ for $s \in \{\mathrm{r}, \mathrm{m}, \mathrm{a}\}$, for N values as listed in the description of the experiment (Section 3.1.2).

Separate K value for each position of a damper is a necessity, as the conditions of the flow dramatically change with varying valve opening. Requested damper position was used to distinguish between cases, not actual position. The latter would give more accurate model, but in the grinding system this variable is not directly controllable by the operator, whereas the requested position is.

Also, individual coefficients for all similar objects were used (e.g., two separate values for two straight runs in tees, even though both tees are very similar). This is because

particular making and fixing of a fitting may noticeably change its loss coefficient [105, Sec. 6.9]. For the same reason, no literature data was used directly as K values in the model — the suggestions from literature were only used as initial values for the optimization procedure that finally determined all the above loss coefficients. The details of optimization procedure are given in Section 3.2.4.5.

3.2.4.4 Pressure losses on butterfly dampers

Numerous works report experimental loss coefficients for partially open butterfly valves, mainly for fully turbulent flows. A few such positions were used in this thesis to determine initial values for loss coefficient optimization procedure, and also to serve as reference when validating optimization results. Namely, literature data used were:

- a single data series from [104] (omitting the infinite K for zero opening[2]);
- four data series from [49] (approximate values read from Fig. 8 there);
- two data series (experiments only) from [47] (approximate values read from Fig. 4 there);
- two data series being averages for the same pipe diameter over different velocities from [18];
- a single data series (experiment only) from [29].

The literature data and their averaged version are presented in Fig. 3.19.

Different valve positions were used in each of these works, so firstly, the original data were inter- or extrapolated to 0...100% range of valve openings with 1% increments. The exact calculation method was to take the decimal logarithm of an original data series, perform linear interpolation (or extrapolation) to the mentioned range of x_{req}, then get back to the original scale by raising 10 to the power of interpolated values. Then, such finely sampled characteristics of $K = f(x_{\mathrm{req}})$ were averaged.

Due to extrapolation, the approximated values outside of the original ranges of valve position are low fidelity data. This applies especially to the range of low damper openings, which were rarely tested in the literature items used here. Taking into account the overall shape of the characteristics, probably the extrapolations for these small openings underestimate the true loss coefficients. Nevertheless, even such extrapolated values may be a valuable guideline when selecting initial K values for optimization algorithm or when veryfying the sensibility of optimization results.

[2] In [104], the author included an infinite loss coefficient for a fully closed damper, which is true for the ideal case of a completely tight sealing around damper's disc. In reality, there is always some leakage around the sealing, the flow is not zero, and the pressure loss coefficient is finite.

Several types of functions were fitted to such literature data, both original and average. In the end, two formulas seemed to quite well mimic the trend in the data (see Fig. 3.20):

$$K = 10^{\left(a(x_{\mathrm{req}}+b)^2+c\right)} \tag{3.59}$$

with tunable parameters $a > 0$, $b < -100$, $c \in \mathbb{R}$; or,

$$K = 10^{\left(\frac{a}{x_{\mathrm{req}}+b}+c\right)} \tag{3.60}$$

with tunable parameters $a > 0$, $b < 0$, $c \in \mathbb{R}$. The shapes provided by these functions or particular parameters a, b, c fitted to literature data (e.g., to their average) may be used in the optimization procedure, as will be detailed in the next sections.

What is important, the presented literature data was based on fully turbulent flow conditions, so it actually shows K_∞ behaviour only (compare with 2-K method (3.51)):

$$K_{\mathrm{lit}} = \left[\frac{K_{1,\mathrm{lit}}}{\mathrm{Re}} + K_{\infty,\mathrm{lit}} \cdot \left(1 + \frac{1}{D_{\mathrm{lit}}}\right)\right]_{\mathrm{Re}\to\infty} \approx K_{\infty,\mathrm{lit}} \cdot \left(1 + \frac{1}{D_{\mathrm{lit}}}\right) \tag{3.61}$$

— so, the literature data reveals nothing on K_1 values. Still, it is reasonable to assume a similar behaviour of K_1 parameters for the dampers.

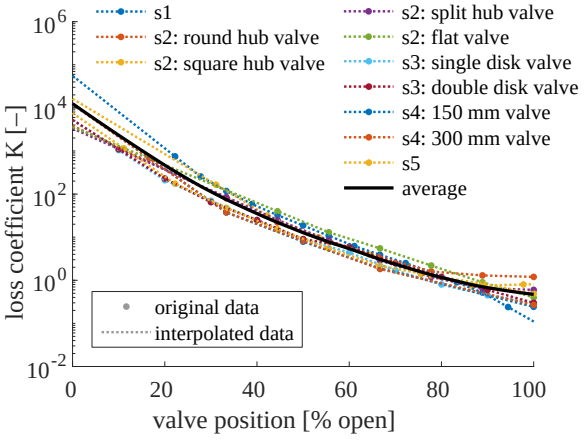

FIGURE 3.19: Literature data on butterfly valve loss coefficients, and their interpolations. Data sources: s1 — [47], s2 — [18], s3 — [104], s4 — [49], s5 — [29]. For details on original data series, see appropriate references.

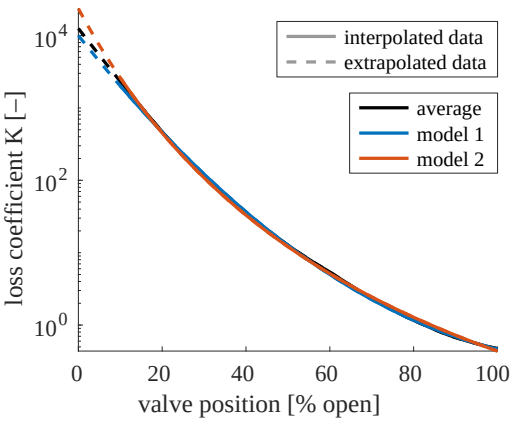

FIGURE 3.20: Functions fitted to the averaged literature data: model 1 is equation (3.59), model 2 is equation (3.60).

3.2.4.5 Optimization of pressure loss coefficients

To achieve good fit of pressure loss model to measurement data, Hooper's K_1 and K_∞ parameters (3.51) for all the above-mentioned loss coefficients were calculated by means

of optimization. Namely, it was minimization of mean absolute error (MAE) between modelled and measured pressure at the ends of the three horizontal pipes:

$$\begin{aligned}\mathbf{K}_{\text{optim}} &= \arg\min MAE\big(\left[p_{\text{rD}}\left(\mathbf{K}\right),\ p_{\text{mD}}\left(\mathbf{K}\right),\ p_{\text{aD}}\left(\mathbf{K}\right)\right],\ \left[p_{\text{r}},\ p_{\text{m}},\ p_{\text{a}}\right]\big) = \\ &= \arg\min \frac{1}{3N_p}\left(\sum_{i=1}^{N_p}\left|p_{\text{rD},i}\left(\mathbf{K}\right)-p_{\text{r},i}\right|+\sum_{i=1}^{N_p}\left|p_{\text{mD},i}\left(\mathbf{K}\right)-p_{\text{m},i}\right|+\right. \\ &\qquad \left.+\sum_{i=1}^{N_p}\left|p_{\text{aD},i}\left(\mathbf{K}\right)-p_{\text{a},i}\right|\right),\end{aligned} \tag{3.62}$$

where i denotes subsequent steady state values at the total of N_p data points, and $\mathbf{K}_{\text{optim}}$ is the vector of optimal parameter values.

Vector of optimized variables $\mathbf{K}$ contains K_1 and K_∞ parameters for bottom (inlet) part of the installation, two tee straight runs (recycle and main) and three tee branches (recycle, main and additional); this is 2 parameters times 6 fittings, i.e. 12 variables. Vector $\mathbf{K}$ also contains the parameters necessary to calculate loss coefficients for dampers (separately for each position x_{req}); this may be achieved in several ways. The following options were tested:

a) All K_1 parameters for a damper are estimated independently, the only requirement is that they should not increase with growing damper opening x_{req}. The same applies to K_∞ parameters. Vector $\mathbf{K}$ then directly contains all $K_{1,s,\text{damp},N\%}$ and $K_{\infty,s,\text{damp},N\%}$ values for $s \in \{\text{r, m, a}\}$ and for all tested damper positions $N\%$. This is 2 parameters times (8+8+7) damper positions (respectively for recycle, main and additional damper), so 44 variables; in total, $12 + 44 = 56$ optimized variables in $\mathbf{K}$ vector.

b) All K_1 parameters for a damper follow a model $K_1 = f(x_{\text{req}})$ as in (3.59). This appends only 3 model parameters $a,\ b,\ c$ to vector $\mathbf{K}$ instead of 7 or 8 parameters, as it is in option a). The same model structure applies to K_∞ parameters of each damper. This gives 2 "$K_\bullet$" parameters times 3 "$a,\ b,\ c$" parameters times 3 dampers, so 18 variables; in total, $12 + 18 = 30$ optimized variables in $\mathbf{K}$ vector. This is much less than in option a), which should result in better performance of optimization solver (e.g., convergence to a local minimum in fewer iterations, shorter calculation time of a single iteration, lower risk of outputting a local minimum which is not a global one). However, this also puts quite tight constraints on dampers' loss coefficients, which may negatively affect the final value of fit function.

c) The conditions are identical to option b), only model (3.60) is used instead of (3.59). This option was tested in case a different mathematical formula supplied to the solver yields substantially different directions of search in the solution space.

Minimization was performed in two ways, with MATLAB built-in functions: `fmincon` (minimization of constrained nonlinear function) [63] and `ga` (genetic algorithm) [65]. In the end, `fmincon` was used, as for this minimization problem it performed significantly faster and gave much better results (in terms of fit function value) than `ga`. The `fmincon` optimization solver was supplied with the following settings:

- stopping criterion: value of fit function differs by less than 10^{-6} from the previous iteration (relative difference),
- no limit on performed iterations of the algorithm or evaluations of fit function,
- fit function as in (3.62),
- initial values of $\mathbf{K}$ elements (Table 3.6) — several variants were tested:
  - literature-based — used for options a), b) and c):

    Where possible, the initial values for K_1 and K_∞ coefficients were based on Hooper's original loss coefficients [40]. As for the dampers, their initial K_∞ values were based on average literature data (Fig. 3.19). It also seemed reasonable to use a multiplication of K_∞ values as initial K_1 values, to preserve the shape of the characteristics $K = f(x_{\text{req}})$. Several scaling factors were tested: $c_{K_1} = \frac{K_1}{K_\infty} = \{1,\ 10,\ 100,\ 1000\}$.
  - based on optimal parameters for a simplified model — used for option a) only:

    Firstly, the model was simplified to include only a single-valued loss coefficient K for each fitting and for each position of each damper. Then, parameters of such simpler model were optimized as usual, with initial values analogous to these in the first approach described above. Such reduction in the number of optimized variables — by a factor of two — was expected to help to find the global minimum of the fit function, or its good approximation. Afterwards, the results would only need to be fine-tuned to incorporate again the 2-K method.

    Thus, the single-valued K coefficients resulting from optimization of the simpler model were scaled down by $(1 + 1/D_{\text{inch}})$ and used as initial values for K_∞ parameters, and multiples of the latter — as initial values for K_1 parameters, in optimization of the standard model that follows the 2-K method. For the tees and the bottom part of the installation, K_1 were set to 1000 times K_∞ values. Such ratio of these two coefficients was included in the mentioned literature [40]. As for the dampers, preliminary optimization runs had shown that 1000 might not be the best proportion, so again, several scaling factors were tested: $c_{K_1} = \{1,\ 10,\ 100,\ 1000\}$.

- lower and upper bounds on values of $\mathbf{K}$ elements (solution found by the solver must lie within these bounds) — also see Table 3.6,

- linear inequality constraints:
  - For option a), values of K_1 and K_∞ for dampers should not increase with growing x_{req}. (For options b)–c), this is already ensured by bounds imposed on a, b, c parameters.)
  - Loss coefficients for tee branches should be greater than for tee straight runs.
  - Loss coefficients for the inlet (bottom) part of the installation should be greater than for the tees. It should also be greater than loss coefficients for much opened dampers, but it is hard to define the particular valve positions to which this rule should apply, so such constraint was not imposed at all.
  - Fittings of similar shape should have comparable loss coefficients — i.e., $K_{1,\bullet,\text{st}}$ for both tees should be similar, and $K_{\infty,\bullet,\text{st}}$ as well; the same for all three tee branches. For these desirably similar $K_\bullet$ values, differences only by a factor of $c_{\text{diff}} = 1.5$ were allowed. It means that for any two coefficients K_a and K_b, these constraints were simultaneously imposed:

$$K_a \leq c_{\text{diff}} \cdot K_b \,, \qquad K_b \leq c_{\text{diff}} \cdot K_a \,. \tag{3.63}$$

- nonlinear inequality constraints:
  - All dampers also are similar in shape, so their K_1 and K_∞ loss coefficients (at the same damper positions) should follow the inequalities (3.63). For options b) and c), this is easy to impose, as their respective models of $K_\bullet = f(x_{\text{req}})$ allow to calculate loss coefficient values for arbitrary x_{req} values.

    However, imposing such constraints for option a) is more complicated because each damper has an individual set of positions present in the experimental data. Thus, to compare all dampers, first an interpolation of loss coefficients is needed, so that their x_{req} values match. The interpolation method was the same as for literature data (see Section 3.2.4.4), so, interpolated values were 10 to the power of linearly interpolated decimal logarithms of the estimated loss coefficients.

    Interpolated coefficients for main and recycle dampers were compared to each other in the full range $x_{\text{req}} = 0...100\%$, with 1% increments. Comparison of these dampers to the additional damper was performed only in the range $x_{\text{req}} = 10...100\%$ — the latter damper did not operate on positions lower than 10%, so loss coefficients were not estimated for them.

Note: For testing purposes, the above nonlinear constraints on similarity of damper coefficients were switched on or off. The results are shown and commented in Section 3.2.4.6.

TABLE 3.6: Initial values, lower and upper bounds for optimized elements of vector **K**. Abbreviations: bnd. – bounds, init.v. – initial value, lit. – literature data, par. – parameter.

Bottom part of installation

Its many elements (including air filter) produce big pneumatic resistance. Hence the high initial values (selected arbitrarily) in the first approach.

Parameter	**Initial value**			**Bounds**
	literature	**simplified model; dampers...**		
		... similar	**... nonsimilar**	
$K_{1,\text{bot}}$	2000	$1000 \cdot K_{\infty,\text{bot}}$		0...∞
$K_{\infty,\text{bot}}$	100	8.8685	9.3315	0...∞

Dampers, option a): $K \neq f(x_{\text{req}})$

$K_{\text{lit.},N\%}$ is the average data from literature (Fig. 3.19) for specific damper position $N\%$. The whole formula was derived from (3.61).

Parameter	**Initial value**							**Bnd.**
	lit.	**simplified model; dampers...**						
		... similar			**... nonsimilar**			
		r	**m**	**a**	**r**	**m**	**a**	
$K_{1,\bullet,\text{damp},N\%}$	$c_{K_1} \cdot K_{\infty,\bullet,\text{damp},N\%}$							0...∞
$K_{\infty,\bullet,\text{damp},N\%}$	$\frac{K_{\text{lit.},N\%}}{1+\frac{1}{D_{\text{inch}}}}$							
– $N = 0\%$	10030	96082	64073	—	1.1188e5	1.7205e5	—	
– $N = 10\%$	1859.0	59783	39856	59783	1.1188e5	30004	1.8229e5	
– $N = 15\%$	825.14	27294	18198	—	1.1188e5	17473	—	
– $N = 20\%$	374.99	9746.3	6499.6	8282.7	1.1187e5	6421.2	8284	all 0...∞
– $N = 30\%$	90.931	858.34	795.32	572.26	1477.5	797.67	572.11	
– $N = 40\%$	28.181	—	118.57	89.838	—	121.29	90.171	
– $N = 50\%$	10.158	21.073	30.209	27.923	34.741	31.077	28.430	
– $N = 70\%$	1.8922	—	—	3.1511	—	—	3.4556	
– $N = 99\%$	0.38996	0.098470	0.084739	0.068768	5.2197	0.019483	0.093867	

TABLE 3.6: (Continued.)

Dampers, option b): $K = f(x_{\text{req}})$ (3.59) and option c): $K = f(x_{\text{req}})$ (3.60)

Parameters $\bullet_{1,\bullet,\text{damp}}$ are used in K_1 calculations; parameters $\bullet_{\infty,\bullet,\text{damp}}$ – in K_∞ calculations. Expression "$+\log(c_{K_1})$" gives $K_{1,\bullet,\text{damp},N\%} = c_{K_1} \cdot K_{\infty,\bullet,\text{damp},N\%}$. Expression "$-\log(...)$" scales the total K to K_∞ – see (3.61). Values $[a,\ b,\ c] = [2.93e{-}4,\ -124,\ -0.499]$ or $[a,\ b,\ c] = [658,\ 78.1,\ -4.05]$ give optimal fit to average literature data (Fig. 3.19).

Par.	Option b)		Option c)	
	init.v. – lit. only	Bounds	init.v. – lit. only	Bounds
$a_{1,\bullet,\text{damp}}$	$a_{\infty,\bullet,\text{damp}}$	$0...\infty$	$a_{\infty,\bullet,\text{damp}}$	$0...\infty$
$b_{1,\bullet,\text{damp}}$	$b_{\infty,\bullet,\text{damp}}$	$-\infty...-100$	$b_{\infty,\bullet,\text{damp}}$	$-\infty...0$
$c_{1,\bullet,\text{damp}}$	$c_{\infty,\bullet,\text{damp}} + \log(c_{K_1})$	$-\infty...\infty$	$c_{\infty,\bullet,\text{damp}} + \log(c_{K_1})$	$-\infty...\infty$
$a_{\infty,\bullet,\text{damp}}$	$2.93 \cdot 10^{-4}$	$0...\infty$	658	$0...\infty$
$b_{\infty,\bullet,\text{damp}}$	–124	$-\infty...-100$	78.1	$-\infty...0$
$c_{\infty,\bullet,\text{damp}}$	$-0.499 - \log\left(1 + \frac{1}{D_{\text{inch}}}\right)$	$-\infty...\infty$	$-4.05 - \log\left(1 + \frac{1}{D_{\text{inch}}}\right)$	$-\infty...\infty$

Tees

Literature-based initial values as for tee with stub-in branch [40], which is the tee type in the grinding installation. Model-based initial $K_{1,\bullet,\text{st}}$ same as in literature because there is no sensible scaling factor for $K_{\infty,\bullet,\text{st}}$ when the latter is close to 0. Final parameters should be similar as in literature, hence limited upper bounds.

Par.	Initial value						Bounds
	lit.	simplified model; dampers...					
		... similar			... nonsimilar		
		r	m	a	r	m	a	
$K_{1,\bullet,\text{st}}$	100	100	100	—	100	100	—	0...200
$K_{\infty,\bullet,\text{st}}$	0	1.8087e-3	1.9469e-3	—	3.0166e-3	3.4534e-3	—	0...1
$K_{1,\bullet,\text{br}}$	1000	$1000 \cdot K_{\infty,\bullet,\text{br}}$						0...2000
$K_{\infty,\bullet,\text{br}}$	1	1.6005	1.0679	1.0691	1.5998	1.0673	1.1429	0...2

3.2.4.6 Final coefficients of the model

Table 3.7 presents the final fit achieved for all model options a), b), c) under all tested initial values of the optimization algorithm (based on literature data or simplified model). Results for option a), which has more variables to be optimized, were significantly better than for the other options. This means that loss coefficients observed in the measured data do not follow exactly the dependencies (3.59) or (3.60), as was in the case of loss coefficients reported in literature (see Fig. 3.20).

Even for the best case, optimization results were not fully satisfactory. Errors were quite big — particularly for the recycle stream, as shown by a more detailed analysis. Thus, one more model variant was tested: constraints (3.63) on similarity of loss coefficients were relaxed for dampers, and kept only for tee branches and straight runs. This enabled the model to better fit the measurements from the recycle stream — apparently, different from the others — without losing accuracy for the other streams. Again, option a) produced the best fit (see Table 3.7). However, this operation improved the final fit only partially. Besides, models b) and c) produced physically incorrect results, as for all tested sets of initial values the final K_1 coefficients for some dampers were very close to zero, with the corresponding K_∞ being abnormally high, or vice versa. (In total, these yielded reasonable K coefficients, but the individual K_1 and K_∞ values were inappropriate.) Thus, these models will not be further analysed; only option a) with non-similar dampers and all options a), b), c) with similar dampers will be listed in the following graphs and tables.

TABLE 3.7: Final fit achieved by the optimization algorithm for all tested model options and all sets of initial parameter values (see Table 3.6). In bold — best case for each model option. Symbols and abbreviations: lit. — literature-based initial values, s.m. — initial values based on a simplified model, c_{K_1} — scaling parameter between initial values for K_1 and K_∞ coefficients for dampers.

		Option a)		**Option b)**	**Option c)**
		lit.	**s.m.**	**lit. only**	**lit. only**
with damper similarity constraints	$c_{K_1} = 1$	317.22	317.14	369.52	391.13
	$c_{K_1} = 10$	314.03	314.18	406.15	390.45
	$c_{K_1} = 100$	314.21	312.96	**361.42**	378.79
	$c_{K_1} = 1000$	314.51	**297.02**	372.60	**358.56**
no damper similarity constraints	$c_{K_1} = 1$	250.23	**222.79**	**299.74**	328.51
	$c_{K_1} = 10$	223.81	227.46	300.52	327.99
	$c_{K_1} = 100$	223.23	259.63	304.64	326.69
	$c_{K_1} = 1000$	223.14	353.06	330.28	**306.44**

Figure 3.21 compares modelled and measured pressures at the ends of horizontal pipes, so, $p_{s\mathrm{D}}$ and p_s values for $s \in \{\mathrm{r}, \mathrm{m}, \mathrm{a}\}$. This is directly related to the fit function values just discussed.

Generally, underpressure in the recycle pipe is largely underestimated. Even the model a) with non-similar damper coefficients (Fig. 3.21a) provides only a slightly better fit to recycle stream pressure. Main stream's pressure is best reflected by option a) models. Additional stream's data are interesting — big underpressures are greatly underestimated, for the others the fit is very good. These errors may be caused by particularly

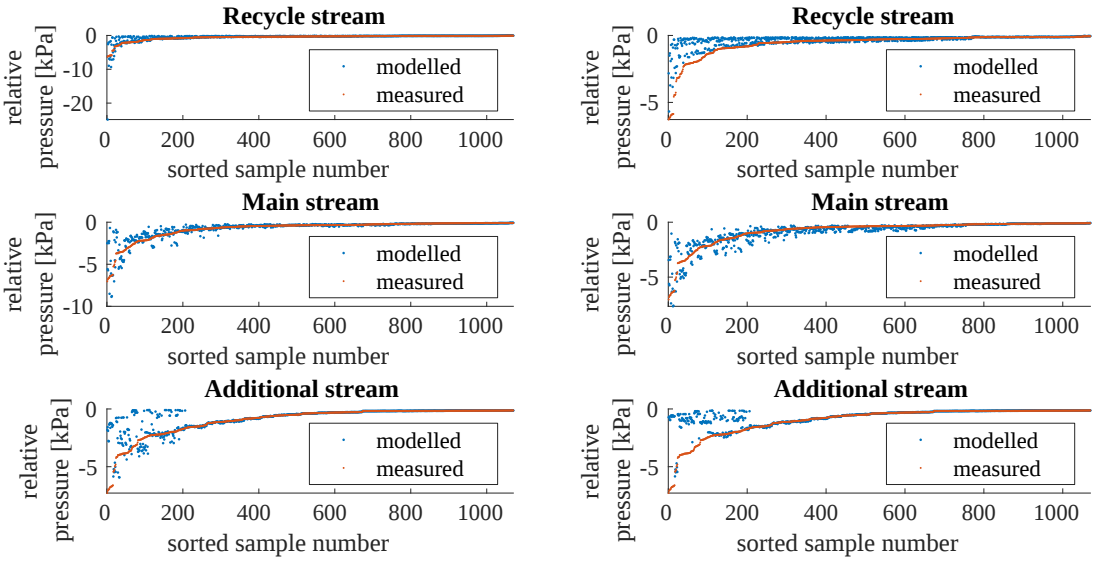

(A) Option a), non-similar damper coefficients

(B) Option a), damper similarity imposed

(C) Option b), damper similarity imposed

(D) Option c), damper similarity imposed

FIGURE 3.21: Relative pressure at the ends of horizontal inlet pipes: output of phenomenological model $p_{s\mathrm{D}}$ compared to real measured values p_s, for $s \in \{\mathrm{r}, \mathrm{m}, \mathrm{a}\}$. Data points sorted by increasing p_s.

low relative accuracy of air velocity measurements at low air speeds (i.e., for only slightly opened damper, which also gives high underpressure).

The next figures provide more detail to the comparison of modelled pressure $p_{s\mathrm{D}}$ and measured pressure p_s. These plots show the error $(p_{s\mathrm{D}} - p_s)$ (Fig. 3.22) and relative error $100\% \cdot (p_{s\mathrm{D}} - p_s)/p_s$ (Fig. 3.23).

The graphs confirm the observations made in association with Fig. 3.21. Clearly visible are the small errors and relative errors for most data points related to the additional pipe.

For the other air streams, often a trend is observed in the plotted errors, which suggests that some deterministic component is missing in the model. Moreover, many data points have errors and relative errors that are unacceptably big.

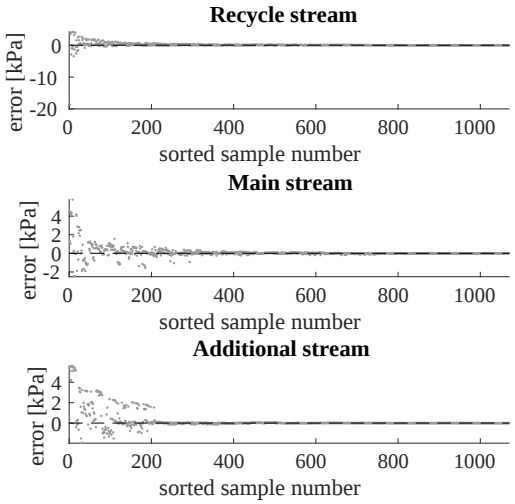

(A) Option a), non-similar damper coefficients

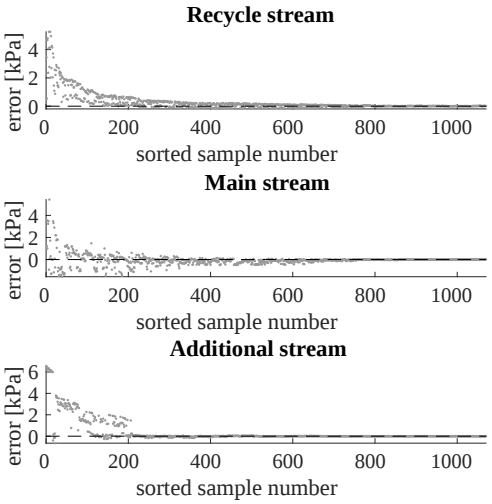

(B) Option a), damper similarity imposed

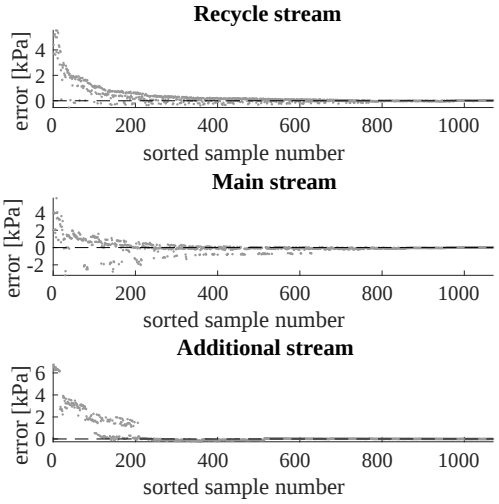

(C) Option b), damper similarity imposed

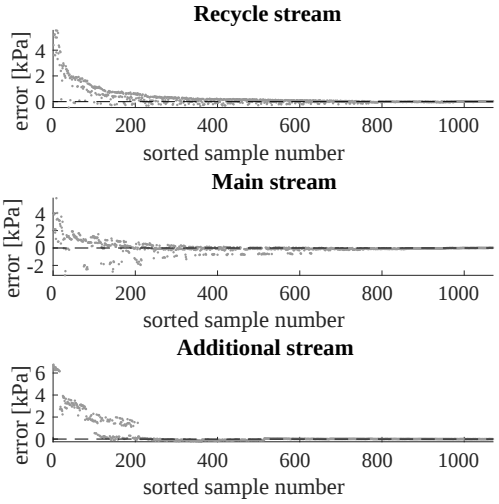

(D) Option c), damper similarity imposed

FIGURE 3.22: Difference (error) between modelled and measured pressure at the ends of horizontal inlet pipes: $p_{s\mathrm{D}} - p_s$, for $s \in \{\mathrm{r}, \mathrm{m}, \mathrm{a}\}$. Data points sorted by increasing p_s. Black lines mark the desired value of zero error.

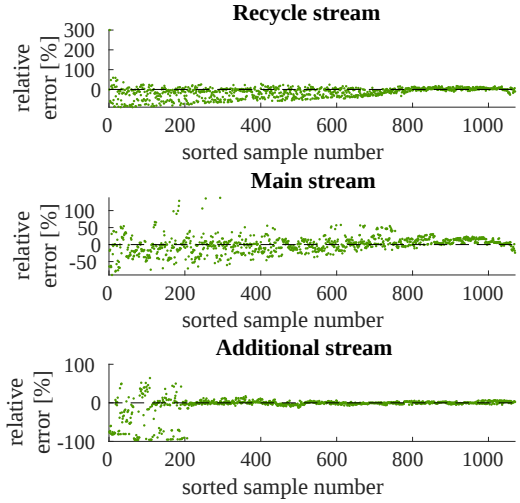

(A) Option a), non-similar damper coefficients

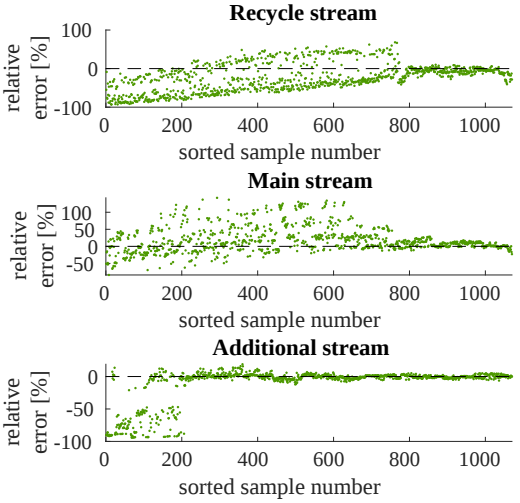

(B) Option a), damper similarity imposed

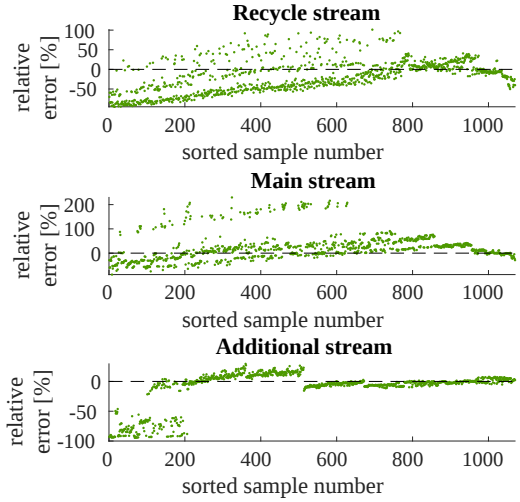

(C) Option b), damper similarity imposed

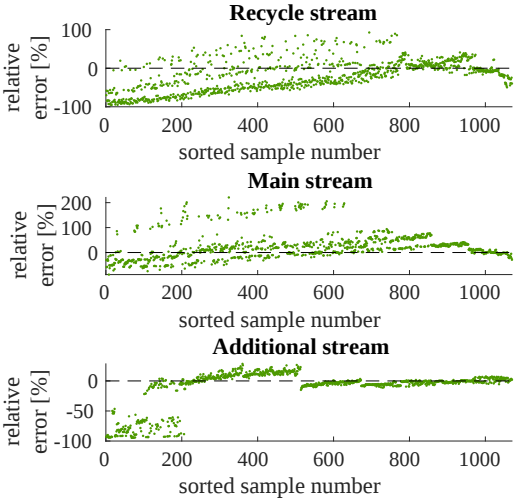

(D) Option c), damper similarity imposed

FIGURE 3.23: Relative difference (relative error) between modelled and measured pressure at the ends of horizontal inlet pipes: $100\% \cdot (p_{s\mathrm{D}} - p_s)\,/p_s$, for $s \in \{\mathrm{r}, \mathrm{m}, \mathrm{a}\}$. Data points sorted by increasing p_s. Black lines mark the desired value of zero relative error.

Table 3.8 lists the final values of optimized model coefficients. The bottom part of the installation was assigned a K_∞ coefficient lower than expected — only slightly above 7, in all presented cases. This is quite low, taking into account the rather thick air filter. Also, tee straight runs were often assigned significantly smaller K_1 coefficients than the literature value of 100, but K_∞ are as expected — close to 0. As for the tee branches, both their K_1 and K_∞ coefficients were usually estimated as higher than in literature (which states $[K_1,\ K_\infty] = [1000,\ 1]$), often over 90% higher.

TABLE 3.8: Optimized coefficients of different structures of the phenomenological model. Abbreviations: Dmp. — Damper, Par. — Parameter, Pos. — Position, n.a. — not applicable. More symbols explained in Fig. 3.17. **Note:** For options b) and c), damper parameters K_1 and K_∞ were not optimized directly, but they followed from the a, b, c parameters. Nevertheless, dampers' K_1 and K_∞ coefficients for these options were included in the table for comparison with option a).

dampers:		**Option a) non-similar**		**Option a) similar**		**Option b) similar**		**Option c) similar**	
final fit (MAE)		222.79		297.02		361.42		358.56	
Fitting		K_1	K_∞	K_1	K_∞	K_1	K_∞	K_1	K_∞
bot		29237	7.5334	11984	7.3114	2000.5	7.3780	7981.2	7.1428
r,st		24.659	4.0600e-3	19.36	4.7540e-4	99.002	0.36571	50.244	0.38805
m,st		28.423	4.6820e-3	23.676	5.6659e-4	100.22	0.54823	74.276	0.58205
r,br		1947.0	1.9964	1905.1	1.9996	1001.5	1.9994	1997.5	2.0000
m,br		1330.7	1.3319	1272.6	1.3332	998.63	1.3332	1332.1	1.3333
a,br		1594.5	1.5050	1857.5	1.3749	1000.2	1.9993	1995.8	1.9999
Dmp.	**Par.**	(n.a.)		(n.a.)		for K_1	for K_∞	for K_1	for K_∞
	a	—		—		6.3836e-5	1.2752e-4	38420	59855
r	b	—		—		-371.23	-315.98	914.20	873.09
	c	—		—		-0.86433	-7.8258	-34.124	-63.643
	a	—		—		7.0171e-5	1.6715e-4	33787	33390
m	b	—		—		-354.75	-257.26	835.80	630.38
	c	—		—		-0.72164	-5.9809	-32.346	-47.879
	a	—		—		2.0359e-4	3.0104e-4	2168.8	5795.6
a	b	—		—		-154.16	-165.57	179.39	236.24
	c	—		—		3.4107	-2.9974	-3.8288	-19.223
Dmp.	**Pos.**	K_1	K_∞	K_1	K_∞	K_1	K_∞	K_1	K_∞
	0%	1.6464e5	2.7153e5	9.6082e7	79300	1.2855e8	1.2075e5	1.1962e8	1.2283e5
	10%	1.2260e5	1.2038e5	5.9782e7	27436	4.1517e7	17321	3.9799e7	18289
	15%	1.0756e5	1.2037e5	2.7294e7	21267	2.3882e7	6752.4	2.3180e7	7215.0
r	20%	54752	1.2036e5	9.7463e6	7782.4	1.3849e7	2683.5	1.3586e7	2887.3
	30%	24322	1471.7	8.5784e5	810.29	4.7714e6	448.99	4.7545e6	482.04
	50%	17720	34.111	22332	21.957	6.2402e5	15.835	6.2520e5	15.733
	99%	17375	4.0505	22257	1.1053	7379.1	0.016062	6261.5	7.9416e-3
	0%	1.7275e5	62863	6.4073e7	52869	8.5704e7	80511	7.9749e7	81890
	10%	30181	30088	3.9868e7	18296	2.9203e7	12965	2.7990e7	13706
	15%	30161	17463	1.8199e7	14180	1.7236e7	5318.3	1.6723e7	5692.6
m	20%	28226	6424.2	6.4999e6	5190.3	1.0248e7	2213.9	1.0046e7	2387.7
	30%	27995	797.52	7.9462e5	730.06	3.7033e6	400.93	3.6850e6	432.37
	40%	822.36	124.24	1.1750e5	120.16	1.3782e6	76.998	1.3804e6	81.281
	50%	283.47	32.203	26143	32.916	5.2821e5	15.682	5.2772e5	15.843
	99%	79.425	0.025775	15789	0.76235	7353.4	0.015056	6242.5	8.5379e-3
	10%	1.8214e5	2.5280e5	5.9776e7	27444	4.3803e7	19445	4.1984e7	20559
	20%	53715	8381.9	8.2827e6	7327.5	1.1882e7	2411.2	1.1187e7	2480.3
	30%	27220	571.87	5.7383e5	540.29	3.5399e6	343.45	3.3825e6	350.76
a	40%	27140	89.761	92339	88.981	1.1583e6	56.196	1.1405e6	57.150
	50%	27067	28.319	29409	29.561	4.1625e5	10.562	4.2280e5	10.570
	70%	26960	3.2604	16252	4.7212	71216	0.56554	73771	0.50327
	99%	5932.6	0.53575	16223	1.1116	10717	0.021721	9161.0	0.011607

Dampers' loss coefficients K_1 and K_∞ are better discussed with the aid of their plotted version (Fig. 3.24). The curvature of function $K_\bullet = f(x_{\mathrm{req}})$ produced by model b) (Fig. 3.24c) and model c) (Fig. 3.24d) is barely noticeable in log scale. However, this curvature is not negligible, as will be visible in the plots of total loss coefficient vs damper position (Fig. 3.25). Deviation from linear (in log scale) dependency is bigger for models a) (Figures 3.24a and 3.24b). Moreover, these shapes indeed do not resemble the model functions (3.59) and (3.60), so the latter did not succeed that much (produced higher MAE).

For all four model types, the ranges of K_∞ coefficients are similar. Parameters K_1 are also of similar range for all models with imposed damper similarity constraints (though for model a), the intermediate values are much different than for the other models). Range of K_1 coefficients is different (much narrower) only for the model in Fig. 3.24a. Apparently, when similarity of damper coefficients was not necessary, it was more feasible to yield more of total K's variability by changing K_∞, not K_1 parameters. Still, these K_∞ values do not differ from each other very strictly — the general shape is similar, only the low K_∞ values (i.e., the ones for widely open valves) show big relative differences, but these are not big absolute differences. Also, an unexpectedly flat fragment is present in the characteristics $K_{\infty,\mathrm{r,damp}} = f(x_{\mathrm{r,req}})$ for low damper openings.

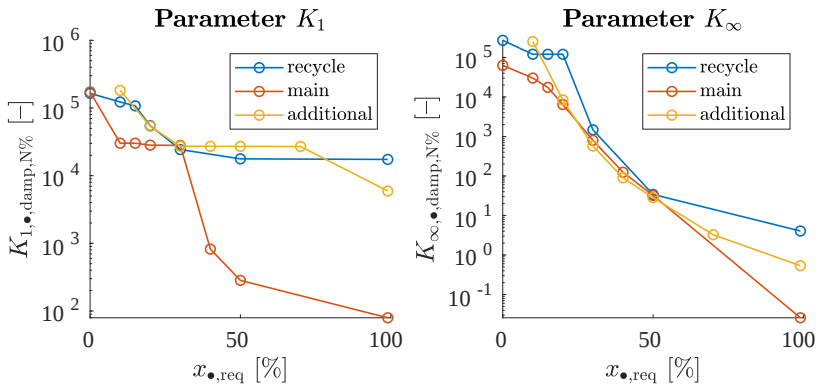

(A) Option a), non-similar damper coefficients

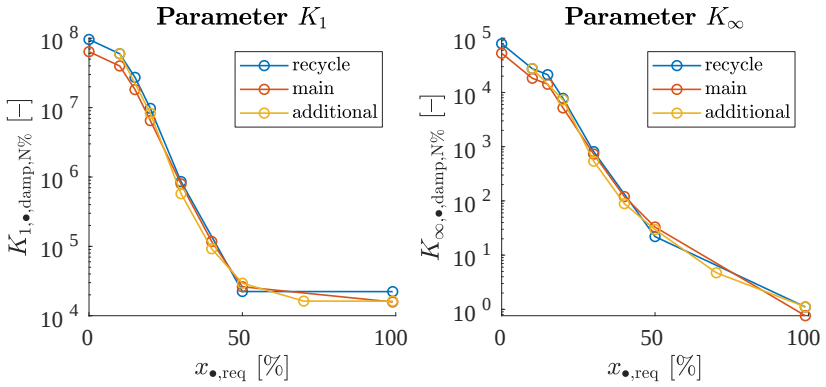

(B) Option a), damper similarity imposed

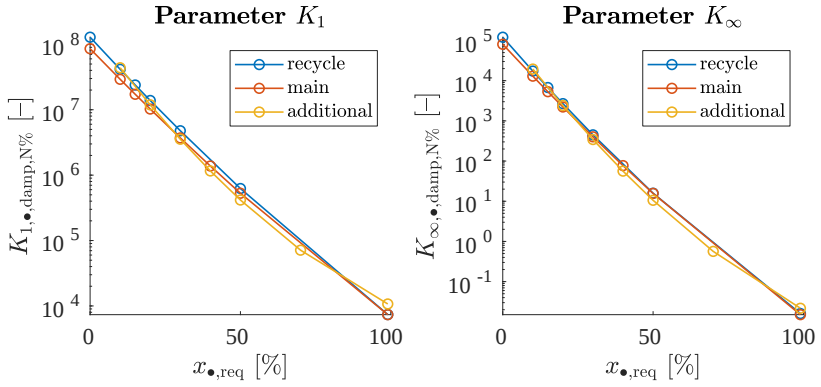

(C) Option b), damper similarity imposed

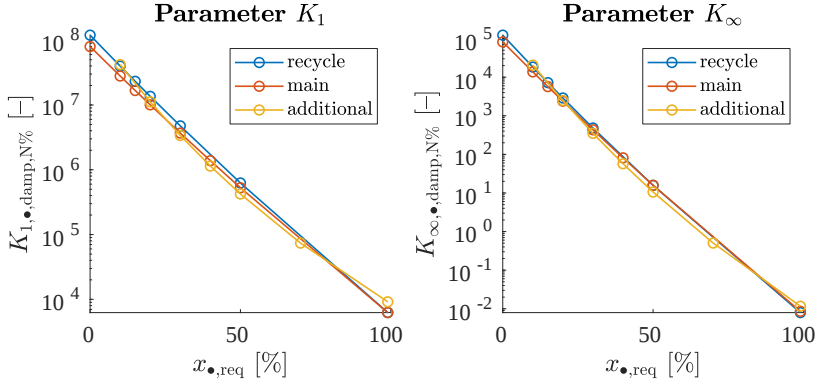

(D) Option c), damper similarity imposed

FIGURE 3.24: Parameters K_1 and K_∞ optimized for the dampers

Figure 3.25 presents the total loss coefficient K calculated from the above two parameters, according to (3.51). The calculation assumed pipe diameter as in the real installation, and several Re values from the range observed in the measurement data.

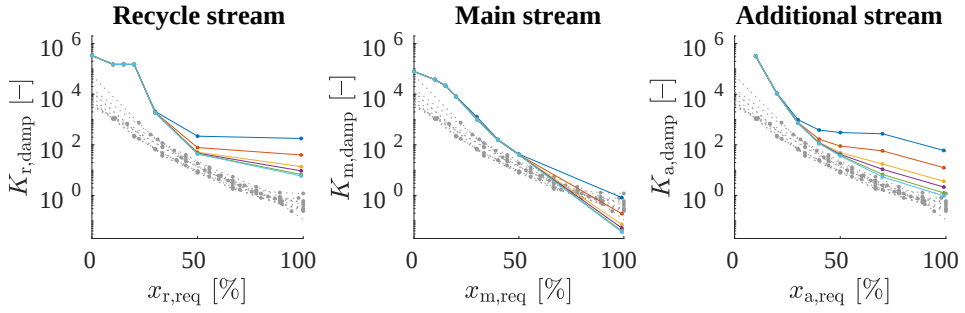

(A) Option a), non-similar damper coefficients

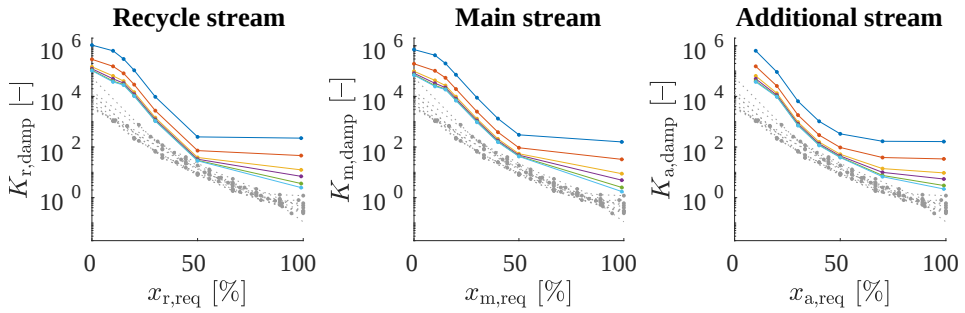

(B) Option a), damper similarity imposed

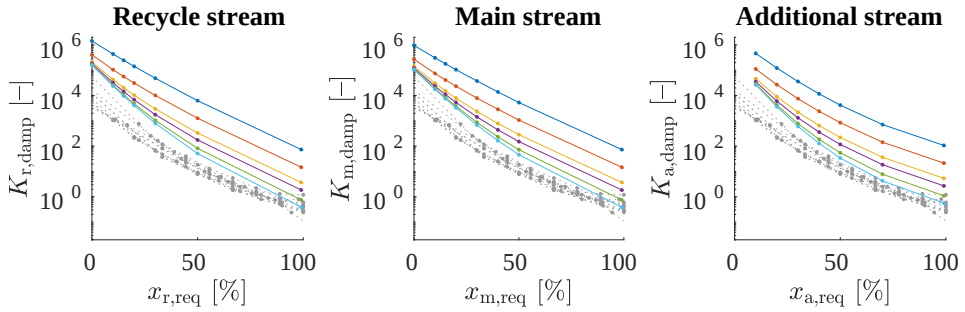

(C) Option b), damper similarity imposed

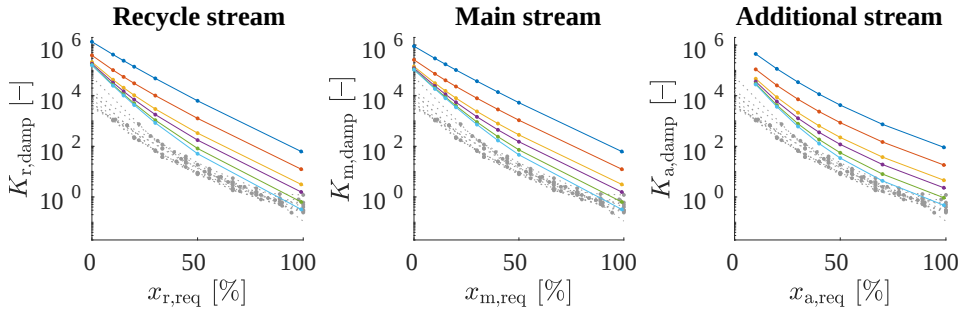

(D) Option c), damper similarity imposed

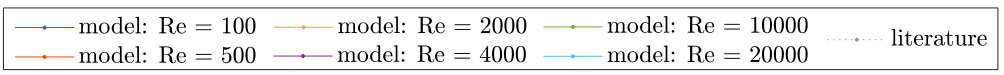

FIGURE 3.25: Total loss coefficients for dampers: output of phenomenological model for several Reynolds numbers Re, compared to literature data for high Re. Lines between data points indicate interpolated data. Sources of literature data: same as in Fig. 3.19.

3.2.4.7 Conclusions

Summarizing, from Fig. 3.21–3.22 it follows that pressure estimations were of particularly bad quality for data points with high measured underpressure. For moderate and low measured underpressures, model outputs fit to them significantly better. One of the reasons for this is probably the accuracy of air velocity measurement: at high underpressures, i.e. for much closed valves, the air flows are small, so relative accuracy of their measurement is not very good. This biases the calculations in the model performed for these data points and affects many of optimized parameters — not only damper loss coefficients for low openings, but also damper coefficients for other valve positions and even loss coefficients for other fittings, because all these parameters are linked by many dependencies.

It is also possible that description of some phenomena is missing in the model structure, and so the fit is not very good. Such hypothesis seems the more plausible that estimated dampers' loss coefficients are much higher than in literature — from several to about ten times higher (see Fig. 3.25). Moreover, there is the case of the functions (3.59) and (3.60): their shapes quite well fit the literature data (Fig. 3.20), but they cannot provide satisfactory fit to the experimental data analysed in this thesis (Fig. 3.21). This is another sign that suggests a missing component in the very structure of the model. Perhaps air leakage in some points of the pipeline should be taken into account, or some other phenomena, yet to be analysed.

In conclusion: the phenomenological model is promising, but it requires some further extension to be properly accurate. Even the best case from the various options tested, i.e. a model with independent loss coefficients for each damper position (option a)), is not accurate enough to be used for plant simulation or for controller design, tuning and validation. Thus, eventually, a black-box model of pressures was used for these purposes — that is, a model of similar structure as the model of air mass flows (see Section 3.2.2). Nevertheless, the current results of phenomenological modelling are interesting and the work is worth continuing.

3.3 Model extension: air flows under the presence of grinding media

As was stated in Section 3.1, the clean-air models may be adjusted to incorporate the effect of material or grinding media, or other factors. Mr Bartosz Kordala, a then-student at the Faculty of Automatic Control, Electronics and Computer Science of the Silesian University of Technology, performed some experiments for his master's thesis [50] that

examined flow of air through the grinding installation, also under the presence of rotating grinding media in the mill chamber. He then shared his experimental results with his supervisors, including dr Szymon Ogonowski. As a result, the latter and the author of this thesis collaborated with other partners on paper [37]. In this research, the task of this thesis' author was to identify incremental static characteristics of air flows in the grinding installation, using measured data from the mentioned master's project.

3.3.1 Identification experiment

Description of the experiment was taken from [50], but it is included here for the sake of completeness of this chapter. The design choices will not be discussed here, as this design was part of the mentioned master's thesis [50]. The author of this dissertation did not take part in planning or performing the experiment; she only processed the available measurement data for her own purposes.

The particular experiment used in the mentioned paper [37] was similar to the one in Section 3.1. The laboratory rig was the same (see Fig. 3.1), but the EM mill was turned on and grinding media (in the standard shape of small rods) were present in the working chamber of the mill. (No raw material was supplied.) Several amounts of grinding media were used: $m_{\text{grind}} = \{500,\ 700,\ 1000\}$ [g]. Also, a few frequencies of supply current to the mill inductor were tested: $f_{\text{EM}} = \{30,\ 50,\ 60\}$ [Hz]. The selected values were typical for such grinding installation and based on previous research, e.g. [78]. Moreover, a "baseline" experiment with no grinding media was performed. This gave a total of $3 \cdot 3 + 1 = 10$ experiment series.

In each such series, successive step changes were applied to the three butterfly dampers. For series with $m_{\text{grind}} = 500$ g or $f_{\text{EM}} = 50$ Hz, many operating points were tested, namely, all combinations of:

$$\begin{aligned} x_{\text{m,req}} &= \{10, 20, 30, 40, 50, 60, 70, 80, 90, 100\}\ [\%]; \\ x_{\text{r,req}} &= \{10, 20, 30, 40, 50, 60, 70, 80, 90, 100\}\ [\%]; \\ x_{\text{a,req}} &= \{10, 30, 50\}\ [\%]. \end{aligned}$$

For the other combinations of m_{grind} and f_{EM}, a smaller subset of damper positions was tested to shorten the — already long — experiment duration:

$$\begin{aligned} x_{\text{m,req}} &= \{10, 30, 90\}\ [\%]; \\ x_{\text{r,req}} &= \{10, 30, 90\}\ [\%]; \\ x_{\text{a,req}} &= \{10, 30, 50\}\ [\%]. \end{aligned}$$

The dampers were repositioned exactly in the order written above: from 10% up, and from the maximum value directly back to 10% (only rising step changes were applied); and main damper was opened the most frequent, then — after its full cycle — recycle damper was moved to the next position and all main damper positions were tested again, and so on. The additional damper was moved the least frequent. Each step response lasted 20 s and then the next step change on the input was applied.

Only steady-state signal values were collected by the author of this experiment. These were air speeds in the horizontal inlet pipes: v_r, v_m, v_a.

3.3.2 Data processing

In the research performed by the author of this dissertation, air speeds were transformed into air flows in inlet pipes: Q_r, Q_m, Q_a, and then into the following quantities:

– flow through the working chamber of the EM mill:

$$Q_\mathrm{w} = c_\mathrm{w,r} \cdot Q_\mathrm{r} + c_\mathrm{w,m} \cdot Q_\mathrm{m} \,, \tag{3.64}$$

– flow through the precise classifier:

$$Q_\mathrm{c} = c_\mathrm{c,r} \cdot Q_\mathrm{r} + c_\mathrm{c,m} \cdot Q_\mathrm{m} + c_\mathrm{c,a} \cdot Q_\mathrm{a} \,, \tag{3.65}$$

where scaling coefficients $c_{\mathrm{w},\bullet} = 1.12$ and $c_{\mathrm{c},\bullet} = 0.2$ followed from specific pipe diameters in the pneumatic system [76]. So, also this model assumed no leakage of false air into the pipeline.

Further, the steady-state values of Q_r, Q_w, Q_c were analysed. These three air flows are critical for operation of the whole grinding circuit, and they are in the scope of upper layer control algorithms [37; 76].

Comparing the different cases of nonzero f_EM and m_grind to the no-grinding case, significant differences in air flows are observed. Some statistics are presented in Table 3.9. Also, Fig. 3.26 illustrates exemplary air flow values. The notable differences in air flows (compared to the no-grinding case) prove the need to update the clean-air static models.

A control scheme was already proposed in [76] that was tuned based on clean air static characteristics. So, the following assumptions were made for the form of the new static models:

TABLE 3.9: Statistic information on the changes in air flow values introduced by the grinding media. Uses relative change $\Delta Q_{rel} = 100\% \cdot (Q_{grind} - Q_{no\ grind}) / Q_{no\ grind}$, where $Q_{grind} = Q_{s,f_{\mathrm{EM}},m_{\mathrm{grind}},x_{\mathrm{r,req}},x_{\mathrm{m,req}},x_{\mathrm{a,req}}}$, $Q_{no\ grind} = Q_{s,0\,\mathrm{Hz},0\,\mathrm{g},x_{\mathrm{r,req}},x_{\mathrm{m,req}},x_{\mathrm{a,req}}}$, air stream $s \in \{\mathrm{r}, \mathrm{w}, \mathrm{c}\}$.

stream s	**min**(ΔQ_{rel})	**max**(ΔQ_{rel})	**mean**$(\lvert\Delta Q_{rel}\rvert)$
r	-86.5%	169.4%	39.6%
w	-75.4%	38.7%	28.9%
c	-65.4%	56.3%	13.3%

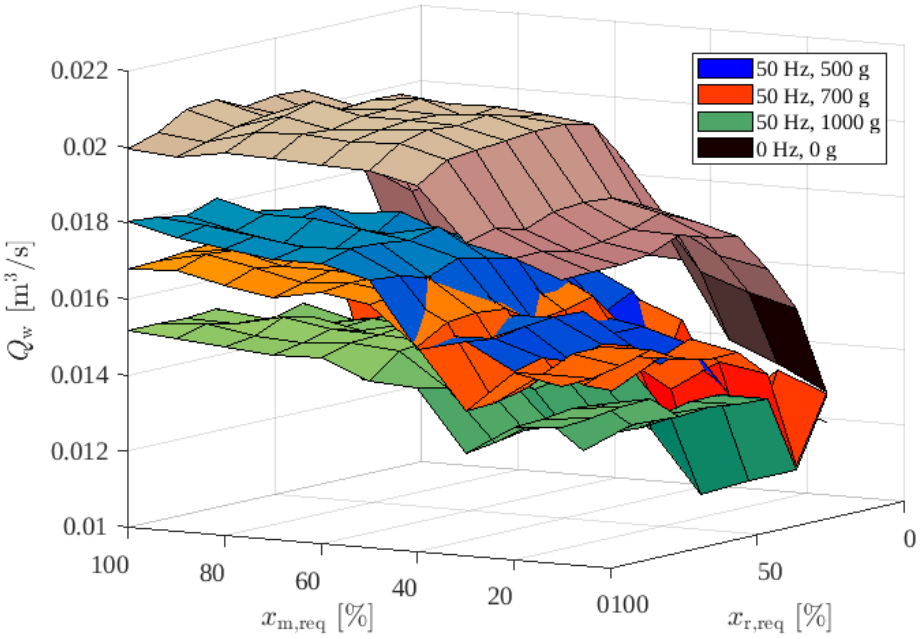

FIGURE 3.26: Air flow through the working chamber of the mill for $x_{\mathrm{a,req}} = 30\%$, at $f_{\mathrm{EM}} = 50$ Hz or none (no grinding)

- their output was incremental (relative to the no-grinding case) — to enable using the new models in compensators that would augment the existing algorithm, such as in [76];
- the models were decomposed with respect to position $x_{\mathrm{a,req}}$— just as with the existing models in the considered control algorithm;
- the models were also decomposed with respect to f_{EM} and m_{grind} values — again, to make them consistent with the existing models (not to introduce new input variables to the models).

Such decomposition provided simpler models and better fit of model outputs to measured data. In the cases when the grinding circuit operates on different values of $x_{\mathrm{a,req}}$, f_{EM}, m_{grind} than the ones tested, interpolation of model outputs (or model coefficients) may be used to find approximate air flow values at these operating points.

In consequence of such assumptions, the final form of the model was:

$$\begin{aligned}\Delta Q_{s,f_{\mathrm{EM}},m_{\mathrm{grind}},x_{\mathrm{r,req}},x_{\mathrm{m,req}},x_{\mathrm{a,req}}} \\ &\stackrel{\mathrm{def}}{=} Q_{s,f_{\mathrm{EM}},m_{\mathrm{grind}},x_{\mathrm{r,req}},x_{\mathrm{m,req}},x_{\mathrm{a,req}}} - Q_{s,0\,\mathrm{Hz},\,0\,\mathrm{g},x_{\mathrm{r,req}},x_{\mathrm{m,req}},x_{\mathrm{a,req}}} \\ &= f\left(x_{\mathrm{r,req}}, x_{\mathrm{m,req}}\right) .\end{aligned} \tag{3.66}$$

Such model was identified for each combination of the other variables: $s \in \{\mathrm{r},\ \mathrm{w},\ \mathrm{c}\}$, $f_{\mathrm{EM}} = \{30,\ 50,\ 60\}$ [Hz], $m_{\mathrm{grind}} = \{500,\ 700,\ 1000\}$ [g], $x_{\mathrm{a,req}} = \{10,\ 30,\ 50\}$ [% open]. Measurement data associated with one such combination (one model) will be called a dataset henceforth.

The specific model structure examined was polynomial approximation:

$$\Delta Q_{s,f_{\mathrm{EM}},m_{\mathrm{grind}},x_{\mathrm{a,req}}}\left(x_{\mathrm{r,req}}, x_{\mathrm{m,req}}\right) = \sum_{i=0}^{N_i}\sum_{j=0}^{N_j} a_{ij} \cdot \left(x_{\mathrm{r,req}}\right)^i \cdot \left(x_{\mathrm{m,req}}\right)^j , \tag{3.67}$$

with: a_{ij} — polynomial coefficients to be estimated; $N_i,\ N_j$ — maximum degrees of input variables. The latter were set to 4, and also only the cross-terms up to degree 4 were used ($i + j \leq 4$). This was to prevent overfitting the model. Consequently, model structure could contain 15 terms (15 a_{ij} coefficients) or less, if some of them were excluded. All possible model versions were estimated, i.e. the full model and all subsets of it, for each dataset. Least squares method was used for parameter estimation.

Before optimizing model coefficients, the signals were scaled — damper positions $x_{\mathrm{r,req}}$, $x_{\mathrm{m,req}}$ by 0.01, and air flow changes ΔQ by 100. So, the exact model used in identification procedure was not (3.67) itself, but a slight modification of it:

$$\widehat{y}^* \stackrel{\mathrm{def}}{=} 100 \cdot \Delta Q_{s,f_{\mathrm{EM}},m_{\mathrm{grind}},x_{\mathrm{a,req}}}\left(x_{\mathrm{r,req}}, x_{\mathrm{m,req}}\right) = \sum_{i=0}^{N_i}\sum_{j=0}^{N_j} a^*_{ij} \cdot \left(\frac{x_{\mathrm{r,req}}}{100}\right)^i \cdot \left(\frac{x_{\mathrm{m,req}}}{100}\right)^j . \tag{3.68}$$

This made all signals be of the same order of magnitude (one), thus providing better numerical properties of the estimation procedure.

Then, least-squares estimation was performed, and adjusted coefficient of determination $\mathrm{R}^2_{\mathrm{adj}}$ was calculated for each model version [99; 116]:

$$\mathrm{R}^2_{\mathrm{adj}} = 1 - \left(1 - \mathrm{R}^2\right)\frac{N-1}{N-n-1} , \tag{3.69}$$

where: N — number of data points in the dataset, n — number of model coefficients (excluding the free coefficient, if used), R^2 — coefficient of determination [106]:

$$\mathrm{R}^2 = 1 - \frac{\sum_{i=1}^{N} (y_i - \widehat{y}_i)^2}{\sum_{i=1}^{N} (y_i - \overline{y})^2} \,. \tag{3.70}$$

The samples of measured output y_i were changes in air flow $\Delta Q_{s,f_{\mathrm{EM}},m_{\mathrm{grind}},x_{\mathrm{a,req}}}$ (from one dataset, as defined before) for all positions $x_{\mathrm{r,req}}$, $x_{\mathrm{m,req}}$. Symbol $\overline{y}$ denotes their mean value, and $\widehat{y}_i$ is model output for the same inputs $x_{\mathrm{r,req}}$, $x_{\mathrm{m,req}}$.

Coefficients of determination $\mathrm{R}^2_{\mathrm{adj}}$ and R^2, when high-valued (close to 1), indicate a good fit of model output to measured data. However, when comparing various structures of models, having different number of parameters n, it is better to use $\mathrm{R}^2_{\mathrm{adj}}$ instead of plain R^2 because the former accounts for the improvement in fit caused simply by larger n.

Finally, for each dataset, all identified model structures were reviewed and the best one was selected, based on the following criteria:

- high value of $\mathrm{R}^2_{\mathrm{adj}}$ (3.69), i.e., good fit;
- low complexity (among model variants having similar values of $\mathrm{R}^2_{\mathrm{adj}}$, the ones with less terms were favoured);
- the same structure for all decomposed models, i.e. for all values of f_{EM}, m_{grind}, $x_{\mathrm{a,req}}$ for one air stream s (needed for compensator design).

3.3.3 Results

As a consequence of the above selection procedure, it turned out that the same structure was the best for all air streams $s \in \{\mathrm{r}, \mathrm{w}, \mathrm{c}\}$. It was the following seven-parameter model:

$$\begin{aligned}\Delta Q_{s,f_{\mathrm{EM}},m_{\mathrm{grind}},x_{\mathrm{a,req}}}(x_{\mathrm{r,req}}, x_{\mathrm{m,req}}) = a_{00} + a_{10} \cdot x_{\mathrm{r,req}} + a_{20} \cdot (x_{\mathrm{r,req}})^2 + \\ + a_{30} \cdot (x_{\mathrm{r,req}})^3 + a_{40} \cdot (x_{\mathrm{r,req}})^4 + a_{01} \cdot x_{\mathrm{m,req}} + a_{02} \cdot (x_{\mathrm{m,req}})^2 \,.\end{aligned} \tag{3.71}$$

Exemplary model output is shown in Fig. 3.27.

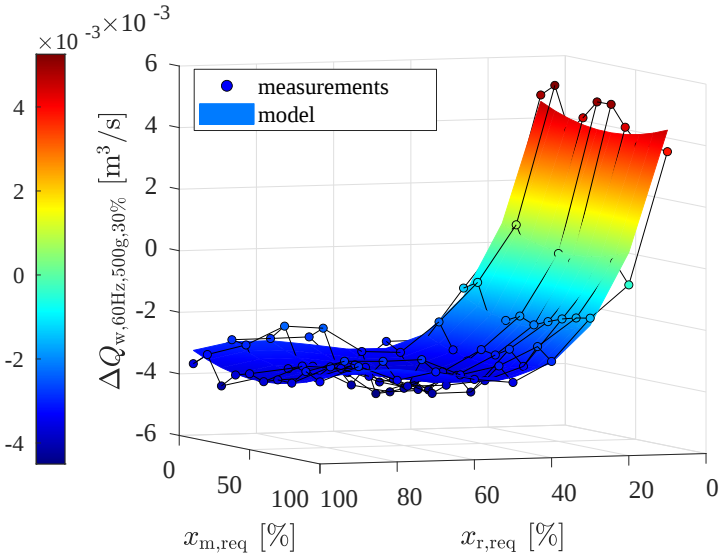

FIGURE 3.27: Model output compared to measured values. Dataset for air flow through the working chamber of the mill, $f_{EM} = 60$ Hz, $m_{grind} = 500$ g, $x_{a,req} = 30\%$.

Chapter 4

Simulation of Air Flows

Static and dynamic models of clean air flow rate and pressure were incorporated into a simulator of the inlet part of the pneumatic system. The simulator was needed to later test the operation of various control algorithms, before the best ones are implemented in hardware.

Simulator structure and results of validation tests were published in [52]. They are also given below, often with more detail than in the paper.

4.1 Simulator development

The simulator of airflow in inlet pipes was built using static characteristics described in Section 3.2.2 and parameters of dynamic models presented in Section 3.2.3. The averaged versions of static characteristics and of model parameters were used, meaning that the simulator did not include hysteretic behaviour of the dampers.

In the simulation, inputs to the plant model were the requested positions of the three air dampers: $x_{\mathrm{r,req}}$, $x_{\mathrm{m,req}}$, $x_{\mathrm{a,req}}$. Outputs were mass flows of air in the three inlet pipes: q_{r}, q_{m}, q_{a}; and if needed, also pressures at the same locations: p_{r}, p_{m}, p_{a}.

The simulator was built in MATLAB Simulink environment. The Simulink block diagram was supported with a MATLAB script that initialized the necessary model parameters, run the simulation and saved the results to a file. Continuous-time blocks, such as integrators, were used to simulate the continuous time domain. The solver was parametrized to use a small fixed-size simulation step $T_{\mathrm{s,plant}} = 1/40$ s, which was 20 times faster than in the control loop (introduced later) and also much faster than the usual values of time constant and time delay of the dynamic models. For example, for air

flow models, median time constant was 1.43 s and median time delay was 2.11 s. Thus, the step size was small enough to treat the simulation time as apparently continuous.

Simulator of air mass flows was built first, as the more important one. Later — for simulation of control schemes that make use of pressure measurements — pressure simulation was added and it followed exactly the same structure. Mass flow and pressure components of the simulation were independent of each other, they only shared the same values of input signals (damper positions).

Structure of simulated models resembled the result of linearization of a nonlinear plant model by Taylor series expansion — the model of each mass flow (or pressure) consisted of a steady-state characteristics plus three dynamic components, each producing the output deviation from steady state in response to deviation from the previous position of one damper. These dynamic models were 1st order systems with delay, as already stated in Section 3.2.3.13. The specific point on the static characteristics as well as parameter values for the dynamic models were selected according to the current operating point of the simulated plant. Namely, all the characteristics and sets of parameter values were stored as 3D matrices with dimensions corresponding to positions of the three dampers. Each such matrix was used as a 3D lookup table indexed with the current positions of all dampers. Note: Time constant T_1 currently used in dynamic model simulation was not directly the one indicated by the current damper positions. Instead, time constant values indicated this way were treated as signal samples, then they were delayed by the current T_0 value, and finally used in the dynamic model.

A schematic diagram of the general idea of such model structure is presented in Fig. 4.1. This structure was repeated six times to calculate mass flows of air q_s and relative pressures p_s in all three horizontal inlet pipes, so, for $s \in \{\mathrm{r}, \mathrm{m}, \mathrm{a}\}$.

The idea is quite simple, but actually, model structure was more complicated. This was because the value from the static characteristics and values of dynamic model parameters were varying with each change in damper positions. Also, there were some limitations due to putting a theoretical concept into a programming language.

Firstly, the usual approach of linearization by Taylor series expansion is that some base steady state is selected, and then deviations from it are approximated with linear dependencies, resulting in estimation of a new steady state. In the simulator, however, the new steady state was immediately turning into the base steady state for a next change in inputs. Moreover, the steady states were not necessarily reached by the signals before new input changes were issued. So, the best solution was to always use this point of the static characteristics that corresponded to the current positions of dampers — not some previous steady state corresponding to some earlier positions. However, this produced

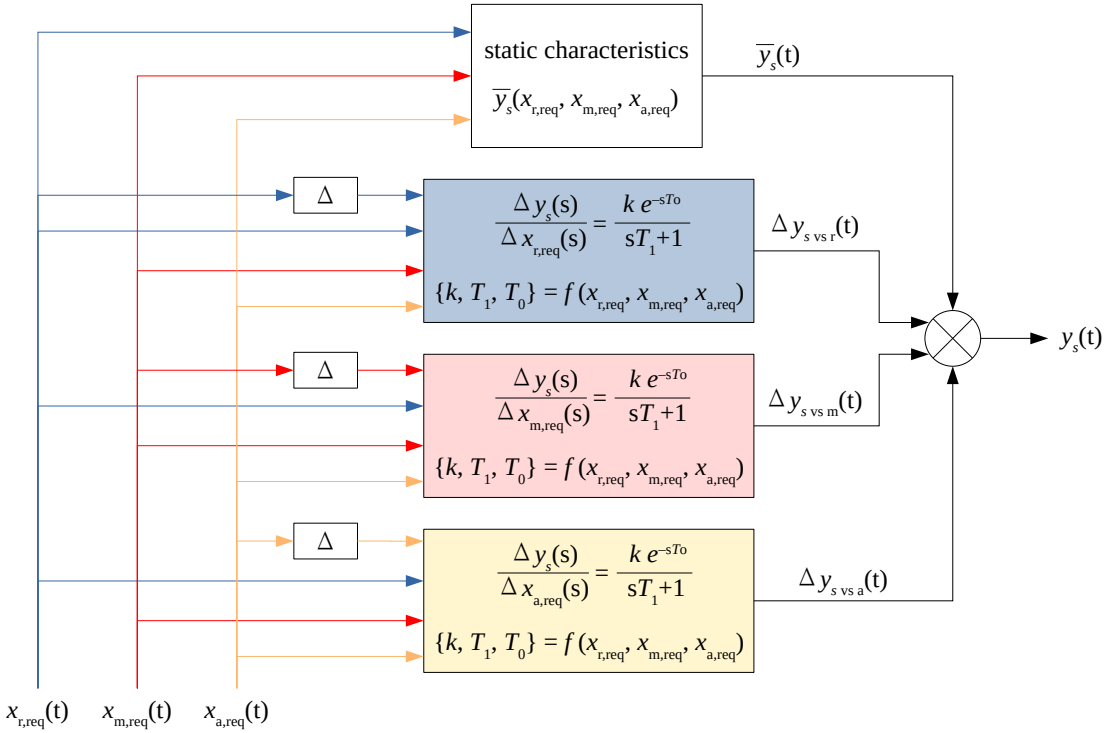

FIGURE 4.1: Schematic diagram of the idea of air flow simulator for a single pipe. Signal y denotes air mass flow q or relative pressure p. Operator Δ means the difference between current and previous signal value; this difference is possible to be calculated because physically, the simulation uses small discrete time steps that only simulate continuous time.

the target (final) steady state at the output of 'static characteristics' block, and not the base steady state. Consequently, the dynamic models of mass flow deviations needed to act a bit counter-intuitively. The dynamic models were not producing some "additive" deviations that should evolve the base steady-state value into a new one; they rather had to create some "subtractive" deviations to slow down the immediate change that happened on the output of 'static characteristics' block. This is schematically plotted in Fig. 4.2.

Note: The graph and the following paragraphs assume changes in input signals in form of step changes. This helped to design the simulator and also made it easier to explain the development process. However, this does not introduce any constraints on the input signals, as each signal shape may be composed of some number of sequential step changes — especially that in the real plant these inputs, i.e. requested positions of dampers, are set by electronic equipment which uses a finite sampling period.

From the graph it follows that after each step change on input, the dynamic model output should contain a single square pulse of length T_0, of amplitude equal to the change in steady state $\overline{y}_s$, but with the opposite sign; and then the signal should settle down (like inertia's impulse response) when the square is switched off. This was achieved by

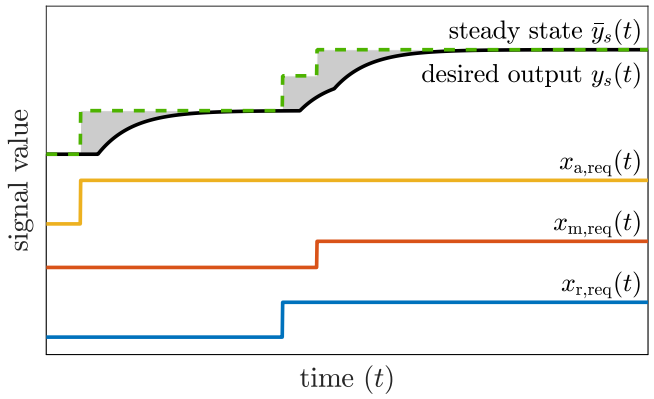

FIGURE 4.2: Schematic graph of signal behaviuor in the plant simulator. Shaded area is the target sum of dynamic models' outputs needed to introduce the desired dynamics into the output signal.

setting unit gains on all dynamic models and exciting them with a processed version of $\Delta\overline{y}_s$ rather than with $\Delta x_{s,\mathrm{req}}$ (because $k \cdot \Delta u = k \cdot \Delta x_{s,\mathrm{req}} = \Delta\overline{y}_s$, and operating in such way guaranteed that the change in 'static characteristics' block output would always be perfectly compensated by dynamic model response).

This mentioned processing of input signal was just generation of proper square pulses. On each change $\Delta\overline{y}_s \neq 0$, a pulse was started with amplitude $-\Delta\overline{y}_s$, and also the current simulation time was registered. Simultaneously, at each simulation step the present simulation time was compared with start times of the square pulses; generation of a pulse was stopped if its duration reached or exceeded the current value of time delay in the plant model. Consequently, the actual excitation signal for the dynamic model was a sum of square pulses shaped by changes in steady-state values and by time delay values in the plant model. A new square pulse for a model was added to the excitation signal only if the change in steady state was caused by repositioning the damper associated with this particular model. In other words, only one dynamic model was additionally excited when one damper was changing position; excitation signals for the other models remained unchanged.

For such scheme to work, additionally, the state variable needed to be reset in the dynamic model. Namely, the state variable of the integrator block was modified with $-\Delta\overline{y}_s$ each time when the dynamic model was to be excited with a new square pulse (so, each time when the damper associated with this model changed its position). As a result, when the new square pulse started on input, the dynamic system acted as if such excitation had already been long present and was only continued. This way, there was achieved the desired sharp edge at the start of the dynamic model response (at its "left side", as visible in Fig. 4.2). Otherwise, the beginning of the response would be a slow-changing transient analogous to the end of the response.

One more modification was needed to account for the situation when multiple dampers (say: N dampers) were re-positioned at the same time instant. If all associated dynamic models reacted, then each of them would produce a response that aimed at initial cancellation of the whole $\Delta\overline{y}_s$, and the total result would be exagerrated: immediately after the step change on inputs, the total deviation from the old steady state would be equal to $(N-1)\cdot(-\Delta\overline{y}_s)$ instead of the desired zero. There were several possible solutions to this problem, for example:

a) Excite only one of the discussed N dynamic models, and leave the other(s) unmodified.

   The excited model could be e.g. the one with the slowest response of all N (at the current operating point). This slowest response could be defined as having maximum $(T_0 + T_1)$ value, or $(T_0 + 3\cdot T_1)$, or similarly. (These values are not arbitrarily chosen, but for 1st order systems with delay, they correspond to times needed to reach 63% and 95% of the final steady state [8] — so, a substantial fraction of the final output value.)

b) Excite only one dynamic model, but with parameters T_0, T_1 that combine in some way the parameters of all discussed N dynamic models at the present operating point.

   The combined values could be e.g. the maximum of the N individual values.

c) Excite all N dynamic models, but with $\frac{1}{N}$ of the usual input signal, i.e. with $\frac{1}{N}\cdot\Delta\overline{y}_s$.

   Contrary to the previous options, this approach would not produce a smooth inertial transient, but a superposition of two or three inertial responses with distinct time constants and time delays.

d) First apply a change in only one damper position, respond with the associated dynamic model. Then, in the same simulation step, apply the change in another damper's position. This would produce another variation of the target steady state, to which the other dynamic model would respond. Finally, repeat for the third damper, if necessary.

   This way, each dynamic model would react only to a part of the overall steady-state change, but these parts would not necessarily be equal, as was in the previous option. This approach may seem somehow natural (in the sense of no "artificial" divisions by N), however, it has some serious drawbacks.

   Firstly, there is no single proper order of re-positioning the dampers; and different orders would result in different magnitudes of the partial changes in steady state, so eventually, these would yield different transients. So, there is no way to scientifically support any selection of the order in which the dampers change positions.

Secondly — and more importantly — such partial changes in target steady-state value could have different signs, i.e., some might be increasing and some decreasing. With distinct, unrelated temporal parameters of all dynamic models, this would easily lead to situations where a fast rising inertial output is then mitigated by a slower inertia aiming at a lower final steady state (or vice versa). Such spikes or ripples in the resulting superposition of inertial responses were definitely not observed in the measurement data, which finally rendered the presented approach unacceptable.

Still, the first three methods were reasonable. Theoretically, it could be debated which of them would be the closest to reality; but practically, the differences in output signals produced with these methods would be so small that any of these designs could be used. Thus, the third one was chosen, simply because it was definitely the easiest to implement in the existing structure of the Simulink diagram.

The final block diagram of a single dynamic model, as built in Simulink, is shown in Fig. 4.3. It may seem complicated, but again, this complexity was only caused by some limitations when implementing the model as a program in a specific environment. The general idea behind this implementation remains as simple as was shown in Fig. 4.1.

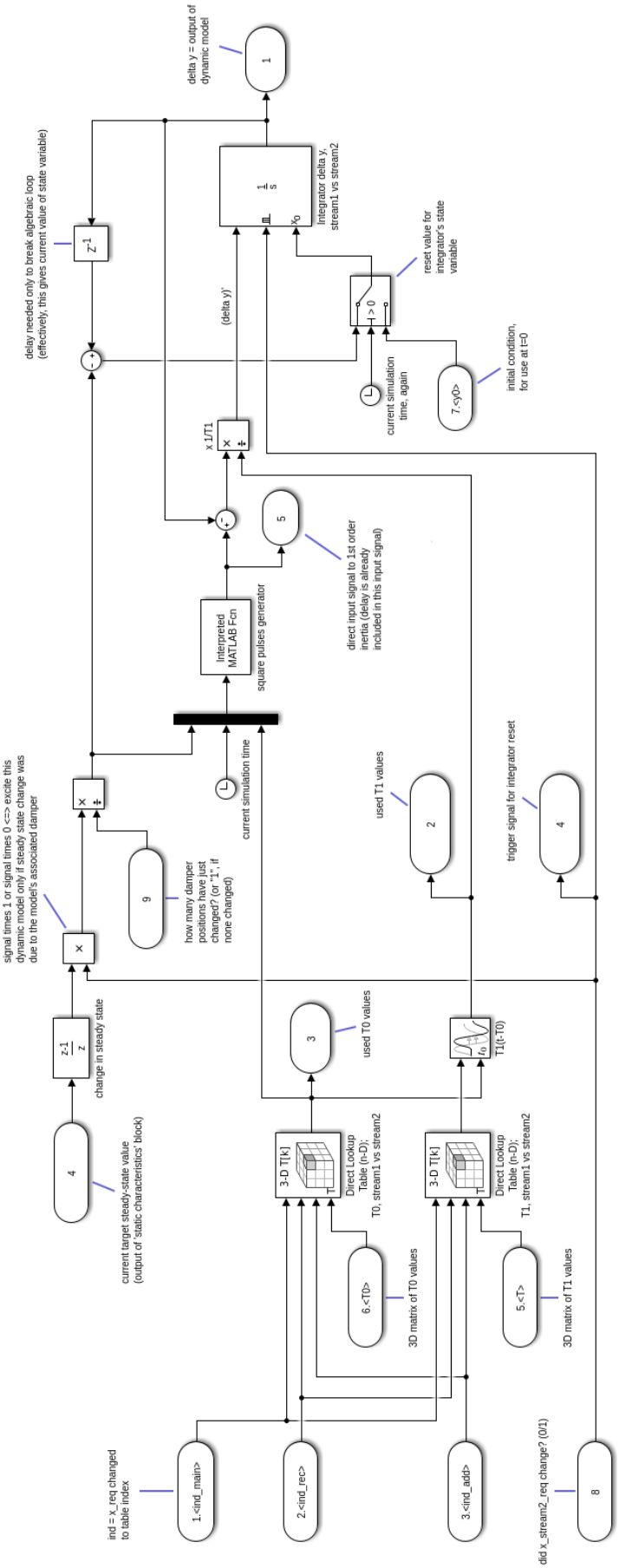

FIGURE 4.3: Screenshot of Simulink block diagram for a single dynamic model in air flows simulator

4.2 Verification and validation

Multiple tests were conducted to check if the simulator worked as intended. Some tests verified if the assumed structure of plant model was correctly implemented, and others validated simulator outputs versus data measured at the plant.

4.2.1 Test 1: one damper moving at a time, with waiting for steady states

The first test simulation was simple: the excitation signals (damper positions) were set to several values, chosen arbitrarily. Only one damper was moved at a time, and model outputs were let to settle down before another step change happened on some input. The resulting mass flows of air are presented in Fig. 4.4.

The plots on the left show the total mass flows. The air flows indeed react to step changes on any damper's position. The transients are shaped according to the right model type (1st order inertia with delay), and their parameters change when the system is moved to another operating point. The air flows reach their expected steady state values, as marked in the plots by static characteristics $\overline{q}_s$.

The plots on the right detail the four components of each air flow: the steady-state value and three deviations from it, caused by three dampers moving. Each deviation signal $\Delta q_{\bullet \text{ vs } s}$ correctly reacts only to repositioning of one appropriate damper s. A step change in damper position $x_{s,\text{req}}$ causes an immediate step change $\Delta\overline{q}_s$ in steady-state value and a dynamic response of $\Delta q_{\bullet \text{ vs } s}$. This transient has an instant rise or fall at the beginning, reaching the value of $-\Delta\overline{q}_s$; then, with varying delay and time constant, it settles back to zero, so that the total flow rate q_s achieves the full steady-state value $\overline{q}_s$. So far, all these observations confirm correct behaviour of the simulated model.

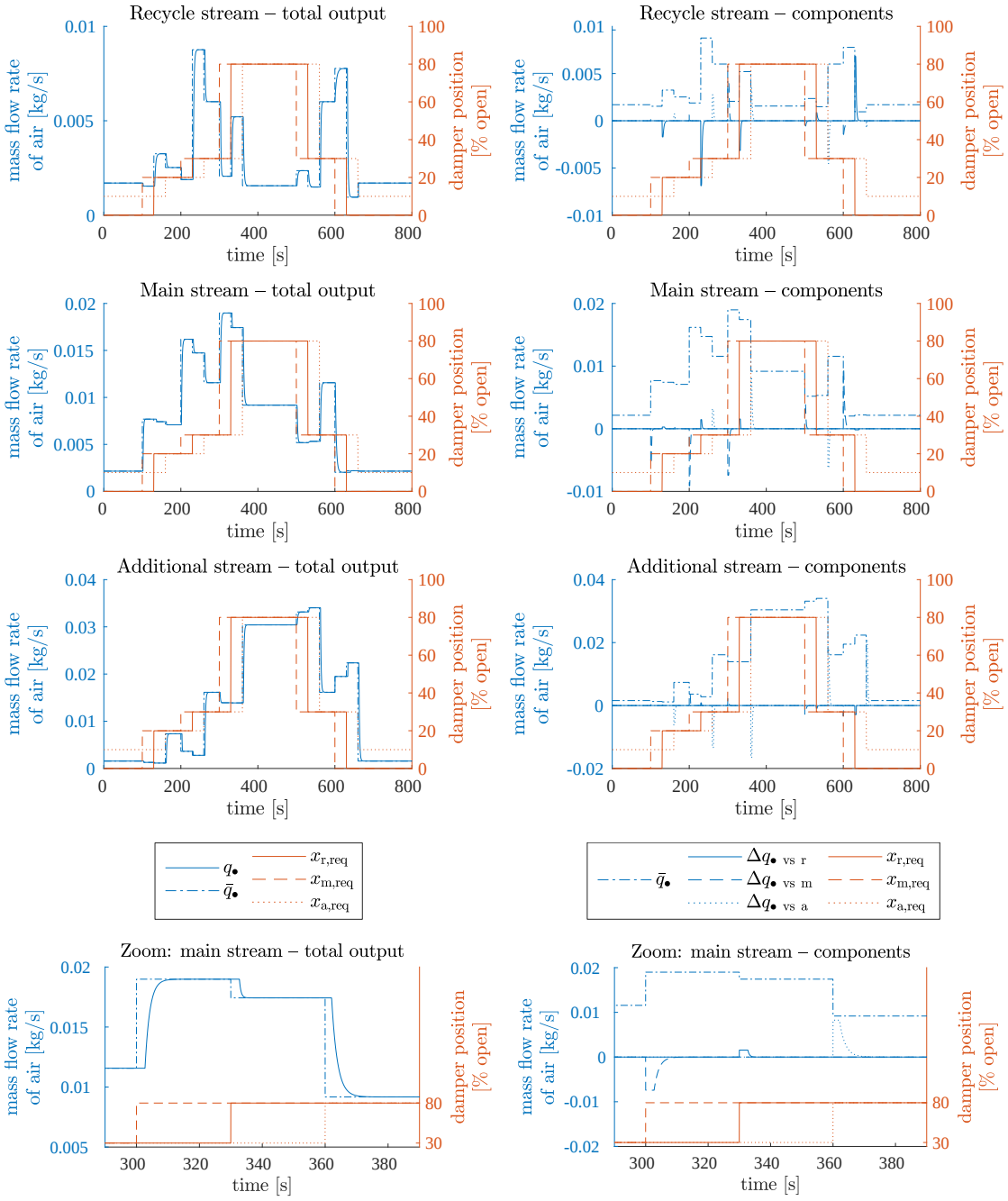

FIGURE 4.4: Simulator output in test 1: mass flows of air (in blue) for plant model excited with arbitrary step inputs (in red). Three top rows show the entire simulation time, the bottom row shows only a fragment.

Bottom row's source [52]: Krauze O. Model and simulator of inlet air flow in grinding installation with electromagnetic mill. *Scientific Reports* **2023**, 13, 8281. https://doi.org/10.1038/s41598-023-34664-0, Fig. 4.

4.2.2 Test 2: multiple dampers moving at once, with waiting for steady states

Next verification test used a scenario where multiple dampers changed positions simultaneously. At the beginning — at simulation times $t = \{25, 50, 75\}$ [s] — each possible pair of dampers was moved at once. Later (at $t = 100$ s), all three dampers were repositioned at the same moment. To simplify the analysis of results, again, the intervals between the successive excitations were long enough for the output signals to settle down.

Exemplary results — the ones for the recycle air stream — are shown in Fig. 4.5. Signal values were correct: deviations $\Delta q_{\mathrm{r\ vs\ }s}$ responded to their associated inputs $x_{s,\mathrm{req}}$, the transients were properly shaped and the total output air flow q_{r} achieved the right steady-state values.

4.2.3 Test 3: without waiting for steady states

This scenario checked simulator operation when new excitations appeared fast, still during the transient phase produced by some recent excitation. The test included several stages:

- at simulation time $t = [0; 55)$ s: a step change in position of damper $s1$, then 3 s interval, then a step change in position of another damper $s2 \neq s1$, finally a longer break — repeated several times for different pairs of $s1$, $s2$;
- at $t = [55; 80)$ s: step changes in positions of all three dampers, one after another, separated by 3 s intervals;
- at $t = [80; 125)$ s: a step change in position $x_{s,\mathrm{req}}$, then 3 s break, then another step change in the same damper's position, then a longer break; repeated for each damper $s \in \{\mathrm{r}, \mathrm{m}, \mathrm{a}\}$;
- at $t = [125; 150]$ s: step changes issued simultaneously on all three dampers' positions; then 1–3 s interval; repeated several times for different positions.

In between these stages and at the very end, no new excitations were issued for longer periods, in order to observe if the output signals reached correct steady states after each part of the test.

Simulation results are presented in Fig. 4.6 — for the recycle stream only, as an example. The simulated signals had appropriately shaped transients and correct steady-state values. This confirmed proper implementation of switching the dynamic models between

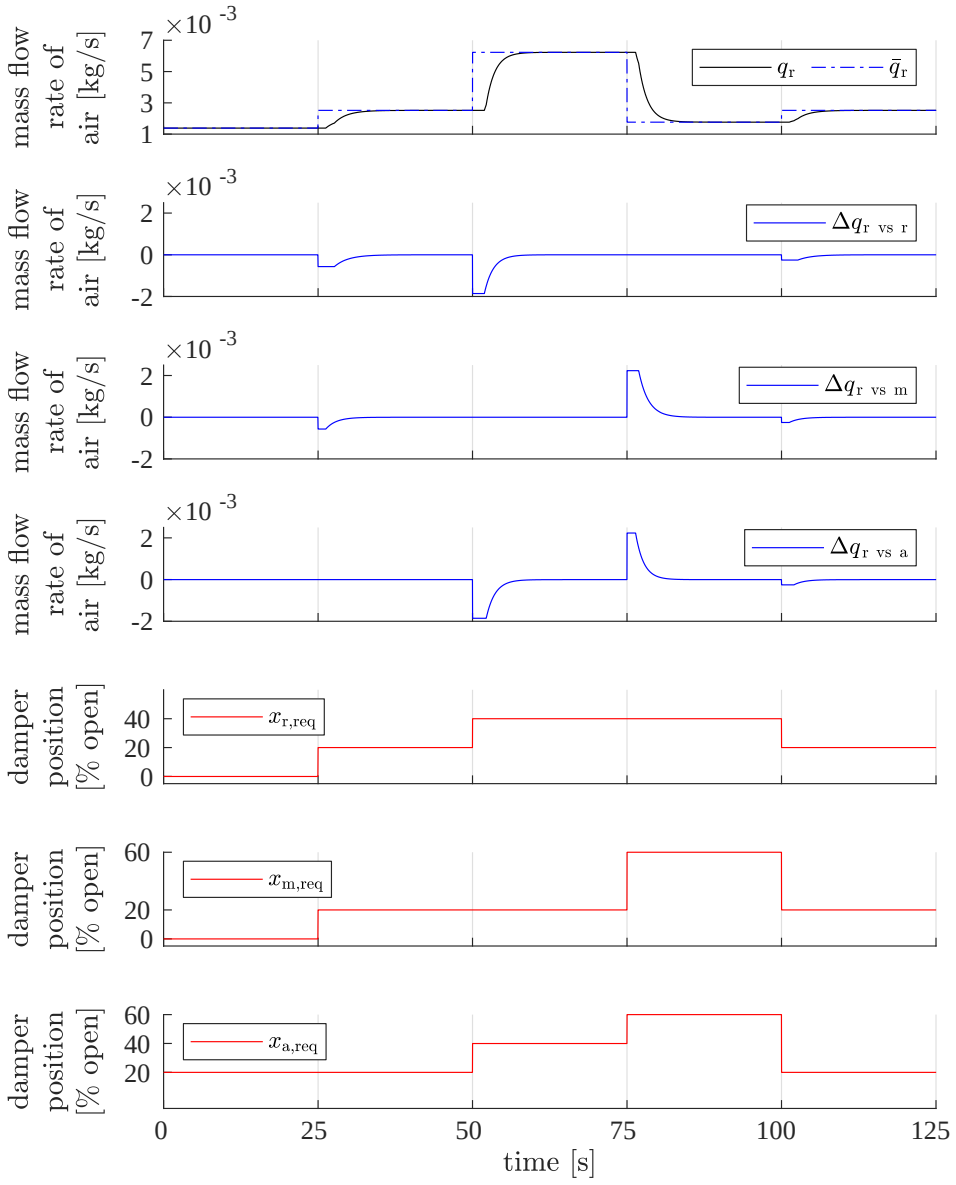

FIGURE 4.5: Simulator output in test 2: recycle air mass flow in response to simultaneous step changes on multiple inputs.
Source [52]: Krauze O. Model and simulator of inlet air flow in grinding installation with electromagnetic mill. *Scientific Reports* **2023**, 13, 8281. https://doi.org/10.1038/s41598-023-34664-0, Fig. 5.
Re-used under Creative Commons Attribution (CC BY) license (https://creativecommons.org/licenses/by/4.0/).

various steady states: generation of square pulses, resetting state variables (accumulators) in integrators, etc. The simulated model operated well even if its outputs did not have enough time to settle down; this proved that the model was able to respond to any shape of excitation signal, not only to single step changes.

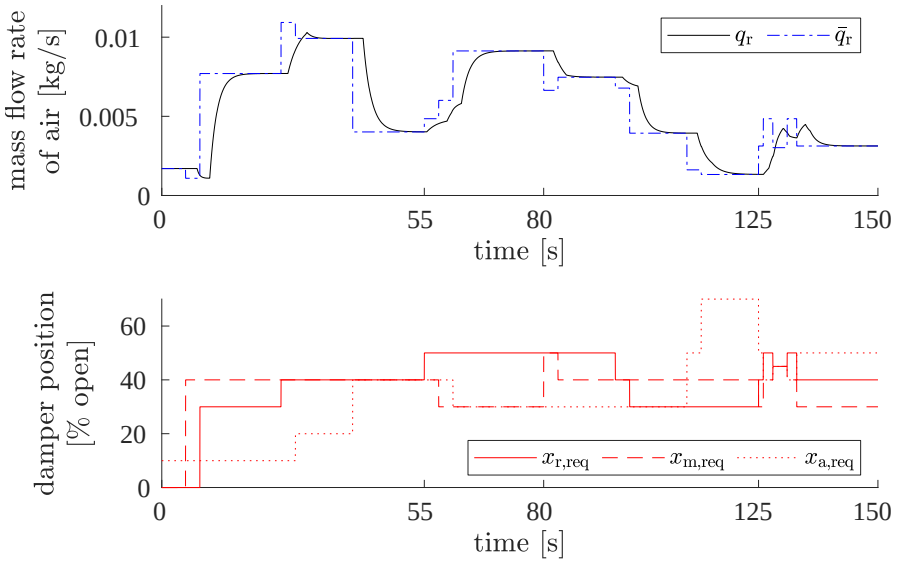

FIGURE 4.6: Simulator output in test 3: air mass flow in recycle stream (top panel) for plant model excited with frequent step changes (bottom panel).
Source [52]: Krauze O. Model and simulator of inlet air flow in grinding installation with electromagnetic mill. *Scientific Reports* **2023**, 13, 8281. https://doi.org/10.1038/s41598-023-34664-0, Fig. 6.
Re-used under Creative Commons Attribution (CC BY) license (https://creativecommons.org/licenses/by/4.0/).

4.2.4 Test 4: validation using data from identification experiment

The above tests verified that simulator structure was implemented as planned. Afterwards, some validation tests were run, which checked similarity between values of simulated and measured (experimental) signals. These tests checked the correctness of simulator implementation, but also of measurement data processing (Section 3.2).

The input signals to the real plant that were previously used in the identification experiment were now fed to the model. The resultant simulator output was compared to the measurements from the experiment. The comparison is plotted in Fig. 4.7–4.8. The former contains a smaller fragment of the output signals, magnified to examine the transients. The latter shows the whole experiment series no. 3 (the other two series are not plotted, but were tested as well). This figure provides an overview on matching between the steady states from simulation and from the experiment.

From Fig. 4.7–4.8 and from the other (not plotted) results it follows that the simulator works well. The transients — their delays, rates of change, shapes — are well reflected. Also, the simulated and measured steady-state values are alike, the discrepancies between them are generally small. Only for the recycle air there are several operating points where experiment and simulation differ much. These differences in steady states come from the fact that the model uses static characteristics which was averaged over all data series (see

Section 3.2.2), and the individual results from these series vary. These variations may be examined in more detail in Fig. 4.9. In each chart, one colored rectangle represents a steady state from one operating point of the installation, with the specific steady-state value indicated by the color. The rectangles form vertical lines, and the lines constitute groups; the first six lines in each group show experimental data from the six datasets (see Section 3.2.2.4), and the rightmost (seventh) vertical line illustrates the averaged smoothed static characteristics, which was made of them and used in the simulator (see Section 3.2.2.8). Looking along the horizontal dimension within one group, the colors are not always identical. This means the steady-state values sometimes varied between datasets, and were also different from the averaged static characteristics. Thus, in simulation results such as in Fig. 4.7–4.8, steady states of simulated signals were not always in perfect accordance with measured data, coming from a single specific dataset.

4.2.5 Conclusions

The above tests proved that the simulator provides good quality data — both dynamic and steady-state. Thus, it may be used for prototyping control algorithms for the air flows in grinding installation, which is indeed done in Chapter 5.

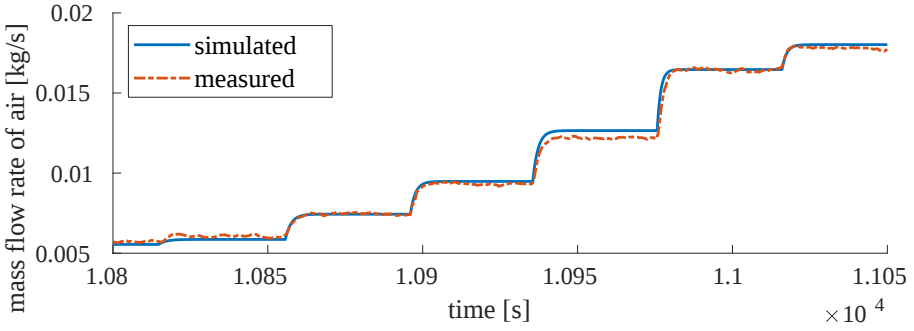

FIGURE 4.7: Result of test 4: mass flow rate of air in the main stream, simulation and experimental data compared. A short fragment illustrating the transients.
Source [52]: Krauze O. Model and simulator of inlet air flow in grinding installation with electromagnetic mill. *Scientific Reports* **2023**, 13, 8281. https://doi.org/10.1038/s41598-023-34664-0, Fig. 8.
Re-used under Creative Commons Attribution (CC BY) license (https://creativecommons.org/licenses/by/4.0/).

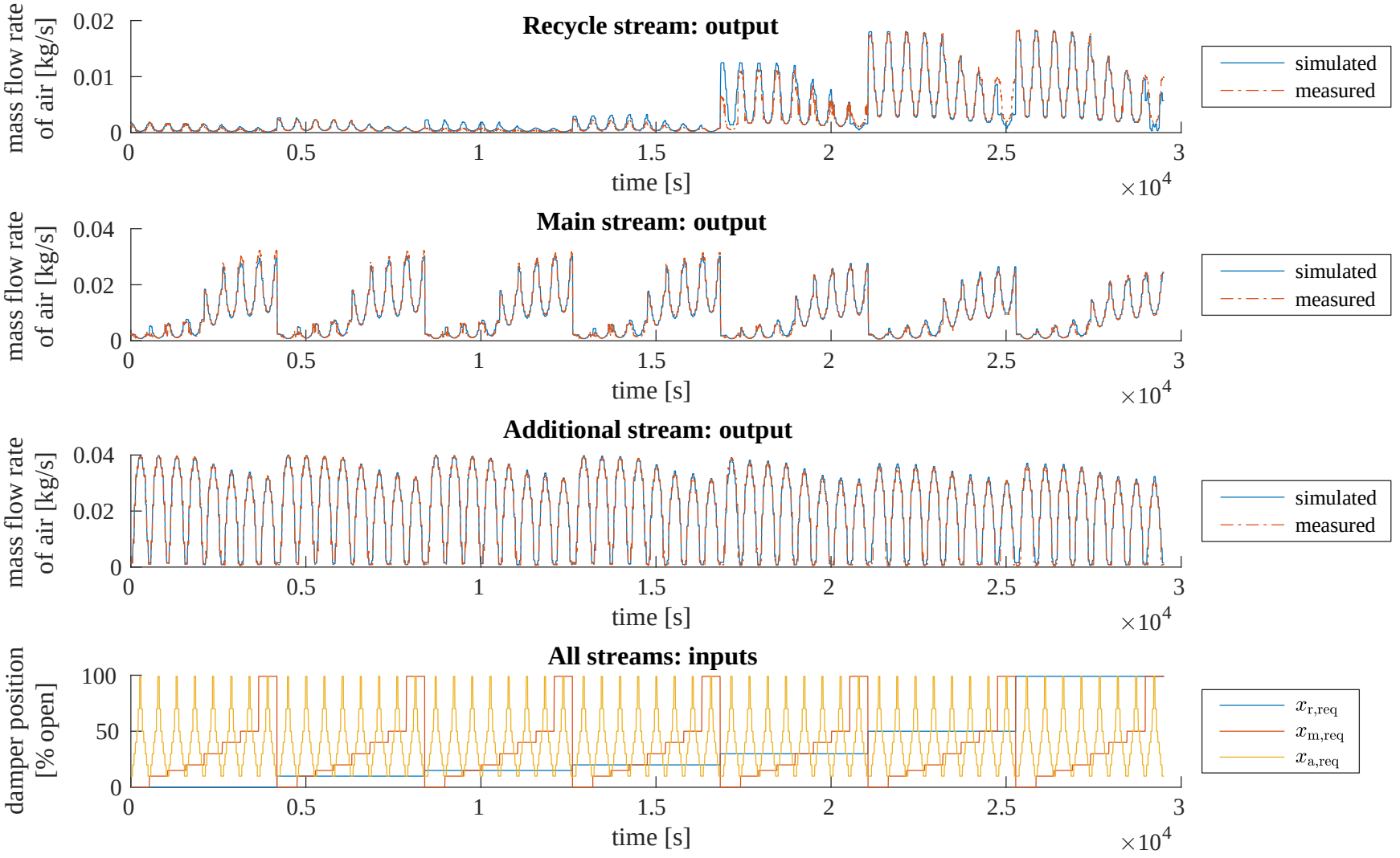

FIGURE 4.8: Result of test 4: mass flow rate of air in all streams, simulation and experimental data compared. A long fragment illustrating the steady states in a whole experiment series.

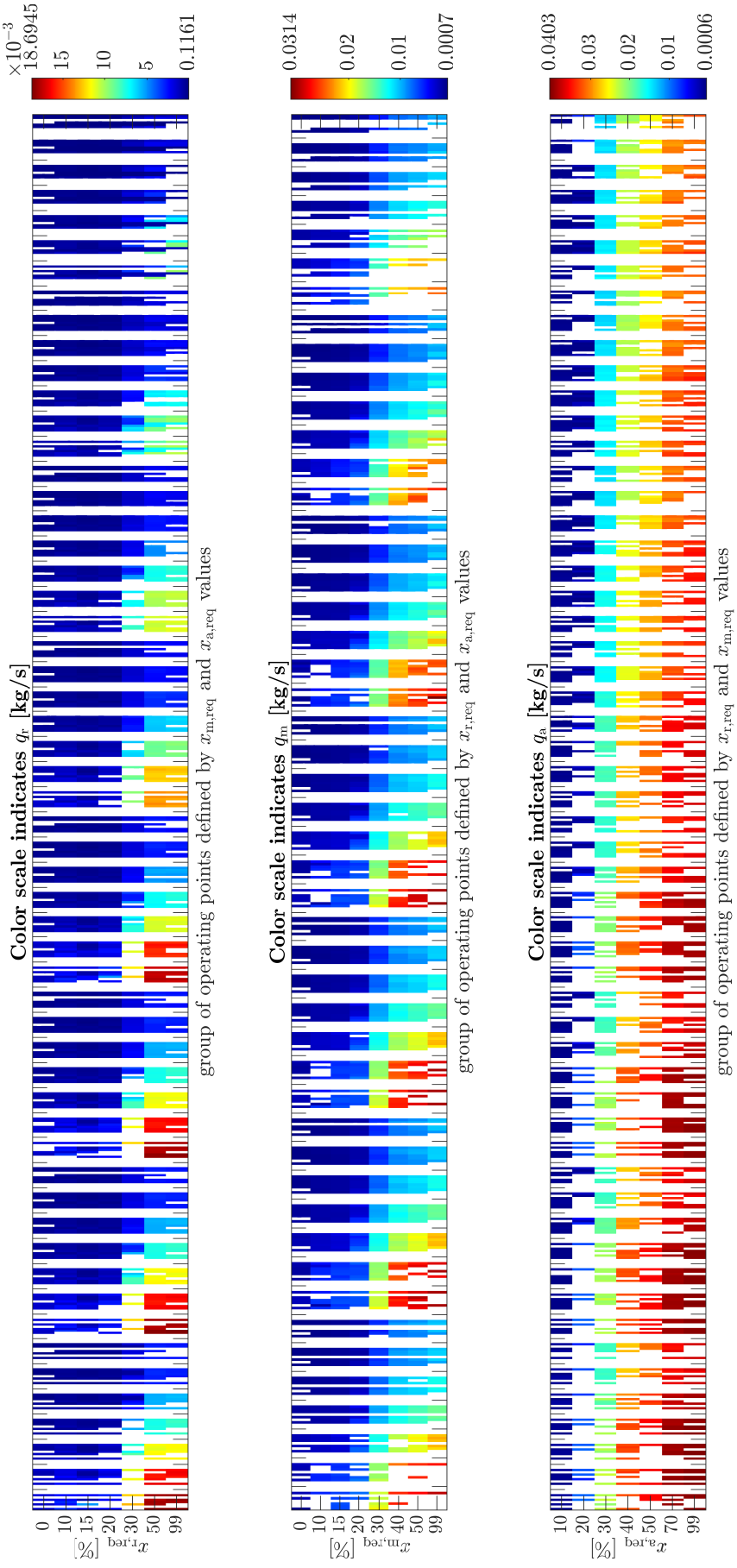

FIGURE 4.9: Steady states of air mass flow rates compared between datasets. In one chart, n-th vertical lines in all line groups illustrate the same dataset. The first six datasets are experimental data, the last (rightmost) dataset is the final combined static characteristics. Empty (white) rectangles indicate missing data points in the experimental datasets, due to excessive turbulences in air flows or possibly outlying measurements.

Chapter 5

Control of Air Flow

5.1 Hierarchical control system of the grinding installation

The grinding circuit is a multiple-input, multiple-output plant. Moreover, the input signals change in much varying time horizons — for example, type of raw material should remain constant for long periods of time, but air flow through different parts of the installation would probably change with much higher rates. This means the control system for the whole plant needs to be a hierarchical one, where each higher layer is responsible for processes (or disturbances) with longer time constants [37; 77–79; 111]. A general structure of a layered control system is sketched in Fig. 5.1.

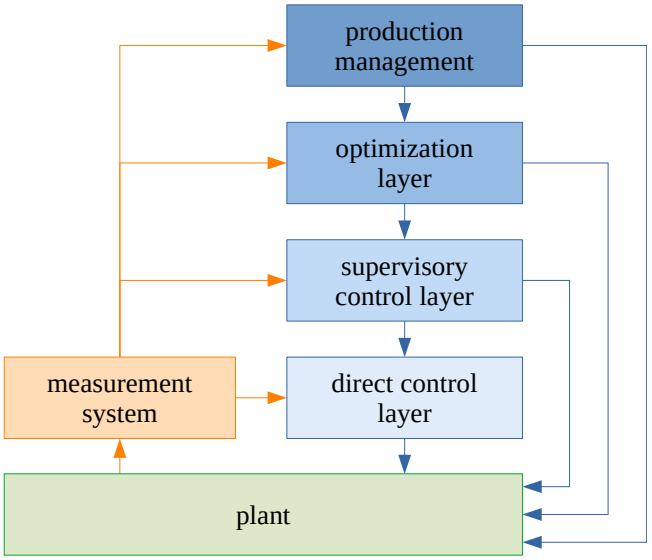

FIGURE 5.1: Structure of a general hierarchical control system. Based on [111, Fig. 7].

In the case of dry grinding installation with electromagnetic mill, the top layer (production management) is responsible for setting e.g. the target throughput (production

rate); desired features of the product, such as particle size (mainly), or additionally particle shape, moisture content, or other physicochemical properties, as needed; average time of grinding; mass and type (shape, material) of the grinding media [77]. Production rate is assumed the leading variable for the lower layers. This means it has a key impact on the functional structure of control loops in these layers [37; 78].

Optimization layer, thoroughly discussed in [78], aims at minimizing energy consumption of the grinding circuit, while keeping the setpoint production rate and final product quality. Energetic efficiency is achieved mainly by controlling the output and base frequencies of the inverter that supplies the EM mill inductor. These inverter frequencies and mass of grinding media are the most important factors affecting the energy consumption of the mill [37; 78]. Moreover, heat recovery system is controlled from the optimization layer [77]. It determines the optimal mix of fresh air and the heated air at the output of fans cooling the EM mill.

Supervisory layer mainly provides setpoint values for the lower layer control loops, taking into account e.g. the cross-couplings between them. This makes the direct controllers simpler and more efficient [77].

Direct control layer in the grinding installation comprises many subsystems. Some examples are the control of [78; 111]:

- air flows in the working chamber of the mill, in the precise classifier and in the recycle stream,
- fill level of the working chamber (amount of material in the working chamber),
- moisture content of the raw material in the mill chamber,
- grinding media amount in the mill.

These control loops mostly serve for disturbance attenuation.

5.2 Air flows control in the grinding installation

For the technology of dry grinding referenced in this thesis, three air flows are of particular importance. These are [37; 76]:

- Air flow through the working chamber of the EM mill (q_w or Q_w). High enough value is necessary to keep the raw material particles suspended in the working area of the grinding media; otherwise, the material would fall onto the mill bottom. On the other hand, too big air flow would blow the particles out of the mill chamber before they are properly ground. This would cause excessive recycle stream generated in the precise classifier. This in turn would result in forced decrease of

fresh feed throughput and deteriorated energetic efficiency of the grinding process. Summarizing, this flow rate is the key factor influencing material residence time in the mill chamber.

– Air flow through the precise classifier (q_c or Q_c). For proper operation of the classifier, higher air flow is needed here than in the mill chamber, so an additional air stream is let into the classifier chamber [112]. The specific value of this air flow affects the classification process — e.g., sharpness of the partition curve and the so-called d_{50} particle size, which describes the diameter of particles that are directed equally often into the coarse and fine product streams [112].

– Air flow in the recycle stream (q_r or Q_r). This air flow carries the recycle material (coarse product of classification) back to the mill chamber, for re-grinding. The requirements for this flow rate are less strict than for the other two, as the recycle air flow just should not fall below a minimum that is capable of transporting the particles of the processed material, but it is not necessary to maintain a single specific value.

Apart from the recycle air flow, these flow rates cannot be measured directly due to technical limitations [76]. The mill and classifier chambers are filled with the processed material (the air is not clean), which is a serious problem for the potential measurement equipment, especially for its durability. Moreover, even if such air flow (or air speed) transducers were mounted in the installation, their readings would be of quite low accuracy — because of the air borne particles possibly affecting the measurements, and also due to lack of required run-in and run-out distances to nearest air flow obstacles. So, rather than being measured, the mill chamber and classifier air flows need to be estimated (modelled) using the available clean air measurements: in the recycle, main and additional inlet air streams (see Fig. 3.1).

Assuming no false air leakage into the pipeline, the above-mentioned flow rates (in steady state) may be estimated in the following way:

- flow through the working chamber of the mill:

$$Q_w = c_{w,r} \cdot Q_r + c_{w,m} \cdot Q_m \,, \tag{5.1}$$

$$q_w = q_r + q_m \,; \tag{5.2}$$

- flow through the precise classifier:

$$Q_c = c_{c,r} \cdot Q_r + c_{c,m} \cdot Q_m + c_{c,a} \cdot Q_a \,, \tag{5.3}$$

$$q_c = q_r + q_m + q_a \,. \tag{5.4}$$

The constants $c_{\bullet,\bullet}$ follow from geometric relationships between pipe diameters in the pneumatic system. Of course, as was already discussed in Chapter 3, it holds that $Q_s = f(x_{\mathrm{r,req}},\ x_{\mathrm{m,req}},\ x_{\mathrm{a,req}})$ and $q_s = f(x_{\mathrm{r,req}},\ x_{\mathrm{m,req}},\ x_{\mathrm{a,req}})$ for $s \in \{\mathrm{r, m, a}\}$.

These simple models may be improved by taking into account the leakage of false air, which is observed in the physical installation. This leakage might be estimated using e.g. pressure readings in the inlet pipes and total air flow measured near the exhaust in the installation. However, this is out of the scope of this dissertation and may be a subject of future works. For the sake of the following considerations, it is enough to assume that there exists an upper layer model, (5.1)–(5.4) or other, of structure $Q_s = f(Q_{\mathrm{r}},\ Q_{\mathrm{m}},\ Q_{\mathrm{a}})$ or $q_s = f(q_{\mathrm{r}},\ q_{\mathrm{m}},\ q_{\mathrm{a}})$ for $s \in \{\mathrm{r, w, c}\}$. So, the requirements for the technologically critical flows $s \in \{\mathrm{r, w, c}\}$ may be transformed (in the mentioned upper layer algorithm) into equivalent setpoints for physically measured flows $s \in \{\mathrm{r, m, a}\}$ in the inlet pipes. (Anyway, all flow rate setpoints are achieved in the same way, that is, by simultaneous manipulation of three air valves' positions: $x_{\mathrm{r,req}}$, $x_{\mathrm{m,req}}$, $x_{\mathrm{a,req}}$.) This way, many direct control schemes may be tested and evaluated, independent of the specific upper layer model of flows through the mill and classifier. Some of these direct control algorithms are described in the following sections of this chapter.

The design, tuning and testing of control algorithms was done in simulation, using Simulink block diagrams and accompanying MATLAB scripts. The plant simulator from Chapter 4 was used, and it was extended with the considered control loops. Compared to on-site tests, such simulation-based approach requires much less time, effort and costs. It is also safer to the installation, as many bugs or erroneous parameter settings may be spotted and elliminated even before the algorithms are run on the real plant. In the future work, selected (best) control schemes may be implemented in hardware in the grinding installation and then subjected to the final tests and corrections.

Note: for simplicity, the direct layer algorithms were treated here as standalone control systems, with setpoint values supplied manually. When these algorithms are plugged into the full layered control system, their structure may require some modifications, or fine-tuning of controller gains may be required. Still, with such standalone testing, it was possible to capture the strengths and weaknesses of the tested algorithms, and to check what was the best possible performance of these control system structures. This way, the acceptable control schemes could be indicated (the ones performing with the desired quality).

5.3 Test scenario

Plant model was simulated in quasi-continuous time, i.e., with very small simulation steps of 1/40 s. It was the same as with the open-loop simulation (Section 4.1). Control algorithms operated in discrete time. Control period was programmable; value of 0.5 s was used to mimic the current setting in the control system of the grinding installation, but other values may also be tested easily. Between the controller outputs and plant model inputs, zero-order hold (ZOH) blocks were used to imitate the hardware operation in the real installation.

The scenario for testing controller performance was, of course, identical for all control algorithms under research. It involved successive step changes on setpoints for all three air flows, mostly on one setpoint value at a time, as this is already a disturbance to the other air flows and so, is an interesting case to examine. The specific setpoint values were picked from among the results of open-loop plant simulation, so they were physically reachable. This was to assess the actual capabilities of the tested control algorithms, without biasing the quality measures with forced errors due to unrealizable setpoints. Several setpoint flow rates were selected for each stream, related to both small and wide damper openings; the differences between the openings (the step changes) were of both positive and negative sign, and of small or big amplitude. The step change was selected as it is a classical signal type for such tests. It is the most abrupt chang possible, so if the control algorithm can handle it satisfactorily, then it will also perform well for smoother changes.

This was not an exhaustive, comprehensive test scenario showing closed-loop system performance in its whole operating range. Such tests would be quite cumbersome and they need to be the subject of a separate study. Instead, this was aimed as a rather simple scenario, still: showing a variety of operating points, but not testing all possibilities.

5.3.1 Scenario 1 – ideal plant model

In the basic test scenario, parameters used for plant model simulation and for controller tuning were exactly the same. This allowed to create controllers of each tested type that were tuned as good as possible. Their performance indicated a supremum that for sure could not be surpassed in a real-world situation. The parameters used here were obtained as described in Sections 3.2.2–3.2.3.

5.3.2 Scenario 2 – non-ideal plant model

Control schemes that performed best in the first scenario were also subjected to the second one, closer to reality. In this case, flow setpoint values were the same as previously, but plant model was simulated with parameters slightly different than the ones in plant model used for controller tuning. This resembled the real-world cases, where any models only approximate the behaviour of the physical plants.

In this scenario, again, controllers were tuned based on the already introduced parameter sets (Sections 3.2.2–3.2.3), that is, on the best available knowledge about the plant. The simulated plant, however, used parameters slightly randomly modified. These values were generated once and then used throughout the tests of all control schemes, to ensure identical conditions in all tests.

To modify the static characteristics of a given signal, firstly, the individual (not averaged) six datasets of measured steady states were gathered (see Section 3.2.2.4), with outliers deleted, and with missing values interpolated (Section 3.2.2.6). Then, for each operating point $\{x_{\mathrm{r,req}},\ x_{\mathrm{m,req}},\ x_{\mathrm{a,req}}\}$ from the "coarse grid" of points visited during the experiment, minimum and maximum of the six individual steady-state values was determined. One of them (minimum or maximum value) was randomly chosen as preliminary value of the target static characteristics at this "coarse-grid" operating point. (Only extreme values were selected because later the hypersurface would be smoothened and variability of values would noticeably decrease.) Then, the values were checked for monotonicity along all three axes (positions of three dampers), and sorted if necessary, to enforce monotonicity. Finally, 3D linear interpolation to fine grid and then 3D smoothening were applied, in the same way as it was done so far.

The resultant randomized static characteristics was compared to the "ideal" model (averaged static characteristics) by calculating statistics on the difference between the two hypersurfaces, denoted δ_{random}. The same statistics were computed on the differences δ_i, $i = 1, 2, ..., 6$, between the averaged characteristics and each of the individual ones. The statistic measures for δ_{random} are similar as for δ_i (see Table 5.1). This indicates that the above method produces randomized static characteristics which reasonably differs from the averaged model, i.e., differs in the extent which might be encountered in the real plant operation.

Similar methodology was applied to the dynamic parameters. The main difference was that here, only two (not all six) individual datasets were used for drawing random values. These were the two sub-datasets from Section 3.2.3.8. Then the randomized values were 3D-interpolated to fine grid and smoothened.

TABLE 5.1: Statistics describing differences δ between averaged static characteristics of air flow rates and: individual experimental data series $i = \{1, 2, ..., 6\}$ (δ_i), or randomized characteristics used in test scenario 2 (δ_{random}). Abbreviations: std. dev. — standard deviation. All quantities given in [kg/s].

Measure	δ_1	δ_2	δ_3	δ_4	δ_5	δ_6	δ_{random}
Additional air stream							
median of $\lvert\delta\rvert$, $\times 10^{-4}$	1.06	2.05	1.17	1.78	2.16	2.01	1.60
mean of $\lvert\delta\rvert$, $\times 10^{-4}$	1.48	2.51	1.46	2.13	2.67	2.46	1.85
minimum δ, $\times 10^{-3}$	-0.849	-1.03	-0.947	-0.964	-1.54	-0.702	-1.19
maximum δ, $\times 10^{-3}$	0.692	0.765	0.711	0.771	1.05	1.19	0.689
std. dev. of δ, $\times 10^{-4}$	1.98	2.51	1.85	2.20	2.79	2.31	2.14
Main air stream							
median of $\lvert\delta\rvert$, $\times 10^{-4}$	1.22	2.10	1.07	2.02	1.57	1.63	1.47
mean of $\lvert\delta\rvert$, $\times 10^{-4}$	1.80	2.76	1.71	3.31	2.36	2.24	2.22
minimum δ, $\times 10^{-3}$	-1.30	-0.943	-1.07	-2.70	-0.607	-1.11	-0.627
maximum δ, $\times 10^{-3}$	1.09	1.31	1.08	0.931	1.19	1.16	1.20
std. dev. of δ, $\times 10^{-4}$	2.60	3.47	2.39	4.33	2.88	2.91	2.60
Recycle air stream							
median of $\lvert\delta\rvert$, $\times 10^{-4}$	0.792	1.38	0.888	1.57	1.11	1.58	0.907
mean of $\lvert\delta\rvert$, $\times 10^{-4}$	1.31	3.41	2.53	4.59	2.09	2.46	2.05
minimum δ, $\times 10^{-3}$	-3.85	-5.31	-3.85	-3.79	-3.85	-1.75	-3.50
maximum δ, $\times 10^{-3}$	1.60	3.76	2.21	5.55	1.52	3.09	1.22
std. dev. of δ, $\times 10^{-4}$	2.45	6.01	4.04	6.85	3.27	3.11	3.95

5.3.3 Evaluation of controller performance

To compare the performance of different control schemes, several quantitative measures were used which were meaningful yet easy to compute automatically. The following notations use symbols: $e = (q_{s,\text{SP}} - q_s)$ — error signal, u — plant excitation, i.e. control input (requested damper position), Δu — difference of consecutive samples of signal u (increment of u). The most important quality indices are marked in bold:

- **integral of absolute error (IAE) [kg]**,
- maximum absolute error (max $|e|$) [kg/s],
- maximum value of control input (max u) [% open],
- minimum value of control input (min u) [% open],
- standard deviation of control input values (std(u)) [% open],
- maximum absolute increment of control input (max $|\Delta u|$) [% open],
- **sum of absolute increments of control input ($\Sigma|\Delta u|$) [% open]**.

The best-case values of these measures are tabularized in the following sections. Average and median values of $|\Delta u|$ were also computed; they were always the same — much below 1 or equal to 0, respectively (which indicated correct operation of control loops) — so they are not shown in the tables.

Moreover, time-domain plots of simulated signals were observed. They are presented in their associated sections of this chapter.

5.4 Applied control schemes

5.4.1 3 × SISO PI control

5.4.1.1 System setup

A basic approach to be tested is an individual controller per each inlet air stream, so three independent control loops (Fig. 5.2). This structure is very simple to build. However, as a result of this independence, the actions of controller A, aiming at stabilising flow rate in stream A, disturb the flow also in streams B and C.

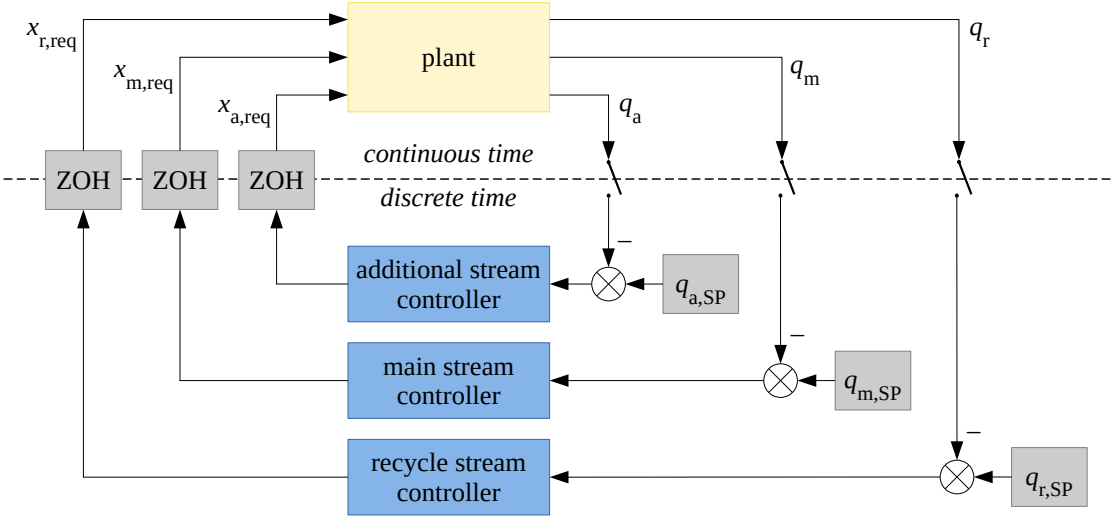

FIGURE 5.2: Diagram of control system with three single-input, single-output (SISO) feedback controllers, one for each air stream

PID-type controllers were tested first, namely: PI controllers. Their outputs were limited to 0–100% (for main stream), or 15–100% (for recycle stream), or 10–100% (for additional stream). Anti-windup method (clamping) was included. Moreover, controller output was rounded to nearest integer, as in the grinding installation, the available settings of damper positions are only whole numbers.

The PI controllers were implemented in simulation using MATLAB Simulink's built-in block called "PID controller" [61]. Its settings were: discrete-time operation, parallel form, trapezoidal integration method, limited output (with limits as above), clamping anti-windup method, zero initial conditions for the integrators, and external controller gains supplied from the MATLAB script as needed.

This setup — especially with fixed-value controller parameters (Sections 5.4.1.3 and 5.4.1.4) — may be treated as a benchmark, as such simple SISO loops with PID-type controllers are undoubtedly the most prevalent control schemes in industry [75, Sec. 1.1].

5.4.1.2 PI controller tuning rules

Rules for controller tuning were based on the plant model (first-order system with delay) in the primary paths: from a damper to air flow rate in the same stream. The rules implemented and tested in simulation were a selection of fourteen methods from an extensive review book [75]. The methods were originally authored by (and are such labeled in the review book):

- robust methods:
  a) Rivera et al., 1986, first version [75, p. 74];
  b) Rivera et al., 1986, second version [75, p. 74];
  c) Ogawa, 1995 [75, p. 75];
  d) Åström and Hägglund, 2006, robust tuning version [75, p. 76];
  e) Åström and Hägglund, 2006, aggressive tuning version [75, p. 76];
- methods shaping process reaction:
  f) Hazebroek and Van der Waerden, 1950 [75, p. 30–31];
  g) Moros, 1999, first version [75, p. 31];
  h) Moros, 1999, second version [75, p. 31];
  i) Wolfe, 1951 [75, p. 31];
- methods providing minimum integral of absolute error:
  j) Shinskey, 1988 [75, p. 33];
  k) Marlin, 1995 [75, p. 38];
  l) Edgar et al., 1997, first version [75, p. 38];
  m) Edgar et al., 1997, second version [75, p. 38];
  n) Shinskey, 2003 [75, p. 39].

See the review book for the specific formulas.

5.4.1.3 PI version 1: fixed parameters, based on averaged plant model

Controller parameters This type of PI controllers was the simplest. Controller parameters were tuned only once, for all operating points simultaneously, and they were not changing throughout the simulation.

Parameters for air flow controller for stream s were calculated based on parameters of dynamic model $\Delta q_{s,\mathrm{SP}}$ vs. $\Delta x_{s,\mathrm{req}}$ averaged over all operating points. This meant that plant parameters at any operating point would be possibly close to the model parameters used for tuning the controller. Some tuning methods, especially robust ones, should manage to handle the fact that the actual plant parameters were not always very close to the model ones.

Simulation results — scenario 1 only Controllers were tuned according to each of the above-mentioned rules, in turn (all three controllers with the same rule). Simulations were carried out, following scenario 1 (ideal knowledge of plant parameters). Plots of simulated signals and values of quality indices were compared, and rule d) was definitely the best. It provided the least IAE for main and recycle air flows; second best IAE for the additional air flow; the least sum of control signal increments for main and additional streams; second best $\Sigma|\Delta u|$ for the recycle stream; and the smallest oscillations in the plant outputs (Fig. 5.3). In all of these criteria, other tuning rules performed significantly worse.

Note: Values of quality indices (Section 5.3.3) for the best case of each version of PI control are collected in Table 5.2.

However, the oscillations were still very significant, whereas none of them are desired on the outputs, and also on control signals (not to wear out the actuators). So, these simulation results show that variability of plant parameters — especially, gains — is too big even for the robust tuning methods. Moreover, the non-oscillatory transients were rather slow.

5.4.1.4 PI version 2: fixed parameters, based on worst-case plant model

Controller parameters The same methodology was used as before, but now, instead of averaged plant model, the worst-case plant parameters were used as input to the tuning rules. These parameters were the maximum gain, and minimum time constant and time delay of dynamic plant model. They were supposed to yield more conservative controller tuning, thus avoiding oscillations in plant output.

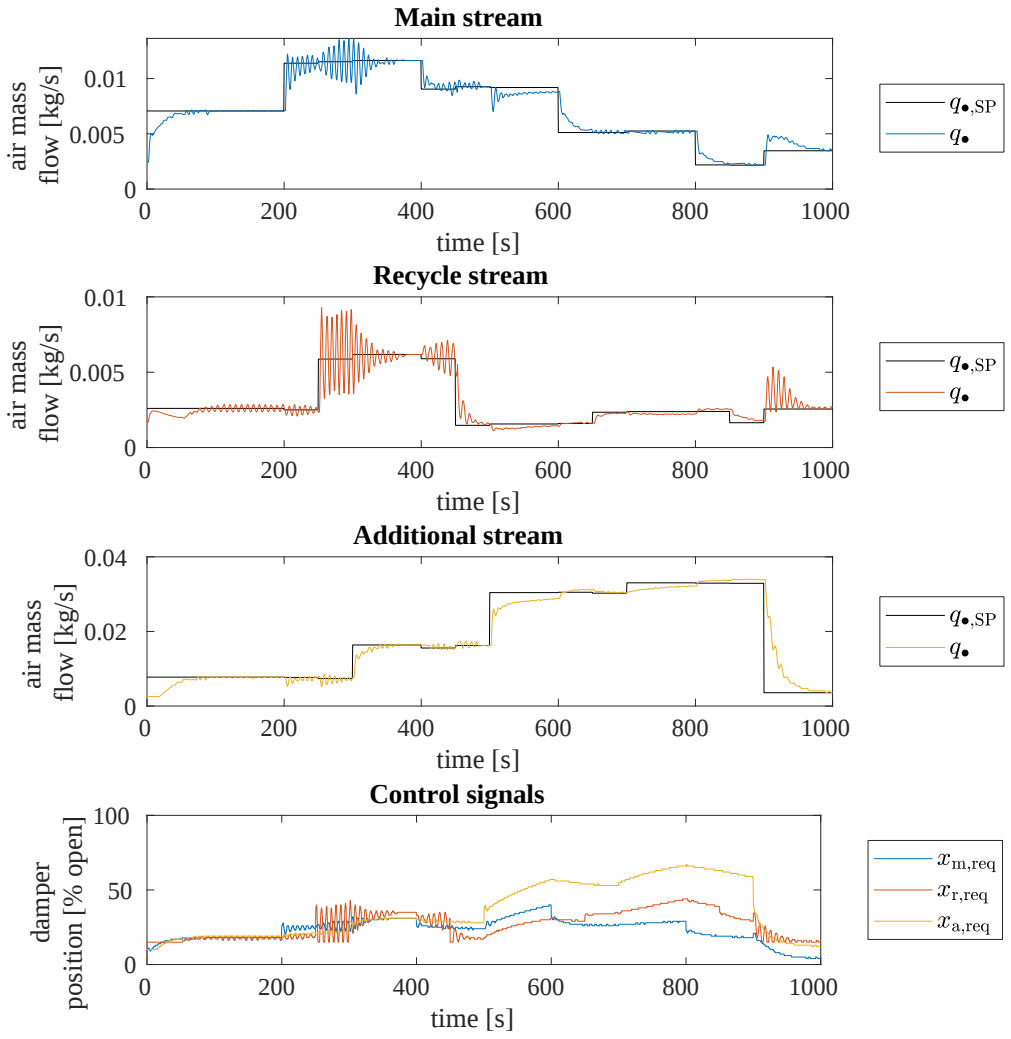

FIGURE 5.3: Simulation result for 3 × SISO PI control in version 1 (fixed parameters based on averaged plant model), test scenario 1. Best case: tuning rule d).

Simulation results — scenario 1 In general, the results were better than for scheme version 1, as the simulated signals contained little oscillations, and better IAE was achieved in a few cases. However, no single tuning rule provided really good results for all three streams at once. So, for each stream a separate "best rule" was determined — one that produced the lowest IAE, smallest oscillations and rather small variability of control inputs. These were rules b), h) and l) for main, recycle and additional controllers, respectively. Then, each stream's controller was tuned according to its own best rule and they were simulated together in the same test scenario as usual.

The result is plotted in Fig. 5.4 and it is better than expected — the oscillations are not frequent and have small amplitudes, and the flow rates settle down relatively fast, compared, e.g., to Fig. 5.3. Most of the quality indices are better than for scheme version 1. Unfortunately, still the main and recycle air flows are often strongly disturbed by changing setpoints of other flow rates.

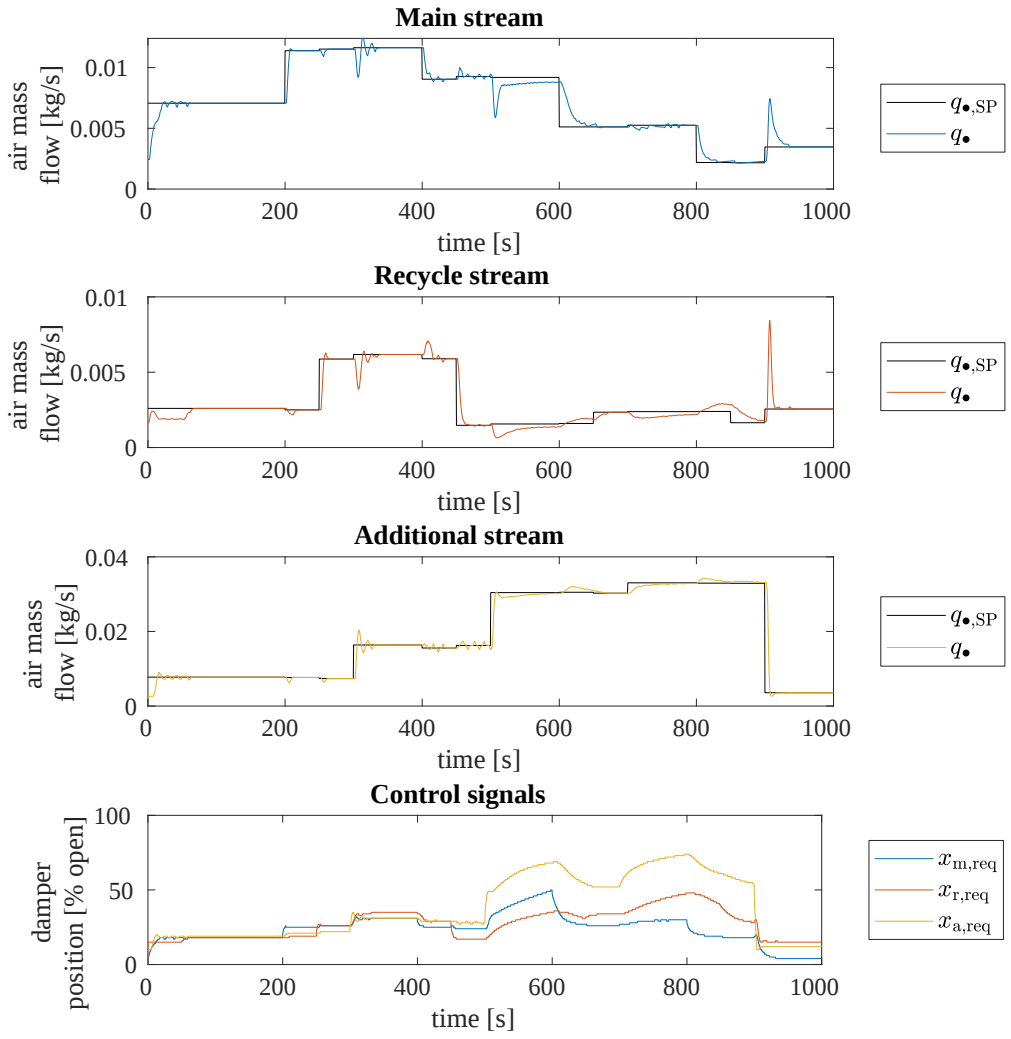

FIGURE 5.4: Simulation result for 3 × SISO PI control in version 2 (fixed parameters based on worst-case plant model), test scenario 1. Best case: tuning rules b), h) and l) for main, recycle and additional controllers, respectively.

Simulation results — scenario 2 Relatively good performance in scenario 1 means it is worth testing the algorithm in scenario 2 as well. Again, no single tuning rule was best (or even good) for all three air streams, but rule b) was selected for the main stream, rule l) — for the additional stream, and rules g), h), j) were equally good for the recycle stream control. Each of these rule combinations was tested in another simulations and then, rules g), h) turned out nearly the same, with the latter barely better for this set of setpoint values. These results are plotted in Fig. 5.5. The transients are usually similar to the result of scenario 1 — obviously, including the significant errors on main and recycle flow rates — but now there are more oscillations, which is not desired. Values of quality indices are similar as previously, IAE is even slightly better, but the quite big oscillations of the recycle flow rate indicate worse performance.

Perhaps the performance of this control scheme could be improved by fine-tuning the controllers to even more conservative gains. However, but this needs substantial effort: trial-and-error procedure or a detailed analysis (e.g., involving Nyquist diagrams). The simple methods, such as using literature formulas based on model parameters, seem to be exhausted.

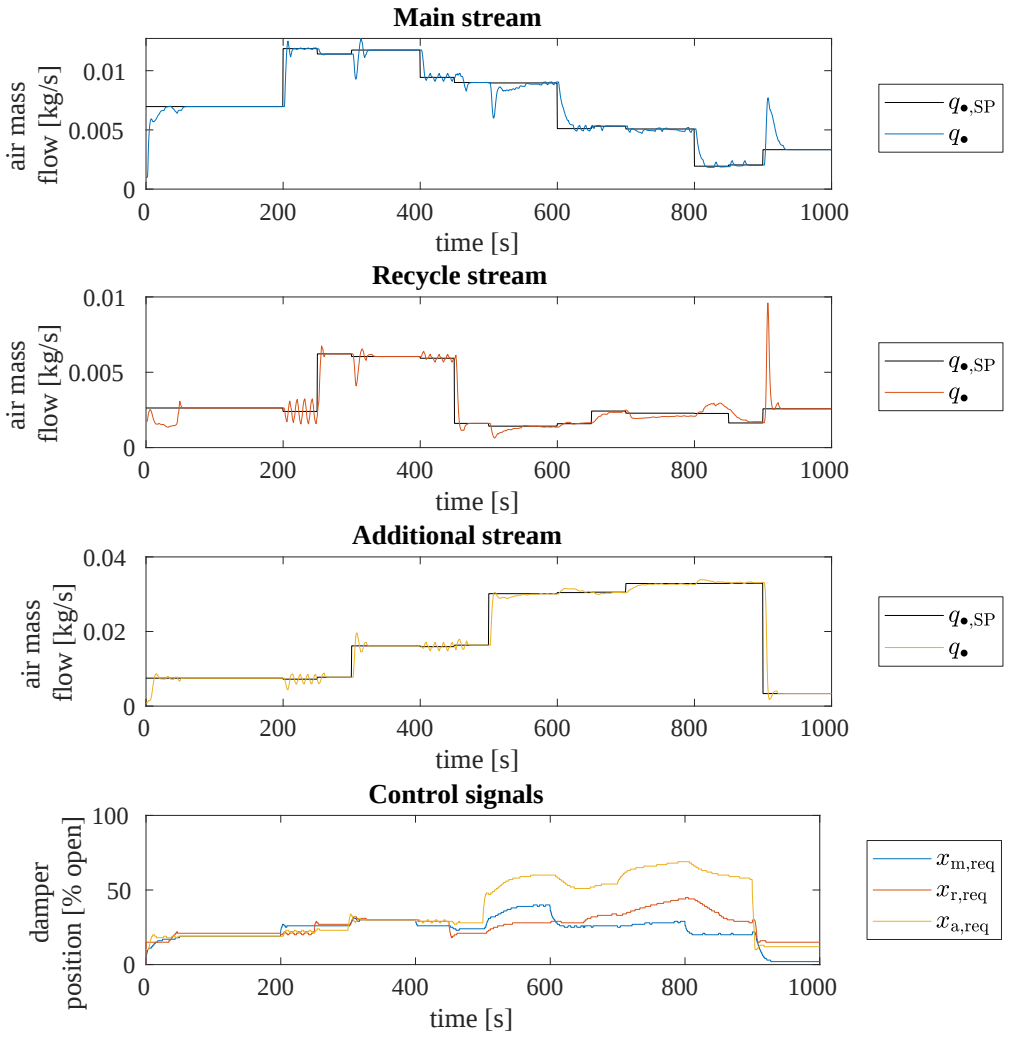

FIGURE 5.5: Simulation result for 3 × SISO PI control in version 2 (fixed parameters based on worst-case plant model), test scenario 2. Best case: tuning rules b), h) and l) for main, recycle and additional controllers, respectively.

5.4.1.5 PI version 3: parameter scheduling

Controller parameters Tuning rule formulas were the same as previously. However, a separate set of controller parameters was prepared for each triple of damper positions $\{x_{\mathrm{r,req}},\ x_{\mathrm{m,req}},\ x_{\mathrm{a,req}}\}$, to achieve maximum fit to the plant model. When implemented in hardware, the algorithm might also use some number of intervals into which the whole operating range would be divided, with one set of controller parameters per one such

3D region in which plant parameters do not vary much. Number of regions (so, number of stored sets of controller parameters) could be suited to the available memory etc. in the hardware system.

All necessary values of controller parameters were calculated before simulation. They were based on coefficients of plant model — time constants, time delays and gains, with the latter being the "theoretical" gains resulting from partial differentiation of the static characteristics (see Section 3.2.2.10). So, no online calculations were necessary during controller operation, a simple lookup table of controller parameters was enough. However, this meant that the plant gains used for controller tuning were valid only in the neighbourhood of the point at which the partial derivatives were calculated. (The size of this neighbourhood was varying with the curvature of the static characteristics.) In consequence, large changes in plant input could result in "apparent" gains[1] of the plant different than these theoretical ones, and the controller tuning could turn out not optimal, or even totally improper.

Simulation results — scenario 1 This time, tuning rule a) was definitely the best in terms of IAE for all air flows. Sums of control signal increments were also the lowest or close to the lowest for this rule. Moreover, the values of IAE were also noticeably better than for the fixed-parameter controllers. The plots (Fig. 5.6) show that oscillations were not present in flow rates nor damper positions. Control inputs were changed a bit more aggressively than in control scheme version 2, but were reasonable anyway. Also, flow rates settled down faster than with the fixed-parameters controllers. Nevertheless, changing flow setpoints on other air streams still caused great momentary errors of main and recycle flows, and rendered the result not fully satisfactory — even though better than previously.

Simulation results — scenario 2 This control scheme performed relatively good, so it was also tested according to scenario 2, where controller tuning and plant simulation are based on slightly different parameter sets. Again, tuning rule a) provided the least errors. Values of quality indices were similar as for scenario 1 — a little worse or a little better. Simulated signals (Fig. 5.7) had similar good and weak points as in scenario 1. To conclude, the algorithm structure and its parameters were robust enough to handle well the inaccuracies in the plant model, but some further improvement is still welcome.

[1] In this chapter, apparent plant gain is understood as the gain actually observed in plant model response to a given input. It could be defined as the slope (along proper dimension) between two points on the static characteristics of the plant, corresponding to the old and new operating point $\{x_{\mathrm{r,req}},\ x_{\mathrm{m,req}},\ x_{\mathrm{a,req}}\}$ (before and after the change on input).

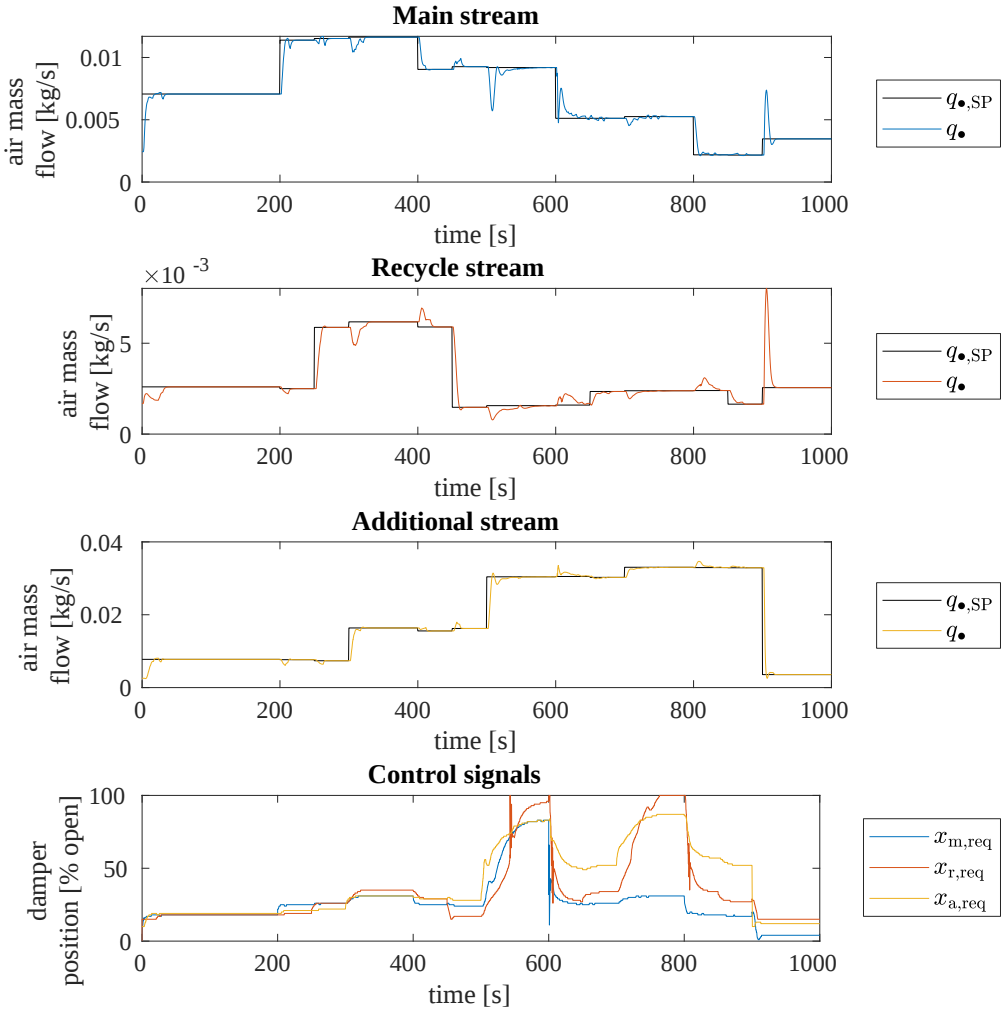

FIGURE 5.6: Simulation result for 3 × SISO PI control in version 3 (with parameter scheduling), test scenario 1. Best case: tuning rule a).

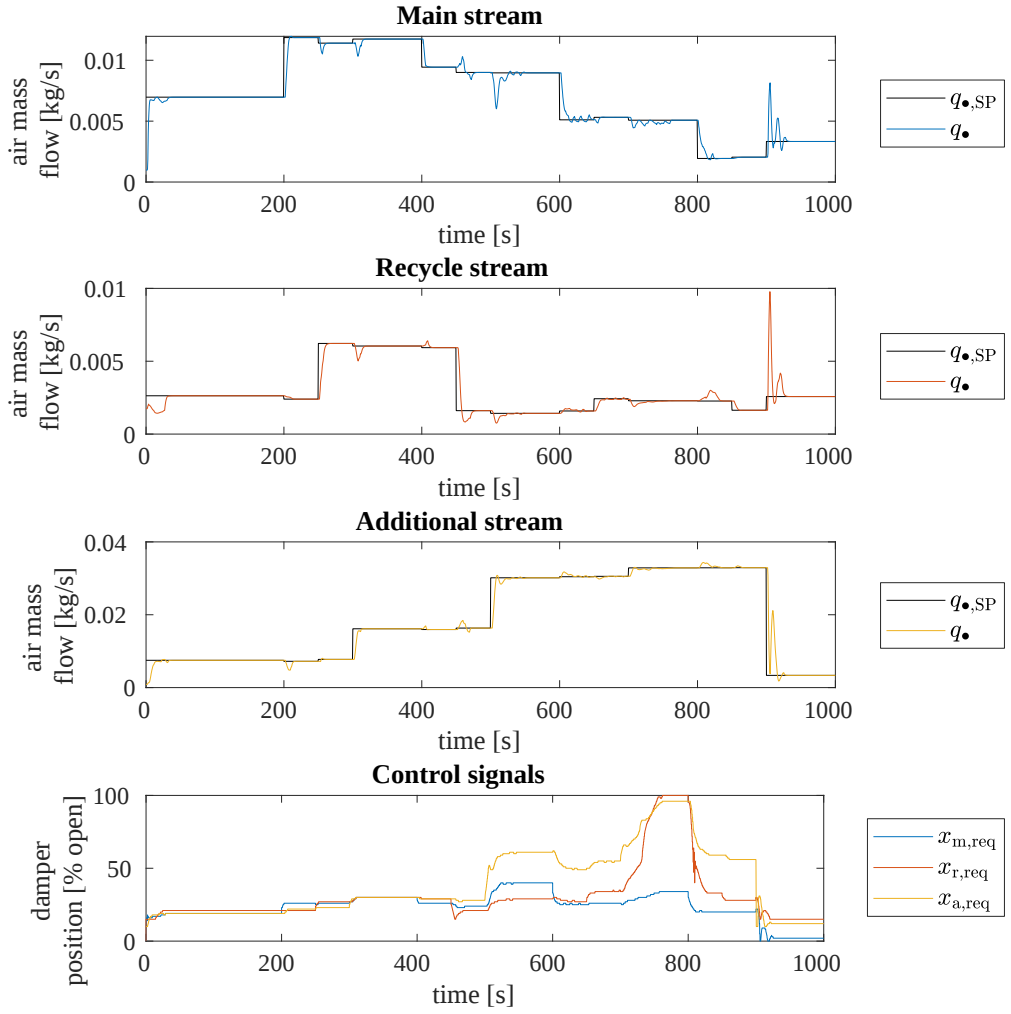

FIGURE 5.7: Simulation result for 3 × SISO PI control in version 3 (with parameter scheduling), test scenario 2. Best case: tuning rule a).

5.4.1.6 PI version 4: parameter scheduling with plant gain adaptation

Controller parameters The controllers were parametrized in a similar way as previously (Section 5.4.1.5), however, current parameters were computed online instead of being pre-calculated and looked up. Again, the tuning was based on time constants and time delays from plant model (known a priori, as before); but instead of the modelled (local, "theoretical") gains, the currently expressed, "apparent" plant gains were used. They were calculated from current and previous points on the known static characteristics of the plant, as the ratio of increment in modelled steady state $\Delta\overline{q}_s$ to increment in damper position on the same stream, $\Delta x_{s,\mathrm{req}}$. This apparent gain is used in simulation when the stream's own damper position has just changed ($\Delta x_{s,\mathrm{req}} \neq 0$); otherwise, the apparent gain is undefined, so the theoretical gain is used.

Simulation results The best results are shown in Fig. 5.8. Once more, tuning rule a) yielded the lowest IAE for all three streams, but the index values were slightly worse than for the previous case. Overshoots in the main and recycle air flows were smaller than for the plain gain-scheduled algorithm, but they were still big at some points. Also, sometimes the control inputs were much varying — not only for this tuning rule, but also for others. The transients in the plots confirm, too, that this control method is probably slightly worse than the two previous ones.

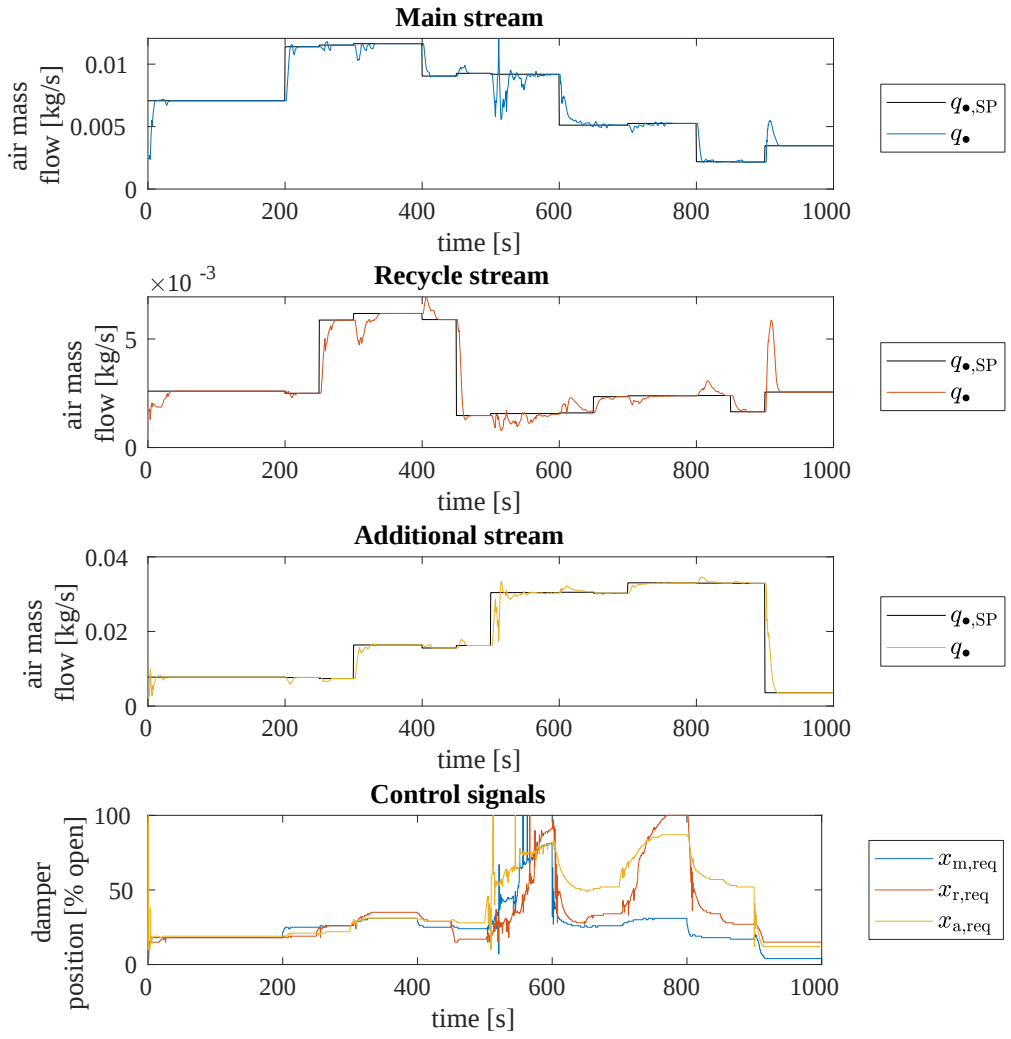

FIGURE 5.8: Simulation result for 3 × SISO PI control in version 4 (with parameter scheduling and adaptation of modelled plant gain), test scenario 1. Best case: tuning rule a).

5.4.1.7 Summary of 3 × SISO PI control

Quality indices (see Section 5.3.3) for the above-mentioned best cases of all versions of the algorithm are listed in Table 5.2. Index values were already commented on next to descriptions of associated algorithm versions, but they are given here collectively for easier comparison.

Relatively good control of the flows could be achieved with some variants of this control scheme, even with fixed (non-scheduled) controller parameters. Unfortunately, substantial errors still occur in recycle and main control loops when setpoints change in other air streams, due to couplings between them. Only the additional air flow is free from these big overshoots — this stream was the easiest to control.

TABLE 5.2: Quality of air flows control with 3 × SISO PI controllers — scenarios 1 and 2, best case for each tested version of the algorithm

Quantity	Scenario 1				Scenario 2	
	Control algorithm version					
	1	**2**	**3**	**4**	**2**	**3**
Additional air stream						
tuning rule	d)	l)	a)	a)	l)	a)
IAE [kg]	1.52	0.654	0.453	0.589	0.623	0.525
max $\|e\|$ [kg/s]	0.0304	0.0297	0.0293	0.0293	0.0298	0.0296
max u [% open]	67	74	87	100	69	96
min u [% open]	10	10	10	10	10	10
std(u) [% open]	18.2	20.8	24.3	23.4	19.3	23.4
max $\|\Delta u\|$ [% open]	18	11	39	90	11	44
$\Sigma\|\Delta u\|$ [% open]	196	212	252	1140	206	268
Main air stream						
tuning rule	d)	b)	a)	a)	b)	a)
IAE [kg]	0.452	0.329	0.212	0.241	0.303	0.212
max $\|e\|$ [kg/s]	0.00463	0.00464	0.00464	0.00464	0.00599	0.00599
max u [% open]	40	50	83	100	40	40
min u [% open]	4	4	1	4	2	0
std(u) [% open]	7.60	9.53	16.5	14.2	8.6053	9.1609
max $\|\Delta u\|$ [% open]	8	3	55	60	4	7
$\Sigma\|\Delta u\|$ [% open]	359	138	370	784	133	154
Recycle air stream						
tuning rule	d)	h)	a)	a)	h)	a)
IAE [kg]	0.374	0.279	0.197	0.218	0.256	0.177
max $\|e\|$ [kg/s]	0.00404	0.00585	0.00544	0.00442	0.00702	0.00718
max u [% open]	44	48	100	100	45	100
min u [% open]	15	15	15	15	15	15
std(u) [% open]	8.95	9.76	24.6	22.3	7.59	19.3
max $\|\Delta u\|$ [% open]	18	4	43	44	4	21
$\Sigma\|\Delta u\|$ [% open]	962	124	814	1346	124	318

Manual tuning of the controllers, without the estimated plant models, would be cumbersome and very difficult. Different tuning rules performed best for different versions of the control algorithm, which makes the tuning not an easy task even when plant models are utilized.

Some further modification of 3 × PI control scheme could be parameter scheduling (in version 3 or 4) based on the actual position of the damper x instead of the requested position x_{req}. This would better reflect the current local curvature of the static characteristics (i.e., the theoretical or apparent gains of incremental dynamic models). Thus, probably, this could further improve the transients. However, to test this, the simulator needs to be extended with a model of x_s vs. $x_{s,\text{req}}$ relationship for each stream s.

As was suggested in Section 3.2.3.13, it might also be worth to test parameter-scheduled PI controllers tuned on the basis of changing plant gain only (with integration time constant fixed and only controller gain scheduled). This would greatly reduce the memory required to store lookup tables on the controller, which might be important for some hardware devices. Tests are needed to check if control quality does not get deteriorated in this scheme.

5.4.2 Open-loop control using MIMO inverse model

5.4.2.1 System setup

The control algorithm used the inverse static characteristics of the air flows, in open loop. This structure was implemented only to test the correctness of inverse model before its further use. It is not meant for implementation on site, as due to lack of feedback, it is completely vulnerable to disturbances and modelling inaccuracies.

This algorithm could be considered as one combining the direct layer and, partially, the supervisory layer of the hierarchical control system. It was a multi-input multi-output (MIMO) system: a single law with 3 inputs (air flow setpoints) and 3 outputs (calculated control signals, i.e. air dampers' positions). System diagram is shown in Fig. 5.9.

Such MIMO block was supposed to suppress the negative effect of separate control loops unintentionally disturbing each other, as was the case with algorithms described in Section 5.4.1. Moreover, feed-forward structures are known to be acting faster than feedback ones, as the former do not require an error to occur on the plant output.

5.4.2.2 Operation of the algorithm

The key part of this scheme was the inverse of air flow static characteristics determined as in Section 3.2.2 (the averaged version was used). The three steady-state characteristics

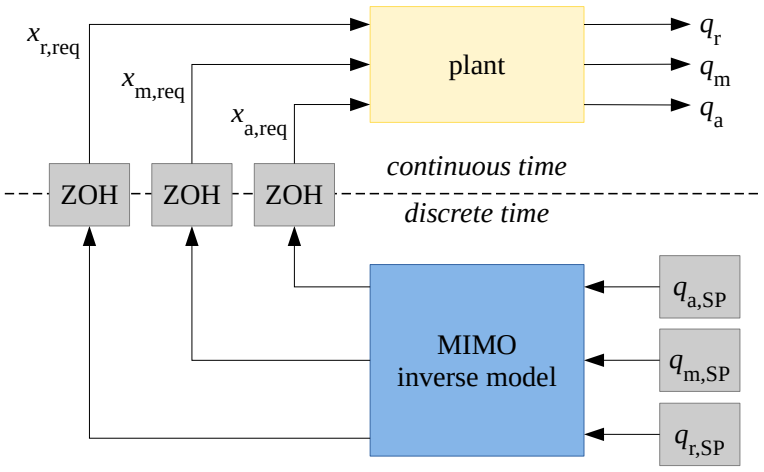

FIGURE 5.9: Diagram of open-loop system with a single multi-input multi-output (MIMO) inverse model

had the form:

$$\begin{aligned} q_\mathrm{r} &= f\left(x_\mathrm{r,req},\ x_\mathrm{m,req},\ x_\mathrm{a,req}\right) , \\ q_\mathrm{m} &= f\left(x_\mathrm{r,req},\ x_\mathrm{m,req},\ x_\mathrm{a,req}\right) , \\ q_\mathrm{a} &= f\left(x_\mathrm{r,req},\ x_\mathrm{m,req},\ x_\mathrm{a,req}\right) \end{aligned} \tag{5.5}$$

and they shared the same inputs, so they might have been considered as a single three-input, three-output relation:

$$\left\{q_\mathrm{r},\ q_\mathrm{m},\ q_\mathrm{a}\right\} = f\left(x_\mathrm{r,req},\ x_\mathrm{m,req},\ x_\mathrm{a,req}\right) . \tag{5.6}$$

Consequently, the inverse characteristics was of the form:

$$\left\{x_\mathrm{r,req},\ x_\mathrm{m,req},\ x_\mathrm{a,req}\right\} = f\left(q_\mathrm{r},\ q_\mathrm{m},\ q_\mathrm{a}\right) . \tag{5.7}$$

When a vector of three flow setpoints $\{q_\mathrm{r,SP},\ q_\mathrm{m,SP},\ q_\mathrm{a,SP}\}$ was supplied to the controller, it compared these setpoints to all known triples of plant outputs' steady states. Such triple $\{q^*_\mathrm{r,SP},\ q^*_\mathrm{m,SP},\ q^*_\mathrm{a,SP}\}$ was selected that was the closest to the originally requested one in terms of a selected distance definition. This minimized distance function between $\{q_\mathrm{r,SP},\ q_\mathrm{m,SP},\ q_\mathrm{a,SP}\}$ and $\{q^*_\mathrm{r,SP},\ q^*_\mathrm{m,SP},\ q^*_\mathrm{a,SP}\}$ vectors could be defined in several ways, e.g. with mean squared error, mean absolute error, maximum absolute error. Also these errors themselves could be calculated in many ways, e.g. as simple differences between corresponding vector elements: $(q_{s,\mathrm{SP}} - q^*_{s,\mathrm{SP}})$ for each stream s; or as relative differences: $(q_{s,\mathrm{SP}} - q^*_{s,\mathrm{SP}})/q_{s,\mathrm{SP}}$; or as differences relative to the range of achievable flow rates for the particular stream. The tested control algorithm implemented a distance function with maximum absolute error, to ensure that no flow rate setpoint would

be changed significantly; and differences relative to whole signal ranges were used, as different air streams have noticeably different air flow ranges (Table 5.3).

TABLE 5.3: Ranges of air mass flow rates in horizontal inlet pipes. Values taken from the smoothed average static characteristics (see Section 3.2.2).

Air stream	**Mass flow rate of air [kg/s]**		
	min	**max**	**range**
recycle	1.61e-4	0.0179	0.0177
main	7.32e-4	0.0299	0.0291
additional	8.08e-4	0.0399	0.0391

Note: when the inverse model is plugged into the full layered control system, this setpoint-processing part of the algorithm will not be needed anymore (or at least, it will be redundant and kept only for safety reasons). It will be the responsibility of the supervisory layer to transform setpoints $\{q_{\mathrm{w,SP}},\ q_{\mathrm{c,SP}},\ q_{\mathrm{r,SP}}\}$ into possiby close, reasonable and physically reachable setpoints $\{q^*_{\mathrm{r,SP}},\ q^*_{\mathrm{m,SP}},\ q^*_{\mathrm{a,SP}}\}$. This conversion may even incorporate current mesurements of air flows, not only their setpoints. However, for the present tests, when the inverse model operates standalone (without the upper layers), such processing stage was necessary as a component of the inverse model itself.

After the reachable flow rate setpoints $\{q^*_{\mathrm{r,SP}},\ q^*_{\mathrm{m,SP}},\ q^*_{\mathrm{a,SP}}\}$ had been determined, the corresponding damper positions were read from the static characteristics of the plant. These positions were the control signals fed to the inputs of plant model.

5.4.2.3 Simulation results

Test scenario already used with SISO PI controllers was also simulated with the inverse model. The plots (Fig. 5.10) show that the output of simulated plant perfectly follows the setpoints in the steady states, and the rate of reaching them is only limited by the dynamics of the simulated plant. This proves the inverse model was correctly implemented.

Figure 5.11 presents simulation of the same test in scenario 2, i.e., with parameters of simulated plant slightly different than the ones known by the inverse model. Of course, the open-loop structure is not capable of reacting to model discrepancies and so, the steady-state errors are nonzero — sometimes they are even significant. This is why the inverse model will actually be only a part of a feedback algorithm (see next section).

Quality indices for both scenarios are listed in Table 5.4, to provide context for similar measures related to other control schemes.

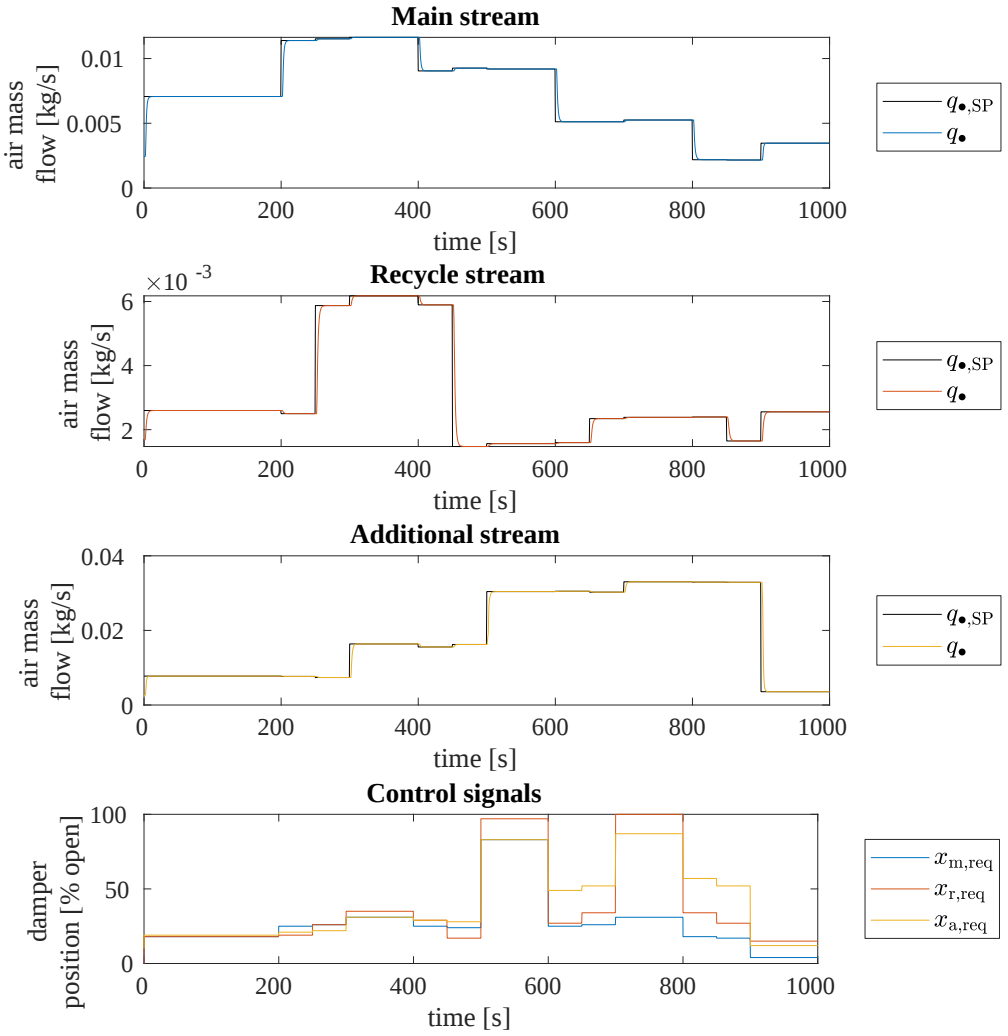

FIGURE 5.10: Simulation result for open-loop control using MIMO inverse model, test scenario 1

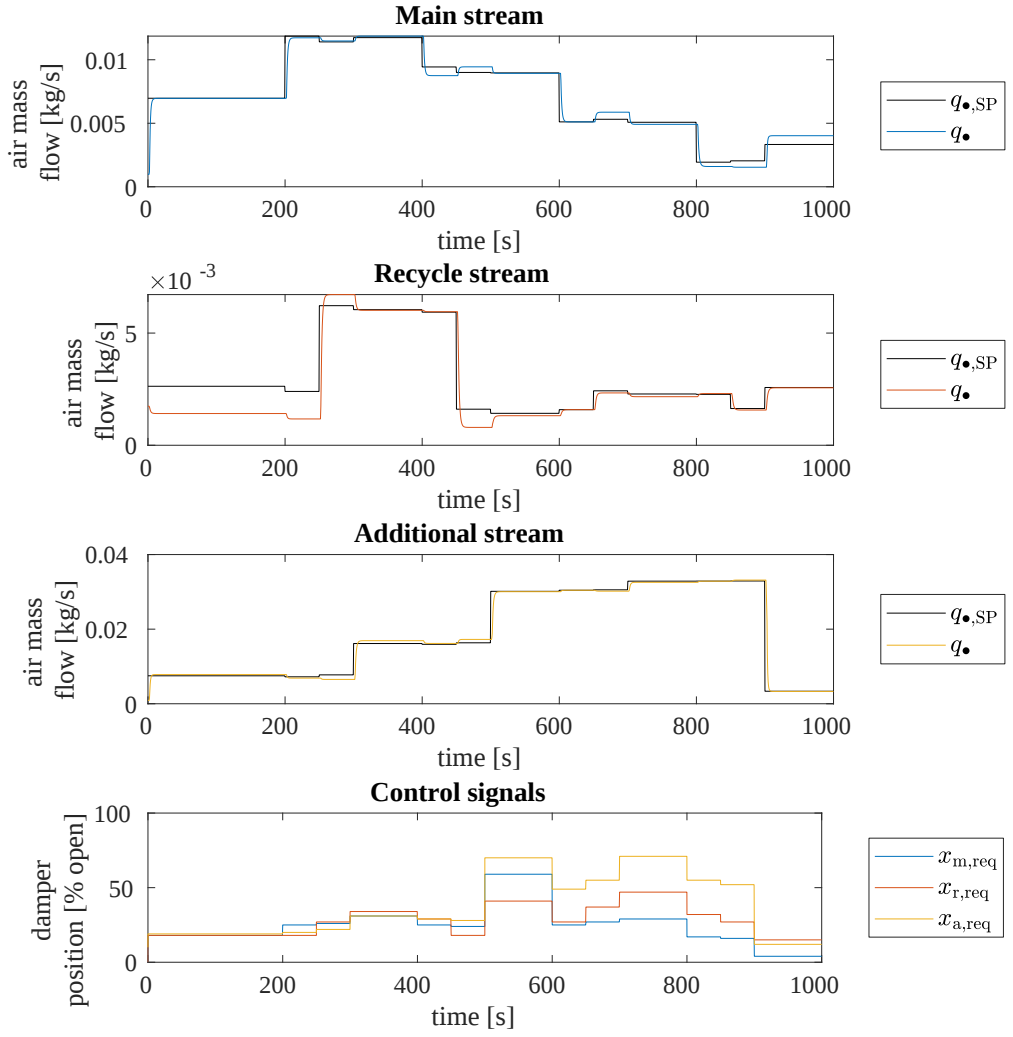

FIGURE 5.11: Simulation result for open-loop control using MIMO inverse model, test scenario 2

TABLE 5.4: Quality of air flows control with MIMO inverse model — scenarios 1 and 2

Quantity	**Scenario 1, stream:**			**Scenario 2, stream:**		
	main	**recycle**	**additional**	**main**	**recycle**	**additional**
IAE [kg]	0.0778	0.0484	0.215	0.308	0.443	0.563
max $\|e\|$ [kg/s]	0.00464	0.00442	0.0293	0.00599	0.00505	0.0298
max u [% open]	83	100	87	59	47	71
min u [% open]	4	15	12	4	15	12
std(u) [% open]	19.9	30.5	25.7	13.5	10.4	20.9
max $\|\Delta u\|$ [% open]	59	80	55	35	23	42
$\Sigma\|\Delta u\|$ [% open]	170	343	217	118	121	159

5.4.3 MIMO inverse model with SISO feedback control

5.4.3.1 System setup

After testing the inverse model, it was used in a more robust structure that included also feedback controllers (namely, SISO PI controllers). This way, the advantages of the two approaches were combined. The MIMO inverse model provided de-coupling of the three air streams and fast response to setpoint changes, whereas the feedback part elliminated the remaining small steady-state errors coming from discrepancies between modelled and real static characteristics of the plant, or from other disturbances. Diagram of such hybrid system is shown in Fig. 5.12.

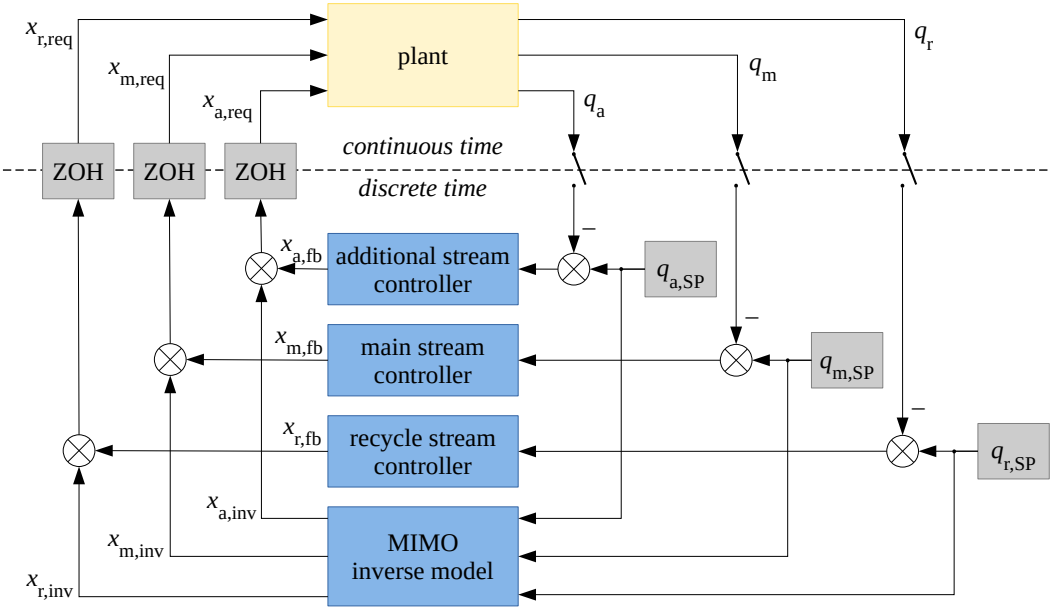

FIGURE 5.12: Diagram of control system with combined MIMO inverse model and three SISO feedback controllers. Symbols: $x_{\bullet,\mathrm{fb}}$ — output of feedback controller, $x_{\bullet,\mathrm{inv}}$ — output of inverse model.

The overall saturation limits $\left[x_{s,\mathrm{req}}^{\mathrm{low}}, x_{s,\mathrm{req}}^{\mathrm{high}}\right]$ for each control signal $x_{s,\mathrm{req}}$ still hold, but now, this control signal is a sum of two components: output of inverse model $x_{s,\mathrm{inv}}$ and output of feedback controller $x_{s,\mathrm{fb}}$. The inverse model produces outputs anywhere within the $x_{s,\mathrm{req}}$ limits, and so, the saturation limits for the feedback controller are not the full $x_{s,\mathrm{req}}$ limits anymore, but they are modified with the current output of inverse model:

$$x_{s,\mathrm{fb}}^{\mathrm{low}} = x_{s,\mathrm{req}}^{\mathrm{low}} - x_{s,\mathrm{inv}}\,, \tag{5.8}$$

$$x_{s,\mathrm{fb}}^{\mathrm{high}} = x_{s,\mathrm{req}}^{\mathrm{high}} - x_{s,\mathrm{inv}}\,. \tag{5.9}$$

This means that controller saturation limits need to change dynamically during the simulation. The built-in MATLAB Simulink block for PI controller does not support

this, so it was edited to incorporate this feature. The new modifiable limits were used in the controller to properly saturate the output signal, but also to provide correct operation of anti-windup mechanism (clamping).

5.4.3.2 Controller parameters

Inverse model was defined as in the previous section.

PI controllers' parameters were selectable from all four versions presented in Section 5.4.1. However, the controllers, in such a structure together with the inverse model, did not aim at reaction to full change in flow setpoint anymore — instead, they only reacted to small errors left after the inverse model performed its job. Thus, tuning of feedback controllers used a modified version of plant gain: multiplied by a factor of 10 (selected experimentally). In effect, controller gain was smaller and the tuning was more conservative.

5.4.3.3 Simulation results

This control scheme was tested on scenario 2 only, as in scenario 1, the feedback controllers are not needed (most of the time there is no error left after the operation of the inverse model). Best results (smallest IAE) were achieved with PI control in version 2 (fixed parameters), with tuning rule i). Simulation result is shown in Fig. 5.13, and quality indices are listed in Table 5.5. Compared to best case of sole PI control, which seems to be the algorithm version 3 (see Table 5.2),this time IAE was slightly worse for main and additional streams and better for the recycle stream. Sum of control signal increments was usually smaller now. The most important change is visible in the plots — the once very big errors near the end of simulation are now very much reduced. Instead, a noticeable error appeared in the recycle stream near simulation time 250 s, but nevertheless, it is smaller than in the case without the inverse model.

Summarizing, this result is the best so far, but the improvement is not quite as clear as was expected. Some further tuning could probably be applied to upgrade it.

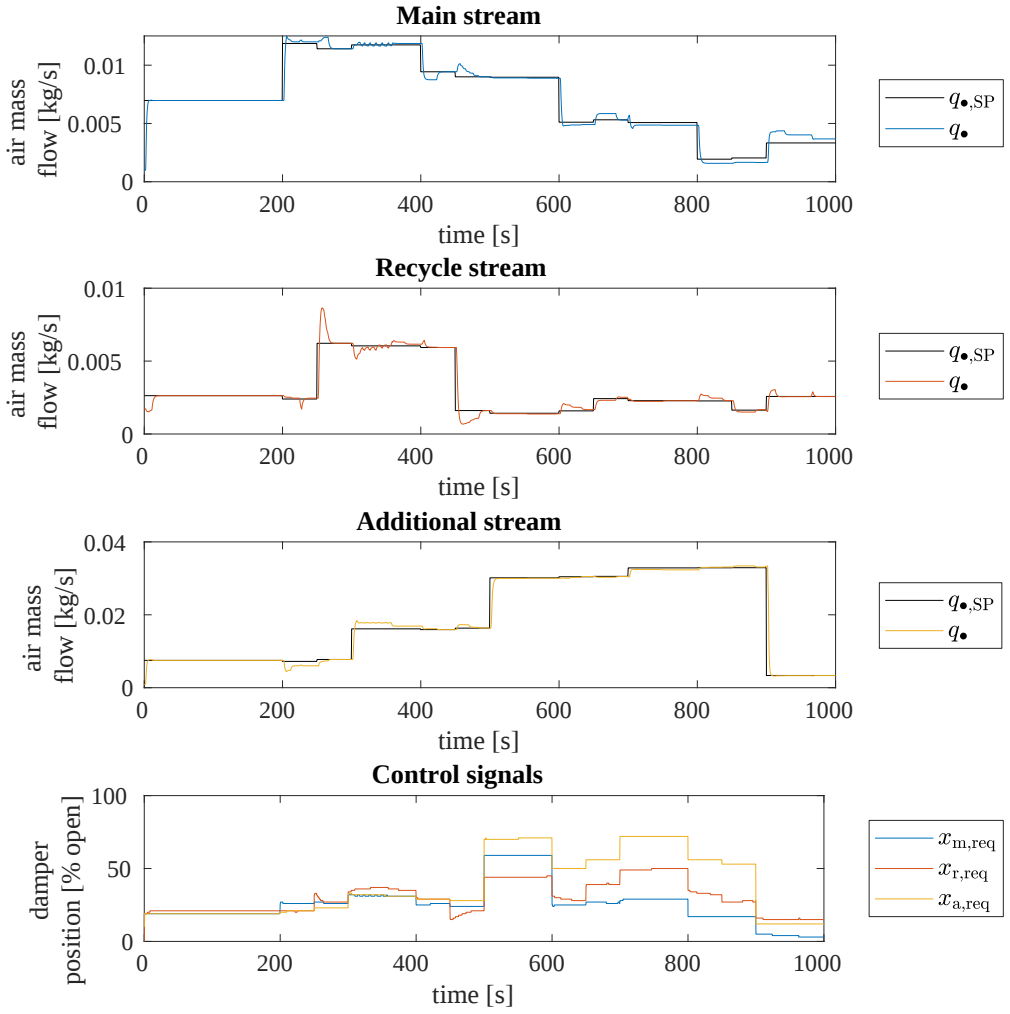

FIGURE 5.13: Simulation result for combined MIMO inverse model and SISO feedback control, test scenario 2. Best case: PI controllers in version 2, tuning rule i).

TABLE 5.5: Quality of air flows control with MIMO inverse model and PI controllers — scenario 2 only

Quantity	**Stream:**		
	main	**recycle**	**additional**
IAE [kg]	0.292	0.163	0.560
max $\lvert e\rvert$ [kg/s]	0.00599	0.00432	0.0300
max u [% open]	59	50	72
min u [% open]	3	15	12
std(u) [% open]	13.4	10.8	21.2
max $\lvert\Delta u\rvert$ [% open]	35	23	42
$\Sigma\lvert\Delta u\rvert$ [% open]	144	167	167

5.5 End notes

The list of control schemes worth testing is by no means exhausted by the above research. In the future, further investigations are planned, e.g., with parameters scheduled according to simulated actual damper positions x instead of the requested ones x_{req}; with air stream de-coupling thanks to simulated pressure readings; with MIMO feedback controllers; with modern control techniques.

The created simulation environment and the developed methodology of estimation of plant model coefficients make the above task much easier. These tools allow to design and verify many control schemes and multiple sets of controller parameters with relatively small effort, keeping the cumbersome hardware implementations and on-site testing to the minimum. This way, the tools developed in this dissertation allow to prepare a well-performing control algorithm suitable for the demanding task of air flow control in the grinding installation.

Chapter 6

Summary

This dissertation concerned a novel grinding system with electromagnetic mill, which aims at improvement of grinding product quality and reduction of energy consumption in the ultrafine comminution process. The topic is important due to grinding processes being extremely common in industry. This field of research is also demanding and diversified, as the considered plant incorporates multiple signals arranged in many interrelated subsystems, which operate in different time scales.

The studies presented here helped to monitor and control the grinding process by developing new methods of indirect measurement. Key quantities describing the raw material — mass flow rate, particle size, moisture content — were assessed this way. These measurement methods were augmented with steady-state mathematical models to enable estimation of selected process parameters in the locations where measurements were very difficult or impossible to conduct. The identified models described material moisture in the installation and its influence on particle classification process.

Another set of models addressed steady-state and dynamic properties of transport air flow in the grinding system. Thanks to developing these models, simulation environment was prepared for testing air flow control algorithms. Selected control schemes were designed and parametrized based on these models as well. The best performance so far was achieved with an algorithm that combined proportional-integral controllers and multivariate inverse model of the pneumatic system. However, more research work is planned to futher improve the performance of this control subsystem, and the prepared simulation environment is going to be used for it.

Conducting numerous experiments and processing of experimental data resulted in new methods and models that: help to monitor the operation of the grinding system, provide feedback or feed-forward information for its control subsystems, propose air flow control algorithms, and enable easier development of new air flow control schemes.

Author Contributions

Contribution to the research described in this thesis

The author of this dissertation made the following original contributions to the research items described herein:

- cooperated in the SYSMEL project team that designed and examined the grinding system with electromagnetic mill;
- designed and performed the experiments for vibrational and acoustic measurements of particle size and flow rate of bulk material (Sections 2.1.3.1–2.1.3.3, Section 2.1.5);
- designed and implemented signal processing algorithms for data from the above experiments (Sections 2.1.3.4 and 2.1.5), analysed the results (Sections 2.1.4, 2.1.6, 2.1.7);
- together with three colleagues, took part in the experiments for vision and thermovision measurement of moisture content (Section 2.2.1.1); this mostly included sieving the raw material into several size fractions, preparing the mixed-size material and drying the material;
- performed higher-level processing of vision data (Section 2.2.1.3); namely, identified and assessed the "direct" models of image intensity vs. sample moisture, defined and assessed the inverse models of sample moisture vs. image intensity;
- together with two colleagues, took part in the experiments on material moisture in grinding installation (Sections 2.2.2.1–2.2.2.3); namely, this involved drying the material, manual sieve analyses, monitoring the installation during the experiments, measuring vibration caused by particles moving in the pipeline (the latter were not described in this thesis due to poor quality of data, but they were mentioned in [11]);

- processed moisture measurements to produce plain and saturated straight line models (Section 2.2.2.5), with only some suggestions from dr inż. D. Buchczik (co-author of the paper [53]);
- processed the same moisture measurements again to identify and assess polynomial models (Section 2.2.2.6);
- calculated partition curves, examined correlations between them and the material moisture (Section 2.2.3), with only some suggestions from dr inż. D. Buchczik (co-author of the paper [53]);
- designed and performed the clean air identification experiment (Section 3.1); in particular, configured and tested the measurement hardware used in this experiment, including calibration of pressure transducers (Sections 3.1.4–3.1.5);
- designed and implemented (in MATLAB scripts) the data processing stages leading to static characteristics of air flow and pressure, and to sets of dynamic models' parameters corresponding to all possible operating points of the installation (Sections 3.2.1–3.2.3); in particular, this included the author's own algorithms for:
  - determination of proportionality constant c (Equation 3.7) and then iterative estimation of Reynolds number and other quantities describing the air flow (page 93),
  - outlier detection in steady-state data (Section 3.2.2.5),
  - initial estimation of parameters of 2nd order models with delay (pages 110–111);
- based on extensive literature research, derived the equations of phenomenological model of pressure losses; then, optimized model coefficients in several ways (Section 3.2.4);
- processed the measurements from the experiment on air flow with grinding media, and determined optimal model structures and their coefficients (Sections 3.3.2–3.3.3);
- developed and tested the open-loop air flows simulator (Chapter 4);
- designed and parametrized the air flow control algorithms (Section 5.4), then implemented them in simulation and tested their performance (Sections 5.3–5.4).

Contribution to the published scientific papers

The author of this dissertation contributed to the published scientific papers in the extent specified in the attached statements of co-authors.

List of (co-)authored scientific papers

Journal papers

1. **Oliwia Krauze**:
   „Model and simulator of inlet air flow in grinding installation with electromagnetic mill".
   Scientific Reports **2023**, 13(1), 8281:1–13.
   DOI: 10.1038/s41598-023-34664-0
   IF (2021): 4.996, 140 pts MEiN[1] .

2. Dariusz Buchczik, Sebastian Budzan, **Oliwia Krauze**, Roman Wyżgolik:
   „Moisture determination for fine-sized copper ore by computer vision and thermovision methods".
   Sensors **2023**, 23(3), 1220:1–32.
   DOI: 10.3390/s23031220
   IF (2021): 3.847, 100 pts MEiN.

3. **Oliwia Krauze**, Dariusz Buchczik, Sebastian Budzan:
   „Measurement-based modelling of material moisture and particle classification for control of copper ore dry grinding process".
   Sensors **2021**, 21(2), 667:1–20.
   DOI: 10.3390/s21020667
   IF (2019): 3.275, 100 pts MEiN.

Conference papers

1. Dariusz Foszcz, Marta Wołosiewicz-Głąb, **Oliwia Krauze**, Szymon Ogonowski, Tomasz Gawenda:
   „Influence of grinding media movement on the throughput of dry grinding circuit with electromagnetic mill".

[1] Points as announced by the Ministry of Education and Science (MEiN) in Poland on their list of scientific journals and reviewed materials from international conferences.

IOP Conference Series: Materials Science and Engineering **2019**, 641, 012018:1–6.
DOI: 10.1088/1757-899X/641/1/012018
Mineral Engineering Conference (MEC) 2019, 16–19.09.2019, Kocierz, Polska.

2. **Oliwia Krauze**, Marek Pawełczyk:
„Modelling dynamics of strongly coupled air paths in pneumatic transport system for milling product".
22nd International Conference on Methods and Models in Automation and Robotics (MMAR) **2017**, pp. 843–848.
DOI: 10.1109/MMAR.2017.8046938
MMAR 2017, 28–31.08.2017, Międzyzdroje, Polska.

3. Jan Wegehaupt, Dariusz Buchczik, **Oliwia Krauze**:
„Preliminary studies on modelling the drying process in product classification and separation path in an electromagnetic mill installation".
22nd International Conference on Methods and Models in Automation and Robotics (MMAR) **2017**, pp. 849–854.
DOI: 10.1109/MMAR.2017.8046939
MMAR 2017, 28–31.08.2017, Międzyzdroje, Polska.

4. Dariusz Buchczik, Jan Wegehaupt, **Oliwia Krauze**:
„Indirect measurements of milling product quality in the classification system of electromagnetic mill".
22nd International Conference on Methods and Models in Automation and Robotics (MMAR) **2017**, pp. 1039–1044.
DOI: 10.1109/mmar.2017.8046973
MMAR 2017, 28–31.08.2017, Międzyzdroje, Polska.

5. **Oliwia Krauze**, Marek Pawełczyk:
„Evaluation of copper ore granularity and flow rate using vibration measurements".
21st International Conference on Methods and Models in Automation and Robotics (MMAR) **2016**, pp. 1267–1272.
DOI: 10.1109/MMAR.2016.7575321
MMAR 2016, 29.08–01.09.2016, Międzyzdroje, Polska.

6. **Oliwia Krauze**, Marek Pawełczyk:
„Estimating parameters of loose material stream using vibration measurements".
17th International Carpathian Control Conference (ICCC) **2016**, pp. 378–383.
DOI: 10.1109/CarpathianCC.2016.7501127
ICCC 2016, 29.05–01.06.2016, Tatrzańska Łomnica, Słowacja.

Bibliography

[1] ABB. Field IT – 2600T series pressure transmitters, 2007. Data Sheet SS/264XS_6 (2007-09).

[2] H. Akaike. Information theory and an extension of the maximum likelihood principle. In *2nd International Symposium on Information Theory*, pages 267–281, 1973.

[3] ARLAB s.c. Przesiewacze przemyslowe [Industrial screens]. http://www.arlab.pl/przesiewp.html. Accessed: 2015-01-22.

[4] G. Ballantyne and M. Powell. Benchmarking comminution energy consumption for the processing of copper and gold ores. *Minerals Engineering*, 65:109–114, 2014. doi:10.1016/j.mineng.2014.05.017.

[5] I. R. Barratt, Y. Yan, B. Byrne, and M. S. A. Bradley. Mass flow measurement of pneumatically conveyed solids using radiometric sensors. *Flow Measurement and Instrumentation*, 11(3):223—-235, 2000. doi:10.1016/S0955-5986(00)00022-4.

[6] Belimo. Technical data sheet LMQ24A-SR. https://www.belimo.com/mam/Datasheets/en-gb/belimo_LMQ24A-SR_datasheet_en-gb.pdf, 2022. Version 2022-05-17. Accessed: 2022-06-17.

[7] beyerdynamic. MM 1 measurement microphone. https://global.beyerdynamic.com/mm-1.html, 2019. Rev. E7/MM 1 (07.19). Accessed: 2022-09-14.

[8] E. Bielinska. Klasyczne metody identyfikacji odpowiedzi skokowej [Classical methods of step response identification]. In J. Kasprzyk, editor, *Identyfikacja procesow [Process identification]*, pages 51–62. Wydawnictwo Politechniki Slaskiej, Gliwice, Poland, 2002.

[9] W. Bolton. System parameters. In *Control Systems*, chapter 4, pages 85–98. Newnes, Oxford, UK, 2002. doi:10.1016/B978-075065461-6/50004-0.

[10] D. Buchczik, S. Budzan, O. Krauze, and R. Wyzgolik. Moisture determination for fine-sized copper ore by computer vision and thermovision methods. *Sensors*, 23(3):1220, 2023. doi:10.3390/s23031220.

[11] D. Buchczik, J. Wegehaupt, and O. Krauze. Indirect measurements of milling product quality in the classification system of electromagnetic mill. In *2017 22nd International Conference on Methods and Models in Automation and Robotics (MMAR)*, pages 1039–1044, 2017. doi:10.1109/MMAR.2017.8046973.

[12] S. Budzan. Automated grain extraction and classification by combining improved region growing segmentation and shape descriptors in electromagnetic mill classification system. In A. Verikas, P. Radeva, D. Nikolaev, and J. Zhou, editors, *Tenth International Conference on Machine Vision (ICMV 2017)*, volume 10696, page 106960B. International Society for Optics and Photonics, SPIE, 2018. doi:10.1117/12.2309765.

[13] S. Budzan, D. Buchczik, M. Pawelczyk, and J. Tuma. Combining segmentation and edge detection for efficient ore grain detection in an electromagnetic mill classification system. *Sensors*, 19(8):1805, 2019. doi:10.3390/s19081805.

[14] S. Budzan and M. Pawelczyk. Grain size determination and classification using adaptive image segmentation with shape information for milling quality evaluation. *Diagnostyka*, 19(1):41–48, 2018. doi:10.29354/diag/80974.

[15] S. Budzan, M. Pawelczyk, and S. Ogonowski. Sposob oceny frakcji ziarnowych oraz powierzchni czynnej rud metali metoda optyczna [Method for assessment of grain fractions and active surface of metal ores by optical method]. Polish patent application no. P.424672, filed 26 February 2018. `https://ewyszukiwarka.pue.uprp.gov.pl/search/pwp-details/P.424672`.

[16] K. P. Burnham and D. R. Anderson. *Model Selection and Multimodel Inference: A Practical Information-Theoretic Approach*. Springer-Verlag, New York, NY, US, 2nd edition, 2002.

[17] C. A. Cantrell. Technical note: Review of methods for linear least-squares fitting of data and application to atmospheric chemistry problems. *Atmospheric Chemistry and Physics Discussions*, 8:5477–5487, 2008. doi:10.5194/acp-8-5477-2008.

[18] W. Chaiworapuek. The engineering investigation of the water flow past the butterfly valve. Master's thesis, Institut National des Sciences Appliquees de Lyon, France; Escola Tecnica Superior d'Enginyeria Industrial de Barcelona, Universitat

Politecnica de Catalunya, Spain; The College of The Holy and Undivided Trinity of Queen Elizabeth near Dublin, Ireland, 2007. Erasmus Mundus Master. http://www.tara.tcd.ie/bitstream/handle/2262/11019/final.pdf.

[19] N.-S. Cheng. Formulas for friction factor in transitional regimes. *Journal of Hydraulic Engineering*, 134:1357–1362, 2008. doi:10.1061/(ASCE)0733-9429(2008)134:9(1357).

[20] A. Chirokov. MATLAB Central File Exchange: Scattered data interpolation and approximation using radial base functions. https://www.mathworks.com/matlabcentral/fileexchange/10056-scattered-data-interpolation-and-approximation-using-radial-base-functions. Published: 2006-10-09. Accessed: 2022-07-01.

[21] D. Clamond. Efficient resolution of the Colebrook equation. *Industrial & Engineering Chemistry Research*, 48(7):3665–3671, 2009. doi:10.1021/ie801626g.

[22] C. F. Colebrook. Turbulent flow in pipes, with particular reference to the transition region between the smooth and rough pipe laws. *Journal of the Institution of Civil Engineers*, 11(4):133–156, 1939. doi:10.1680/ijoti.1939.13150.

[23] Crane Co. Flow of fluids through valves, fittings, and pipe, 1982. Technical paper no. 410M. 4th printing.

[24] J. A. Curry, M. J. Ismay, and G. J. Jameson. Mine operating costs and the potential impacts of energy and grinding. *Minerals Engineering*, 56:70–80, 2014. doi:10.1016/j.mineng.2013.10.020.

[25] M. Cwiakala, J. Szymanska, R. Sosinski, and W. Nowak. Aktywowanie popiolow lotnych z wegla brunatnego Elektrowni Patnow w mlynie elektromagnetycznym [Brown coal fly-ash from Electric Power Station "Patnow" activation in electromagnetic mill]. *Engineering and Protection of Environment*, 11(4):491–502, 2008.

[26] R. Darby. Correlate pressure drops through fittings. *Chemical Engineering*, 106(7):101–104, 1999.

[27] R. Darby. Correlate pressure drops through fittings. *Chemical Engineering*, 108(4):127–130, 2001.

[28] F. J. del Río, J. Riu, and F. X. Rius. Prediction intervals in linear regression taking into account errors on both axes. *Journal of Chemometrics*, 15:773–788, 2001. doi:10.1002/cem.663.

[29] A. Del Toro. Computational fluid dynamics analysis of butterfly valve performance factors. Master's thesis, Utah State University, Logan, Utah, USA, 2012. DOI: 10.26076/9551-16be. https://digitalcommons.usu.edu/etd/1456.

[30] Delta OHM. HD29... series temperature, humidity and air speed transmitters. https://www.deltaohm.com/wp-content/uploads/document/DeltaOHM_HD2903_datasheet_ENG.pdf, 2022. Rev. 2.0 (2022-05). Accessed: 2022-06-17.

[31] Delta OHM. HD48... series, HD49... series passive or active transmitters – temperature, relative humidity and temperature, dew point and temperature. https://www.deltaohm.com/wp-content/uploads/document/DeltaOHM_HD48_HD49_datasheet_ENG.pdf, 2022. Rev. 1.3 (2022-03). Accessed: 2022-06-17.

[32] J. Drzymala. Section 2.2.3.2.3: Partition curve. In *Mineral processing. Foundations of theory and practice of minerallurgy*, pages 89–91. Oficyna Wydawnicza Politechniki Wroclawskiej, Wroclaw, Poland, 1st edition, 2007. URL http://www.dbc.wroc.pl/Content/2070/Drzymala_mineral.pdf.

[33] DYNA Instruments. DYNAvel. For the determination of solids velocity. https://www.dynainstruments.com/en/productlinks/dynavel.html. Accessed: 2022-08-29.

[34] ELTRAF, Lubliniec, Poland. *Dokumentacja techniczna nr 04 wzbudnika magnetycznego typu WZB.MAGϕ200 [Technical documentation no. 04 for magnetic inductor of type WZB.MAGϕ200]*, 2017.

[35] ELTRAF, Lubliniec, Poland. *Instrukcja obslugi nr 05 wzbudnika magnetycznego typu WZB.MAGϕ100 [User manual no. 05 for magnetic inductor of type WZB.MAGϕ100]*, 2017.

[36] T. D. Fahlenbock. Coriolis mass flow meter: High accuracy for high flowrates. *Powder and Bulk Engineering*, 19(9):29–33, 2005.

[37] D. Foszcz, M. Wolosiewicz-Glab, O. Krauze, S. Ogonowski, and T. Gawenda. Influence of grinding media movement on the throughput of dry grinding circuit with electromagnetic mill. *IOP Conference Series: Materials Science and Engineering*, 641(1):012018, 2019. doi:10.1088/1757-899x/641/1/012018.

[38] M. Galonska. Pomiar przeplywu materialow sypkich w czasie rzeczywistym [Measuring flow rate of loose solids in real time]. *Pod kontrola*, 34(4):6–8, 2015.

[39] P. Harlan. Methods of measuring solids flow. https://www.jaspereng.com/methods-of-measuring-solids-flow/. Accessed: 2022-09-17.

[40] W. B. Hooper. The two-K method predicts head losses in pipe fittings. *Chemical Engineering*, August 24:96–99, 1981.

[41] Y. Hu, X. Huang, X. Qian, L. Gao, and Y. Yan. Online particle size measurement through acoustic emission detection and signal analysis. In *IEEE Instrumentation and Measurement Technology Conference Proceedings*, pages 949–953, Montevideo, Uruguay, 2014. doi:10.1109/I2MTC.2014.6860883.

[42] C. M. Hurvich and C.-L. Tsai. Regression and time series model selection in small samples. *Biometrika*, 76(2):297–307, 1989. doi:10.1093/biomet/76.2.297.

[43] B. Illowsky and S. Dean. Testing the significance of the correlation coefficient. In *Collaborative statistics*, chapter 12.7, pages 536–540. Connexions, Rice University, Houston, TX, USA, 2012. URL http://cnx.org/content/col10522/1.40/.

[44] Industrio Service. Okragle sito wibracyjne serii VS [VS series round vibrating sieve]. http://www.industrio.pl/baza-maszyn-uzywanych/single-view/article/okragle-sito-wibracyjne-serii-vs/. Accessed: 2015-01-22.

[45] International Civil Aviation Organization. Manual of the ICAO standard atmosphere extended to 80 kilometres (262 500 feet), 1993. 3rd edition. Doc 7488/3.

[46] J. Engelsmann AG. JEL easyVib. http://www.engelsmann.de/en/products/screening-technology/vibration-screening-machines.html. Accessed: 2015-01-22.

[47] S. Y. Jeon, J. Y. Yoon, and M. S. Shin. Flow characteristics and performance evaluation of butterfly valves using numerical analysis. *IOP Conference Series: Earth and Environmental Science*, 12:012099, 2010. doi:10.1088/1755-1315/12/1/012099.

[48] KAMIKA Instruments. Analyzer AWK 3D. http://kamika.pl/en/AWK_3D. Accessed: 2015-01-22.

[49] T. Kimura, T. Tanaka, K. Fujimoto, and K. Ogawa. Hydrodynamic characteristics of a butterfly valve – prediction of pressure loss characteristics. *ISA Transactions*, 34(4):319–326, 1995. doi:10.1016/0019-0578(95)00024-0.

[50] B. Kordala. Statyczne modele elementow ukladu mielenia z mlynem elektromagnetycznym [Static models of the elements of grinding installation with electromagnetic mill]. Master's thesis, Silesian University of Technology, Gliwice, Poland, 2018. Unpublished.

[51] O. Krauze. Zastosowanie pomiarow akustycznych i pomiarow drgan w ukladzie mielenia mlynem elektromagnetycznym [Application of acoustic and vibration measurements to analysis of grinding process in electromagnetic mill]. Master's thesis, Silesian University of Technology, Gliwice, Poland, 2015.

[52] O. Krauze. Model and simulator of inlet air flow in grinding installation with electromagnetic mill. *Scientific Reports*, 13:8281, 2023. doi:10.1038/s41598-023-34664-0.

[53] O. Krauze, D. Buchczik, and S. Budzan. Measurement-based modelling of material moisture and particle classification for control of copper ore dry grinding process. *Sensors*, 21(2):667, 2021. doi:10.3390/s21020667.

[54] O. Krauze and M. Pawelczyk. Estimating parameters of loose material stream using vibration measurements. In *2016 17th International Carpathian Control Conference (ICCC)*, pages 378–383, 2016. doi:10.1109/CarpathianCC.2016.7501127.

[55] O. Krauze and M. Pawelczyk. Evaluation of copper ore granularity and flow rate using vibration measurements. In *2016 21st International Conference on Methods and Models in Automation and Robotics (MMAR)*, pages 1267–1272, 2016. doi:10.1109/MMAR.2016.7575321.

[56] O. Krauze and M. Pawelczyk. Modelling dynamics of strongly coupled air paths in pneumatic transport system for milling product. In *2017 22nd International Conference on Methods and Models in Automation and Robotics (MMAR)*, pages 843–848, 2017. doi:10.1109/MMAR.2017.8046938.

[57] J. Kwasniewski. Eksperymentalne metody wyznaczania modeli matematycznych [Experimental methods for determining mathematical models]. In *Podstawy automatyki: Przykladowe zadania z rozwiazaniami [Control fundamentals: Example problems with solutions]*, chapter 3. 2003. Retrieved from `http://home.agh.edu.pl/~pautom/wykladPrzykladoweZadania.php`. Accessed 2023-04-25.

[58] H. Lokiec and T. Lokiec. Wzbudnik mlyna elektromagnetycznego [Inductor for electromagnetic mill]. Polish Patent PL 226554, filed 19 May 2015, issued 16 February 2017, published 31 August 2017. `https://ewyszukiwarka.pue.uprp.gov.pl/search/pwp-details/P.412389`.

[59] G. C. Lowrison. *Crushing and grinding: The size reduction of solid materials*. Butterworths, London, England, 1974.

[60] T. E. Marlin. *Process Control: Designing Processes and Control Systems for Dynamic Performance*, chapter 6, sec. 6.3, pages 201–209. McGraw-Hill, Inc., New

York, NY, USA, 2 edition, 1995. Also available online: http://pc-textbook.mcmaster.ca/Marlin-Ch06.pdf (accessed: 2023-04-25).

[61] MathWorks. MATLAB documentation: Discrete PID controller. https://www.mathworks.com/help/simulink/slref/discretepidcontroller.html. Accessed: 2023-06-14.

[62] MathWorks. MATLAB documentation: fit function. https://www.mathworks.com/help/curvefit/fit.html. Accessed: 2023-04-28.

[63] MathWorks. MATLAB documentation: fmincon function. https://www.mathworks.com/help/optim/ug/fmincon.html. Accessed: 2022-07-12.

[64] MathWorks. MATLAB documentation: fminsearch function. https://www.mathworks.com/help/matlab/ref/fminsearch.html. Accessed: 2022-07-30.

[65] MathWorks. MATLAB documentation: ga function. https://www.mathworks.com/help/gads/ga.html. Accessed: 2022-07-12.

[66] MathWorks. MATLAB documentation: gradient function. https://www.mathworks.com/help/matlab/ref/gradient.html. Accessed: 2022-08-01.

[67] MathWorks. MATLAB documentation: scatteredInterpolant function. https://www.mathworks.com/help/matlab/ref/scatteredinterpolant.html. Accessed: 2022-07-01.

[68] MathWorks. MATLAB documentation: smooth3 function. https://www.mathworks.com/help/matlab/ref/smooth3.html. Accessed: 2022-07-01.

[69] Monitor Technologies, LLC. QuantiMass. Mass flow measurement sensor for powders & bulk solids. http://www.monitortech.com/mass-flow-meter.shtml, 2014. Accessed: 2022-08-29.

[70] L. F. Moody. Friction factors for pipe flow. *Transactions of the American Society of Mechanical Engineers*, 66:671–684, 1944.

[71] M. Morrissey. Can you go with the flow? Solids flowmeters for industrial applications. *Bulk Solids Handling*, 34(1):40–42, 2014.

[72] T. Napier-Munn. Is progress in energy-efficient comminution doomed? *Minerals Engineering*, 73:1–6, 2015. doi:10.1016/j.mineng.2014.06.009. Special issue: Comminution.

[73] National Instruments. High-speed M series multifunction DAQ for USB – 16-bit, up to 1.25 MS/s, integrated BNC connectivity, 2014.

[74] O. D. Neikov. Chapter 11. Processing of powders and processing equipment. In O. D. Neikov, S. S. Naboychenko, I. V. Murashova, V. G. Gopienko, I. V. Frishberg, and D. V. Lotsko, editors, *Handbook of Non-Ferrous Metal Powders*, pages 227–264. Elsevier, Oxford, 2009. doi:10.1016/B978-1-85617-422-0.00011-2.

[75] A. O'Dwyer. *Handbook of PI and PID Controller Tuning Rules*. Imperial College Press, London, UK, 3rd edition, 2009. doi:10.1142/p575.

[76] S. Ogonowski, Z. Ogonowski, and M. Pawelczyk. Model of the air stream ratio for an electromagnetic mill control system. In *2016 21st International Conference on Methods and Models in Automation and Robotics (MMAR)*, pages 901–906, 2016. doi:10.1109/MMAR.2016.7575257.

[77] S. Ogonowski, Z. Ogonowski, and M. Pawelczyk. Multi-objective and multi-rate control of the grinding and classification circuit with electromagnetic mill. *Applied Sciences*, 8(4):506, 2018. doi:10.3390/app8040506.

[78] S. Ogonowski, Z. Ogonowski, and M. Swierzy. Power optimizing control of grinding process in electromagnetic mill. In *2017 21st International Conference on Process Control (PC)*, pages 370–375, 2017. doi:10.1109/PC.2017.7976242.

[79] S. Ogonowski, Z. Ogonowski, M. Swierzy, and M. Pawelczyk. Control system of electromagnetic mill load. In *2017 25th International Conference on Systems Engineering (ICSEng)*, pages 69–76, 2017. doi:10.1109/ICSEng.2017.23.

[80] S. Ogonowski, M. Wolosiewicz-Glab, Z. Ogonowski, D. Foszcz, and M. Pawelczyk. Comparison of wet and dry grinding in electromagnetic mill. *Minerals*, 8(4), 2018. doi:10.3390/min8040138.

[81] M. Pawelczyk, Z. Ogonowski, and S. Ogonowski. Sposob sterowania wypelnieniem komory roboczej mlyna elektromagnetycznego w ukladzie z transportem pneumatycznym [Method for controlling the filling of the electromagnetic mill working chamber in the arrangement with pneumatic transport]. Polish patent application no. P.421160, filed 3 April 2017. https://ewyszukiwarka.pue.uprp.gov.pl/search/pwp-details/P.421160.

[82] M. Pawelczyk, Z. Ogonowski, S. Ogonowski, D. Foszcz, D. Saramak, and T. Gawenda. Sposob mielenia na sucho w mlynie elektromagnetycznym [Method of dry milling in electromagnetic mill]. Polish Patent PL 228350, filed 6 July 2015, issued 25 October 2017, published 30 March 2018. https://ewyszukiwarka.pue.uprp.gov.pl/search/pwp-details/P.413041.

[83] PCB Piezotronics. Triaxial ICP® accelerometer, model number 356A17. Rev. F.

[84] K. Pearson. Mathematical contributions to the theory of evolution. III. Regression, heredity, and panmixia. *Philosophical Transactions of the Royal Society of London. Series A, Containing Papers of a Mathematical or Physical Character*, 187:253–318, 1896. doi:10.1098/rsta.1896.0007.

[85] Radwag. MA 110.R moisture analyzer. https://radwag.com/en/wagosuszarka-ma-110-r,w1,6Q2,101-103-108-103. Online. Accessed: 2022-07-30.

[86] C. Sammut and G. I. Webb. Leave-one-out cross-validation. In C. Sammut and G. I. Webb, editors, *Encyclopedia of Machine Learning*, pages 600–601. Springer, Boston, MA, US, 2010. doi:10.1007/978-0-387-30164-8_469.

[87] K. Slawinski, K. Knas, M. Gandor, and W. Nowak. Suszenie wegla brunatnego w energetyce – mozliwosci zastosowania mlyna elektromagnetycznego [Brown coal drying in the power industry – the possibility of application of an electromagnetic mill]. *Scientific Letters of Rzeszow University of Technology. Mechanics*, 86(3/14):453–460, 2014.

[88] K. Slawinski, K. Knas, and W. Nowak. Sposob suszenia i domielania materialow, zwlaszcza wegla brunatnego i kamiennego oraz urzadzenie do suszenia i domielania materialow, zwlaszcza wegla brunatnego oraz kamiennego [Method for drying and regrinding of materials, preferably brown coal and hard coal and the device for drying and regrinding of materials, preferably brown coal and hard coal]. Polish Patent PL 228605, filed 29 July 2015, issued 14 November 2017, published 30 April 2018. https://ewyszukiwarka.pue.uprp.gov.pl/search/pwp-details/P.412932.

[89] Smay. PJB – przepustnica okragla jednoplaszczyznowa [PJB – circular single-plane damper]. https://www.smay.pl/wp-content/uploads/download-manager-files/pjb_smay_pl.pdf, 2020. Version 7.0.0 (2020-09-17). Accessed: 2022-06-17.

[90] R. Sosinski. *Opracowanie metodyki projektowania trojfazowych wzbudnikow z biegunami jawnymi pola wirujacego do mlynow elektromagnetycznych [Development of design methodology for three-phase salient-pole exciters of rotating field for electromagnetic mills]*. PhD thesis, Czestochowa University of Technology, Czestochowa, Poland, 2006.

[91] R. Sosinski, W. Nowak, P. Rolicz, and A. Szczypiorowski. Mlyn elektromagnetyczny [Electromagnetic mill]. Polish patent application P.382610, filed 8 June 2007. https://ewyszukiwarka.pue.uprp.gov.pl/search/pwp-details/P.382610.

[92] B. Spalinska, R. Stec, and K. Sztaba. Miejsce i rola przerobki rudy w kompleksie technologicznym KGHM Polska Miedz S.A. [the location and role of ore processing

in technological complex of KGHM Polska Miedz S.A.]. In *Monografia KGHM PM SA*, pages 463–472. KGHM CUPRUM Sp. z o.o. CBR, Lubin, Poland, 2007.

[93] C. Spearman. The proof and measurement of association between two things. *The American Journal of Psychology*, 15(1):72–101, 1904. doi:10.2307/1412159.

[94] S. Styla. A new grinding technology using an electromagnetic mill – testing the efficiency of the process. *ECONTECHMOD: An International Quarterly Journal on Economics of Technology and Modelling Processes*, 6(1):81–88, 2017.

[95] S. Styla and W. Pietrzyk. Mlyn elektromagnetyczny z trojfazowym wzbudnikiem pola wirujacego [Electromagnetic mill with the three-phase rotating field exciter]. Polish Patent PL 221027, filed 17 June 2011, issued 17 February 2015, published 29 February 2016. https://ewyszukiwarka.pue.uprp.gov.pl/search/pwp-details/P.395321.

[96] SWR engineering. SolidFlow 2.0 – dry bulk solids measurement. http://www.swr-engineering.com/en/products/throughput-measuring-dry-bulk-solids-measuring-flow-metering.html. Accessed: 2015-01-22.

[97] K. Szczepaniak, B. Skorupska, and N. Kubacz. Badania procesu domielania polproduktow miedziowych w mlynie elektromagnetycznym [research into regrinding process of copper middlings in the electromagnetic mill]. *Cuprum Ore Mining Scientific and Technical Magazine*, 2(75):47–53, 2015.

[98] tec-science. Viscosity of liquids and gases. https://www.tec-science.com/mechanics/gases-and-liquids/viscosity-of-liquids-and-gases/. Uploaded: 2020-03-25. Accessed: 2022-06-21.

[99] H. Theil. *Economic forecasts and policy*. North-Holland Pub. Co., Amsterdam, 2 edition, 1961.

[100] Visual Capitalist for Coalition for Eco Efficient Comminution (CEEC). Comminution and why smart companies are focusing on it. https://www.ceecthefuture.org/images/infographic/comminution-infographic.png. Accessed: 2022-08-24.

[101] J. Wegehaupt and D. Buchczik. Sposob ciaglego pomiaru wilgotnosci materialow sypkich podczas ich transportu oraz urzadzenie do realizacji tego sposobu [Method for continuous measurements of humidity of loose materials in transport and the device for the execution of this method]. Polish Patent PL 239592, filed 13 January 2017, issued 22 September 2021, published 20 December 2021. https://ewyszukiwarka.pue.uprp.gov.pl/search/pwp-details/P.420181.

[102] J. Wegehaupt and D. Buchczik. Moisture measurement of bulk materials in an electromagnetic mill. In *2017 18th International Carpathian Control Conference (ICCC)*, pages 353–358, 2017. doi:10.1109/CarpathianCC.2017.7970425.

[103] J. Wegehaupt, D. Buchczik, and O. Krauze. Preliminary studies on modelling the drying process in product classification and separation path in an electromagnetic mill installation. In *2017 22nd International Conference on Methods and Models in Automation and Robotics (MMAR)*, pages 849–854, 2017. doi:10.1109/MMAR.2017.8046939.

[104] J. Weisbach and E. B. Coxe. *Mechanics of engineering. Theoretical mechanics, with an introduction to the calculus*, page 902 (Table VI). D. Van Nostrand, New York, USA, 6th American edition, 1882.

[105] F. M. White. *Fluid mechanics*. McGraw-Hill, New York, USA, 7th edition, 2011.

[106] J. B. Willett and J. D. Singer. Another cautionary note about R^2: its use in weighted least-squares regression analysis. *The American Statistician*, 42(3):236–238, 1988. doi:10.1080/00031305.1988.10475573.

[107] K. Wnek. Analiza uziarnienia on-line [On-line granularity analysis]. http://www.grupa-wolff.eu/cp/art/pomiar-uziarnienia-materialow-sypkich-online/pomiar-uziarnienia-materialow-sypkich-online.pdf. Accessed: 2022-08-29.

[108] WOLFF GROUP. Screening machines. http://www.grupa-wolff.com/equipment-powders/screening-machines/. Accessed: 2022-08-29.

[109] M. Wolosiewicz-Glab, D. Foszcz, and T. Gawenda. Analysis of possiblilities of obtaining the fine particle size in mills of various designs. *Inzynieria Mineralna*, 17(1):223–231, 2016.

[110] M. Wolosiewicz-Glab, D. Foszcz, D. Saramak, T. Gawenda, and D. Krawczykowski. Analysis of a grinding efficiency in the electromagnetic mill for variable process and feed parameters. *E3S Web Conf.*, 18:01012, 2017. doi:10.1051/e3sconf/201712301012.

[111] M. Wolosiewicz-Glab, S. Ogonowski, and D. Foszcz. Construction of the electromagnetic mill with the grinding system, classification of crushed minerals and the control system. *IFAC-PapersOnLine*, 49(20):67–71, 2016. doi:10.1016/j.ifacol.2016.10.098. 17th IFAC Symposium on Control, Optimization and Automation in Mining, Mineral and Metal Processing MMM 2016.

[112] M. Wolosiewicz-Glab, S. Ogonowski, D. Foszcz, and T. Gawenda. Assessment of classification with variable air flow for inertial classifier in dry grinding circuit with electromagnetic mill using partition curves. *Physicochemical Problems of Mineral Processing*, 54:440–447, 2018.

[113] M. Wolosiewicz-Glab, S. Ogonowski, D. Foszcz, and T. Gawenda. Assessment of classification with variable air flow for inertial classifier in dry grinding circuit with electromagnetic mill using partition curves. *Physicochemical Problems of Mineral Processing*, 54(2):440–447, 2018. doi:10.5277/ppmp1867.

[114] M. Wolosiewicz-Glab, P. Pieta, D. Foszcz, T. Niedoba, and T. Gawenda. Adjustment of limestone grinding in an electromagnetic mill for use in production of sorbents for flue gas desulphurization. *Physicochemical Problems of Mineral Processing*, 55(3):779–791, 2019. doi:10.5277/ppmp19011.

[115] M. Wolosiewicz-Glab, P. Pieta, T. Niedoba, and D. Foszcz. Approximation of partition curves for electromagnetic mill with inertial classifier – case study. *IOP Conference Series: Earth and Environmental Science*, 95(4):042037:1–8, 2017. doi:10.1088/1755-1315/95/4/042037.

[116] C. Yau. R tutorial: Adjusted coefficient of determination. http://www.r-tutor.com/elementary-statistics/multiple-linear-regression/adjusted-coefficient-determination. Online. Accessed: 2022-09-27.

[117] D. York, N. M. Evensen, M. Lopez Martinez, and J. De Basabe Delgado. Unified equations for the slope, intercept, and standard errors of the best straight line. *American Journal of Physics*, 72(3):367–375, 2004. doi:10.1119/1.1632486.

[118] Zoom. H4n Pro Black. https://zoomcorp.com/en/de/handheld-recorders/handheld-recorders/h4n-pro/. Accessed: 2022-09-14.